

Electronic Thesis and Dissertation Repository

12-15-2011 12:00 AM

Nanoplasmonic Sensors based on Periodic Arrays of Gold Nanoparticles

Hao Jiang, *The University of Western Ontario*

Supervisor: Dr. Jayshri Sabarinathan, *The University of Western Ontario*

Joint Supervisor: Dr. Silvia Mittler, *The University of Western Ontario*

A thesis submitted in partial fulfillment of the requirements for the Doctor of Philosophy degree in Electrical and Computer Engineering

© Hao Jiang 2011

Follow this and additional works at: <https://ir.lib.uwo.ca/etd>



Part of the [Electromagnetics and Photonics Commons](#)

Recommended Citation

Jiang, Hao, "Nanoplasmonic Sensors based on Periodic Arrays of Gold Nanoparticles" (2011). *Electronic Thesis and Dissertation Repository*. 329.

<https://ir.lib.uwo.ca/etd/329>

This Dissertation/Thesis is brought to you for free and open access by Scholarship@Western. It has been accepted for inclusion in Electronic Thesis and Dissertation Repository by an authorized administrator of Scholarship@Western. For more information, please contact wlsadmin@uwo.ca.

Nanoplasmonic Sensors based on Periodic Arrays of Gold Nanoparticles

(Spine title: Nanoplasmonic Sensors based on Gold Nanoparticle Arrays)

(Thesis format: integrated articles)

by

Hao Jiang

Graduate Program
in
Engineering Science
Electrical and Computer Engineering

A thesis submitted in partial fulfillment
of the requirements for the degree of
Doctor of Philosophy

School of Graduate and Postdoctoral Studies
The University of Western Ontario
London, Ontario, Canada

© Hao Jiang 2011

Certificate of Examination

THE UNIVERSITY OF WESTERN ONTARIO
SCHOOL OF GRADUATE AND POSTDOCTORAL STUDIES

Supervisor:

Dr. Jayshri Sabarinathan

Examiners:

Dr. Kazimierz Adamiak

Co-Supervisor:

Dr. Silvia Mittler

Dr. Robert Sobot

Dr. Amarjeet Bassi

Dr. Stephen O'Leary

The thesis by

Hao Jiang

entitled:

Nanoplasmonic Sensors based on Periodic Arrays of Gold Nanoparticles

is accepted in partial fulfillment of the

requirements for the degree of

Doctor of Philosophy

Date: _____

Chair of Examination Board

Abstract

Nanoplasmonic sensors use the localized surface plasmon resonance (LSPR) of metal nanostructures to sense the refractive index change in a surface-bound layer caused by biomolecular interactions or changing chemical environment. In this thesis, four types of sensor configurations based on gold nanoparticle arrays are thoroughly investigated.

The first configuration is a periodic array of gold nanoparticles excited by the evanescent field of an optical waveguide mode. Since light carried by a waveguide mode propagates along the same plane of the periodicities, the coupling of nanoparticles are strongly affected by the photonic crystal lattice. This configuration is investigated both in simulations and in experiments, focusing on the sensing aspects of various spectral features attributed to different types of LSPRs. In simulation, it was found that, the LSPR modes of the gold nanoparticle array excited by the waveguide modes demonstrated similar trends as the array being excited by normal transmission. However, under waveguide excitation, the coherent interactions of the periodic array are through the grating order carried by the waveguide mode. Selective suppression of LSPR and grating-induced mode were also found from the waveguide excitation, which extended the existing knowledge of the optical properties of the periodic array. Under waveguide excitation, both quadrupolar and dipolar resonance peaks are sensitive to the surface-bound layer, however, the grating-induced mode is not sensitive. Preliminary experiments were conducted on ion-exchanged channel waveguides on BK7 glass and the trends of the dipolar resonance peak has been proved.

The second configuration is a biosensor based on gold nanodisk arrays under normal transmission. By varying the lattice constant, the refractive index resolution was found to depend on the lattice constant, as a result of the figure of merit and signal/noise ratio together. The best refractive index resolution achieved is better than 1.5×10^{-4} RIU, when lattice constant equals to 550 nm. The sensor structure was used in detecting the binding of antigen (human IgG) and antibody (anti-human IgG) and a limit of detection better than 1 ng/mL (equivalent to 8 pM) was achieved.

The third configuration is a chemical sensor based on a gold nanocrescent array combined with hydrogel. Under changing chemical environment, the hydrogel thin

film can swell or shrink, depending on the pH of the solution. The swelling or shrinking of hydrogel thin film changes the refractive index, which can be detected by the near-infrared LSPR peak shift of the gold nanocrescent array. The sensor was proved to function in the range 4.5 pH - 6.4 pH and the detection resolution is better than 0.045 pH. At the most sensitive point, $\text{pH} = \text{p}K_a = 5.45$, the peak-shift sensitivity is 11.1 nm/pH and transmission-shift sensitivity is 1.16 /pH.

The fourth configuration is periodic array of gold nanorings under normal transmission. The effects of coherent interactions on the sensing characteristics of periodic arrays of gold nanorings were investigated in detail. In simulations, it was found that, the sensitivity, figure of merit both significantly depend on the lattice constant. The structure with highest figure of merit was found to be the one with lattice constant smaller than and close to the resonant lattice constant. The periodic array can improve the figure of merit by more than 2.5 times, compared to a single nanoring, which demonstrates the great sensing capabilities of periodic arrays. The simulated trend was proved by the experiments of the gold nanoring arrays patterned on top of pyrex substrate. A method was also demonstrated on how to tune the sensor structure to function in a desired spectrum window, with high figure of merit and high signal/noise ratio, at the same time. The highest figure of merit achieved from experiment is around 5.1, which is among the highest in literature.

Keywords: localized surface plasmon resonance, coherent interaction, periodic array, gold nanoparticle, gold nanodisk, gold nanocrescent, gold nanoring, waveguide, ion-exchange, evanescent spectroscopy, photonic crystal, nanofabrication, bio/chemical sensor, hydrogel, electron beam lithography.

Acknowledgements

I would like to thank my supervisors Prof. Jayshri Sabarinathan and Prof. Silvia Mittler for their kind support in my graduate study. From them, I learned not only the science of 'nano' and but also the science of 'academia', which are so invaluable to me. I am proud to be their student and I wish one day they will be proud of me too. So many people have done me favors in my research. Whether big or small favors, I really appreciate their generous help. Sometimes, even a random talk or a pointless joke can make things much easier. I try my best to list here all the names that have helped me, supported me and given me guidance in my research during all these many years. They are my dear colleagues, my co-workers, my teachers and staffs of the labs: Aref Bakhtazad, Todd Simpson, Tim Goldhawk, Rick Glew, Tingjie Li, Erden Ertorer, Weiqing Shi, James Pond, Xuan Huo, Rajat Dey, Yi Wang, Surabhi Mittal, Amith Gujjula, Jan Markowski, Anna Sauer, Anil Murdroboyina, Qiuquan Guo, Sandra Vilovski, Jun Yang, Ian Mitchel, Xueliang Sun, John Murkin, Reuven Gordon, Nancy Bell, Amarjeet Bassi, Touraj Manifar, Hossein Hojjati, Abdollah Hassanzadeh, Asad, Christopher, Thomas, Teige, Dmetro Grebenn, Yi Gan, Maryam, Behafarid, Sonia, David, Irenusz, Maher, Betty, Sarvesh. I really hope some of them will not blame me for not knowing their last names... Thanks to all my dear friends, who have always been supporting me. They are the great treasure of my life. This thesis is dedicated to my parents and my wife, Can. Their constant love are the energy and courage that have been taking me forward.

Co-authorship Statement

The following thesis contains material from previously published manuscripts co-authored by Hao Jiang, Jayshri Sabarinathan, Silvia Mittler, Jan Markowski, Touraj Manifar, Tingjie Li, and Jun Yang. The manuscripts in preparation are also co-authored by Aref Bakhtazad, Hossein Hojjati and Erden Ertorer.

Hao Jiang conducted most of the experimental work, all the numerical simulations and all the theoretical analysis. In detail, the fabrications of the gold nanoparticles and scanning electron microscope characterizations of the fabricated structures were all performed by Hao Jiang. The fabrications of the channel waveguides and the coupling angle characterizations were all done by Hao Jiang. All the simulations, data analysis and theoretical interpretations were carried out by Hao Jiang. All the measurement setups, including normal transmission and waveguide transmission, were designed and constructed by Hao Jiang, and all the measurement results from these setups were acquired by Hao Jiang, too. Hao Jiang has also done all the surface chemistry procedures presented in Chapter 2, Chapter 5 and Chapter 7.

The waveguide pattern photo-mask used in the work presented in Chapter 4 was designed by Aref Bakhtazad. The pH-responsive hydrogel thin film in Chapter 6 was coated by Jan Markowski. The fluidic devices used in Chapter 5, Chapter 7 and Chapter 8 were constructed by Tingjie Li. The atomic force microscope images in Chapter 4 were acquired by Qiuquan Guo.

to my parents and my wife, Can

Table of Contents

Certificate of Examination	ii
Abstract	iii
Acknowledgements	v
Co-authorship Statement	vi
Table of Contents	viii
List of Tables	xii
List of Figures	xiii
Acronyms	xvii
1 Introduction	1
1.1 Nanoplasmonic sensors	1
1.2 LSPR sensor based on gold nanoparticles	5
1.2.1 LSPR of gold nanoparticles	5
1.2.2 Main performance characteristics	6
1.3 Motivations and objectives	9
1.3.1 Periodic array of gold nanoparticles	10
1.3.2 Waveguide-excited LSPR	11
1.3.3 Biosensor applications	12
1.3.4 Chemical sensor applications	12
1.4 Overview of the thesis	13

2	Numerical and Experimental Techniques	23
2.1	Finite difference time domain	23
2.1.1	3-D FDTD with non-uniform mesh	24
2.1.2	Simulation boundaries in 3-D FDTD	26
2.1.3	Simulation configuration for simulating gold nanoparticles under normal transmission	27
2.1.4	Simulation examples	29
2.2	Fabrication of gold nanoparticle arrays by electron beam lithography	32
2.2.1	Fabrication procedures	32
2.2.2	Dose calibration	35
2.2.3	Formation of gold nanocrescents and gold nanorings	35
2.3	Measurement of the extinction spectrum	38
2.3.1	Normal transmission measurement	38
2.3.2	Quantification of the peak shift	42
2.4	Surface functionalization	44
2.5	Example in sensing biotin-streptavidin interactions	46
2.6	Summary	51
3	3-D FDTD Analysis of Gold-Nanoparticle-based Photonic Crystal on Slab Waveguide	57
3.1	Introduction	57
3.2	3-D FDTD simulation with non-uniform mesh	58
3.3	Localized surface plasmon resonance of single gold nanoparticle	62
3.4	Effects of lattice constants	64
3.5	Effect of slab thickness	66
3.6	Effect of the local dielectric environment	68
3.7	Conclusions	70
3.8	Acknowledgements	70
4	Periodic Arrays of Gold Nanodisks Coupled with Evanescent Spectroscopy	74
4.1	Introduction	74
4.2	Sample fabrication	75
4.3	Waveguide transmission measurement	79
4.4	Experimental results	81
4.5	FDTD simulation	84
4.6	Simulation results	85
4.7	Conclusion	91
4.8	Acknowledgements	91

5	A Biosensor based on Periodic Arrays of Gold Nanodisks under Normal Transmission	96
5.1	Introduction	96
5.2	Experiment	98
5.2.1	Sample fabrication and measurement	98
5.3	Sensing characteristics	99
5.4	Antibody-antigen recognition	105
5.5	Discussion	108
5.6	Conclusion	109
5.7	Acknowledgements	109
6	Near-Infrared Optical Response of Thin Film pH-sensitive Hydrogel Coated on a Gold Nanocrescent Array	114
6.1	Introduction	114
6.2	Fabrication of the sensor device	115
6.3	Measurement and simulation of the LSPR	118
6.4	Sensor response vs. pH	120
6.5	Discussions	122
6.6	Acknowledgements	123
7	Effects of Coherent Interactions on the Sensing Characteristics of Near-Infrared Gold Nanorings	127
7.1	Introduction	127
7.2	Experiment	129
7.2.1	Sample fabrication and measurement	129
7.2.2	Experimental results	130
7.3	Numerical calculations	133
7.4	Discussions	141
7.5	Conclusions	145
7.6	Acknowledgements	146
8	A Nanoplasmonic Sensor based on Gold Nanoring Arrays Operating in the Optical Communication Window	152
8.1	Introduction	152
8.2	Research methods	154
8.2.1	Sample fabrication and measurement	154
8.2.2	Numerical simulations	155
8.3	Results and discussions	157
8.4	Biosensor applications	164
8.5	Conclusions	165
8.6	Acknowledgements	165

9	Summary and Further Development	171
9.1	Summary	171
9.1.1	Periodic arrays of gold nanodisks coupled with the evanescent field of a waveguide	171
9.1.2	Biosensor based on periodic array of gold nanodisks under normal transmission	172
9.1.3	Chemical sensor based on pH sensitive hydrogel thin film coated on the gold nanocrescent array	173
9.1.4	LSPR sensor based on gold nanoring arrays	174
9.2	Further development	175
9.2.1	Waveguide fabrication	175
9.2.2	Integration with PDMS fluidic channels for multiplexed detections	176
9.2.3	Other development	178
 Appendices		
A	Copyright Permission for Material Contained in Chapter 3	181
B	Copyright Permission for Material Contained in Chapter 5	183
C	Copyright Permission for Material Contained in Chapter 6	185
	Curriculum Vitae	187

List of Tables

1.1	List of the main performance characteristics of gold nanoparticles from literature	10
2.1	Comparison of required computational resources between non-uniform mesh and uniform mesh in simulating a gold nanoring	26
2.2	Summary of the conductive treatments on the substrates used in each chapter.	34
2.3	Configuration of the measurement setup for different nanoplasmonic structures	43
7.1	Simulated spectral and sensing characteristics of a single gold nanoring on substrate	139

List of Figures

1.1 Schematic of surface plasmon wave and conventional surface plasmon resonance sensor.	2
1.2 Schematic of localized surface plasmon resonance and localized surface plasmon resonance sensor.	4
1.3 Size and shape effects on the LSPR of gold nanoparticles	6
1.4 Schematic of the waveguide-integrated LSPR sensors.	11
1.5 Schematic of the sensor chip based on a periodic array of gold nanoparticles for detecting antigens.	12
1.6 Schematic of hydrogel LSPR sensors.	13
1.7 Schematic highlight of research work presented in Chapter 5.	14
1.8 Schematic highlight of research work presented in Chapter 6.	15
1.9 Schematic highlight of research work presented in Chapter 7 and 8.	16
2.1 Yee’s cell in 3-D FDTD simulations.	24
2.2 Non-uniform mesh used to discretize the simulation region with a gold nanoring.	25
2.3 Simulation boundaries used in the configuration where light propagates in the plane of periodicity.	27
2.4 FDTD configuration to simulate LSPR of the gold nanoring.	28
2.5 The simulated LSPR properties of a single gold nanocrescent.	30
2.6 The simulated extinction spectrum and mode profile of periodic array of gold nanorings with $a = 1050$ nm.	31
2.7 Diagram of electron beam lithography.	33
2.8 Schematic of the fabrication process.	34
2.9 SEM images to illustrate proximity effects.	36
2.10 The image processing results of the SEM image of a gold nanodisk array.	37
2.11 The size of fabricated nanodisks vs. the given dose for each lattice configuration determined from dose calibration procedures.	37
2.12 Formation of the gold nanorings.	39
2.13 The diagram of the setup to measure the extinction spectrum in normal transmission.	40
2.14 The photo of the measurement setup corresponding to the diagram of Figure 2.13.	41
2.15 Microscope image of the sensor elements on one device recorded by the camera.	42
2.16 Schematic of the structures of the SAM molecules.	46

2.17	Schematic of the EDC/NHS chemistry to bind streptavidin to the carboxylic group in SAM layer.	47
2.18	Data fitting of measured extinction spectrum into polynomial.	48
2.19	Response of biorecognition of streptavidin onto biotin.	49
3.1	Schematic of periodic array of gold nanoparticles on top of slab waveguide.	58
3.2	Simulation of the extinction spectra of periodic gold nanoparticles on 140nm thick ITO film coated glass substrate under normal incidence (from Z direction) of linearly polarized light.	61
3.3	FDTD simulation setup. The top figure is top view and the bottom figure is side view.	62
3.4	Normalized absorption spectra of a single gold nanoparticle on top of ITO slab waveguide for TE_0 mode and TM_0 mode.	63
3.5	Absorption spectra of changing a_x , in Set A and changing a, where $a = a_x = a_y$, in Set B.	65
3.6	Absorption peak wavelength vs. a_x , with $a_y = 350$ nm (Set C, black line with open squares) and $a_y = 450$ nm (Set A, red line with open circles) respectively.	67
3.7	Extinction of varying slab thickness	69
3.8	Effects of local dielectric environment at the surface of gold nanoparticles.	71
4.1	Diagram of the the structure configuration.	76
4.2	Scheme of fabrication of the waveguides in BK7 glass using ion-exchange technique.	78
4.3	Refractive index profile of the BK7 glass ion-exchanged waveguide (45 min), characterized by waveguide coupling angle measurements.	78
4.4	Scheme of the fabrication of the periodic array of elliptical gold nanodisks.	79
4.5	AFM images of fabricated nanodisk arrays for different lattice constants.	80
4.6	Microscope image of the fabricated gold nanoparticles array, waveguide and the registration marks.	81
4.7	Scheme of the waveguide transmission setup.	82
4.8	Measured extinction spectra for the structures of different lattice constants coupled with TE mode and TM mode of the waveguide.	83
4.9	3-D FDTD simulation configuration.	85
4.10	FDTD simulation results of a periodic array of gold nanodisks on top of a waveguide.	87
4.11	Spectral positions of the sharp extinction peak and the dips in the extinction spectra.	88
4.12	Simulated extinction spectra of unequal lattice constant configurations	88
4.13	The simulated mode profile at the wavelength of the sharp extinction peak for the device $a = 500$ nm.	90

4.14	The simulated mode profile at the wavelength of the extinction dip for the device $a=500$ nm.	90
5.1	Scheme of the sensor configuration.	98
5.2	Fabrication scheme for periodic arrays of gold nanodisks.	100
5.3	Construction of transparent flow cell for transmission measurements.	100
5.4	Measured extinction spectra of sensor devices with different lattice constants immersed in water.	102
5.5	Sensing characteristics of the extinction peaks for different lattice constants a	103
5.6	Experimental detection uncertainty, refractive index resolution, figure of merit and signal-to-noise ratio, for varying lattice constants.	104
5.7	Signal-to-noise ratio determined from the statistics of the measured intensity spectra recorded over 30 minutes.	105
5.8	The surface chemistry procedures for detecting antibody-antigen recognition.	107
5.9	Dose response of human IgG binding to anti-human IgG immobilized on the gold surface.	108
6.1	Fabrication of the gold nanocrescent array.	117
6.2	Measured and simulated extinction spectra of the fabricated device.	119
6.3	Sensor response of the gold nanocrescent array structure coated with hydrogel thin film.	121
7.1	The fabricated nanorings and measured extinction spectra.	131
7.2	The measured spectral and sensing characteristics of periodic array of gold nanorings vs. lattice constant a	134
7.3	Simulation results for $n_B = 1.0$ and $n_B = 1.33$	137
7.4	The extinction peaks vs. bulk refractive index of the single nanoring and the periodic array of different lattice constants.	138
7.5	The simulated sensing characteristics as a function of lattice constant	142
7.6	The calculated confinement factor vs. lattice constant a	144
8.1	Fabrication of the gold nanorings on pyrex substrate.	156
8.2	Construction of transparent flow cell for near-infrared transmission measurement.	157
8.3	The extinction spectra of the structures of different lattice constants in water	159
8.4	The characteristics of the extinction peaks of measured and simulated spectra under water background.	161
8.5	The interrogation spectral range for each lattice constant determined by the extinction peak wavelength and linewidth.	162
8.6	The experimental and simulation results of the gold nanorings array.	163

8.7	Sensor response of device $a = 1000$ nm for detection of the biotin molecules.	166
9.1	BPM simulation of the waveguide mode of K^+ - Na^+ ion-exchange waveguide.	177
9.2	The development of the PDMS microfluidic device integrated with the nanoplasmonic sensors.	179

Acronyms

AFM	<i>Atomic Force Microscope</i>
ATR	<i>Attenuated Reflection</i>
BPM	<i>Beam Propagation Method</i>
BSA	<i>Bovine Serum Albumin</i>
DDA	<i>Discrete Dipole Approximation</i>
DFT	<i>Discrete Fourier Transform</i>
DNA	<i>Deoxyribonucleic Acid</i>
EBL	<i>Electron Beam Lithography</i>
EDC	<i>1-ethyl-3-(3-dimethylaminopropyl) carbodiimide</i>
FDL	<i>Field Decay Length</i>
FDTD	<i>Finite Difference Time Domain</i>
FOM	<i>Figure of Merit</i>
fwhm	<i>full width half maximum</i>
IPA	<i>Isopropanol</i>
ITO	<i>Indium Tin Oxide</i>
InGaAs	<i>Indium Gallium Arsenide</i>
LOD	<i>Limit of Detection</i>
LSPR	<i>Localized Surface Plasmon Resonance</i>
NA	<i>Numerical Aperture</i>
NHS	<i>N-hydroxysuccinimide</i>
NIL	<i>Nanoimprint Lithography</i>
NPGS	<i>Nanometer Pattern Generation System</i>
NSL	<i>Nanosphere Lithography</i>
PBS	<i>Phosphate Buffered Saline</i>
PC	<i>Photonic Crystal</i>
PDMS	<i>Polydimethylsiloxane</i>
PML	<i>Perfectly Matched Layer</i>
RIU	<i>Refractive Index Unit</i>

SAM	<i>Self-Assembled Monolayer</i>
SEM	<i>Scanning Electron Microscope</i>
SERS	<i>Surface Enhanced Raman Scattering</i>
SNR	<i>Signal-to-Noise Ratio</i>
SPR	<i>Surface Plasmon Resonance</i>
SPW	<i>Surface Plasmon Wave</i>
TE	<i>Transverse Electric</i>
TM	<i>Transverse Magnetic</i>

Units

Å	<i>Angstrom (10^{-10} m)</i>
dB	<i>decibel</i>
Hz	<i>Hertz</i>
M	<i>molar (mole/litre)</i>
ng	<i>nanogram (10^{-9} g)</i>
nm	<i>nanometer (10^{-9} m)</i>
µg	<i>microgram (10^{-6} g)</i>
µm	<i>micrometer (10^{-6} m)</i>
pM	<i>picomolar (10^{-12} M)</i>

Chapter 1

Introduction

1.1 Nanoplasmonic sensors

Plasmonics refers to the study of optical effects attributed to surface plasmons, i.e., collective oscillations of free electrons existing at a metal/dielectric interface. The intense electromagnetic fields associated with surface plasmons offer massive enhancements of optical interactions with materials, such as surface-enhanced Raman scattering (SERS) and surface second-harmonic generations. The study of various optical phenomena in plasmonic structures has become a very hot research topic with many important applications. One particular application is label-free plasmonic sensing, using the strong fields confined at the nanoscale to detect biomolecular interactions or chemical reactions taking place at the metal/dielectric interface.

Conventional plasmonic sensors, generally referred as surface plasmon resonance (SPR) sensors, are based on the surface plasmon wave (SPW) propagating along the interface of a thin film of metal and a dielectric material, as shown in Figure 1.1(a). The development of SPR sensors began in the late 1970s, when the potentials of using SPR for sensor applications were first recognized. In 1982, the first SPR sensor for gas detection using a prism coupling configuration was reported by Nylander et al. [1]. In 1990, Biacore Inc., the market leader in SPR sensors, developed its first commercial SPR-based analytical instrument for detecting biomolecular interactions, comprising surface chemistry, flow systems and optical detections. Since then, the rapid development of the SPR techniques has been driven by the increasing demand for studying molecular interactions in many fields, including biomolecular research, analytical chemistry, environmental monitoring, drug discovery and medical diagnostics. Compared with other sensor techniques, SPR sensors have the advantages of being label-free, highly sensitive, real-time and providing detailed information on the kinetic processes, binding affinity, and analyte concentrations. Most of the existing SPR sensors implement the Kretschmann configuration and are based on attenuated

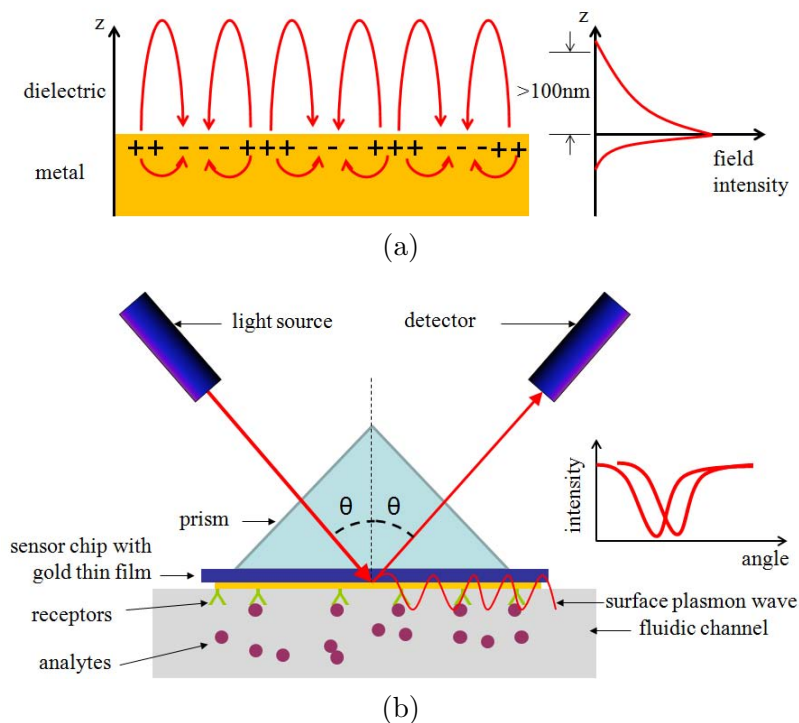


Figure 1.1: Schematic of (a) surface plasmon wave and (b) conventional surface plasmon resonance sensor. The surface plasmon wave in the sensor is excited by the laser using prism coupling, the reflected light is collected by the photodetector. When target biomolecules bind to the receptors on the gold surface, a change in the signal can be detected.

total reflection (ATR), for example, the first Biacore machines described by Lofas et al. [2] and Karlsson et al. [3]. In such a configuration, schematically illustrated in Figure 1.1(b), a prism is used to achieve K-vector matching which is required to excite the SPWs. The sensor response, either the SPW coupling angle or the reflected intensity at a fixed angle, is recorded in real-time to monitor the target biomolecules binding to the specific receptors immobilized on the sensor surface. Towards high sensitivity and compactness, various novel SPR sensor configurations have also emerged, such as the phase-sensitive SPR sensor [4], metallic-gratings-based SPR sensor [5], waveguide-based SPR sensors [6–9], and fiber-optic SPR sensors [10].

In recent years, advancement in nanofabrication and synthesis techniques have allowed for precise control of metal nanostructures with sizes comparable to the wavelength of light. Unlike the aforementioned interface-bound surface plasmon waves at the interface of metal and a dielectric, the surface plasmons in metal nanostructures

are locally confined within a nanoscale volume, known as localized surface plasmon resonance (LSPR), as shown in Figure 1.2(a). LSPRs are the basis for the study of nanoplasmonics and the metal nanostructures are often referred to as nanoplasmonic structures. LSPRs possess three unique optical properties. First, the field intensity outside the nanoparticle is the greatest at the surface and falls evanescently with distance, confining most of the field energy within a distance of a few nanometers. Second, the optical extinction is maximum at the resonance wavelength, determined by the particle's shape, composition and the refractive index of the surrounding medium. Third, the extinction peak shifts when the refractive index of surrounding medium is changed. Due to these properties, metal nanoparticles and other metal nanostructures supporting LSPRs are attractive for label-free sensing applications, leading to a novel type of sensors based on nanoplasmonic structures, referred to as localized surface plasmon resonance (LSPR) sensors.

The function of LSPR sensors is schematically plotted in Figure 1.2(b). A light beam propagates through a sensor area with gold nanoparticles and the extinction peak is acquired from the transmitted light. When the target biomolecules bind to the specific receptors immobilized to the sensor surface, a change of refractive index is induced very close to the sensor surface and a red-shift of the extinction peak is obtained. The amount of peak shift $\Delta\lambda$ can be quantitatively related to the concentration of analytes of interest. While preserving the main virtues of conventional SPR sensors as being label-free, highly sensitive and real-time, the LSPR sensors have additional advantages. Due to the localized nature, the LSPR can be directly excited by a free-space light beam, without using prisms or gratings. Therefore, the optical detection system in LSPR sensor is much simpler and can be achieved using common optical and mechanical components.

Side-by-side comparisons between SPR sensors and LSPR sensors have been reported by Svedendahl et al. [11] and Otte et al. [12]. These two types of sensors exhibit similar performance in detecting the build up of a very thin layer bounded to the sensor surface, such as in biomolecular interactions. However, the SPR sensors show more than three orders of magnitudes of higher sensitivity than LSPR sensors in detecting the refractive index of bulk analytes. The difference in the two types of sensing is attributed to the much larger field decay length of propagating surface plasmons than the localized surface plasmons [11], as schematically demonstrated in Figure 1.1(a) and Figure 1.2(a). This difference will be further discussed in section

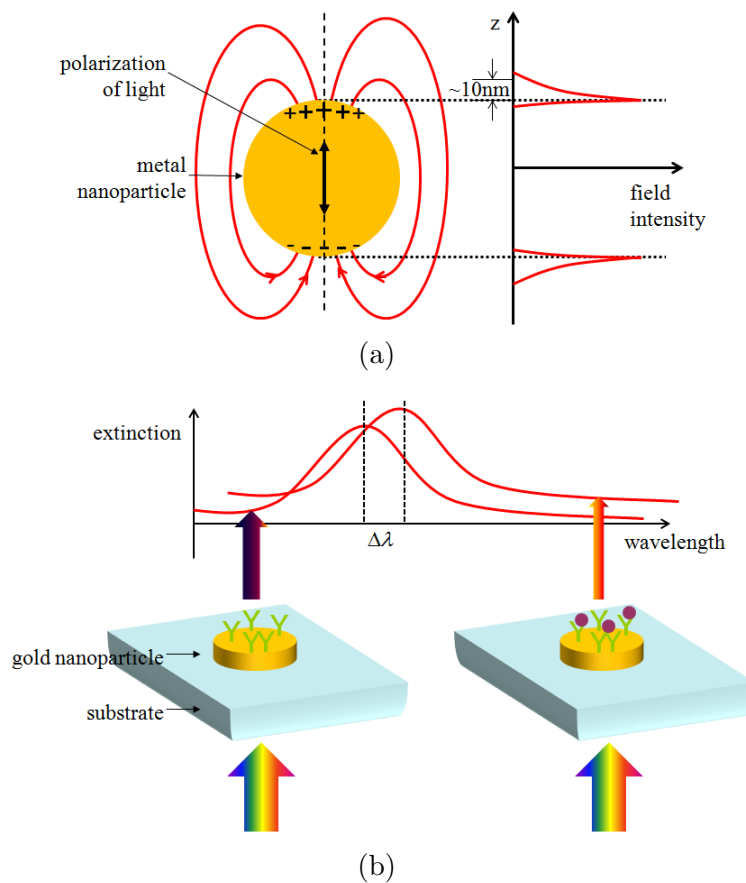


Figure 1.2: Schematic of (a) localized surface plasmon resonance and (b) localized surface plasmon resonance sensor. In the sensor, the localized surface plasmon resonance of the gold nanoparticle is excited by the light beam and the scattering or extinction spectrum is acquired by the spectrometer. When biomolecules bind to the receptors on gold surface, the spectrum red-shifts.

1.2.2.1.

During the past decade, many different types of metal nanostructures have been investigated and much research effort has been dedicated to improving the performance of LSPR sensors [13, 14]. However, the LSPR sensing is still not yet able to replace the SPR sensing in studying biomolecular interactions and there is still a lot of room for improvement of the detection signal-to-noise (S/N) ratio, the surface chemistry, the reproducibility and long-term stability.

1.2 LSPR sensor based on gold nanoparticles

1.2.1 LSPR of gold nanoparticles

Metal nanoparticles studied in nanoplasmonics are nanoscale particles typically composed of noble metals, such as gold and silver. For label-free LSPR sensing, gold nanoparticles are the most widely used candidates due to the ease of surface chemistry on gold and the LSPR in visible and near-infrared spectral range. The LSPR property of a single gold nanoparticle is determined by its shape, size and surrounding dielectric environment [15]. As illustrated in Figure 1.3(a), as the shape of a gold nanoparticle changes, the LSPR can be tuned over a very wide range of wavelengths¹. For solid gold nanoparticles smaller than 100 nm, such as gold nanospheres and gold nanocubes, the LSPR is generally in the visible spectral range. For gold nanoparticles of larger size or larger aspect ratios, such as gold nanorods, gold nanotriangles and gold nanodisks, the LSPR lies in the visible/near-infrared range. If the nanoparticles are made into hollow shapes, such as gold nanorings [16] and gold nanocrescents [17], the LSPR can be further tuned into the near-infrared/mid-infrared range. For a given shape of gold nanoparticle, the LSPR can be additionally tuned by varying its size. Generally speaking, by increasing the size, the LSPR peak red-shifts. The extinction spectra of gold nanodisks of different sizes are simulated using 3-D finite difference time domain method² and presented in Figure 1.3(b). As the diameter of

1. This is not a strict definition of the LSPR peak for each type of nanoparticle geometry but rather an illustrative map. It should be noted that the extinction peak also depends on the light polarization and the order of the resonance. Generally speaking, for gold nanorings, the dipolar peak is in the near-infrared while higher order resonance may lie in the visible.

2. The simulation method will be presented in Section 2.1.

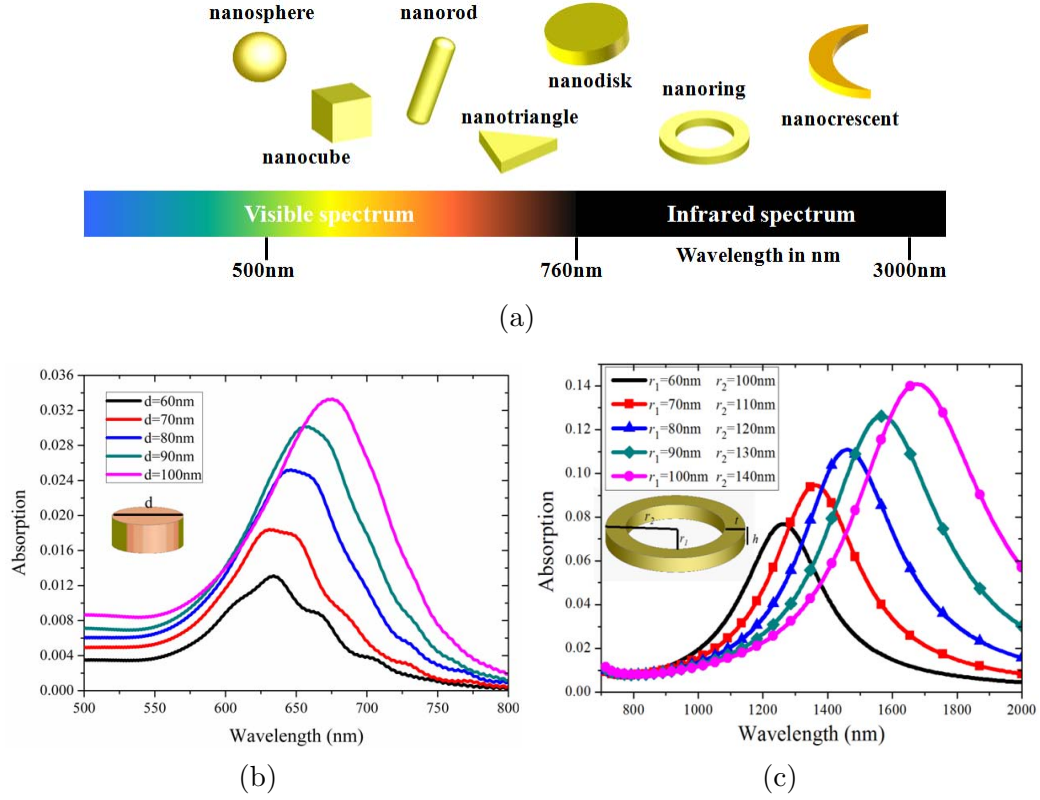


Figure 1.3: Size and shape effects on the LSPR of gold nanoparticles. a) schematic map of gold nanoparticles of different shapes and the approximate LSPR peak range. Extinction spectra of b) nanodisks and c) nanorings in different sizes, calculated by finite difference time domain method. In the simulations shown in (b) and (c), the incident light is propagated downward with light polarization parallel with the substrate surface.

the nanodisks increases from 60 nm into 100 nm, the LSPR peak red-shifts by 50 nm. In hollow nanorings, displayed in Figure 1.3(c), as the inner radius and outer radius of the nanorings increases by 40 nm, the LSPR peak drastically red-shifts by more than 400 nm. The size effects are much more pronounced in hollow nanoparticles, due to the strong coupling of surface plasmons between inner and outer metal/dielectric interfaces [16, 18].

1.2.2 Main performance characteristics

Owing to the great flexibility in tuning the LSPR of gold nanoparticles, many different geometries have been studied for LSPR sensing applications [13, 14, 19, 20]. For a

given type of LSPR sensor, there are three major characteristics that determine the sensor's performance: sensitivity, limit of detection, and figure of merit.

1.2.2.1 Sensitivity

Sensitivity describes the change in sensor signal responding to the change in the analytes to be measured. The definition of sensitivity is thus related to the sensor signal type and the targeted analytes. In LSPR sensing, intensity, phase and spectral extinction peak position λ_p can all be used as the sensor signal. λ_p is the most commonly used signal and is used throughout this thesis. For different types of analytes, the applications can be classified into two types, bulk refractive index sensing and surface sensing.

Bulk refractive index sensing is used to measure the change of the refractive index in a bulk background n_B . The refractive index has a unit known as refractive index unit (RIU). Bulk refractive index sensitivity m_B is defined in Equation 1.1.

$$m_B = \frac{\delta\lambda_p}{\delta n_B} \quad (1.1)$$

Surface sensing is used to measure a very thin dielectric layer binding to the surface of the gold nanoparticles, which is then used to describe the sensor's ability in detecting biomolecular interactions. The mass density of the target biomolecules that bind to the sensor surface is usually assumed to be directly proportional to the effective thickness d_S of a surface bound layer with refractive index n_S . Therefore, the surface sensitivity m_S is defined in Equation 1.2.

$$m_S = \frac{\delta\lambda_p}{\delta d_S} \quad (1.2)$$

It should be noted that the bulk sensitivity and surface sensitivity are not independent and can be approximately related as

$$\Delta\lambda \approx m_B(n_S - n_0)\left(1 - e^{-\frac{2\Delta d}{l_d}}\right) \quad (1.3)$$

where $\Delta\lambda$ is the LSPR peak shift caused by a very thin layer with thickness Δd and refractive index n_S adsorbed to the surface of gold nanoparticles, n_0 is the refractive index of the background, l_d is the evanescent field decay length (FDL) of the surface

plasmon mode. Field decay length describes how tightly the electromagnetic field is confined to the metal/dielectric interface, and determines the sensing distance. l_d of a LSPR sensor is generally around a few nanometers, comparable to the effective Δd that can be induced by binding biomolecules. In the conventional SPR sensor based on propagating surface plasmon wave, l_d is hundreds of nanometers, much larger than Δd . This explains the phenomenon that although the SPR sensors demonstrate much higher bulk index sensitivity than LSPR sensors, they performed similarly in sensing biomolecular interactions taking place directly at the gold surface [11].

1.2.2.2 Limit of detection

Limit of detection (LOD) is the minimum change of analytes that can be detected. In an LSPR sensor, if the minimum detectable change of signal is given by σ and the sensitivity is m , its limit of detection is as defined as

$$LOD = \frac{\sigma}{m} \tag{1.4}$$

In bulk refractive index sensing ($m = m_B$), the corresponding LOD is referred to be the refractive index resolution of the sensor. It should be noted that, σ is related to the detection uncertainty $\Delta\lambda_{un}$ (uncertainty in determining the extinction peak position), and the desired confidence level. For a confidence level of 99.7%, $\sigma = 3 \Delta\lambda_{un}$, meaning that only the peak shift larger than three times of the detection uncertainty can be trusted as a real shift, discernible from the baseline. The LOD is the most important parameter that describes the overall performance of the entire sensor equipment, including the gold nanoparticles and the optical detection system. One can deduce that to improve the LSPR sensor's performance, the essential target is to increase the sensitivity and to decrease the detection uncertainty. However, LOD cannot directly provide fair evaluations on the potentials of different nanoparticles for LSPR sensing, as the LOD is additionally affected by the system noise, quality of surface chemistry, the receptor-analyte binding affinity, etc. For example, a poorly sensitive nanoparticle might reach a better limit of detection than a highly sensitive one, provided that the former was loaded in an optical system of much higher S/N ratio.

1.2.2.3 Figure of merit

To compare the inherent potentials of different metal nanoparticles in LSPR sensing, a fair value is the figure of merit (FOM) [21], defined as

$$FOM = \frac{m}{\Gamma} \quad (1.5)$$

where m is the sensitivity, m_B or m_S , respectively, and Γ is the linewidth of the extinction peak given as full width at half-maximum. Γ is also sometimes denoted as *fwhm* in this thesis. The term Γ enters the definition of figure of merit because when excluding all other factors, the detection uncertainty $\Delta\lambda_{un}$ is proportional to Γ [22], meaning that from a sharper extinction peak, λ_p can be quantified with a smaller uncertainty.

According to the different types of sensitivity of interest, the FOM can be bulk sensing figure of merit $FOM_B = m_B/\Gamma$ or surface sensing figure of merit $FOM_S = m_S/\Gamma$. From the current literature, large variety of different metal nanoparticles have been investigated. These nanoparticles were demonstrated in detecting different biomolecules and with various surface chemistry protocols. This makes the surface sensing figure of merit difficult to be quantified and compared with a universal standard. The bulk sensitivity, however, can be conveniently determined by introducing solutions of different refractive indices. Therefore, the bulk sensing figure of merit is the most commonly used parameter to directly compare the sensing capabilities of different gold nanoparticles.

The main performance characteristics, including LSPR peak wavelength, linewidth, bulk index sensitivity and figure of merit, from current literature, are listed in Table 1.1. Part of the list is adapted from the review by Mayer et al. [19]. This is by no means a complete list but attempts to cover most of the representative examples.

1.3 Motivations and objectives

Although many successful examples of LSPR sensors already exist, there is still a lot of room for improvement of LSPR sensor performance and to explore novel sensing applications. The overall objective of this thesis is to investigate several novel configurations of LSPR sensors based on gold nanoparticles, for biosensing and chemical

Table 1.1: List of the main performance characteristics of gold nanoparticles from literature

nanoparticle shape	type	λ_p (nm)	Γ (nm)	m_B (nm/RIU)	FOM_B
nanobranched [23]	ensemble	1141	879	703	0.8
nanoshell (Au/SiO ₂) [24]	ensemble	770	350	314	0.9
nanorice [25]	ensemble	1600	600	801	1.3
nanorod [26]	ensemble	720	125	170	1.3
nanosphere [27]	ensemble	530	60	90	1.5
nanoshell (Au/AuS) [28]	single	660	77	117	1.5
nanoring [29]	ensemble	1223	n/a	880	~2
nanopyramid [30]	single	680	114	221	2.2
nanocrescent [17]	ensemble	1795	209	596	2.4
nanorattle [31]	single	570	52	199	3.8
nanobipyramid [32]	ensemble	681	52	352	4.5
nanostar [33]	single	770	124	665	5.4

sensing applications. In terms of sensor configurations, of particular interests are periodic arrays and waveguide configurations.

1.3.1 Periodic array of gold nanoparticles

The study of effects due to periodic arrays is motivated by the significance of interactions between gold nanoparticles. Apart from the aforementioned factors in section 1.2.1, the interactions among nanoparticles in an ensemble play an equally important role in the LSPR properties of the gold nanoparticles. Such interactions in a periodic array is of coherent nature, having unique properties. Meier et al. have theoretically studied the dipolar interactions of periodic arrays of nanoparticles and predicted the array effects on the plasmon peak and radiative damping [34], which were confirmed later in many experiments on 2D periodic arrays of gold and silver nanoparticles [35–38]. Narrow extinction peaks due to selective suppression have been reported from periodic arrays of gold nanoparticles on optical waveguides [39, 40]. Sharp plasmon peaks due to coherent interaction of disordered silver nanoparticle arrays have been demonstrated [41]. Sharp grating-induced plasmon modes of periodic arrays of metal nanoparticles have been studied theoretically and experimentally [42–45]. However, the sensing characteristics of periodic arrays of metal nanoparticles have not been investigated yet. Certain features from the periodic array, such as sharp

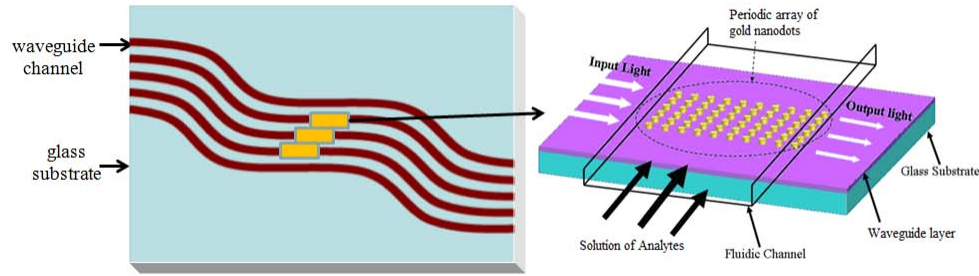


Figure 1.4: Schematic of the waveguide-integrated LSPR sensors. The panel on the left shows the integrated channel waveguides with double-S bends. The top and bottom waveguide are used as reference, and the middle three waveguide are used as sensor channels giving responses in the detection. Each sensor channel is depicted in the panel on the right. Periodic arrays of gold nanoparticles are fabricated on top and the LSPR is excited by the evanescent field of the incident waveguide mode.

linewidth and large extinction cross-section, are very much favored by LSPR sensing applications to achieve high performance. It can be expected that the LSPR sensors based on periodic arrays are superior to those based on random ensembles or single nanoparticles.

1.3.2 Waveguide-excited LSPR

The study of waveguide effects on the LSPR is motivated by the idea of photonic crystals (PCs). Photonic crystals are dielectric or metallic-dielectric structures with periodic spatial alternations of the refractive index on the scale of the wavelength of light [46]. By fabricating the periodic array of gold nanoparticles on top of a waveguide, the structure can be considered as a 2-D metallic PC structure. The unique aspect of this configuration is that the surface plasmons can be excited by the evanescent field of the waveguide mode with the wave-vector in the same plane of periodicity, which may provide strong light-matter interactions resulting from the flat dispersion bands [46]. In addition, waveguides allow for integrating the LSPR sensors into the optical circuits together with a light source and detectors. A scheme of the integrated LSPR sensor is plotted in Figure 1.4. The biosensing approach based on gold nanoparticles immobilized on the surface of the waveguide has been studied [47, 48], but the periodic arrays interacting with the evanescent field of the waveguide mode have not been thoroughly studied yet.

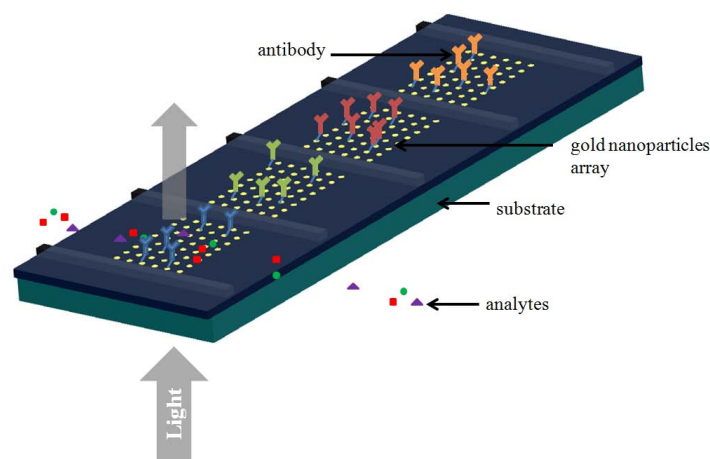


Figure 1.5: Schematic of the sensor chip based on a periodic array of gold nanoparticles for detecting antigens. Periodic arrays of gold nanoparticles are compactly fabricated on top of the sensor substrate. Each array can act as an independent LSPR sensor and is functionalized with a certain type of antibody, targeting a specific type of antigen. Fluidic channels are integrated with the sensor chip to make each sensor individually addressable by the analytes. The response of each element is measured by the transmission of a broad-band light beam.

1.3.3 Biosensor applications

For biosensing applications, e.g. the antibody-antigen binding is of interest. The concentration of the target antigens can be detected and quantified, which provides important information for medical diagnostics, such as early detection of leukemia and lung cancer. Gold nanoparticle-based LSPR sensors allow each sensor element to occupy a very small area, therefore many elements can be compactly integrated onto the same sensor chip. This allows for immobilizing different types of antibodies on each sensor element so that multiple types of antigens can be detected at the same time. This is demanded by accurate diagnostics because each leukemia subtype corresponds to a specific combination of certain types of proteins in the white blood cells. The idea is schematically shown in Figure 1.5.

1.3.4 Chemical sensor applications

For chemical sensing applications, hydrogel based chemical sensing is of interest. Hydrogel is a polymer that can reversibly respond to the chemical stimuli, such as pH

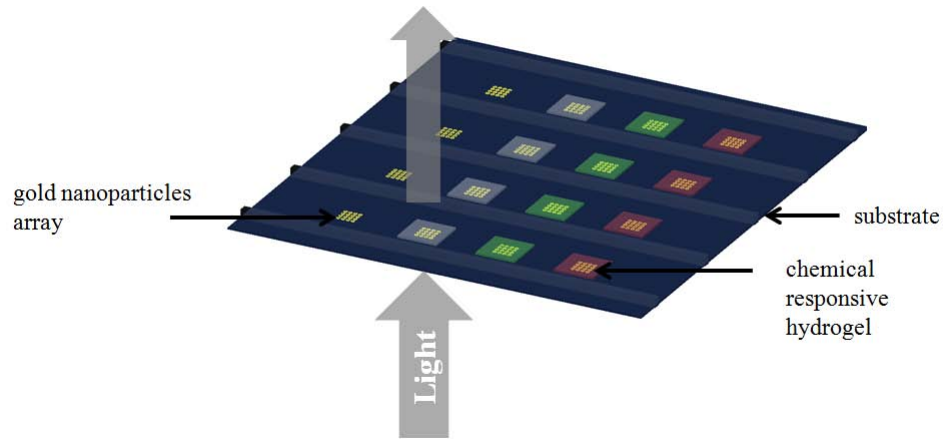


Figure 1.6: Schematic of hydrogel LSPR sensors. Periodic arrays of gold nanoparticles are compactly fabricated on top of the sensor substrate. Each array can act as an independent LSPR sensor and is coated with a specific type of hydrogel thin film which respond to a certain type of chemical stimulus. The optical response of each element is measured by the transmission of a broad-band light beam.

and ionic strength. When the chemical environment is changed, the functional hydrogel thin film swells or shrinks, leading to a change of the refractive index, detectable by the LSPR sensor. By combining hydrogel and LSPR sensors, the capability of LSPR spectroscopy can be extended into the chemical sensing applications. The idea is schematically demonstrated in Figure 1.6.

1.4 Overview of the thesis

The main body of this thesis are integrated articles presenting the completed research work towards the aforementioned objectives. This section provides the overview of the contents of the following chapters, describes the link of each chapter with the objectives and mentions the connections between chapters.

Chapter 2 introduces the numerical and experimental techniques used in the research work covered by this thesis, with the emphasis on the finite difference time domain simulations, electron beam lithography fabrications, measurement setup and surface chemistry procedures.

Chapter 3 theoretically investigates the periodic arrays of gold nanoparticles on slab waveguides using finite difference time domain simulations with non-uniform

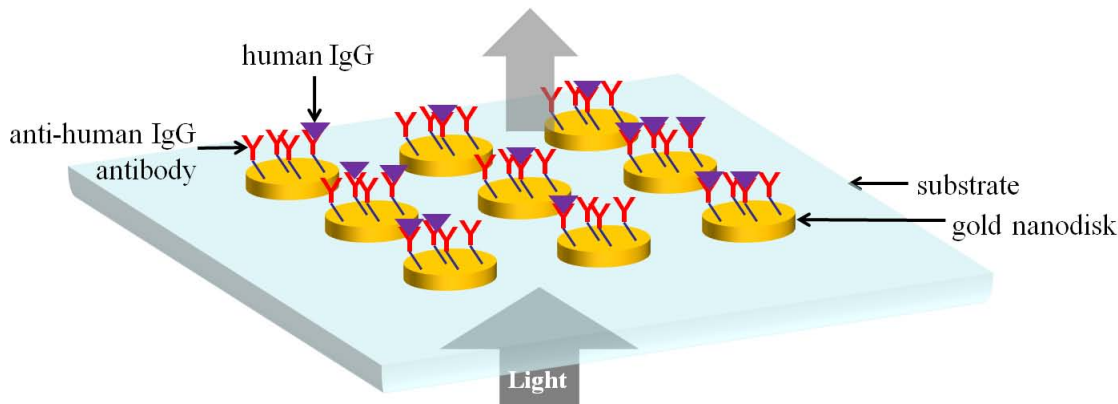


Figure 1.7: Schematic highlight of research work presented in Chapter 5. Periodic array of gold nanodisks are fabricated on top of the BK7 glass. The extinction spectra are measured by the normal transmission.

mesh. The periodic effects and the waveguide effects on the optical properties of the nanoplasmonic structure are the focus. This work provides the theoretical basis for the waveguide-integrated sensor scheme proposed in Figure 1.4.

Chapter 4 investigates the waveguide LSPR in experiments and simulations. The waveguides are fabricated by the thermal ion-exchange technique, and the periodic array of gold nanodisks are patterned right on its top. The extinction spectra are measured by the waveguide transmission setup. Corresponding simulations are also carried out to study the overlap of the photonic band gap with the plasmon resonance of the nanoparticles. This work is the extension of the work shown in Chapter 3, and gives directions for future development.

Chapter 5 demonstrates a biosensor based on periodic arrays of gold nanodisks patterned on top of the BK7 glass substrate. The work is schematically plotted in Figure 1.7. The LSPR was measured by normal transmission of a broadband light beam. The refractive index resolutions of the sensors with different lattice constants were compared and optimized. The focus of the work is to study the sensor's performance in detecting the antibody-antigen interactions which provides the basis for the biosensor chip proposed in Figure 1.5. To test its function, anti-IgG antibodies were first immobilized on the gold nanodisks through surface chemistry. IgGs of different concentrations were then introduced into the sensor and the sensor signal was recorded in real-time to monitor the binding of IgG to the anti-IgG.

Chapter 6 demonstrates a pH-sensitive chemical sensor based on gold nanocre-

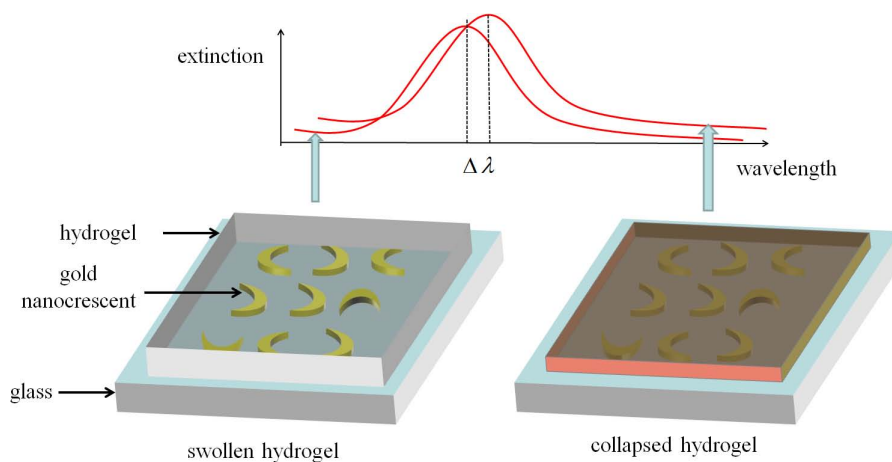


Figure 1.8: Schematic highlight of research work presented in Chapter 6. Gold nanocrescent array is fabricated on top of the conductively coated glass substrate. pH-sensitive hydrogel thin film is then coated on the surface and chemically bonded to the glass surface. The extinction peak is measured by the transmission of the broad-band light beam. The shift of the peak is related to the swelling state of the hydrogel thin film.

scents coated with hydrogel thin film. The work is schematically plotted in Figure 1.8. The gold nanocrescents were fabricated into a close-packed periodic array, but individual nanocrescents were in random orientations. The structure was characterized and we found extinction peaks in the near-infrared. A hydrogel thin film is the chemical-responsive element, which can swell or shrink depending on the pH of the solutions added, leading to a changing amount of water content in the hydrogel thin film and consequently changing refractive index. The gold nanocrescents served as the optical transducer to probe the change in the refractive index at the hydrogel thin film and the extinction peak wavelength was related to the pH of the solution. This work provides the basis for the chemical sensor chip proposed in Figure 1.6

Although the nanodisks and the nanocrescents have been successfully implemented towards sensing applications in Chapter 5 and 6, the figure of merit of the nanoplasmonic structure is not high. In the following chapters, gold nanorings become the basis of the nanoplasmonic structure owing to its high sensitivity, well controlled geometries produced from fabrications, small contact area with the substrate and hollow cores accessible by the biomolecules.

Chapter 7 investigates in detail the effects of coherent interactions on the sensing characteristics of the periodic arrays of gold nanorings on glass substrates. The work is

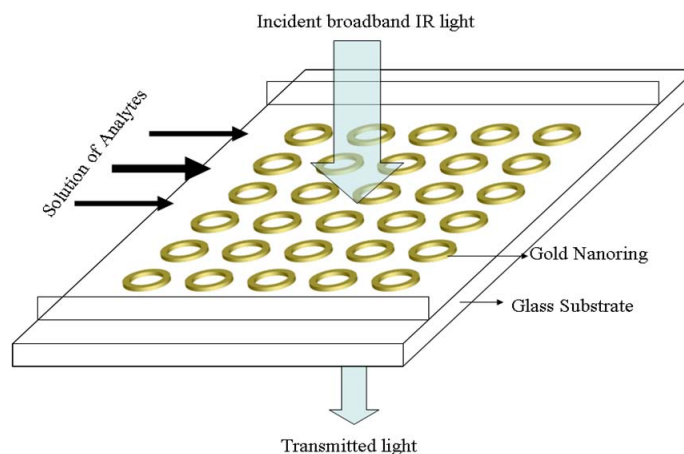


Figure 1.9: Schematic highlight of research work presented in Chapter 7 and 8. The periodic arrays of gold nanorings are fabricated on top of the glass. The LSPR peak is probed by the normal transmission of broad-band light beam.

schematically plotted in Figure 1.9. The aim of the work in this chapter is to find out how to optimize the LSPR sensor based on the periodic array of gold nanorings. In the study, lattice constants were varied across a wide range and the features of extinction peaks were acquired from simulations. Main performance characteristics, including peak wavelength, linewidth fwhm, bulk sensitivity, surface sensitivity, bulk sensing figure of merit and surface sensing figure of merit, were all studied and the trends were explained with considerations of a special substrate effect. The performance characteristics of a single nanoring was also simulated. By comparison, the periodic array was shown to be superior to a single nanoparticle in LSPR sensing.

Chapter 8 presents experimental verifications on the effects and trends discovered in Chapter 7 and implemented the trends to achieve a near-infrared LSPR sensor functioning in the fiber-optical communication window, with high figure of merit. A detection scheme based on tunable laser was also discussed, aimed at improving the S/N ratio of the sensor. Proof-of-concept experiments to detect the bindings of biotin to the streptavidin immobilized on the surface of gold nanorings were also demonstrated.

Chapter 9 summarizes all the previous chapters and presents the further development, especially the proposed schemes on the waveguide-based LSPR sensors and the integration of the nanoplasmonic sensors with microfluidic devices.

References

- [1] C. Nylander, B. Liedberg, and T. Lind, “Gas detection by means of surface plasmons resonance,” *Sensors and Actuators*, vol. 3, pp. 79–88, 1982.
- [2] S. Lofas, M. Malmqvist, I. Ronnberg, E. Stenberg, B. Liedberg, and I. Lundstrom, “Bioanalysis with surface plasmon resonance,” *Sensors and Actuators B: Chemical*, vol. 5, no. 1-4, pp. 79 – 84, 1991.
- [3] R. Karlsson, A. Michaelsson, and L. Mattsson, “Kinetic analysis of monoclonal antibody-antigen interactions with a new biosensor based analytical system,” *Journal of Immunological Methods*, vol. 145, no. 1-2, pp. 229 – 240, 1991.
- [4] S. Patskovsky, M. Meunier, P. N. Prasad, and A. V. Kabashin, “Self-noise-filtering phase-sensitive surface plasmon resonance biosensing,” *Opt. Express*, vol. 18, no. 14, pp. 14 353–14 358, Jul 2010.
- [5] D. Cullen, R. Brown, and C. Lowe, “Detection of immuno-complex formation via surface plasmon resonance on gold-coated diffraction gratings,” *Biosensors*, vol. 3, no. 4, pp. 211 – 225, 1987-1988.
- [6] P. Stocker, B. Menges, U. Langbein, and S. Mittler, “Multimode waveguide mode surface plasmon coupling: a sensitivity and device realizability study,” *Sensors and Actuators A: Physical*, vol. 116, no. 2, pp. 224 – 231, 2004.
- [7] P. Berini, “Bulk and surface sensitivities of surface plasmon waveguides,” *New Journal of Physics*, vol. 10, no. 10, p. 105010, 2008.
- [8] J. Homola, J. Ctyroky, M. Skalsky, J. Hradilova, and P. Kolarova, “A surface plasmon resonance based integrated optical sensor,” *Sensors and Actuators B: Chemical*, vol. 39, no. 1-3, pp. 286 – 290, 1997.
- [9] J. Dostalek, J. Ctyroky, J. Homola, E. Brynda, M. Skalsky, P. Nekvindova, J. Spirkova, J. Skvor, and J. Schrofel, “Surface plasmon resonance biosensor

- based on integrated optical waveguide,” *Sensors and Actuators B: Chemical*, vol. 76, no. 1-3, pp. 8 – 12, 2001.
- [10] R. Jorgenson and S. Yee, “A fiber-optic chemical sensor based on surface plasmon resonance,” *Sensors and Actuators B: Chemical*, vol. 12, no. 3, pp. 213 – 220, 1993.
- [11] M. Svedendahl, S. Chen, A. Dmitriev, and M. Kall, “Refractometric sensing using propagating versus localized surface plasmons: A direct comparison,” *Nano Letters*, vol. 9, no. 12, pp. 4428–4433, 2009.
- [12] M. A. Otte, B. Sepulveda, W. Ni, J. P. Juste, L. M. Liz-Marzan, and L. M. Lechuga, “Identification of the optimal spectral region for plasmonic and nano-plasmonic sensing,” *ACS Nano*, vol. 4, no. 1, pp. 349–357, 2010.
- [13] K. A. Willets and R. P. Van Duyne, “Localized surface plasmon resonance spectroscopy and sensing,” *Annu. Rev. Phys. Chem.*, vol. 58, pp. 267–297, 2007.
- [14] J. N. Anker, W. P. Hall, O. Lyandres, N. C. Shah, J. Zhao, and R. P. Van Duyne, “Biosensing with plasmonic nanosensors,” *Nature Materials*, vol. 7, pp. 442–453, 2008.
- [15] C. Noguez, “Surface plasmons on metal nanoparticles: The influence of shape and physical environment,” *The Journal of Physical Chemistry C*, vol. 111, no. 10, pp. 3806–3819, 2007.
- [16] J. Aizpurua, P. Hanarp, D. S. Sutherland, M. Kall, G. W. Bryant, and F. J. Garcia de Abajo, “Optical properties of gold nanorings,” *Phys. Rev. Lett.*, vol. 90, no. 5, p. 057401, 2003.
- [17] R. Bukasov and J. S. Shumaker-Parry, “Highly tunable infrared extinction properties of gold nanocrescents,” *Nano Letters*, vol. 7, no. 5, pp. 1113–1118, 2007.
- [18] C. L. Nehl, N. K. Grady, G. P. Goodrich, F. Tam, N. J. Halas, and J. H. Hafner, “Scattering spectra of single gold nanoshells,” *Nano Letters*, vol. 4, no. 12, pp. 2355–2359, 2004.
- [19] K. M. Mayer and J. H. Hafner, “Localized surface plasmon resonance sensors,” *Chemical Reviews*, vol. 111, no. 6, pp. 3828–3857, 2011.

- [20] S. Durocher, A. Rezaee, C. Hamm, C. Rangan, S. Mittler, and B. Mutus, “Disulfide-linked, gold nanoparticle based reagent for detecting small molecular weight thiols,” *Journal of the American Chemical Society*, vol. 131, no. 7, pp. 2475–2477, 2009.
- [21] L. J. Sherry, S.-H. Chang, G. C. Schatz, R. P. Van Duyne, B. J. Wiley, and Y. Xia, “Localized surface plasmon resonance spectroscopy of single silver nanocubes,” *Nano Letters*, vol. 5, no. 10, pp. 2034–2038, 2005.
- [22] A. Unger and M. Kreiter, “Analyzing the performance of plasmonic resonators for dielectric sensing,” *J. Phys. Chem. C*, vol. 113, pp. 12 243–12 251, 2009.
- [23] H. Chen, X. Kou, Z. Yang, W. Ni, and J. Wang, “Shape- and size-dependent refractive index sensitivity of gold nanoparticles,” *Langmuir*, vol. 24, no. 10, pp. 5233–5237.
- [24] F. Tam, C. Moran, and N. Halas, “Geometrical parameters controlling sensitivity of nanoshell plasmon resonances to changes in dielectric environment,” *The Journal of Physical Chemistry B*, vol. 108, no. 45, pp. 17 290–17 294, 2004.
- [25] H. Wang, D. W. Brandl, F. Le, P. Nordlander, and N. J. Halas, “Nanorice: A hybrid plasmonic nanostructure,” *Nano Letters*, vol. 6, no. 4, pp. 827–832, 2006.
- [26] K. M. Mayer, S. Lee, H. Liao, B. C. Rostro, A. Fuentes, P. T. Scully, C. L. Nehl, and J. H. Hafner, “A label-free immunoassay based upon localized surface plasmon resonance of gold nanorods,” *ACS Nano*, vol. 2, no. 4, pp. 687–692, 2008.
- [27] S. Underwood and P. Mulvaney, “Effect of the solution refractive index on the color of gold colloids,” *Langmuir*, vol. 10, no. 10, pp. 3427–3430, 1994.
- [28] G. Raschke, S. Brogl, A. S. Susha, A. L. Rogach, T. A. Klar, J. Feldmann, B. Fieres, N. Petkov, T. Bein, A. Nichtl, and K. Krzinger, “Gold nanoshells improve single nanoparticle molecular sensors,” *Nano Letters*, vol. 4, no. 10, pp. 1853–1857, 2004.
- [29] E. M. Larsson, J. Alegret, M. Kall, and D. S. Sutherland, “Sensing characteristics of NIR localized surface plasmon resonances in gold nanorings for application as ultrasensitive biosensors,” *Nano Letters*, vol. 7, no. 5, pp. 1256–1263, 2007.

- [30] J. Lee, W. Hasan, and T. W. Odom, "Tuning the thickness and orientation of single Au pyramids for improved refractive index sensitivities," *The Journal of Physical Chemistry C*, vol. 113, no. 6, pp. 2205–2207, 2009.
- [31] Y. Khalavka, J. Becker, and C. Sonnichsen, "Synthesis of rod-shaped gold nanorattles with improved plasmon sensitivity and catalytic activity," *Journal of the American Chemical Society*, vol. 131, no. 5, pp. 1871–1875, 2009.
- [32] J. Burgin, M. Liu, and P. Guyot-Sionnest, "Dielectric sensing with deposited gold bipyramids," *The Journal of Physical Chemistry C*, vol. 112, no. 49, pp. 19 279–19 282, 2008.
- [33] C. L. Nehl, H. Liao, and J. H. Hafner, "Optical properties of star-shaped gold nanoparticles," *Nano Letters*, vol. 6, no. 4, pp. 683–688, 2006.
- [34] M. Meier, A. Wokaun, and P. F. Liao, "Enhanced fields on rough surfaces: dipolar interactions among particles of sizes exceeding the Rayleigh limit," *J. Opt. Soc. Am. B*, vol. 2, no. 6, pp. 931–949, 1985.
- [35] B. Lamprecht, G. Schider, R. T. Lechner, H. Ditlbacher, J. R. Krenn, A. Leitner, and F. R. Aussenegg, "Metal nanoparticle gratings: influence of dipolar particle interaction on the plasmon resonance," *Phys. Rev. Lett.*, vol. 84, no. 20, pp. 4721–4724, 2000.
- [36] J. Sung, E. M. Hicks, R. P. Van Duyne, and K. G. Spears, "Nanosphere spectroscopy: dipole coupling in two-dimensional arrays of L-shaped silver nanoparticles," *J. Phys. Chem. C*, vol. 111, pp. 10 368–10 376, 2007.
- [37] J. Sung, E. M. Hicks, R. P. Van Duyne, and K. G. Spears, "Nanoparticle spectroscopy: plasmon coupling in finite-sized two-dimensional arrays of cylindrical silver nanoparticles," *The Journal of Physical Chemistry C*, vol. 112, no. 11, pp. 4091–4096, 2008.
- [38] C. L. Haynes, A. D. McFarland, L. Zhao, R. P. Van Duyne, G. C. Schatz, L. Gunnarsson, J. Prikulis, B. Kasemo, and M. Kall, "Nanosphere lithography: plasmon coupling in finite-sized two-dimensional array of cylindrical silver nanoparticles," *J. Phys. Chem. B*, vol. 107, pp. 7337–7342, 2003.

- [39] S. Linden, A. Christ, J. Kuhl, and H. Giessen, “Selective suppression of extinction within the plasmon resonance of gold nanoparticles,” *Appl. Phys. B*, vol. 73, pp. 311–316, 2001.
- [40] S. Linden, J. Kuhl, and H. Giessen, “Controlling the interaction between light and gold nanoparticles: selective suppression of extinction,” *Phys. Rev. Lett.*, vol. 86, no. 20, pp. 4688–4691, 2001.
- [41] S. Malynych and G. Chumanov, “Light-induced coherent interactions between silver nanoparticles in two-dimensional arrays,” *J. Am. Chem. Soc.*, vol. 125, pp. 2896–2898, 2003.
- [42] S. Zou, N. Janel, and G. C. Schatz, “Silver nanoparticle array structures that produce remarkably narrow plasmon lineshapes,” *J. Chem. Phys.*, vol. 120, no. 23, pp. 10 871–10 875, 2004.
- [43] S. Zou and G. C. Schatz, “Silver nanoparticle array structures that produce remarkably narrow plasmon lineshapes,” *J. Chem. Phys.*, vol. 121, no. 24, pp. 12 606–12 612, 2004.
- [44] E. M. Hicks, S. Zou, G. C. Schatz, K. G. Spears, R. P. Van Duyne, L. Gunnarsson, T. Rindzevicius, B. Kasemo, and M. Kall, “Controlling plasmon line shapes through diffractive coupling in linear arrays of cylindrical nanoparticles fabricated by electron beam lithography,” *Nano Letters*, vol. 5, no. 6, pp. 1065–1070, 2005.
- [45] N. Felidj, G. Laurent, J. Aubard, G. Levi, A. Hohenau, J. R. Krenn, and F. R. Aussenegg, “Grating-induced plasmon mode in gold nanoparticle arrays,” *J. Chem. Phys.*, vol. 123, p. 221103, 2005.
- [46] J. D. Joannopoulos, R. D. Meade, and J. N. Winn, *Photonic Crystals: Molding the Flow of Light*. Princeton University Press, 1995.
- [47] S. Hashemi Rafsanjani, T. Cheng, S. Mittler, and C. Rangan, “A novel biosensing approach based on linear arrays of immobilized gold nanoparticles,” *Journal of Applied Physics*, vol. 107, no. 7, p. 094303, 2010.
- [48] P. Rooney, A. Rezaee, S. Xu, T. Manifar, A. Hassanzadeh, G. Podoprygorina, V. Bohmer, C. Rangan, and S. Mittler, “Control of surface plasmon resonances in

dielectrically coated proximate gold nanoparticles immobilized on a substrate,”
Phys. Rev. B, vol. 77, p. 235446, 2008.

Chapter 2

Numerical and Experimental Techniques

This chapter introduces the techniques and methods used in the work presented in this thesis, with the emphasis on the simulation method, fabrication techniques, measurements strategies and surface chemistry procedures. At the end of this chapter, a brief introduction to a sensor's function as a biosensor is also presented.

2.1 Finite difference time domain

Finite difference time domain (FDTD) is a numerical technique for solving Maxwell's equations in arbitrary metallic/dielectric structures. The basic principle is to discretize the simulation space into nodes and substitute the curl equations and partial time differentials of Maxwell's equations with finite central differences in both spatial domain and time domain [1]. Using FDTD simulations, gold nanoparticles of any arbitrary shape can be conveniently and accurately simulated. Even structures with very complicated geometries and material compositions can be easily simulated by FDTD. Such a task cannot be simple and may even be unsolvable using analytical approaches, such as Mie's theory [2]. FDTD is a time domain method meaning that from one simulation, the optical response over a broadband of frequencies could be acquired through discrete Fourier transforms (DFT). This is a big advantage over frequency domain methods, such as discrete dipole approximation (DDA) [3], for which each frequency point takes one simulation. In addition, FDTD can be conveniently applied in high performance parallel computing, which can greatly reduce the computation time for simulating large scale structures. All the FDTD simulations in this thesis were modeled using FDTD Solution software package from Lumerical Inc. and computed on high performance parallel computing grids.

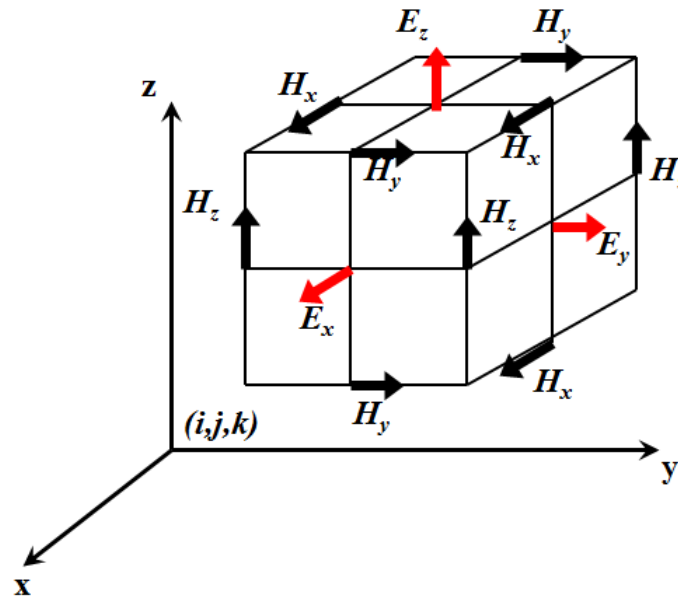


Figure 2.1: Yee's cell in 3-D FDTD simulations. The computational domain is meshed into cuboid cells by the grids. The cross-point of three orthogonal grid lines gives a computational node. On each node, only one particular component of the electromagnetic field is calculated. The arrangement of the field components on the nodes are determined by the mathematical forms of Maxwell's equations.

2.1.1 3-D FDTD with non-uniform mesh

The FDTD simulations on gold nanoparticles require 3-D configurations, because the LSPR mode has a 3-D nanoscale profile. A 2-D approximation of gold nanoparticles cannot produce reasonable results. In 3-D FDTD simulations, the simulation region is meshed into cuboid cells, known as Yee's cells. As shown in Figure 2.1, each field component is located at a computational node. At each time step, the field value at each node are calculated by iterations of algebraic equations, using only the field values of this same node and four neighboring nodes.

The primary challenge with simulating gold nanoparticles in 3-D is that due to the lossy and dispersive property of gold, ultra-small grid size has to be used to mesh the gold, in order to guarantee numerical stability. Generally speaking, the grid size should be smaller than one hundredth of the wavelength. As a result, the total amount of the stored fields data on these finely meshed grids is huge and can easily exceed the available amount of memory. Such a drawback can be overcome by using a non-uniform mesh configuration. Since gold nanoparticles are very small and

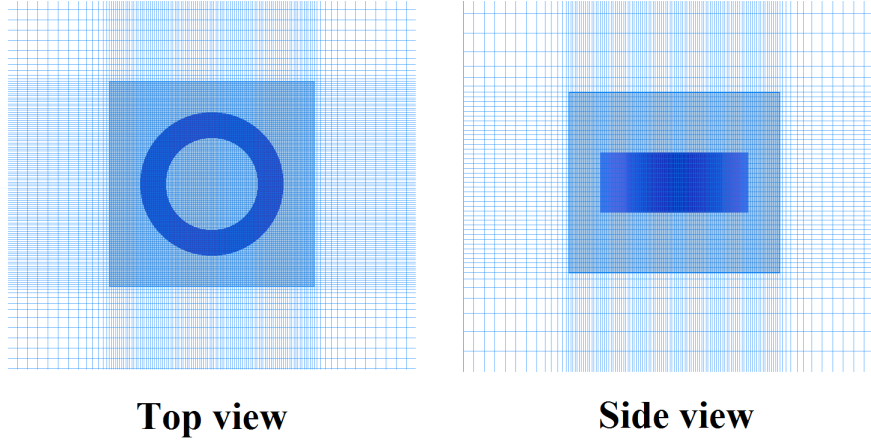


Figure 2.2: Non-uniform mesh used to discretize the simulation region with a gold nanoring. The region that the gold nanoring occupies is meshed with ultra-fine grids of 4 nm. Other regions are meshed with much coarse grids, larger than 10 nm. The grids at the boundaries between the finely-meshed region and coarsely-meshed region vary gradually.

occupy a very small space, the simulation region could be meshed in such a way that, gold and its vicinity is meshed with ultra-fine grids, while other regions are meshed with more coarse grids. A meshing configuration of a gold nanoring is shown in Figure 2.2. The region that the gold nanoring occupies is meshed by 4 nm grids. The fine mesh region has to cover the space with strong variation of electromagnetic field intensity associated with the LSPR. It should be noted, that, the regions connected to the finely meshed region are meshed with gradually varying grid sizes to guarantee the numerical stability. Such a non-uniform mesh is very effective in performing the simulations. A comparison of different mesh configurations used in simulating gold nanorings with outer diameter of 280 nm and height of 50 nm in a $1 \mu\text{m} \times 1 \mu\text{m} \times 2 \mu\text{m}$ simulation region is given in Table 2.1. It can be observed that as the mesh is refined, the memory required for the non-uniform mesh goes up slightly while it drastically increases for the uniform mesh.

The stability factor of FDTD S_{FDTD} is defined as

$$S_{FDTD} = \frac{c\Delta t}{d} \quad (2.1)$$

where c is the speed of light in vacuum, Δt is the time step and d is the smallest grid size. In all the simulations presented in this thesis, S_{FDTD} is set to be equal to 0.29,

Table 2.1: Comparison of required computational resources between non-uniform mesh and uniform mesh in simulating a gold nanoring

minimum grid size	non-uniform mesh		uniform-mesh	
	Yee's nodes	memory	Yee's nodes	memory
8 nm	1.98919 M	86 MB	5.48386 M	218 MB
4 nm	6.4152 M	259 MB	38.0389 M	1.441 GB
2 nm	23.0368 M	891 MB	281.74 M	10.483 GB
1 nm	113.259 M	4.309 GB	2163.63 M	79.78 GB

which gives very good numerical stability.

2.1.2 Simulation boundaries in 3-D FDTD

Since any computational resource can only deal with a finite matrix size, the simulation region has to be terminated by appropriate boundaries. Perfectly matched layer (PML) and periodic boundary are the two types of boundaries used in this thesis.

PML is an artificial layer that can efficiently absorb the numerical waves with very little reflection from the interface. PMLs are implemented in the simulation boundaries to absorb the wave scattered out of the simulation region and to minimize the reflections, that were caused by the numerical iterations on the boundaries. Such reflections can go back to the simulation region and cause unphysical results. In this thesis, 40 PML layers are used in the appropriate boundary. The performance of such configured PML layers is very high, with only -200 dB reflection of numerical waves ¹.

Periodic boundaries are used in pairs, on the two parallel boundaries. The function of the periodic boundaries is that the electromagnetic wave that exits from one boundary will re-enter the simulation region from the opposite boundary with the same amplitude and phase. With periodic boundaries, a periodic array could be simulated using only a unit cell, which greatly reduces the computational intensity. However, it should be noted that, the periodic boundaries could not be applied to the boundaries perpendicular to the wave-vector of the light source, as there is a phase difference of the wave on the two boundaries. For example, in the configuration in

1. The 'dB' unit in this case is the scale defined as $10 \times \log_{10}(P_r/P_0)$, where P_r is the reflected power and P_0 is the source power.

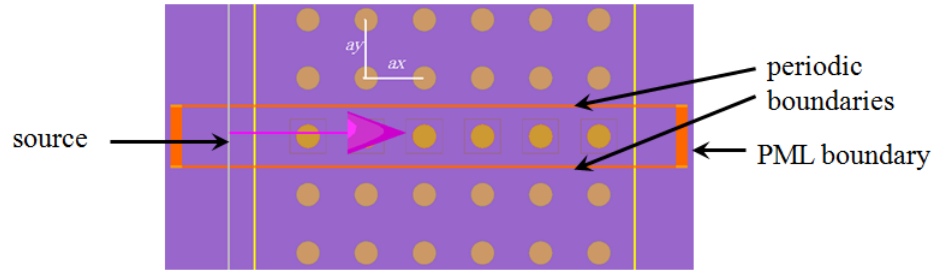


Figure 2.3: Simulation boundaries used in the configuration where light propagates in the plane of periodicity. The periodic array of the gold nanoparticles are located on top of the waveguide in the simulation region. The LSPRs of the gold nanoparticles are excited by the evanescent field of the waveguide mode, which propagates from left to right. Periodic boundaries are used in the vertical directions and PMLs are used in horizontal directions.

Figure 2.3, light is propagating horizontally. Periodic boundaries can be applied in the vertical directions but not in the horizontal directions.

2.1.3 Simulation configuration for simulating gold nanoparticles under normal transmission

The simulation configuration for studying the waveguide-excited LSPR will be presented in detail in Chapter 3 and 4. The configuration for simulating gold nanoparticles under normal transmission are used in the work presented in Chapter 5, 6, 7 and 8 but no details are provided in those chapters. It is worthwhile to present the details of the configuration in this section.

Taking a periodic array of gold nanorings as an example, such a configuration is shown in Figure 2.4(a). A nanoring is located on top of the substrate (substrate is hidden from the graph) and PML boundaries are used in vertical directions (pink color). The configuration of simulation boundaries in the horizontal directions depends on the targeted problem. If LSPR of a single gold nanoparticle is the target, PML boundaries should be used in horizontal directions. If LSPR of a periodic array is of interest, periodic boundaries should be used, with the length of the simulation region equal to the corresponding lattice constant. A plane wave source is excited and propagates downward, carrying a pulse containing the frequencies of interest (Figure 2.4(b)). The transmitted light is recorded by the power monitor in the simulation

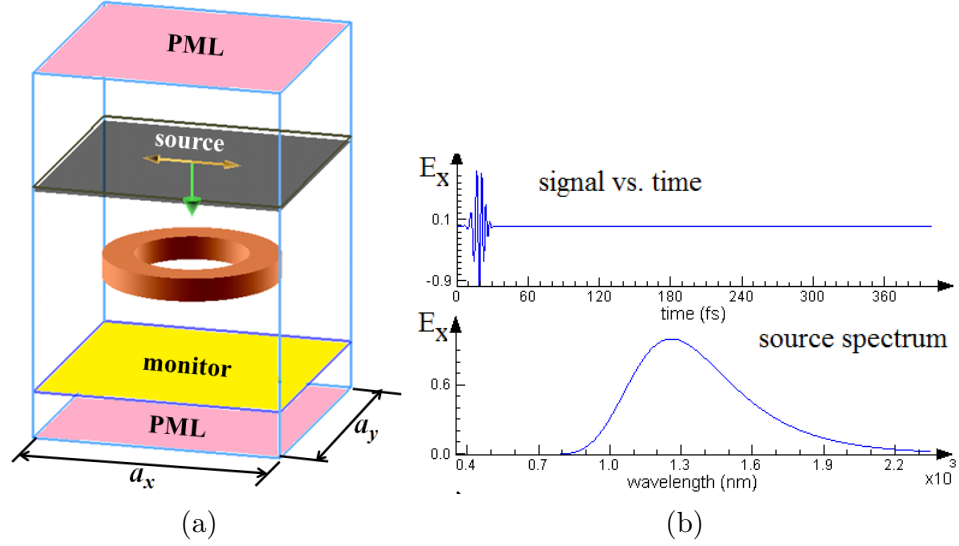


Figure 2.4: FDTD configuration to simulate LSPR of the gold nanoring. (a) the simulation configuration (b) the source signal and spectrum. The polarization direction (yellow arrow) of the plane wave is along the x direction, and the wave propagation direction (green arrow) is towards downward. The lateral dimension is given as a_x and a_y . These values are determined by the targeted problems. If periodic boundaries are used, a_x and a_y is equal to the corresponding lattice constant in the periodic array.

region ². Using DFT, the complex amplitudes of the field components are calculated and mode profile at given frequencies and power transmission spectrum $T(\lambda)$ can thus both be obtained.

The optical extinction spectrum $Ext(\lambda)$ is given in either linear scale as

$$Ext(\lambda) = 1 - T(\lambda) \quad (2.2)$$

or in logarithmic scale as

$$Ext(\lambda) = -\ln(T(\lambda)) \quad (2.3)$$

2. The monitor is a plane of interest specified in the simulation. Electromagnetic field data of the computational nodes on this plane are recorded in every iteration.

2.1.4 Simulation examples

In this section, two examples related to the later chapters are briefly introduced. The first example is the 3-D FDTD simulation of a single gold nanocrescent on top of the indium tin oxide (ITO) coated glass substrate. In this case, PML boundaries are used in all directions so that the gold nanocrescent is truly isolated. The geometry of the nanocrescent and obtained extinction spectrum and the mode profile at the resonance is shown in Figure 2.5³. The mode profile is the calculated field enhancement factor of the electric field in dB scale⁴. The gold nanocrescent demonstrates striking field confinement that can 'focus' light into nanoscale volumes on the sharp tips. Such nanoscale volumes with strong electromagnetic field intensity in nanoplasmonic structures are often called 'hot spots'. According to Unger et al. [4], the figure of merit of LSPR sensor is proportional to the field confinement factor, implying the high sensing potential of gold nanocrescents. The strong 'hot spot' makes the gold nanocrescent an appealing platform in other nano-optic applications too, such as surface enhanced Raman spectroscopy (SERS) [5].

The second example is the simulation of the periodic array of gold nanorings on top of the pyrex substrate. In this case, periodic boundaries are used in the horizontal directions. Detailed simulation results with varying lattice constants will be presented in Chapter 8. In this section, the simulated mode profile of the gold nanoring with lattice constant equal to 1050 nm is demonstrated in Figure 2.6. The mode is the lowest order of resonance with dipolar nature. It should be noted that, there are strong field confinements both inside and outside the walls of gold nanorings. The unique property of the gold nanoring results from the electromagnetic coupling between the inner and outer ring walls, a similar effect with the nanoshells [6]. Compared to nanoshells, the gold nanorings are more advantageous, as being vacant from the center that makes them more accessible by the analytes in sensing applications.

3. This is the detailed result of the same simulations that are presented in Chapter 6

4. The 'dB' unit in this case is the scale defined as $10 \times \log_{10}(E_1/E_0)$, where E_1 is the electric field intensity simulated with the presence of a gold nanoparticle and E_0 is the electric field intensity simulated without any gold nanoparticle. The ratio of them gives the magnitude of field enhancement caused by the gold nanoparticle.

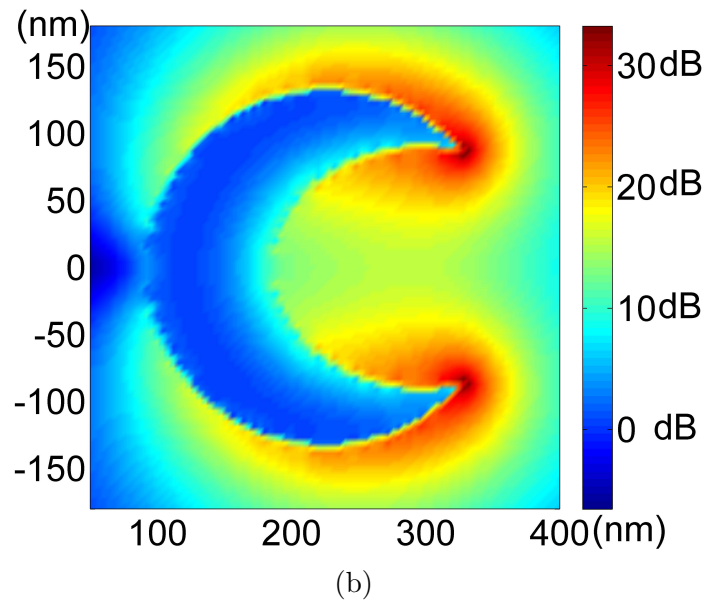
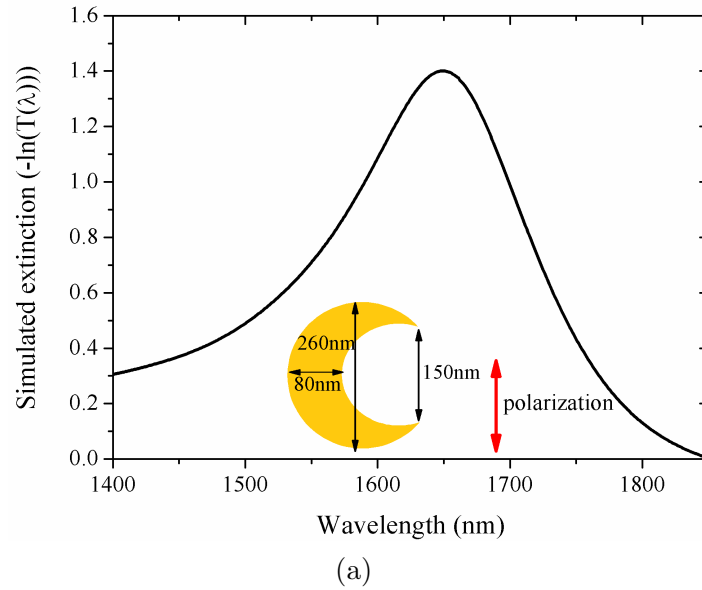
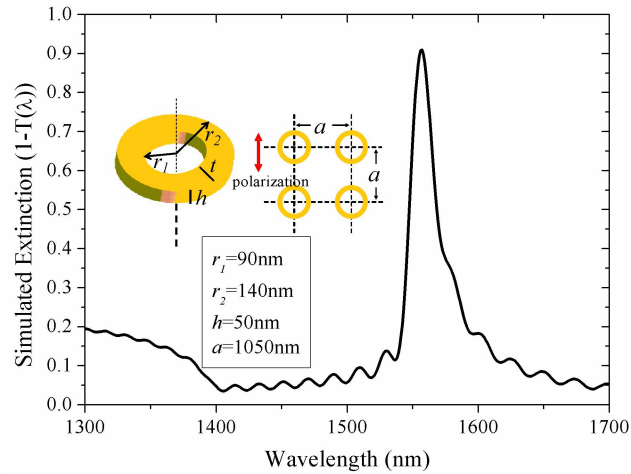
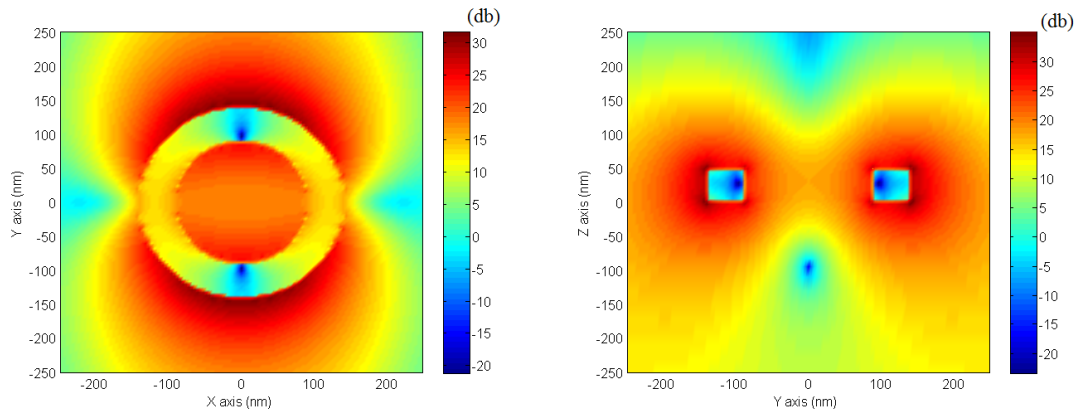


Figure 2.5: The simulated LSPR properties of a single gold nanocrescent. (a) the simulated extinction spectrum. (b) the simulated electric field intensity enhancement profile. The polarization of the light is indicated in (a) relative to the geometry of the nanocrescent. On the two sharp tips of the nanocrescent, more than 30 dB field enhancement is obtained.



(a) extinction spectrum



(b) mode profile, top view

(c) mode profile, side view

Figure 2.6: The simulated extinction spectrum and mode profile of periodic array of gold nanorings with $a = 1050$ nm. (a) the simulated extinction spectrum of the periodic array. (b) the simulated field enhancement profile, acquired along the plane of horizontal cut. (c) the simulated field enhancement profile, acquired along the plane of vertical cut. The geometrical parameters of the simulated gold nanoring array are shown in the inset of (a), together with the direction of light polarization. A dipolar LSPR resonance mode is obtained from the nanoring as indicated in (b) and (c).

2.2 Fabrication of gold nanoparticle arrays by electron beam lithography

To study the interactions of metal nanoparticles, the particle shape, size and particle spacings (lattice constants) all have to be precisely controlled at the same time. Electron beam lithography (EBL) is very suitable for this purpose. EBL can provide the high resolution required by fabricating nanoplasmonic structures. In addition, EBL is a lithography technique without using any mold or mask, meaning that the structures of interest can be modified by simply changing the pattern design from the computer. This offers great flexibility for studying nanostructures of different geometries and pattern. The weakness of the EBL is that the fabrication process is expensive and slow, not efficient for fabricating large scale structures. Therefore, EBL is generally used for research purposes and is a widely used technique in studying nanoplasmonic structures [7–15].

Metal nanoparticles have also been fabricated by other methods, such as nanoimprint lithography [16, 17], nanosphere lithography [18–21]. These are low-cost techniques suitable for producing large scale structures. In recent years, lithography-directed assembly of metal nanoparticles [22, 23], DNA-assisted assembly of metal nanoparticles [24] and controlled growth using chemical vapor deposition [25–27], have also emerged as appealing techniques to fabricate complex nanoparticle arrays. These techniques can be potentially used in the future to produce large scale LSPR sensor chips based on gold nanoparticles. Within the scope of this thesis, for the research purpose of studying periodic array of the gold nanoparticles, EBL is used to fabricate all the nanostructures. Generally speaking, the EBL system can achieve a resolution better than 10 nm, which is sufficient for fabricating gold nanoparticles.

2.2.1 Fabrication procedures

A simple diagram of an EBL system is given in Figure 2.7. The core component of the system is a scanning electron microscope (SEM) which can generate a focused electron beam and direct the beam to a substrate coated by a thin layer of electron-beam-sensitive photoresist. The exposure position and the exposure dose are precisely controlled an XY scanning coil and a beam blanker respectively. When using the EBL system, the pattern designed in the computer is processed by a nanometer pattern

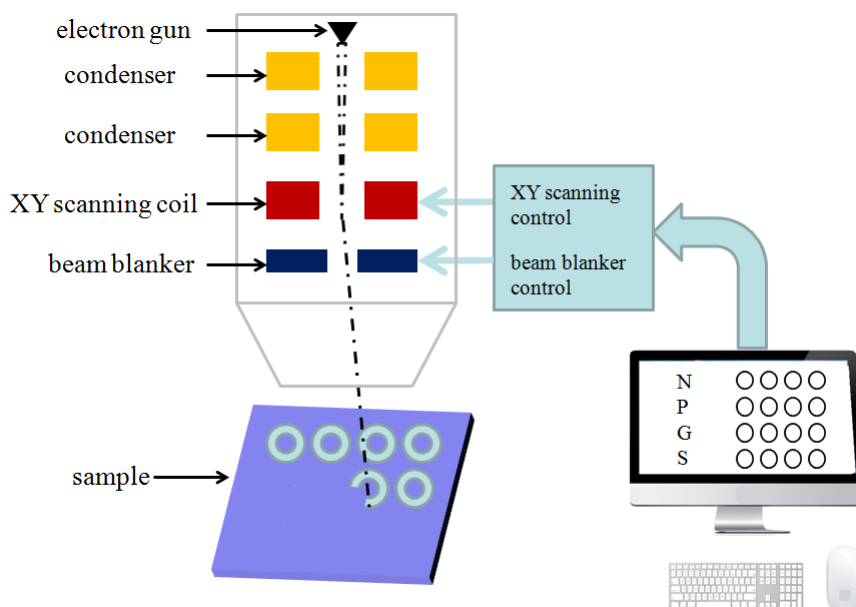


Figure 2.7: Diagram of electron beam lithography.

generation system (NPGS) software and the data are transmitted to the control unit of XY scanning and beam blanker, which commands the SEM to 'draw' the pattern onto the photoresist coated on the substrate.

The fabrication processes used in Chapter 4, 5, 6, 7 and 8 are slightly different, depending on the types of substrates used. The detailed fabrication procedures will be described in the corresponding chapters. In this section, a typical process is schematically demonstrated in Figure 2.8. A glass slide is used as the substrate, with its surface coated with a 25 nm ITO thin film to make the surface conductive. Electron beam sensitive photoresist (ZEP 520A, ZEON corporation) is spin coated on the substrate. Pattern of gold nanoparticles are then exposed into the photoresist by EBL. After exposure, the photoresist is developed in ZED-N50 developer (amyl acetate), rinsed and blown dried under flow of nitrogen. The exposed region of photoresist is then removed, leaving openings in the photoresist thin film. Then 2 nm thick titanium and 50 nm thick gold thin films are deposited on the sample by evaporation deposition technique. Titanium serves as a 'glue' to adhere gold to the glass substrate. After deposition, the sample is exposed to UV to decompose the photoresist. Then the sample is immersed into N-methyl-2-pyrrolidone solvent overnight. The photoresist is completely dissolved and the metal right on its top is removed. Only the metal deposited inside the openings remains on the substrate and yields the desired pattern

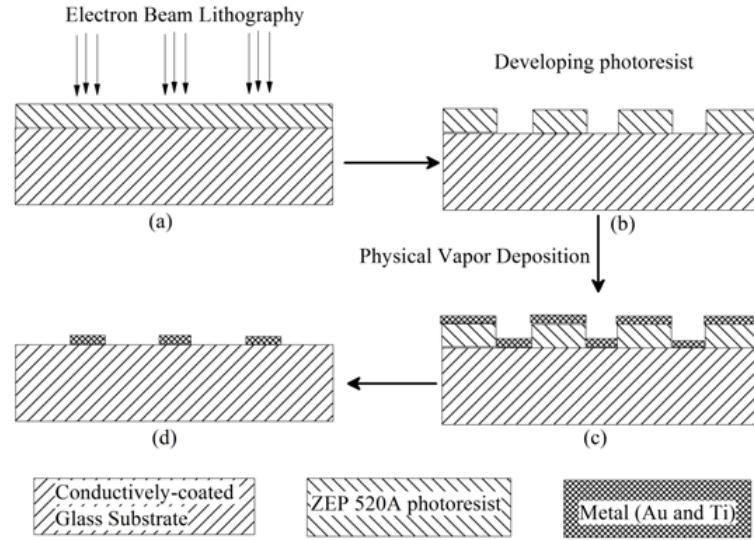


Figure 2.8: Schematic of the fabrication process.

Table 2.2: Summary of the conductive treatments on the substrates used in each chapter.

chapter No.	substrate	conductive layer	deposition method
4	ion-exchanged BK7 glass	20 nm Cr	sputtering
5	BK7 glass	2 nm Cr	evaporation
6	HQ float glass	25 nm ITO	sputtering
7	HQ float glass	25 nm ITO	sputtering
8	pyrex glass	20 nm Cr	sputtering

of gold nanoparticles.

It should be stressed that EBL requires the substrate to be conductive, which can be achieved by either coating conductive ITO film directly on the glass or by depositing a thin sacrificial chromium layer on top of the photoresist before EBL. The chromium layer is removed after EBL by immersing the sample in chromium etchant 1020 (Transene Company Inc.) for 30 seconds. It should be noted that, the lateral geometries of the fabricated structures are defined and controlled by the pattern design and exposure dose while the vertical height is controlled only by the thickness of the deposited metal. In the latter chapters of this thesis, the fabrication parameters are different depending on the types of substrates used. The substrates and the conductive treatment method used in later chapters are summarized in Table 2.2.

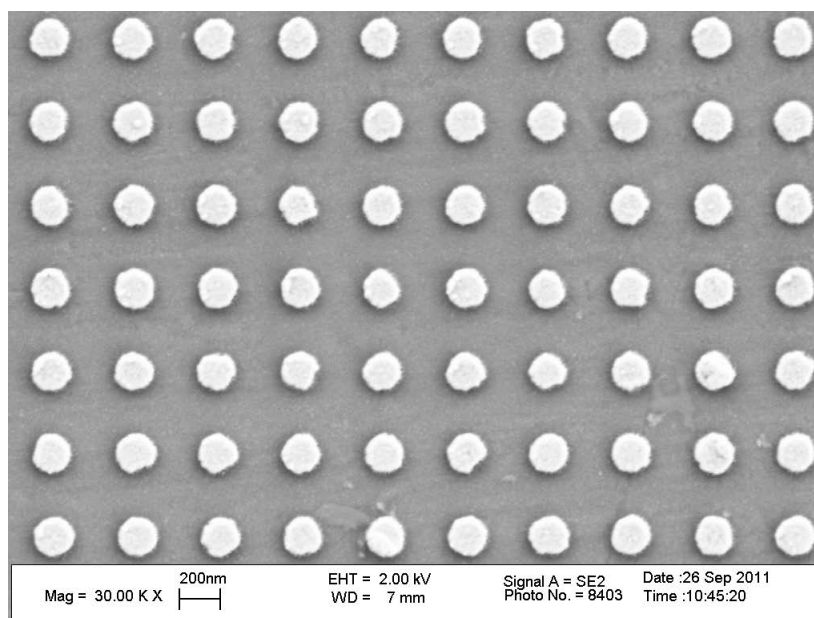
2.2.2 Dose calibration

The resolution of an optical lithography system is generally limited by the optical wavelength due to diffraction. The diffraction of electrons in an EBL system is not a problem as the electrons exhibit very short wavelengths (0.2 - 0.5 Å). The resolution of EBL is mainly limited by electron-optic aberrations and, more importantly, the scattering of electrons in the photoresist and substrate. Due to the scattering, the electron beam exposed in one spot will spread into an area. As a result, an object written in one area can be significantly affected by the exposure of objects located in its proximity and deviates from the intended size. This effect is referred to as the proximity effect. For example, in fabricating a periodic array of gold nanodisks with different lattice constants, as shown in Figure 2.9, the beam exposure dose is set to be the same on each individual object and the only difference is in the density of the nanodisks. However, due to proximity effects, the denser pattern gives obviously larger nanodisks, because the object in a denser pattern collects more electrons from its neighboring objects.

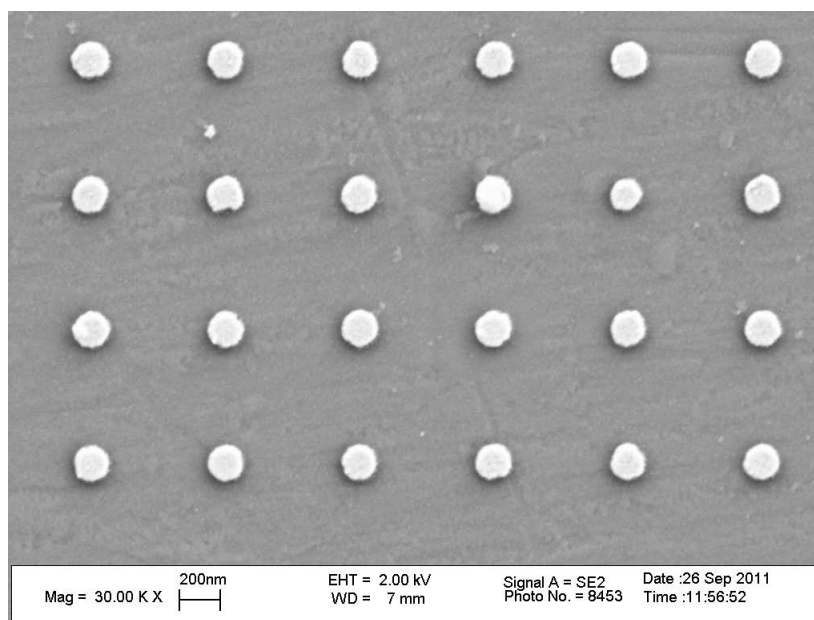
In order to study the periodic array effects, the average size of gold nanoparticles in each array should be kept nearly unchanged for different lattice constants. Therefore, the exposure dose on each array has to be calibrated to compensate the proximity effects. Taking gold nanodisks as an example, for a given lattice constant configuration, the pattern is written in multiple times with gradually increasing exposure dose. After fabrication, SEM images were acquired from each pattern. By image analyses, the statistics of the average size and standard deviation are obtained. For example, the SEM image of Figure 2.9(a) is processed by ImageJ software, and the recognized particle pattern is plotted in Figure 2.10. From these analysis, the dependence of the size of nanodisks in terms of numbers of pixels vs. the exposure dose for each lattice configuration is determined and fitted into linear equations. The experimental data for different lattice configurations are plotted together in Figure 2.11. With these relations, the exposure dose required for fabricating a certain size of nanodisk can be determined for each lattice constant.

2.2.3 Formation of gold nanocrescents and gold nanorings

In section 6.2, a procedure of formation of the gold nanocrescents is demonstrated. In section 7.2.1, a procedure of formation of the gold nanorings is described. It



(a) Pattern with lattice constant 400nm



(b) Pattern with lattice constant 650nm

Figure 2.9: SEM images to illustrate proximity effects. Fabricated periodic array of gold nanodisks with lattice constant equal to (a) 400nm and (b) 650nm. These two arrays were fabricated using the same exposure dose on individual object. Due to the proximity effects, the gold nanoparticles in the denser pattern are larger.

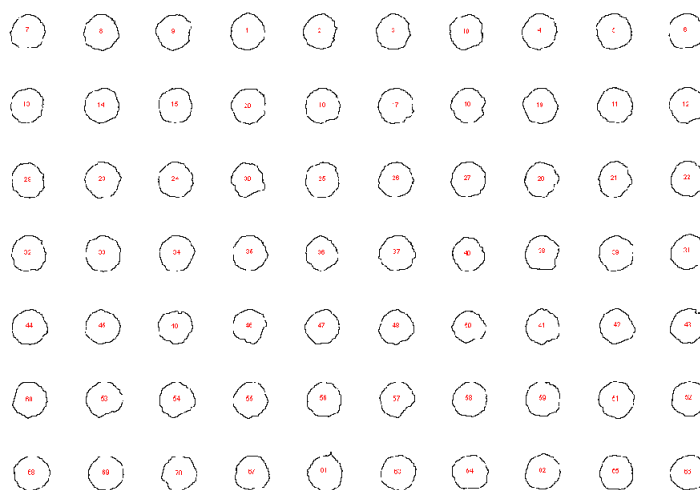


Figure 2.10: The image processing results of the SEM image in Figure 2.9(a). The original SEM image is processed by ImageJ software which generates the outlines of recognized gold nanoparticles. The size of each particle is calculated from the number of pixels enclosed in each outlined circle.

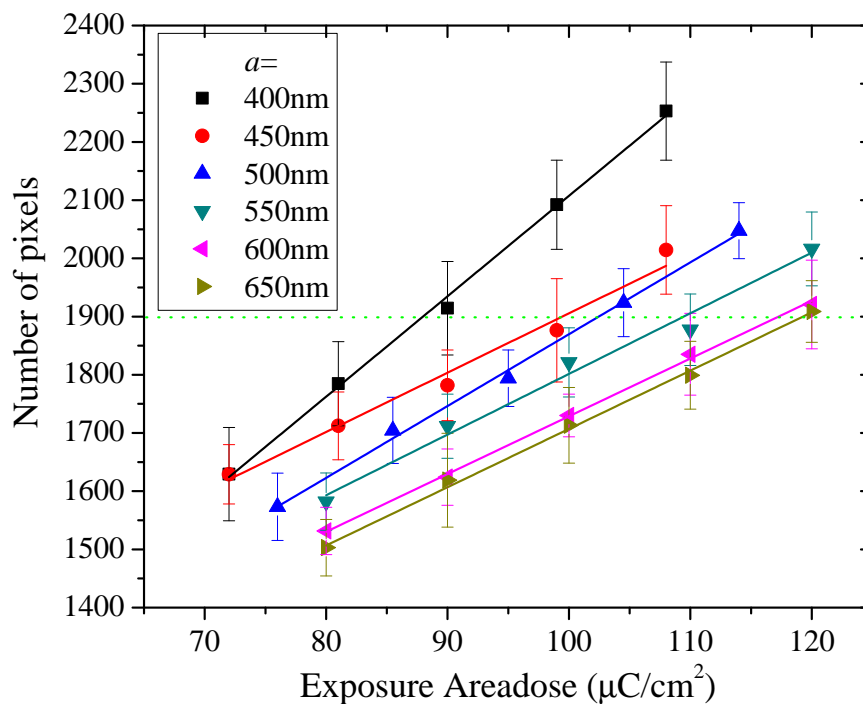


Figure 2.11: The size of fabricated nanodisks vs. the given dose for each lattice configuration determined from dose calibration procedures. Each data point represents the average size of fabricated nanoparticles, in terms of number of pixels, and the error bar is given by the standard deviation of the size statistics.

should be noted that, whether gold nanocrescents or gold nanorings will be formed is depending on the exposure dose. More specifically, nanocrescents are produced from high exposure dose and nanorings from low exposure dose.

It is worthwhile to briefly demonstrate these differences in this section. The schematic of the formation of gold nanocrescents is shown in Figure 6.1 in section 6.2. A designed pattern consisted of periodic arrays of circular lines (diameter 220 nm, periodicities 330 nm) are written by EBL onto 200 nm thick photoresist on ITO-coated glass. The exposure dose used in that case is 0.7 nC/cm. Because of the high exposure dose, the center post in the hole has a very small contact area with the substrate and collapses towards random orientation onto the edge of the hole leaving a crescent shape opening.

With the very same designed pattern and substrate, if the exposure dose is reduced to 0.4 nC/cm, the center post is sufficiently robust and will not collapse. The result is the formation of gold nanorings. This procedure is shown in Figure 2.12.

2.3 Measurement of the extinction spectrum

2.3.1 Normal transmission measurement

In Chapter 5, 6, 7 and 8, the sensor devices are measured by the normal transmission of broadband light focused onto the sensor device. The experimental setup is shown in Figure 2.13. A light source with a halogen lamp emits light covering a spectrum range of 360 nm - 2000 nm. The light is coupled into a multi-mode fiber ⁵, and collimated into a parallel light beam. The beam first propagates through an iris and then modified by long-pass filter ⁶, chopper ⁷ and polarizer ⁸. The configurations of these components are determined by the targeted application. The beam is then deflected

5. Multi-mode fibers from Ocean Optics, working wavelength 400 nm to 2000 nm.

6. Long-pass filters from Thorlabs Inc., cut-off wavelength of 715 nm or 1000 nm is used, depending on the structures to be measured.

7. Chopper from Terahertz Technologies Inc., operating frequency is 400 Hz.

8. Linear polarizer from Thorlabs Inc., working wavelength 650 nm to 2000 nm and extinction ratio 1000:1. The polarization direction is set to be parallel to one of the directions of periodicity.

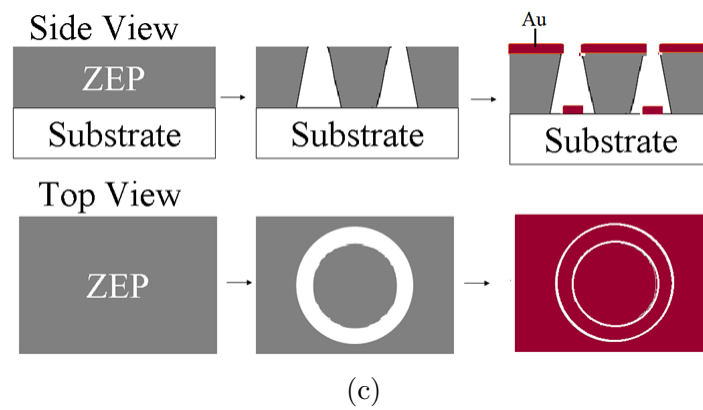
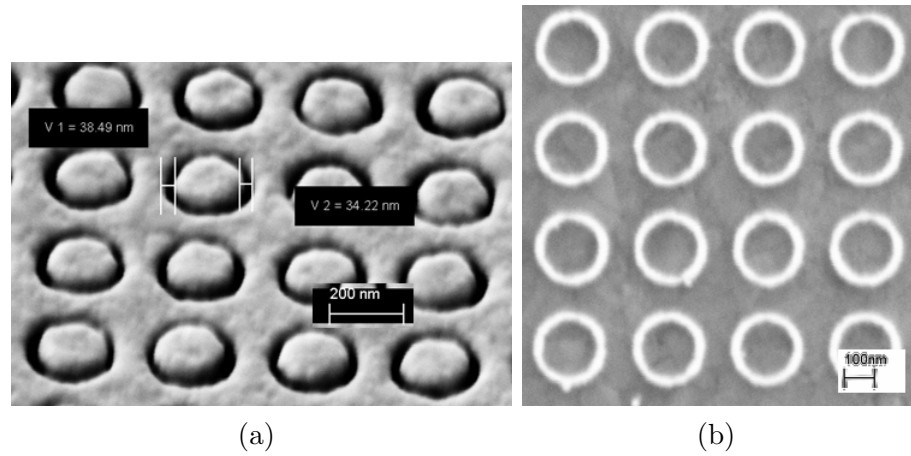


Figure 2.12: Formation of the gold nanorings. (a) SEM figure of the pattern right after metal deposition, demonstrating the ring-shaped openings on the photoresist. (b) SEM figure of the fabricated gold nanorings, after lift-off process. (c) Schematic of the formation of the gold nanorings.

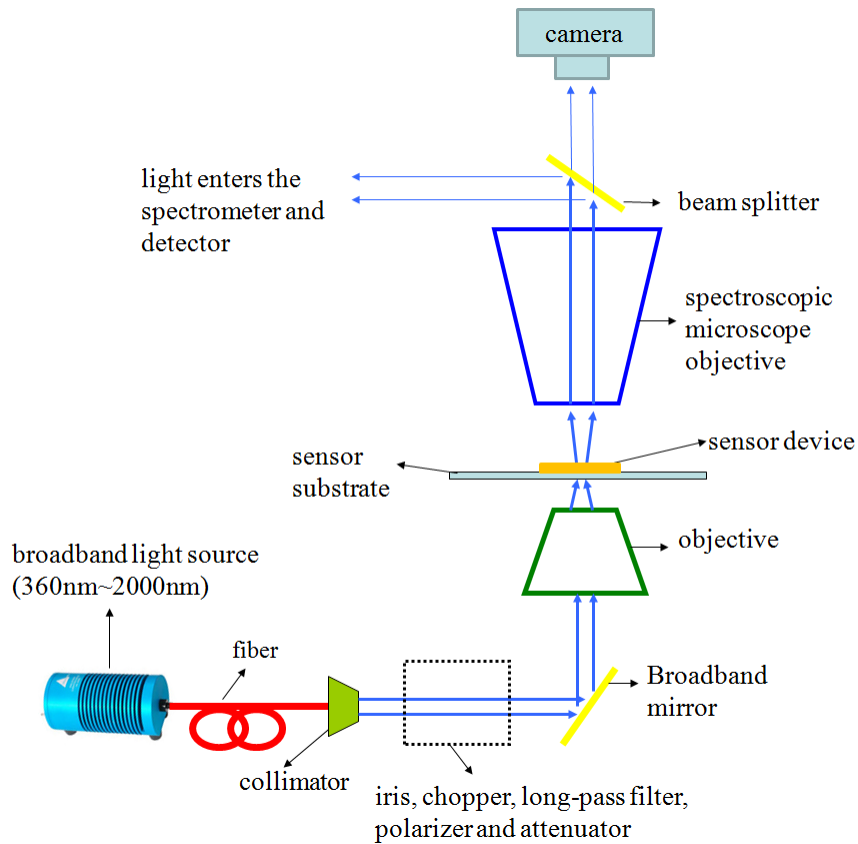


Figure 2.13: The diagram of the setup to measure the extinction spectrum in normal transmission.

by a broadband mirror into the upward direction and focused by an microscope objective lens onto the surface of the sensor device. The transmitted light is collected into a spectroscopic microscope lens and divided by a beam splitter into two paths: the transmitted light is collected by a camera which records the microscope image of the sensor device and the reflected light is collected by a spectrometer which measures the intensity spectrum $I(\lambda)$.

A photo of core components of the measurement setup in reality is given in Figure 2.14. In order to achieve accurate alignment of the optical components, comprehensive tilting and translation controls are provided on the optical mounts.

The sensor device probed in normal transmission is consisted of multiple elements arranged in an array fabricated on top of the substrate. Each element occupies an area smaller than $120 \mu\text{m} \times 120 \mu\text{m}$. This size is limited by the size of the writing

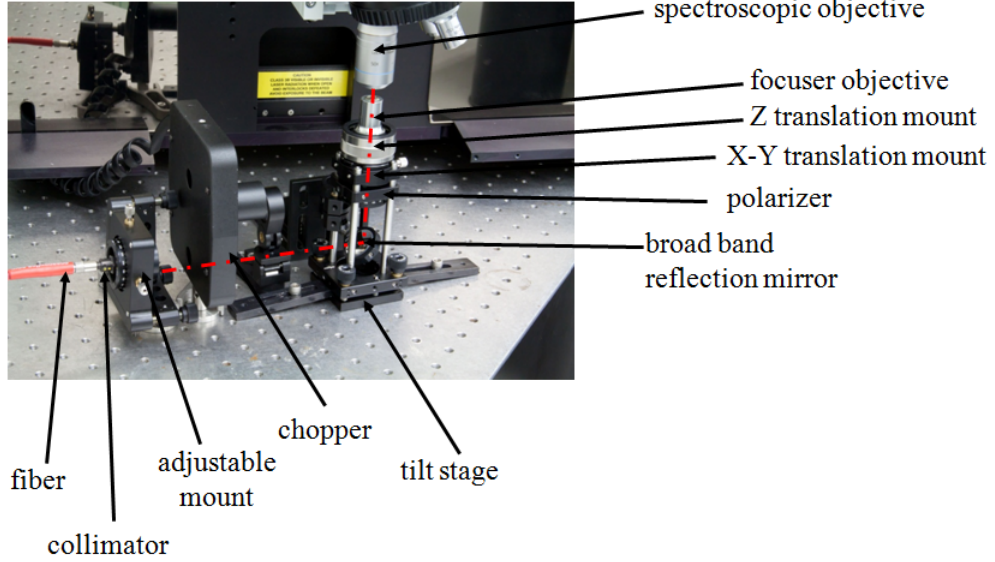


Figure 2.14: The photo of the measurement setup corresponding to the diagram of Figure 2.13.

field of EBL⁹. As demonstrated in Figure 2.15, these sensor elements are compactly integrated into a sub-millimeter area. Each element is an independent nanoplasmonic structure consisted of periodic array of gold nanoparticles. With the iris and focuser objective lens, the light beam is focused into a spot smaller than $40 \mu\text{m} \times 40 \mu\text{m}$. Therefore, only one sensor element is measured at a time and it is completely isolated from other sensor elements. To measure an extinction spectrum, a transmission spectrum $I_{ref}(\lambda)$ is first measured from a location without any structure and then a second transmission spectrum $I_{dev}(\lambda)$ is measured through the sensor element. The measured extinction spectrum $Ext(\lambda)$ is then given in either linear scale as

$$Ext(\lambda) = 1 - \frac{I_{dev}(\lambda)}{I_{ref}(\lambda)} \quad (2.4)$$

or in logarithmic scale as

$$Ext(\lambda) = -\ln \frac{I_{dev}(\lambda)}{I_{ref}(\lambda)} \quad (2.5)$$

9. All the patterns presented in this thesis, were written in an EBL system using a magnification of 600X, which gives a maximum writing field size of $148 \mu\text{m} \times 148 \mu\text{m}$. To avoid the edge effects in the EBL, at least $10 \mu\text{m}$ margin should be left blank from each bound of the writing field. Therefore, the structure in one EBL writing is usually smaller than $120 \mu\text{m} \times 120 \mu\text{m}$.

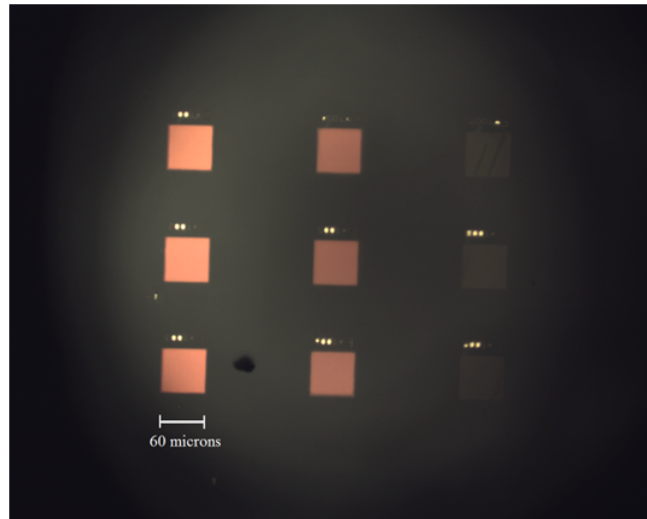


Figure 2.15: Microscope image of the sensor elements on one device recorded by the camera. Each sensor element occupies a very small area and multiple elements are arranged into a sensor array.

The gold nanodisks, gold nanorings and gold nanocrescents, investigated in this thesis have LSPR peaks in different spectrum ranges. Therefore, the measurement set up is configured according to the structure being studied. Table 2.3 summarizes the parameters used for these different nanoplasmonic structures.

2.3.2 Quantification of the peak shift

As previously mentioned in Section 1.2.1, the limit of detection of an LSPR sensor is determined by the sensitivity and the minimum detectable change of signal. The latter is related to the detection uncertainty $\Delta\lambda_{un}$ in determining the resonance peak. Therefore, the peak shift has to be quantified with high accuracy to achieve a better limit of detection. In the biosensor based on gold nanodisks presented in Chapter 5, a method reported by Dahlin et al. is used to quantify the peak shift [28]. In this method, the peak shift is quantified from the shift of centroid peak λ_c , which is the mass center of an extinction spectrum as defined in Equation 2.7. This is different from the peak shift quantified from the extinction peak maximum $\Delta\lambda_p$. According to Dahlin et al., $\Delta\lambda_c$ can be quantified with much higher accuracy, $<5 \times 10^{-4}$ nm, with a S/N ratio ~ 2000 [28].

From the biosensor based on the periodic array of gold nanodisks, a measured extinction spectrum data $e_{exp}(\lambda)$ is obtained from the device with $a = 550$ nm. The

Table 2.3: Configuration of the measurement setup for different nanoplasmonic structures

structure type	LSPR peak	detector type	detector range
nanodisk	750 nm - 1050 nm	silicon detector array (2048 pixels)	200 nm - 1100 nm
nanoring	1100 nm - 1600 nm	InGaAs, single channel	800 nm - 1700 nm
nanocrescent	1600 nm - 1900 nm	extended InGaAs, single channel	1200 nm - 2600 nm

measured curve is plotted as crosses in top panel of Figure 2.18. The measured spectrum is first fitted into a n th order polynomial $e_{fit}(\lambda)$, given in Equation 2.6. In this case, 10th order polynomial is used with relative fitting error $< 7 \times 10^{-4}$. The fitted polynomial curve is given as the red line in the same figure. In the following, a spectrum range $[\lambda_1, \lambda_2]$ has to be determined first for calculating the mass center. Two wavelengths λ_1 and λ_2 with a span S , i.e. $\lambda_2 - \lambda_1 = S$, are solved from the fitted curve, satisfying $e_{fit}(\lambda_1) - e_{fit}(\lambda_2) = 0$, and the extinction at the solved wavelength is $e_{fit}(\lambda_1) = e_{fit}(\lambda_2) = e_{base}$. It should be pointed out that, the choice of S depends on the linewidth fwhm Γ of the spectrum. Different S values have been experimented and $S = \Gamma - 20$ gives the best results. The distance S is determined to be 80 nm in this case. In the following, the mass center λ_c of the fitted extinction spectrum from λ_1 to λ_2 is calculated using Equation 2.7. The uncertainty in determining λ_c in this case is < 0.012 nm. It should be noted that, the uncertainty obtained from extinction peak maximum in a Lorentzian curve fitting strategy is at least three times larger.

$$e_{fit}(\lambda) = \sum_{i=0}^n P_{i+1} \lambda^i \quad (2.6)$$

$$\lambda_c = \frac{\int_{\lambda_1}^{\lambda_2} \lambda (e_{fit}(\lambda) - e_{base}) d\lambda}{\int_{\lambda_1}^{\lambda_2} (e_{fit}(\lambda) - e_{base}) d\lambda} = \frac{\sum_{i=0}^n [\frac{P_{i+1}}{i+2} (\lambda_2^{i+2} - \lambda_1^{i+2})] - \frac{e_{base}}{2} (\lambda_2^2 - \lambda_1^2)}{\sum_{i=0}^n [\frac{P_{i+1}}{i+1} (\lambda_2^{i+1} - \lambda_1^{i+1})] - e_{base} (\lambda_2 - \lambda_1)} \quad (2.7)$$

2.4 Surface functionalization

For biosensor applications, the surface functionalization of receptors onto the sensor surface is of great importance. The quality of the surface chemistry has direct impact on the sensor's limit of detection, reproducibility and robustness.

In this thesis, organic molecules containing the thiol group are used to functionalize the surface of gold nanoparticles. The thiol group, also called 'mercapto', consists of sulfur and hydrogen bond, given as '-SH'. Due to the strong binding energy between sulfur in the thiol group and the gold, these molecules are immobilized on the surface of gold and form into a well-organized self-assembled monolayer [29–31]. The structure of the molecules consists of thiol group at one end, alkyl chain (C_nH_{2n+1}) as the backbone of the molecule, and the functional group at the other end, as depicted in Figure 2.16. Different types of frequently used functional groups are also plotted in

the same figure. The choice of the functional groups depends on the applications. Hydroxyl group is generally used to make the sensor surface hydrophilic, which can help prevent non-specific binding of biomolecules [31]. Carboxylic group and amine group are generally used to conjugate to the protein through peptide bonds. Biotin group is used to bind streptavidin biomolecules onto the surface due to the exceptionally high affinity between biotin and streptavidin [31]. To avoid the steric hindrance, the SAM molecules used in the surface functionalization are often a mixture of two thiol molecules of heterogeneous lengths. One molecule has hydroxyl functional group and a short backbone, and serves as spacer to prevent non-specific binding. The other molecule has carboxylic, amine or biotin functional group and a longer backbone, and serves as linker for receptors.

Two types of methods have been used in this thesis to immobilize the streptavidin (a protein) onto the sensor surface. In the first method, SAM layer containing biotin functional group is used and streptavidin directly bind to the biotin group on the SAM. This method will be shown in Section 2.5. Another method is to implement SAM layer containing carboxylic group and link the streptavidin to the SAM molecule through peptide bond formed between the carboxylic group on the SAM and the amine group in the streptavidin molecule. To form the peptide bond, the carboxylic groups on the SAM surface have to be activated first. A general procedure is the EDC/NHS chemistry ¹⁰, as depicted in Figure 2.17. This is the surface functionalization procedure used in Chapter 5 and Chapter 8. After immobilization of the SAM layer, the surface of gold is covered by a mixture of SAM molecules containing the hydroxyl group and the carboxylic group, respectively. The EDC in water solution is then introduced onto the sensor surface and reacts with the carboxylic group to form an unstable structure. NHS solution is then introduced, and NHS replaces unstable EDC and forms a succinimide ester which is very reactive to amine group. After this stage, the carboxylic group is already activated and ready to react with proteins. It should be noted that the NHS reaction is reversible, meaning that after the activation of carboxylic group, proteins should be introduced immediately. The amine group in the streptavidin molecule then reacts with the succinimide esters and forms a peptide bond with the carboxylic group. It should be noted that, EDC is not stable in water and only freshly prepared EDC solution should be used in each

10. EDC stands for 1-ethyl-3-(3-dimethylaminopropyl) carbodiimide and NHS stands for N-hydroxysuccinimide

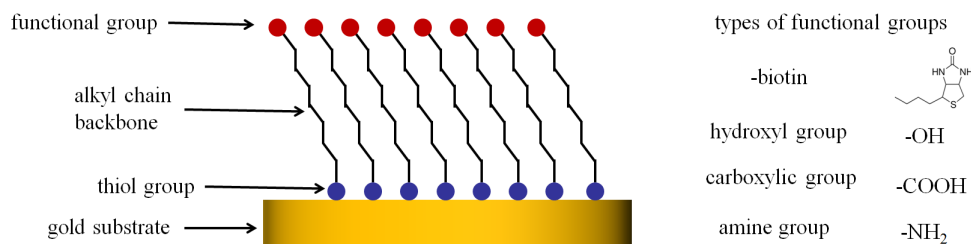


Figure 2.16: Schematic of the structures of the SAM molecules.

experiment.

2.5 Example in sensing biotin-streptavidin interactions

As a proof-of-concept, the sensor based on periodic array of gold nanodisks is shown in this section to detect the binding of streptavidins and biotins. Streptavidin is a protein and biotin is a vitamin. These two biomolecules have exceptionally high affinity (association constant $K_A \sim 10^{14} M^{-1}$) [32, 33].

After the sensor being thoroughly cleaned, the sensor is immersed in an ethanol solution consisting of 0.45 mM 11-Mercapto-1-undecanol and 0.05 mM thiol-PEG-biotin molecules to form a well-organized SAM layer. The chemical formulas of these two types of molecules are shown in 2.19(a). After being immersed for 12 hours, the sensor is thoroughly rinsed with deionized water and ethanol, attached to the flow cell, and loaded into the measurement system described in section 2.3.1. On the sensor surface, as shown in Figure 2.19(a), the biotin-terminated molecules are the receptors used to capture targeted biomolecules and the hydroxyl-group-terminated molecules are spacers used to prevent non-specific binding [29, 31].

Extinction spectra are recorded in real-time with an interval of 11 seconds. λ_c of each spectrum is calculated using the aforementioned method with the same order of polynomial fitting. The spectrum range used to calculate the mass center varies, but the spectrum span S is kept constant. The calculated centroid peak is plotted vs. time in Figure 2.19(b). In the beginning, a phosphate-buffered saline (PBS) solution, with pH = 7.4, is used to rinse the sensor and a stabilized baseline is acquired. Then streptavidin (analytes) in the concentration of 1.1 μM in PBS solution is injected onto the sensor at a constant flow rate of 5 $\mu L/min$. The flow rate is controlled by a syringe

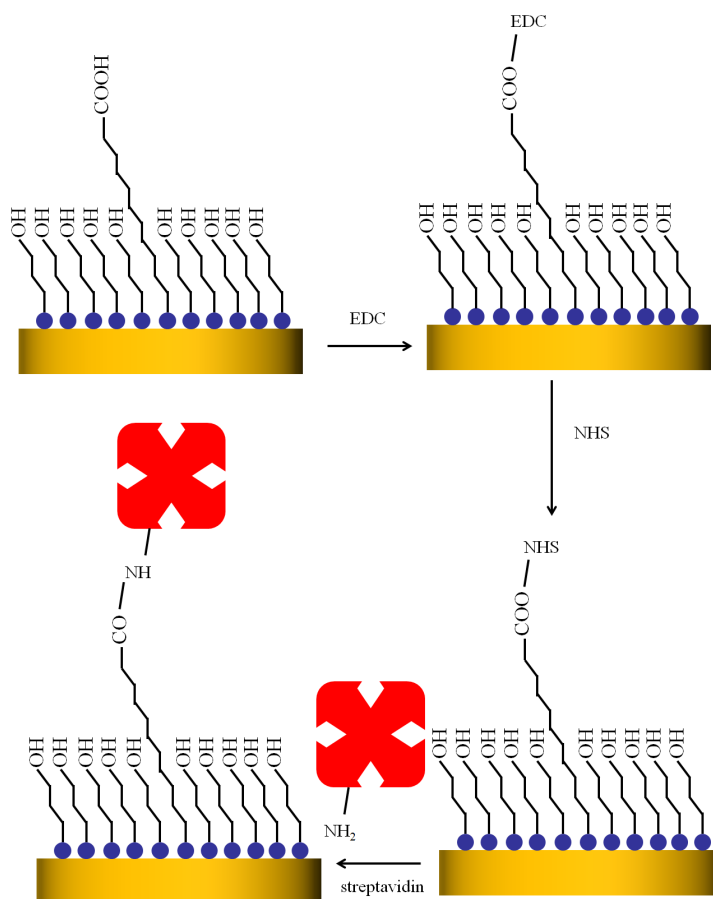


Figure 2.17: Schematic of the EDC/NHS chemistry to bind streptavidin to the carboxylic group in SAM layer.

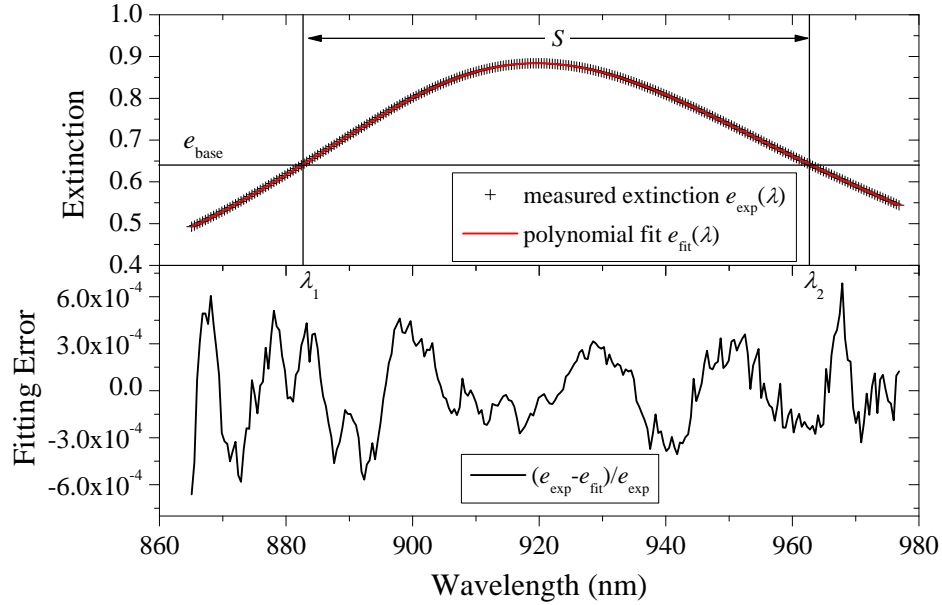


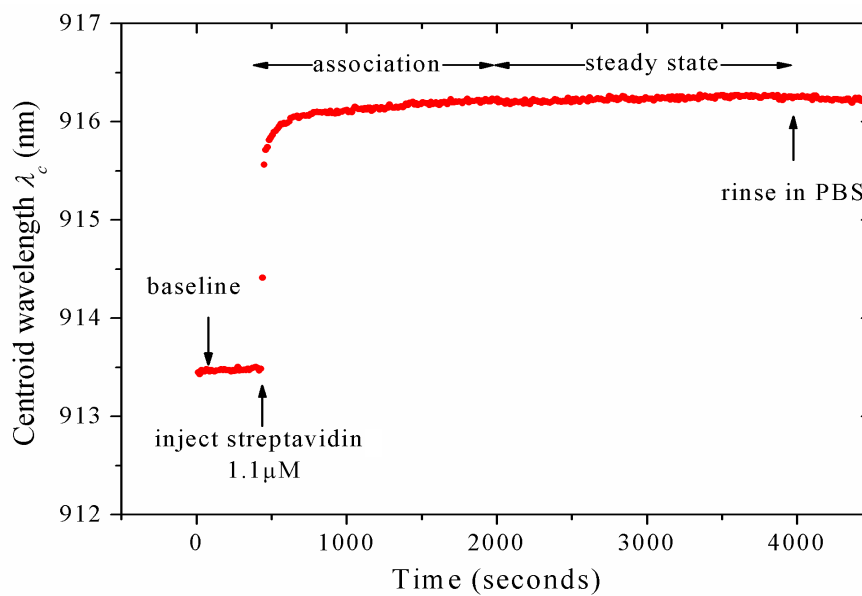
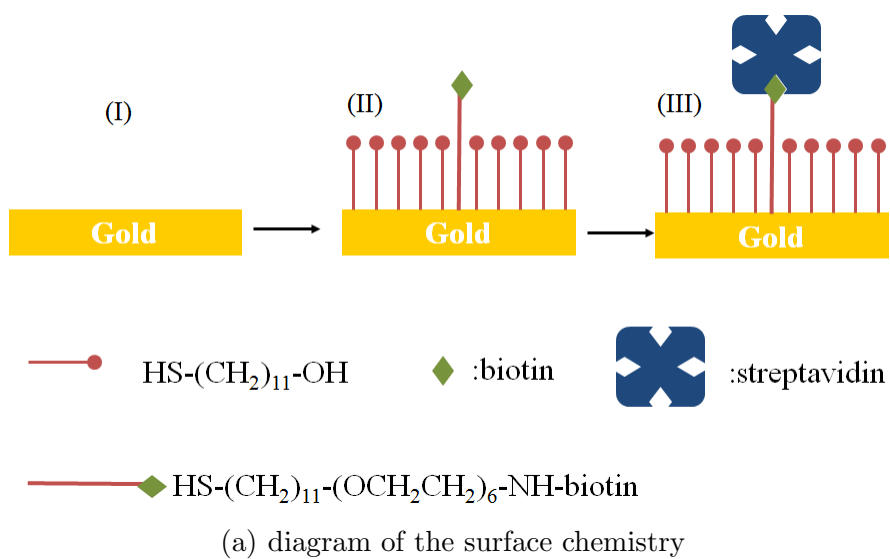
Figure 2.18: Data fitting of measured extinction spectrum into polynomial.

pump. The sensor response λ_c displays a red-shift signal caused by the streptavidin binding to the biotin. This step is called association stage. After about 2000, the red-shift saturates, meaning that the analytes and the receptors have reached an equilibrium. This is called the steady state. At the time around 4000, PBS solution is injected to rinse the sensor and non-specifically physisorbed streptavidin is rinsed out from the surface. It should be noted that, due to the exceptional high affinity between biotin and streptavidin, there is no dissociation observed from the signal in this experiment. For common binding pairs with much lower affinity, in the step of rinsing, the analytes will begin to dissociate from the receptors. This step is called dissociation stage.

The kinetics of association stage, steady state and dissociation stage have been well studied by many researchers. Like the equations described by Oshannessy et al. [34], the kinetic equations for this LSPR sensor can be similarly derived.

The binding of the analytes in the solution with the receptors immobilized on the sensor surface is a dynamic and reversible process. Assume the surface concentration of the receptors is $[R]$ and the analyte concentration is $[A]$, the surface concentration of the formed complexes is $[RA]$.

The process of interactions between receptors (R) and analytes (A) can be



(b) sensor response

Figure 2.19: Response of biorecognition of streptavidin onto biotin. (a) diagram of surface functionalization and (b) the sensor response in real-time. The chemical formulas of the compounds used in SAM layer formation are given in (a).

described as



where the association and dissociation happen at the same time, with different rates.

The rate of association is given as $k_a[R][A]$, where k_a is the association rate constant with the unit $M^{-1}s^{-1}$ while the rate of dissociation is given as $k_d[RA]$, where k_d is the dissociation rate constant with the unit s^{-1} . Therefore, the rate of formation of complexes at a given time t is given in Equation 2.9.

$$\frac{d[RA]}{dt} = k_a[R][A] - k_d[RA] \quad (2.9)$$

The concentrations of the already formed complexes and remaining receptors are related as $[R] = [R]_0 - [RA]$, where $[R]_0$ is the concentration of receptors before introducing the analytes. Thus, the following Equation 2.10 can be obtained.

$$\frac{d[RA]}{dt} = k_a[A]([R]_0 - [RA]) - k_d[RA] \quad (2.10)$$

In the experiment, the analyte is continuously flown over the surface, therefore, the concentration $[A]$ is a constant value, letting $[A] = C_A$. The sensor signal, i.e. the centroid peak shift, $\Delta\lambda_c$, is linearly dependent on the formation of complexes as

$$\Delta\lambda_c = m_c[RA] \quad (2.11)$$

where m_c is a sensitivity coefficient. Considering when the maximum sensor response occurs, meaning that all the receptors have bonded to the analytes, $[RA] = [R]_0$, the corresponding signal is given as $\Delta\lambda_{max}$. Thus, $[R]_0 = \Delta\lambda_{max}/m_c$.

The Equation 2.10 can now be written into a form expressed in Equation 2.12.

$$\frac{d\Delta\lambda_c}{dt} = C_A k_a (\Delta\lambda_{max} - \Delta\lambda_c) - k_d \Delta\lambda_c \quad (2.12)$$

The integration form can accordingly be obtained as Equation 2.13.

$$\Delta\lambda_c(t) = \frac{C_A k_a \Delta\lambda_{max} [1 - e^{-(C_A k_a + k_d)(t-t_0)}]}{C_A k_a + k_d} \quad (2.13)$$

Therefore, when the analytes are introduced into the sensor surface, the signal red-shifts exponentially and then saturates into a value determined by the ana-

lyte concentration C_A . As $t \rightarrow \infty$, $\Delta\lambda_c = \frac{C_A k_a \Delta\lambda_{max}}{C_A k_a + k_d}$ reaches a steady state. At the steady state, the association and dissociation reaches equilibrium, meaning that $k_a[R][A] = k_d[RA]$. Thus, at steady state, one obtains

$$\frac{[RA]}{[R][A]} = \frac{k_a}{k_d} = K_A = \frac{1}{K_D} \quad (2.14)$$

where K_A is named as the association constant and K_D is named as the dissociation constant. K_A and K_B should be differentiated from the association *rate* constant k_a and the dissociation *rate* constant k_d . This is known as Langmuir isotherm.

When rinsing the sensor with only the buffer solution, the analyte concentration suddenly drops to zero, and there is only dissociation. The rate of dissociation of the RA complexes is

$$\frac{d[RA]}{dt} = -k_d[RA] \quad (2.15)$$

and the sensor response in the dissociation stage can be accordingly written as

$$\Delta\lambda_c(t) = \Delta\lambda_{c0} e^{-k_d(t-t_0)} \quad (2.16)$$

where $\Delta\lambda_{c0}$ is the signal at $t = t_0$ when the rinsing begins.

It has to be pointed out that, the dissociation of streptavidin and biotin is very slow. The dissociation rate constant k_d is around $2.4 \times 10^{-6} s^{-1}$ [35], meaning that it takes $\ln(0.99)/k_d \approx 4187$ seconds to dissociate one percent of RA complexes. The very slight signal drop in Figure 2.19(b), in the rinsing step, is caused by the slight difference in background refractive index and the removal of non-specifically bound streptavidin, weakly physisorbed to the sensor surface. Generally speaking, the binding pairs of streptavidin and biotin can be considered as permanent binding. Thus the biotin-avidin complex has been used as a very versatile mediator in a wide variety of bioanalytical applications [32].

2.6 Summary

The fundamental research methods, including simulation approaches, fabrication techniques, measurement setups and surface chemistry procedures have been introduced in this chapter. In each following chapter, the work will be presented in the

article format and may not cover full details of the research methods being used. Those details shall be found either from this chapter or from the appendices.

References

- [1] A. Taflove and S. C. Hagness, *Computational Electrodynamics: The Finite-Difference Time-Domain Method*. Artech House, 2000.
- [2] A. T. Williams, “Absorption spectra of metallic colloidal solutions, and emission and absorption of metallic films,” *Nature*, vol. 130, pp. 963–964, 1932.
- [3] B. T. Draine and P. J. Flatau, “Discrete-dipole approximation for scattering calculations,” *J. Opt. Soc. Am. A*, vol. 11, no. 4, pp. 1491–1499, 1994.
- [4] A. Unger and M. Kreiter, “Analyzing the performance of plasmonic resonators for dielectric sensing,” *J. Phys. Chem. C*, vol. 113, pp. 12 243–12 251, 2009.
- [5] Y. Lu, G. L. Liu, J. Kim, Y. X. Meja, and L. P. Lee, “Nanophotonic crescent moon structures with sharp edge for ultrasensitive biomolecular detection by local electromagnetic field enhancement effect,” *Nano Letters*, vol. 5, no. 1, pp. 119–124, 2005.
- [6] F. Tam, C. Moran, and N. Halas, “Geometrical parameters controlling sensitivity of nanoshell plasmon resonances to changes in dielectric environment,” *The Journal of Physical Chemistry B*, vol. 108, no. 45, pp. 17 290–17 294, 2004.
- [7] B. Lamprecht, G. Schider, R. T. Lechner, H. Ditlbacher, J. R. Krenn, A. Leitner, and F. R. Aussenegg, “Metal nanoparticle gratings: influence of dipolar particle interaction on the plasmon resonance,” *Phys. Rev. Lett.*, vol. 84, no. 20, pp. 4721–4724, 2000.
- [8] N. Felidj, G. Laurent, J. Aubard, G. Levi, A. Hohenau, J. R. Krenn, and F. R. Aussenegg, “Grating-induced plasmon mode in gold nanoparticle arrays,” *J. Chem. Phys.*, vol. 123, p. 221103, 2005.
- [9] J. Sung, E. M. Hicks, R. P. Van Duyne, and K. G. Spears, “Nanosphere spectroscopy: dipole coupling in two-dimensional arrays of L-shaped silver nanoparticles,” *J. Phys. Chem. C*, vol. 111, pp. 10 368–10 376, 2007.

- [10] J. Sung, E. M. Hicks, R. P. Van Duyne, and K. G. Spears, "Nanoparticle spectroscopy: plasmon coupling in finite-sized two-dimensional arrays of cylindrical silver nanoparticles," *The Journal of Physical Chemistry C*, vol. 112, no. 11, pp. 4091–4096, 2008.
- [11] S. Linden, A. Christ, J. Kuhl, and H. Giessen, "Selective suppression of extinction within the plasmon resonance of gold nanoparticles," *Appl. Phys. B*, vol. 73, pp. 311–316, 2001.
- [12] S. Linden, J. Kuhl, and H. Giessen, "Controlling the interaction between light and gold nanoparticles: selective suppression of extinction," *Phys. Rev. Lett.*, vol. 86, no. 20, pp. 4688–4691, 2001.
- [13] E. M. Hicks, S. Zou, G. C. Schatz, K. G. Spears, R. P. Van Duyne, L. Gunnarsson, T. Rindzevicius, B. Kasemo, and M. Kall, "Controlling plasmon line shapes through diffractive coupling in linear arrays of cylindrical nanoparticles fabricated by electron beam lithography," *Nano Letters*, vol. 5, no. 6, pp. 1065–1070, 2005.
- [14] B. Auguie and W. L. Barnes, "Diffractive coupling in gold nanoparticle arrays and the effect of disorder," *Optics Letters*, vol. 34, no. 4, pp. 401–403, 2009.
- [15] A. K. Sheridan, A. W. Clark, A. Glide, J. M. Cooper, and D. R. S. Cumming, "Multiple plasmon resonances from gold nanostructures," *Appl. Phys. Lett.*, vol. 90, p. 143105, 2007.
- [16] S. Y. Chou, P. R. Krauss, and P. J. Renstrom, "Imprint of sub-25 nm vias and trenches in polymers," *Applied Physics Letters*, vol. 67, pp. 3114–3116, 1995.
- [17] S. Kim, J.-M. Jung, D.-G. Choi, H.-T. Jung, and S.-M. Yang, "Patterned arrays of au rings for localized surface plasmon resonance," *Langmuir*, vol. 22, pp. 7109–7112, 2006.
- [18] L. J. Sherry, R. Jin, C. A. Mirkin, G. C. Schatz, and R. P. Van Duyne, "Localized surface plasmon resonance spectroscopy of single silver triangular nanoprisms," *Nano Letters*, vol. 6, no. 9, pp. 2060–2065, 2006.
- [19] M. Retsch, M. Tamm, N. Bocchio, N. Horn, R. Forch, U. Jonas, and M. Kreiter, "Parallel preparation of densely packed arrays of 150-nm gold-nanocrescent resonators in three dimensions," *Small*, vol. 5, no. 18, pp. 2105–2110, 2009.

- [20] R. Bukasov and J. S. Shumaker-Parry, “Highly tunable infrared extinction properties of gold nanocrescents,” *Nano Letters*, vol. 7, no. 5, pp. 1113–1118, 2007.
- [21] W. Li, W. Zhao, and P. Sun, “Fabrication of highly ordered metallic arrays and silicon pillars with controllable size using nanosphere lithography,” *Physica E: Low-dimensional Systems and Nanostructures*, vol. 41, no. 8, pp. 1600 – 1603, 2009.
- [22] S. Sun, P. Mendes, K. Critchley, S. Diegoli, M. Hanwell, S. D. Evans, G. J. Leggett, J. A. Preece, and T. H. Richardson, “Fabrication of gold micro- and nanostructures by photolithographic exposure of thiol-stabilized gold nanoparticles,” *Nano Letters*, vol. 6, no. 3, pp. 345–350, 2006.
- [23] S. Gilles, C. Kaulen, M. Pabst, U. Simon, A. Offenhusser, and D. Mayer, “Patterned self-assembly of gold nanoparticles on chemical templates fabricated by soft UV nanoimprint lithography,” *Nanotechnology*, vol. 22, no. 29, p. 295301, 2011.
- [24] S. J. Tan, M. J. Campolongo, D. Luo, and W. Cheng, “Building plasmonic nanostructures with DNA,” *Nature Nanotechnology*, vol. 6, pp. 268–276, 2011.
- [25] A. Rezaee, A. K. A. Aliganga, and S. Mittler, “Control of density of randomly grown OMCVD gold nanoparticles by means of ion irradiation,” *The Journal of Physical Chemistry C*, vol. 113, no. 36, pp. 15 824–15 833, 2009.
- [26] A. Rezaee, A. K. A. Aliganga, L. C. Pavelka, and S. Mittler, “Control of the average spacing between aligned gold nanoparticles by varying the fib dose,” *Phys. Chem. Chem. Phys.*, vol. 12, pp. 4104–4111, 2010.
- [27] A. Rezaee, L. Pavelka, and S. Mittler, “Binary mixtures of SH- and CH₃- terminated self-assembled monolayers to control the average spacing between aligned gold nanoparticles,” *Nanoscale Research Letters*, vol. 4, no. 11, pp. 1319–1323, 2009.
- [28] A. B. Dahlin, J. O. Tegenfeldt, and F. Hook, “Improving the instrumental resolution of sensors based on localized surface plasmon resonance,” *Analytical Chemistry*, vol. 78, no. 13, pp. 4416–4423, 2006.

- [29] S. Mittler-Neher, J. Spinke, M. Liley, G. Nelles, M. Weisser, R. Back, G. Wenz, and W. Knoll, "Spectroscopic and surface-analytical characterization of self-assembled layers on au," *Biosensors and Bioelectronics*, vol. 10, no. 9-10, pp. 903 – 916, 1995.
- [30] S. Busse, J. Kashammer, S. Kramer, and S. Mittler, "Gold and thiol surface functionalized integrated optical Mach-Zehnder interferometer for sensing purposes," *Sensors and Actuators B: Chemical*, vol. 60, no. 2-3, pp. 148 – 154, 1999.
- [31] J. Spinke, M. Liley, F.-J. Schmitt, H.-J. Guder, L. Angermaier, and W. Knoll, "Molecular recognition at self-assembled monolayers: Optimization of surface functionalization," vol. 99, no. 9, pp. 7012–7019, 1993.
- [32] M. Wilchek and E. A. Bayer, "The avidin-biotin complex in bioanalytical applications," *Analytical Biochemistry*, vol. 171, no. 1, pp. 1 – 32, 1988.
- [33] S. Busse, V. Scheumann, B. Menges, and S. Mittler, "Sensitivity studies for specific binding reactions using the biotin/streptavidin system by evanescent optical methods," *Biosensors and Bioelectronics*, vol. 17, no. 8, pp. 704 – 710, 2002.
- [34] D. Oshannessy, M. Brighamburke, K. Sonesson, P. Hensley, and I. Brooks, "Determination of rate and equilibrium binding constants for macromolecular interactions using surface plasmon resonance: Use of nonlinear least squares analysis methods," *Analytical Biochemistry*, vol. 212, no. 2, pp. 457 – 468, 1993.
- [35] U. Piran and W. J. Riordan, "Dissociation rate constant of the biotin-streptavidin complex," *Journal of Immunological Methods*, vol. 133, no. 1, pp. 141 – 143, 1990.

Chapter 3

3-D FDTD Analysis of Gold-Nanoparticle-based Photonic Crystal on Slab Waveguide¹

3.1 Introduction

Metallic nanoparticles, particularly gold nanoparticles, have received a lot of attention due to their Localized Surface Plasmon Resonance (LSPR) properties. For a single gold nanoparticle, LSPR depends on the particle size, shape, and surrounding dielectric environment. For an ensemble of gold nanoparticles, LSPR is additionally influenced by the interactions of individual nanoparticles [1]. By patterning the gold nanoparticles into a periodic array, interesting effects arise due to the interaction of the gold nanoparticles with the Photonic Crystal (PC) lattice. Such an interaction can result in unique optical properties useful for manipulating light at the nanoscale regime or strong local field enhancements. Lamprecht et al. [1] first experimentally demonstrated the significant variations in plasmon resonance of this periodic structure with a lattice constant due to in-phase superposition of scattered light. Linden et al. [2, 3] experimentally presented the selective suppression of the extinction of periodic array of gold nanoparticles using an Indium Tin Oxide (ITO) layer as a waveguide. In their work, the light is illuminated from free space and the energy coupled to waveguide modes is counted as part of the extinction.

1. A version of this chapter has been published. H. Jiang, J. Sabarinathan, T. Manifar and S. Mittler, published in *Journal of Lightwave Technology*, 27 (13), pp. 2264-2270, 2009. Reprinted (adapted) with permission from (H. Jiang, J. Sabarinathan, T. Manifar and S. Mittler, '3-D FDTD Analysis of Gold-Nanoparticle-based Photonic Crystal on Slab Waveguide', *Journal of Lightwave Technology*, 27 (13), pp. 2264-2270, 2009). ©2009 IEEE. (see Appendix A for copyright permission)

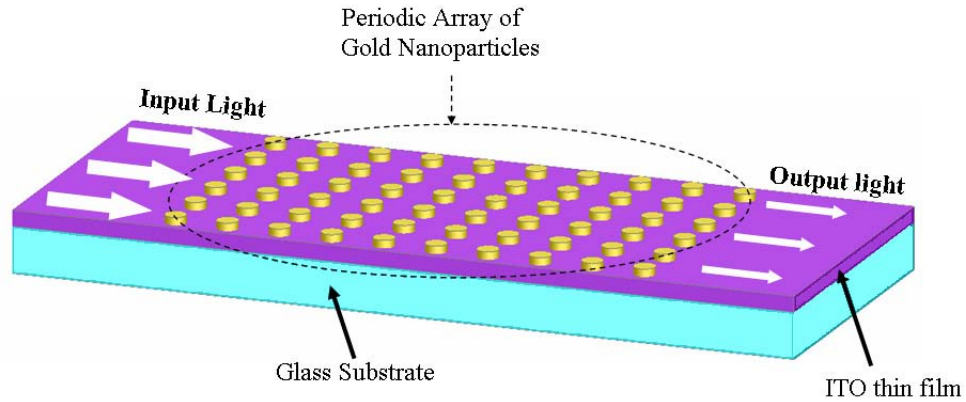


Figure 3.1: Schematic of periodic array of gold nanoparticles on top of slab waveguide.

Most existing work [1–4] is focused on illuminating light from the top of the gold nanoparticles and measuring the transmission of light through the structures. However, the *waveguide-excited* LSPR of the periodic gold nanoparticles in which the gold nanoparticles are coupled to the evanescent field of a slab waveguide has not been well studied. In our investigation, light propagating along a slab waveguide (ITO slab on glass substrate) excites the gold nanoparticles which are patterned into a 2-D periodic array (Figure 3.1). This configuration is important for studying the potential for integrated planar sensors based on the interactions between gold nanoparticles and slab waveguides.

In this paper, the 3-D FDTD simulation method with a non-uniform mesh will be presented and validated first. Based on simulations, the effects of the lattice constants on the absorption of the gold nanoparticles, the effects of the slab thickness on the extinction of the waveguide mode, and the effects of the local dielectric environment will be discussed subsequently.

3.2 3-D FDTD simulation with non-uniform mesh

FDTD simulation techniques were used as they have the advantage in being able to simulate any arbitrary geometry of nanostructures. In our study, full 3-D simulations are used instead of 2-D simulations because the gold nanoparticles in our investigation are coupled to the *evanescent* field of a slab waveguide mode. 2-D simulations cannot really describe the periodic array of gold nanoparticles on top of a slab waveguide and

thus cannot simulate the coupling between the gold nanoparticles and the evanescent field of the slab's waveguide mode. In addition, the scattering of light out of the slab waveguide due to the gold nanoparticles cannot be captured by 2-D simulations. We have compared both 2-D and 3-D simulation results to experimental results as discussed later in this section, and we found that 2-D simulation results did not match the experimental data. For these reasons, full 3-D FDTD simulations must be used, although they are more computationally intensive.

A drawback of the FDTD technique is the requirement of an ultra-fine mesh for simulating plasmonic structures such as gold nanostructures to achieve convergent results. Using the conventional uniform mesh in 3-D generates a large number of cells for these types of structures. However, by using a non-uniform mesh, the number of cells required is significantly reduced while still maintaining the same accuracy. Liu et al. has presented a triangular-mesh-based FDTD technique for simulating periodic plasmonic structures which improved the efficiency and accuracy of their 2-D simulations [5]. In our study, we implemented full 3-D FDTD simulation techniques based on rectangular non-uniform mesh. Based on this technique, the grid size used to mesh gold nanoparticles was set at 4 nm while the grid size used to mesh other regions (away from the PC) was set at around 15 nm. In this way, the accuracy and convergence of the simulations are both guaranteed while the requirements on computational resources are reasonable enough to run. Typically, a 3-D simulation with the non-uniform mesh requires 2.8 GB memory while a 3-D simulation with the conventional uniform mesh requires more than 6.0 GB for the same accuracy. It should be noted that if we further refine the mesh, the memory required for the non-uniform mesh goes up slightly while it drastically increases for the uniform mesh.

The dispersion of gold in the spectrum range from 400 nm to 750 nm can be well described by a Drude-Lorentz model [6, 7]. The complex relative permittivity of gold as a function of angular frequency is given by

$$\epsilon_r(\omega) = \epsilon_\infty - \frac{\omega_p^2}{\omega^2 + iT_D\omega} + \frac{\epsilon_L\omega_0^2}{\omega_0^2 - iT_L\omega - \omega^2} \quad (3.1)$$

where ω_p is the plasma frequency for Drude term, ω_0 is the pole resonance for Lorentz term, ϵ_L is weighting coefficient for Lorentz term, T_D and T_L are damping coefficients. These parameters used in our simulations are determined based on the experimental data of Johnson and Christy [8], with $\epsilon_\infty=7.0765$, $\epsilon_L=2.3231$, $\omega_p=9.1522$ eV,

$\omega_0=3.0501$ eV, $T_D=9.2848\times 10^{-9}$ eV and $T_L=1.2197$ eV.

In order to validate our simulation techniques, we simulated the periodic gold nanoparticles under normal incidence of linearly polarized light which has already been experimentally studied by other groups [1–4]. We compared our simulated results as shown in Figure 3.2 with experimental results obtained by Linden et al. [2]. There is an excellent agreement of the data to each other taking fabrication uncertainty into account. Due to the elliptical shape of the gold nanoparticles, two different extinction peaks associated with the two polarizations [2] are clearly obtained in our simulation. Since the nanoparticles are longer in the X axis (120nm) than in the Y axis (100nm), the LSPR peak excited by the X polarization has a smaller photon energy than that by the Y polarization [2]. In addition, we have also implemented the same mesh configuration for a similar configuration of gold nanostructures on top of a glass waveguide. The simulation results matched the experimental measurements closely.

With our simulations now doubly validated by two separate experimental techniques, the simulation configuration investigated in this paper is shown in Figure 3.3. The slab waveguide consists of an ITO ($n = 1.90$) thin film on top of a glass substrate ($n = 1.51$). Other types of slab waveguides, such as polymer waveguides or glass waveguides, can also be simulated using this configuration. a_x and a_y are the lattice constants along X and Y direction respectively and t is the thickness of the ITO slab. The waveguide was designed to hold only the TE_0 mode and the TM_0 mode propagating in the X direction in the spectral range from 400 nm to 750 nm. Periodic boundaries are used in the Y direction (perpendicular to the source injection direction) to simulate a unit cell. Since the X direction is the same direction as the source injection, periodic boundaries can not be applied to this direction. Instead, absorbing boundaries in this direction with a finite number of columns of gold nanoparticles are used. According to our convergence study, 6 columns are enough to simulate the properties of a periodic array which is infinitely extended in the X direction. Therefore, in the works presented in this paper, only 6 columns of gold nanoparticles in the X direction are simulated.

The absorption spectrum of the gold nanoparticles is calculated by measuring the net power flowing into an enclosed surface surrounding the gold nanoparticles.

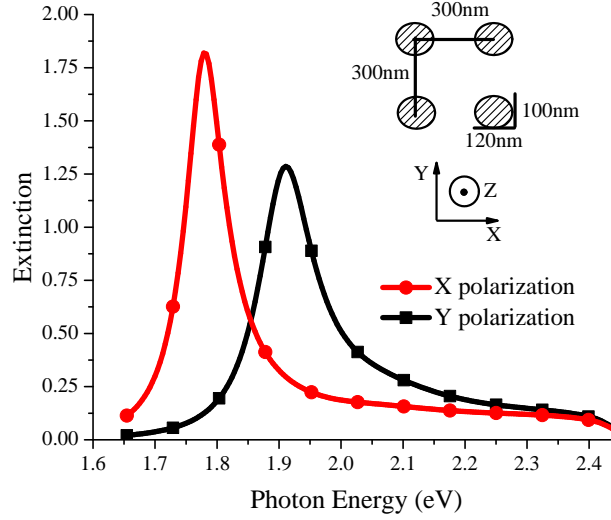


Figure 3.2: Simulation of the extinction spectra of periodic gold nanoparticles on 140 nm thick ITO film coated glass substrate under normal incidence (from Z direction) of linearly polarized light. The nanoparticles are in elliptical shape with diameters equal to 120 nm and 100 nm along X and Y axis respectively and arranged into square array with lattice constant equal to 300 nm, as shown in the inset. Spectra for polarization along X and Y directions were both given.

The extinction spectrum is calculated as

$$Extinction(\lambda) = -\ln\left(\frac{P_{out}(\lambda)}{P_{in}(\lambda)}\right) \quad (3.2)$$

where $P_{in}(\lambda)$ is the input transmission spectrum measured in front of the first column of gold particles and $P_{out}(\lambda)$ is the output transmission spectrum measured at the output end. Light scattered away from the waveguide region due to the presence of the gold nanoparticles does not transmit through the output end of the waveguide, so the scattering loss of light by the gold nanoparticles is included in the extinction spectrum calculation. The spectral resolution is better than 1 nm in all spectral plots shown in this paper.

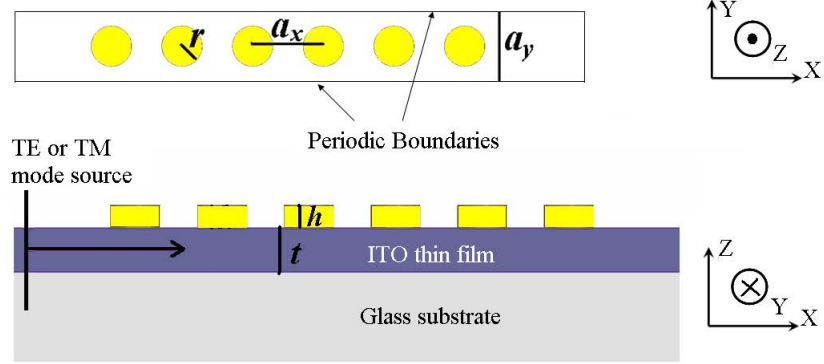
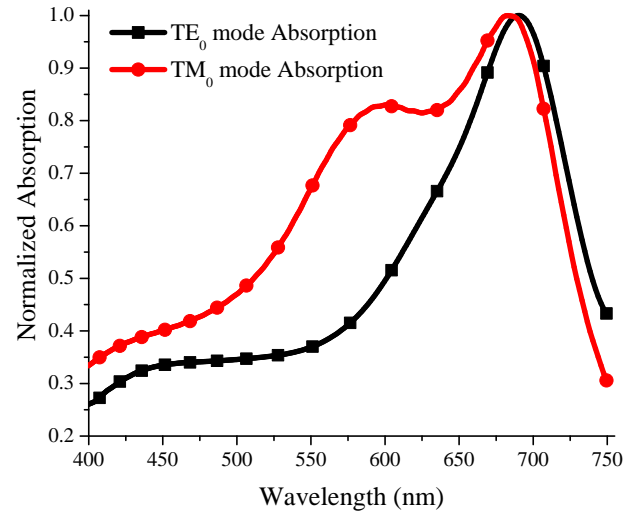


Figure 3.3: FDTD simulation setup. The top figure is top view and the bottom figure is side view.

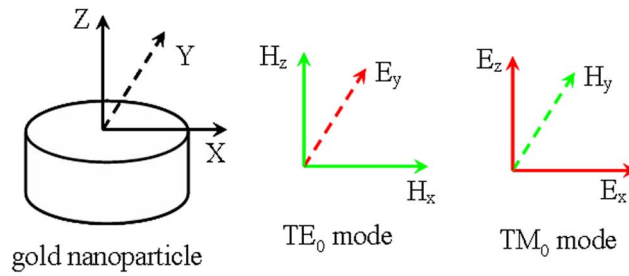
3.3 Localized surface plasmon resonance of single gold nanoparticle

Since we are interested in the interactions of a periodic array of gold nanoparticles, the size and shape of particles are kept constant (the radius $r=100\text{nm}$ and the height $h=100\text{nm}$). This size is somewhat large for a gold nanoparticle, however, it helps to increase the accuracy of simulation and the dielectric function of gold need not to be modified according to electron scattering as is necessary for nanostructures smaller than the electron free path. In addition, gold nanoparticles in this size can be easily fabricated by electron beam lithography techniques for comparison. The plasmon absorption of a single gold nanoparticle is simulated by applying absorbing boundaries in all directions. The absorption spectrum normalized with respect to the maximum absorption value for the TE_0 mode and TM_0 mode are shown in Figure 3.4(a). For the TE_0 mode (main field components are E_y, H_x, H_z), there is only one absorption peak at 690 nm because the electric field of the TE_0 mode is polarized only in the Y direction and thus excites only one LSPR mode in the gold nanoparticle, as indicated in Figure 3.4(b). However, for the TM_0 mode (main field components are E_x, E_z, H_y), two peaks exist because TM_0 polarization excites particle plasmon resonances in both the X and Z directions, as indicated in Figure 3.4(b). There is a peak around 690 nm for both TE_0 and TM_0 mode because the circular shape of gold nanoparticle supports degenerate modes.

In the following sections, the LSPR of the periodic array of gold nanoparticles excited by the evanescent field of waveguide mode will be presented. Our study is



(a)



(b)

Figure 3.4: (a) Normalized absorption spectra of a single gold nanoparticle on top of an ITO slab waveguide for TE₀ mode and TM₀ mode. (b) Schematic of the polarization of TE₀ mode and TM₀ mode with respect to the axes of a single gold nanoparticle.

aimed at tuning the LSPR peak for sensor applications, where the LSPR peak shifts with changing dielectric environment. For this purpose, TE₀ mode is better than TM₀ mode because TE₀ mode excites only one LSPR peak so that the shift of this LSPR peak can be clearly determined without being possibly mixed together with other LSPR peaks. TM₀ mode, which excites two different LSPR peaks, would increase the complexity in understanding the trends of the shift of the two LSPR peaks. Therefore, in the following discussions, we focused on the TE₀ mode excitation.

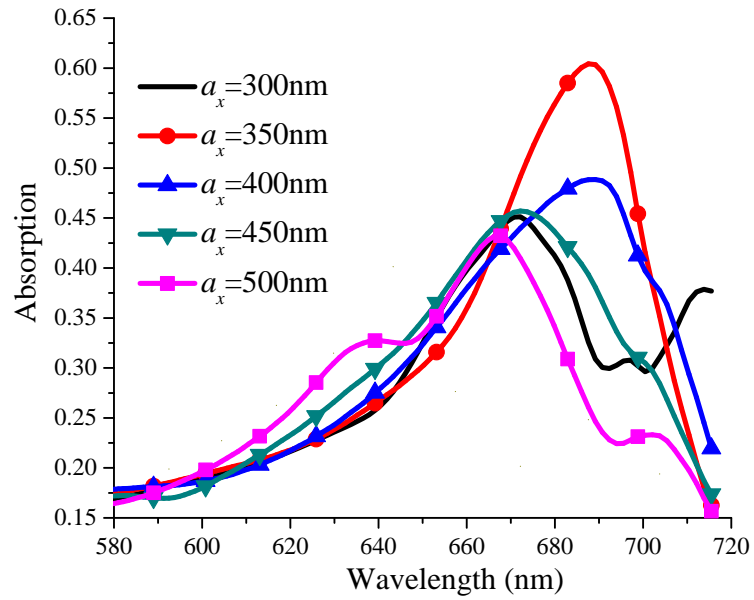
3.4 Effects of lattice constants

In order to investigate the periodic effects on the LSPR of the gold nanoparticles, the absorption spectra were simulated for different lattice constants. For comparison, the reference structure is chosen to be $a_x = a_y = 450$ nm, $t = 200$ nm. We first studied the effects of changing the lattice constant in the X direction, by increasing a_x from 300nm to 500nm with 50nm steps and leaving a_y constant (termed as Set A). The absorption spectra shown in Figure 3.5(a) are very different compared to that of a single nanoparticle. The absorption peak of the periodic array of nanoparticles shifts in the range from 667nm to 689nm due to the quadrupolar interactions of periodic gold nanoparticles.

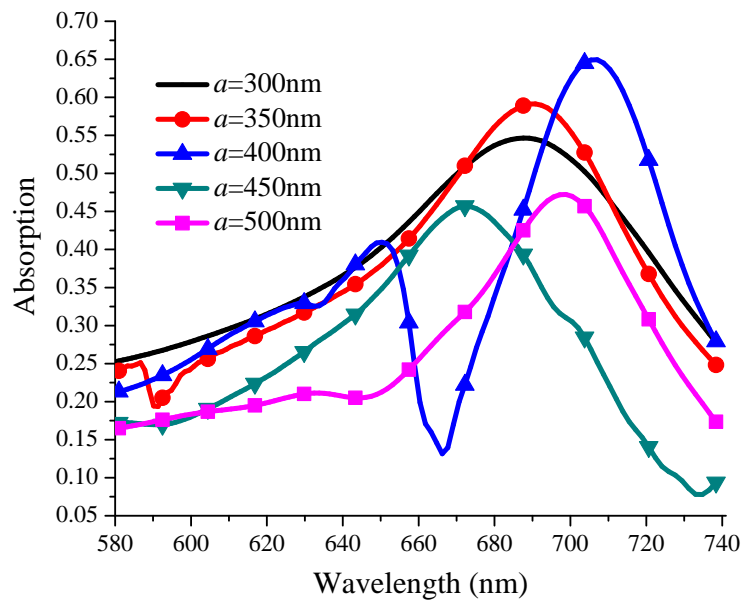
We also carried out simulations of varying lattice constants in both the X and Y directions with the relationship $a_x = a_y = a$, changing from 300 nm to 500 nm with 50 nm steps (termed as Set B). The absorption spectra obtained are shown in Figure 3.5(b). The absorption peak changes over a wider range (672 nm \sim 707 nm) than in the previous case potentially because the spacing among nanoparticles is more affected by changing overall periodicities together. Selective enhancement or suppression of the LSPR of the gold nanoparticles are observed by comparing the spectrum for $a = 400$ nm and $a = 450$ nm. The peak around 670nm for $a = 400$ nm corresponds to the valley for $a = 450$ nm.

In order to understand the complex trends in the shift of absorption peaks vs. the lattice constants, another type of sample was also simulated with configuration of $a_y=350$ nm and increasing a_x from 300 nm to 500 nm with 50 nm steps (termed as Set C). The absorption peak wavelength of Set A and Set C are plotted together in Figure 3.6 for comparison. The data shown has better sampling resolution of lattice constant for the range of $350 \text{ nm} < a_x < 450 \text{ nm}$ to allow us to study this region more closely. The shift of the plasmon resonance in periodic array is due to the in-phase additions of the periodic gold nanoparticles through the emerging radiating grating order at the grazing angles (in the plane of the periodic gold nanoparticles) with critical grating constant a_c [1, 4]. With increasing a_x , in the range $a_x < a_c$, the resonance peak redshifts; in the range $a_x > a_c$, the resonance peak blueshifts [1, 4].

In our case, light is propagating in the waveguide mode so we can assume that the light is incident at the grazing angle from a dielectric medium with the index approximately equal to the effective index of the waveguide mode, n_{eff} . For



(a)



(b)

Figure 3.5: Absorption spectra of (a) changing a_x , in Set A and (b) changing a , where $a = a_x = a_y$, in Set B.

a grating order at the grazing angle, it can either be propagating in the forward or backward direction. For the grating order propagating forward, no critical grating constant condition could be applied. However, for the m th grating order propagating backward at the grazing angle, the critical grating constant can be given by

$$a_c = m\lambda/(n_{eff} + n') \quad (3.3)$$

where λ is the wavelength, n' can be equal to n_{eff} or the index of air, depending on the radiating grating order is carried by waveguide or by air. The condition of critical grating constant $a_c = \lambda/n_{eff}$ ($m = 2$, $n' = n_{eff} \approx 1.672$) is plotted as a dashed line in Figure 3.6. The trends of the absorption peaks match the theoretical prediction very well in both Set A and C. The absorption peak first redshifts with increasing a_x until it reaches a_c . When a_x is larger than a_c , the absorption peak starts to blueshift. There is also a slight redshift for even larger a_x , which could be due to the emergence of the second grating order radiating in air ($m = 2$, $n' = 1$). This indicates that the modification of LSPR vs. changing a_x in our case is mainly through the second grating order propagating backward at the grazing angle carried by the waveguide. Since the waveguide mode is a well confined mode, the interaction is enhanced compared to the grating order radiating in the air.

3.5 Effect of slab thickness

In order to investigate the coupling between the evanescent field of the waveguide mode and the periodic gold nanoparticles, we further investigated the extinction of the waveguide mode which is composed of both the absorption of gold nanoparticles and the scattering loss in free space. In this section, $a_x = a_y = 450$ nm are kept constant but the slab thickness t is changed from 100 nm to 375 nm with 25 nm steps (termed as Set D), and the extinction spectra are simulated for varying thickness t . As shown in Figure 3.7(a), the extinction peak redshifts with increasing t and appears in a wide spectral range from 650 nm to 705 nm. This indicates that changing slab thickness can be potentially another effective method in tuning the interactions of the gold nanoparticles or has to be taken into consideration in the design.

The dependence of the extinction peak on the slab thickness can be understood from the waveguide dispersion and the in-phase addition of gold nanoparticles. For

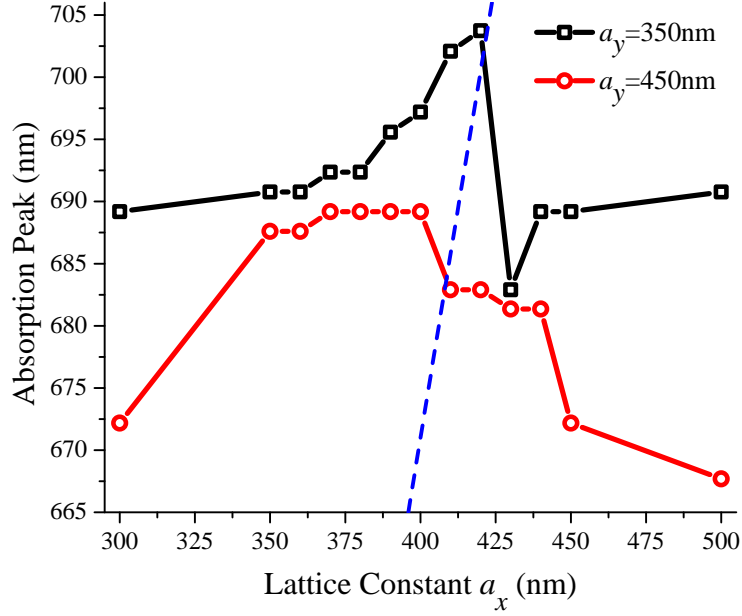


Figure 3.6: Absorption peak wavelength vs. a_x , with $a_y = 350$ nm (Set C, black line with open squares) and $a_y = 450$ nm (Set A, red line with open circles) respectively. The dashed line represents the condition of critical grating constant: $a_c = \lambda/n_{eff}$.

a given slab thickness t , the waveguide dispersion relation is noted as $\lambda_t(k)$, where k is the wavevector of the waveguide mode. The LSPR of the array appears when the LSPR of the individual particles excited by the waveguide mode are added in-phase to each other. At a given slab thickness $t = t_0$, the wavevector corresponding to the in-phase addition is given by k_0 , which is calculated from the LSPR peak wavelength and the waveguide dispersion relation $\lambda_{t_0}(k)$.

When t is changed, the waveguide dispersion is changed, however, the lattice constants of the gold nanoparticles remain the same. Therefore, the wavevector for in-phase addition can be approximated as k_0 . The LSPR peak λ_{LSPR} for the array with slab thickness t can thus be given by

$$\lambda_{LSPR} = \lambda_t(k_0) \quad (3.4)$$

The peaks predicted by Equation 3.4 show the resonance peak redshifts from 622 nm to 715 nm when t is increasing from 100 nm to 375 nm, which matched the trend of the simulated peaks shown in Figure 3.7(b) qualitatively. This match provides strong evidence that the interactions of the periodic array of gold nanoparticles are

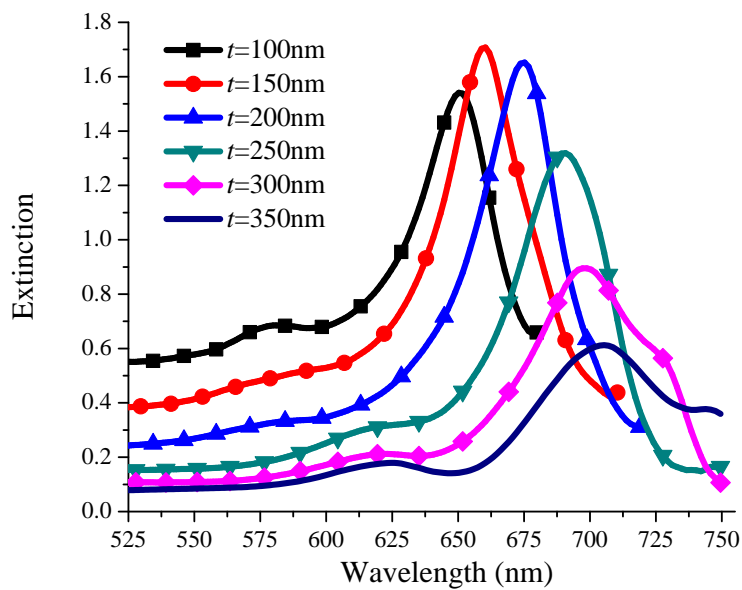
strongly affected by the dispersion of the waveguide. However, there is fairly good quantitative match only in the slab thickness range from 175 nm to 325 nm, because the wave-vector is well approximated as the in-phase addition condition only in the range around $t=t_0$. In other ranges, the condition needs to be modified to include the LSPR of a single gold nanoparticle.

The amplitude of extinction also depends on the coupling of gold nanoparticle array to the evanescent field of the waveguide mode. As the slab thickness increases, the penetration depth of the evanescent field decreases and the proportion of power carried by the evanescent field with respect to the total power also decreases. Therefore, the coupling of the gold nanoparticle array to the waveguide decreases resulting in a reduction in the amplitude of extinction.

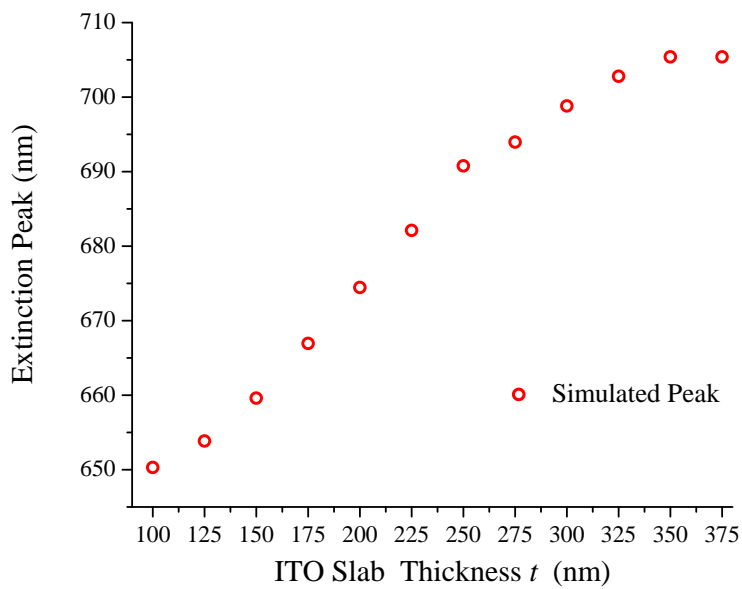
3.6 Effect of the local dielectric environment

An important application of the plasmon resonance is the detection of bio/chemical materials with high sensitivity. However, most of the existing devices involve prism based structures which prohibits their applications as on-chip devices. Although previous published works [9–13] have demonstrated integrated sensors based on metallic thin films on top of waveguides and have presented sensor devices based on LSPR of metallic nanostructures [14, 15], integrated sensor devices based on gold nanoparticles on top of optical waveguide have not been well investigated.

In the design of a bio-affinity sensor to detect protein or DNA hybridization [15], the extinction peaks should be sensitive to the change of the dielectric environment very close to the surface of gold nanoparticles. In order to study the potential of using periodic array of gold nanoparticles on top of a slab waveguide as an integrated sensor, we simulated the effects of the coating thickness of a dielectric material ($n = 1.5$) surrounding gold nanoparticles of the reference structure dipped into water ($n = 1.33$). The coating thickness is changed from 5 nm to 40 nm. As shown in Figure 3.8, the extinction peak redshifts with increasing the coating thickness. The spectral shift of the extinction peak is more sensitive for thinner coating films due to the stronger field near the surfaces of gold nanoparticles. According to the simulation, a wavelength shift of 13 nm in the extinction peak can be obtained when the gold nanoparticles are surrounded by 40 nm thick layer. Since the interaction of gold



(a)



(b)

Figure 3.7: Extinction of varying slab thickness t . (a) extinction spectra of different t . (b) extinction peak vs. t .

nanoparticles can be tuned by lattice constants and slab thickness, the sensitivity of this device can potentially be increased.

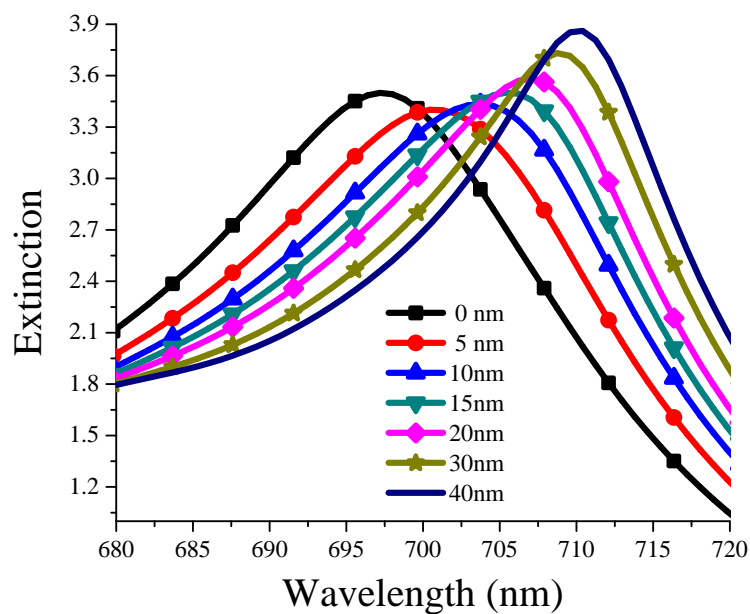
3.7 Conclusions

Based on our 3-D FDTD simulation studies, the plasmon absorption peak of the gold nanoparticle excited by the evanescent field of TE_0 slab waveguide mode was shown to be tunable by changing lattice constants due to the second grating order propagating backward at the grazing angle. The particle-induced extinction peak of the TE_0 waveguide mode redshifts with increasing slab thickness which is determined by the waveguide dispersion. These gold nanoparticles were shown to be sensitive to the local dielectric environment surrounding the gold nanoparticles and can be potentially used towards integrated sensor devices.

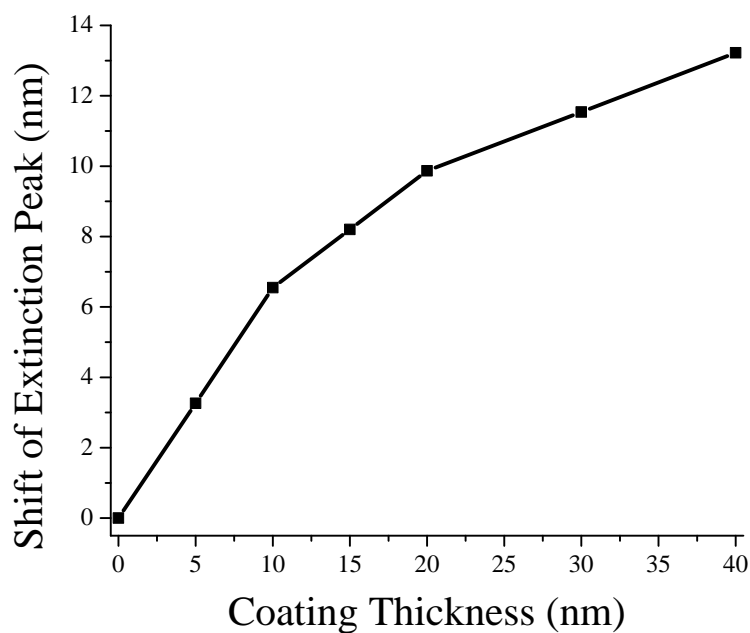
Although we have focused our discussions in this paper on TE_0 mode excitation, it should be pointed out that for TM_0 excitation we observed similar trends of the shift of the two LSPR peaks associated with X and Z polarizations of the electric field of TM_0 mode. There are additional distinct features for the TM_0 mode which show additional absorption peaks with longer wavelengths than the LSPR peaks. We attribute these additional peaks to grating-induced modes which have already been experimentally studied by Felidj et al. [4], in which work the gold nanoparticle array was excited by plane waves. The properties of these grating-induced modes excited by the evanescent field of the TM_0 mode are not fully understood yet and are currently being studied in our group.

3.8 Acknowledgements

We would like to acknowledge the funding of TEN program from Canadian Institute for Photonic Innovations (CIPI). We acknowledge the technical support on the 3-D FDTD from Lumerical Inc. The simulations were performed using the parallel computing resources of WESTGRID and SHARCNET.



(a)



(b)

Figure 3.8: Effects of local dielectric environment at the surface of gold nanoparticles. (a) extinction spectra of different coating thickness. (b) spectral shift of extinction peak vs. coating thickness.

References

- [1] B. Lamprecht, G. Schider, R. T. Lechner, H. Ditlbacher, J. R. Krenn, A. Leitner, and F. R. Aussenegg, “Metal nanoparticle gratings: influence of dipolar particle interaction on the plasmon resonance,” *Phys. Rev. Lett.*, vol. 84, no. 20, pp. 4721–4724, 2000.
- [2] S. Linden, A. Christ, J. Kuhl, and H. Giessen, “Selective suppression of extinction within the plasmon resonance of gold nanoparticles,” *Appl. Phys. B*, vol. 73, pp. 311–316, 2001.
- [3] S. Linden, J. Kuhl, and H. Giessen, “Controlling the interaction between light and gold nanoparticles: selective suppression of extinction,” *Phys. Rev. Lett.*, vol. 86, no. 20, pp. 4688–4691, 2001.
- [4] N. Felidj, G. Laurent, J. Aubard, G. Levi, A. Hohenau, J. R. Krenn, and F. R. Aussenegg, “Grating-induced plasmon mode in gold nanoparticle arrays,” *J. Chem. Phys.*, vol. 123, p. 221103, 2005.
- [5] Y. Liu, C. Sarris, and G. Eleftheriades, “Triangular-mesh-based FDTD analysis of two-dimensional plasmonic structures supporting backward waves at optical frequencies,” *Journal of Lightwave Technology*, vol. 25, no. 3, pp. 938–945, 2007.
- [6] A. Vial, A.-S. Grimault, D. Macias, D. Barchiesi, and M. L. de la Chapelle, “Improved analytical fit of gold dispersion: application to the modeling of extinction spectra with a finite-difference time-domain method,” *Phys. Rev. B*, vol. 71, p. 085416, 2005.
- [7] K.-Y. Jung and F. Teixeira, “Multispecies ADI-FDTD algorithm for nanoscale three-dimensional photonic metallic structures,” *Photonics Technology Letters, IEEE*, vol. 19, no. 8, pp. 586–588, 2007.
- [8] P. B. Johnson and R. W. Christy, “Optical constants of the noble metals,” *Phys. Rev. B*, vol. 6, pp. 4370–4379, 1972.

- [9] J. Homola, J. Ctyroky, M. Skalsky, J. Hradilova, and P. Kolarova, "A surface plasmon resonance based integrated optical sensor," *Sensors and Actuators B: Chemical*, vol. 39, no. 1-3, pp. 286 – 290, 1997.
- [10] J. Dostalek, J. Ctyroky, J. Homola, E. Brynda, M. Skalsky, P. Nekvindova, J. Spirkova, J. Skvor, and J. Schrofel, "Surface plasmon resonance biosensor based on integrated optical waveguide," *Sensors and Actuators B: Chemical*, vol. 76, no. 1-3, pp. 8 – 12, 2001.
- [11] J. C. Abanulo, R. D. Harris, P. N. Bartlett, and J. S. Wilkinson, "Waveguide surface plasmon resonance sensor for electrochemically controlled surface reactions," *Appl. Opt.*, vol. 40, no. 34, pp. 6242–6245, 2001.
- [12] M. Skorobogatiy and A. V. Kabashin, "Photon crystal waveguide-based surface plasmon resonance biosensor," *Applied Physics Letters*, vol. 89, p. 143518, 2006.
- [13] P. Debackere, S. Scheerlinck, P. Bienstman, and R. Baets, "Surface plasmon interferometer in silicon-on-insulator: novel concept for an integrated biosensor: Reply," *Opt. Express*, vol. 15, no. 21, pp. 13 651–13 653, 2007.
- [14] T. Okamoto, I. Yamaguchi, and T. Kobayashi, "Local plasmon sensor with gold colloid monolayers deposited upon glass substrates," *Opt. Lett.*, vol. 25, no. 6, pp. 372–374, 2000.
- [15] D.-K. Kim, K. Kerman, M. Saito, R. R. Sathuluri, T. Endo, S. Yamamura, Y.-S. Kwon, and E. Tamiya, "Label-free DNA biosensor based on localized surface plasmon resonance coupled with interferometry," *Analytical Chemistry*, vol. 79, no. 5, pp. 1855–1864, 2007.

Chapter 4

Periodic Arrays of Gold Nanodisks

Coupled with Evanescent Spectroscopy ¹

4.1 Introduction

The extensive research interest in nanometer-dimension metallic nanoparticles has been mainly driven by their broad impact on the emerging disciplines of nanoengineering and nano-optics. Gold nanoparticles, in particular, have been the focus of numerous investigations in recent years because of the promises offered by their optical, electronic, and chemical properties [1–4]. The unique optical property is due to the localized surface plasmon resonance (LSPR) of the gold nanoparticles, which is a collective oscillation of the free electron gas confined in a nanoscale volume. The LSPR provides a remarkable enhancement in the evanescent electromagnetic field at the surface of the nanoparticles, which have found important applications in surface enhanced Raman spectroscopy [5, 6] and LSPR sensing [7–12].

By patterning the gold nanoparticles into a periodic array, additional effects arise due to the interaction of the gold nanoparticles with the photonic crystal (PC) lattice [13]. Such an interaction can result in unique optical properties useful for manipulating light at the nanoscale and leads to strong local field enhancements. Meier et al. have theoretically studied the dipolar interactions of periodic arrays of nanoparticles, and predicted the array effects on the plasmon peak and the radiative damping [14]. Lamprecht et al. [15] first experimentally demonstrated the significant variations in the plasmon resonances of these periodic structures with lattice constants due to the in-phase superposition of scattered light. Linden et al. [16, 17] experimentally presented the selective suppression of the extinction of a periodic array of

1. A version of this chapter is in preparation for publication. H. Jiang, T. Manifar, A. Bakhtazad, H. Hojjati, J. Sabarinathan and S. Mittler, 'Periodic array of gold nanodisks coupled with evanescent spectroscopy'.

gold particles on an indium tin oxide waveguide. The sharp grating-induced plasmon mode of the periodic array of metal nanoparticles has been studied theoretically and experimentally [18–21].

Waveguide evanescent spectroscopy is based on the concept of exciting the micro/nano-objects using the evanescent field of the waveguide and collecting the transmitted light [22]. Combining the gold nanoparticles with a waveguide can couple the LSPR with the evanescent field, providing interesting nano-optical phenomenon, such as enhanced cross-talk [23, 24]. The biosensing approach based on gold nanoparticles immobilized on the surface of waveguide has been studied [25, 26]. In previous work, we have theoretically studied the gold-nanoparticle-based photonic crystal on top of a slab waveguide for sensing applications [26].

In this study, light is propagating as a TE_0 or TM_0 waveguide mode in a channel waveguide. The fabricated waveguide channel is tapered to a $100\ \mu\text{m}$ width in the region overlapping with the gold nanoparticle arrays. Therefore, the waveguide beneath the gold nanoparticle arrays can be approximated as a slab waveguide. The pattern of the chosen gold nanodisks is a square lattice 2-D periodic array as depicted schematically in Figure 4.1. The LSPR is probed by the evanescent field of the waveguide mode. The unique property of this configuration is that the wave-vector of the light is in the same plane as the periodicities, which is the frequently used configuration in studying the 2-D dielectric photonic crystal structures [13]. We have chosen ion-exchanged glass waveguides as the substrate [27, 28], but this approach can be easily translated to other types of waveguides, especially to step index waveguides fabricated out of polymers or inorganic dielectrics.

4.2 Sample fabrication

The channel waveguides were fabricated using ion-exchange technique on metal-masked Schott BK7 glass (Hellma Optics). Prior to ion-exchange, titanium fiducial marks were first fabricated on top of the BK7 glass using photolithography, metal deposition and lift-off. In the later steps, the waveguide channels and the gold nanodisk arrays will both be aligned relative to the same fiducial marks. The complete process of ion-exchange is schematically described in Figure 4.2. The glass was first thoroughly cleaned using nanostrip (Cyantek Inc.) and coated with 5 nm chromium and 100 nm gold by evaporation deposition. Then the sample was coated with positive

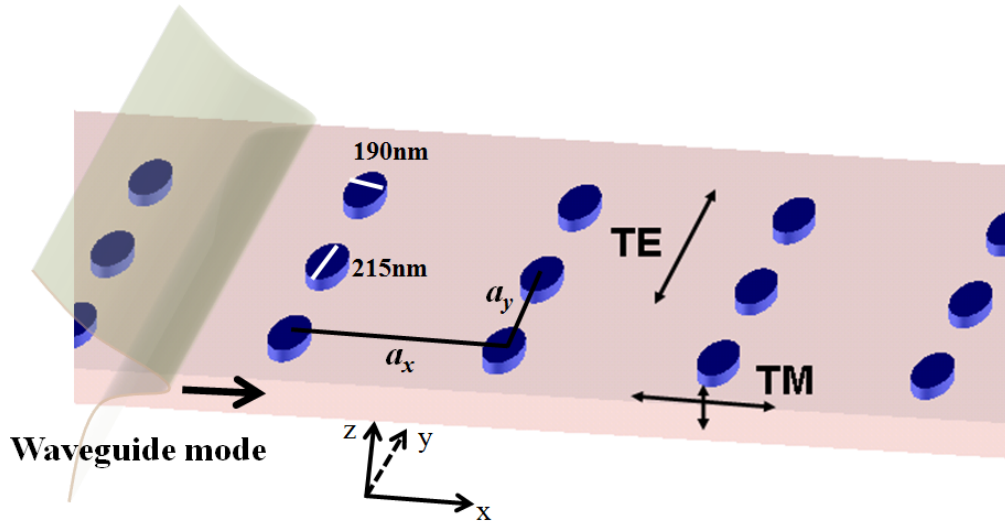


Figure 4.1: Diagram of the the structure configuration. A 2-D periodic array of elliptical gold nanodisks are patterned on top of a waveguide. The LSPR is excited by the evanescent field of the waveguide mode. The polarization directions of the TE and the TM waveguide mode are shown with respect to the nanodisk geometry. The ellipticity of the nanodisk has been exaggerated to show the difference.

photoresist (S1805, Shipley, USA) and a photolithography using 405 nm wavelength (Karl Suss MA6 mask aligner) exposed the waveguide pattern from the hard mask onto the photoresist. It should be noted that, prior to the exposure, the waveguide channels were first aligned to the aforementioned fiducial marks. After being developed, the photoresist became a pattern with waveguide openings. Wet chemical etching was used to etch gold and chromium sequentially, which transferred the pattern from the photoresist into the metal film. Gold was etched by a gold etchant (TFA, Transene Company Inc.) for 60 seconds and chromium was etched by a chromium etchant (Cr etchant 1020, Transene Company Inc.) for 30 seconds. Then the photoresist was removed by N-methyl-2-pyrrolidone solvent and the sample was thoroughly cleaned again using nanostrip (Cyantek Inc.). After this step, the sample with the patterned metal mask was ready for ion-exchange. The sample was then immersed into the molten salt consisting of a mixture of NaNO_3 and AgNO_3 (molar ratio 9:1), following the procedures described by Weisser et al. [27]. The temperature was controlled to be 360 °C, and the Ag^+ in the molten salt exchanged with the Na^+ in the top surface layer of glass for 45 min. Since Ag^+ ions have a larger polarizability than Na^+ ions, the refractive index of the glass material with exchanged ions is in-

creased. Since the ion-exchange can only take place within a few microns from the surface of the substrate, and only through the openings in the metal mask, a high refractive index region was thus formed and surrounded by low refractive index regions, yielding an optical channel waveguide. After the ion-exchange step, the metal mask was removed using the gold etchant and chromium etchant. In the following, the end-surfaces of the sample were polished using diamond lapping films (Buehler Canada).

The waveguide pattern was designed into a double-S bend configuration. The bends implemented here can remove higher order waveguide modes and substrate modes. In the region where nanoplasmonic structures were expected to be fabricated, the waveguides were tapered to 100 μm width. Therefore, this active region of the waveguide can be assumed as a slab waveguide. The refractive index profile of the slab waveguide region is plotted in Figure 4.3. It should be noted that this refractive index profile was obtained by the ion-exchange under the same condition on a blank BK7 glass substrate without a metal mask, which is a true slab waveguide. We assume the vertical index profile of this true slab waveguide to be very close to that in the wide opening region of the channel waveguides. The index profile was calculated from the effective indices of different waveguide modes, characterized by a waveguide coupling angle measurement using a 632.8 nm laser [29]. The diffusion depth of the ion-exchange was found to be around 3.2 μm .

The gold nanodisk arrays in square lattice were fabricated on top of the ion-exchanged waveguides by electron beam lithography (EBL) technique [30]. The fabrication process is schematically outlined in Figure 4.4. After the waveguide substrate was thoroughly cleaned using nanostrip (Cyantek Inc.), 300 nm thick photoresist (ZEP520A, ZEON Corporation) was first spin-coated on top. A 20 nm thick sacrificial chromium layer was sputter deposited on top of the photoresist to make the substrate conductive. Before EBL exposure, an alignment software was implemented to align the pattern relative to the fiducial marks located besides the waveguides. In this way, the pattern of the gold nanoparticles can be written on top of the waveguide with sufficient accuracy in positioning. Pattern of nanodisk arrays, precisely controlled by the EBL system, were then exposed onto the photoresist. After EBL, the chromium layer was first removed by the chromium etchant (Cr etchant 1020, Transene Company Inc) followed by developing the photoresist in amyl acetate (Sigma-Aldrich) for 180 seconds. After developing the photoresist, 2 nm chromium

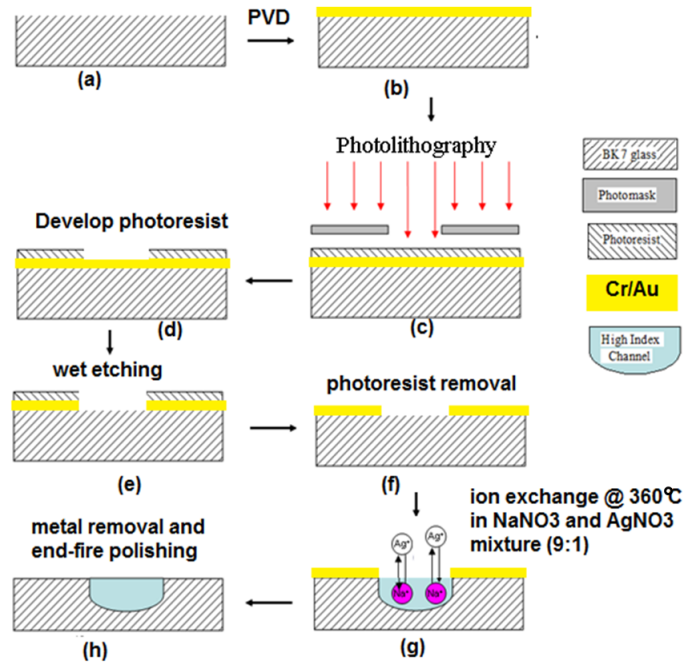


Figure 4.2: Scheme of fabrication of the waveguides in BK7 glass using ion-exchange technique.

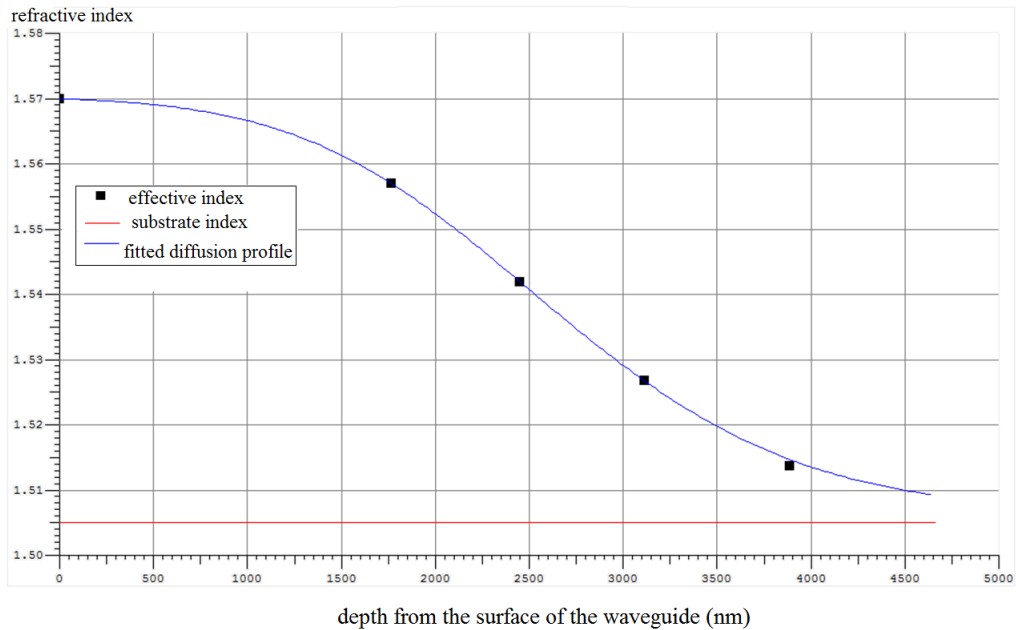


Figure 4.3: Refractive index profile of the BK7 glass ion-exchanged waveguide (45 min), characterized by waveguide coupling angle measurements. The measurement was carried out by coupling the waveguide modes using a prism. The effective indices of the modes were directly related to the coupling angles.

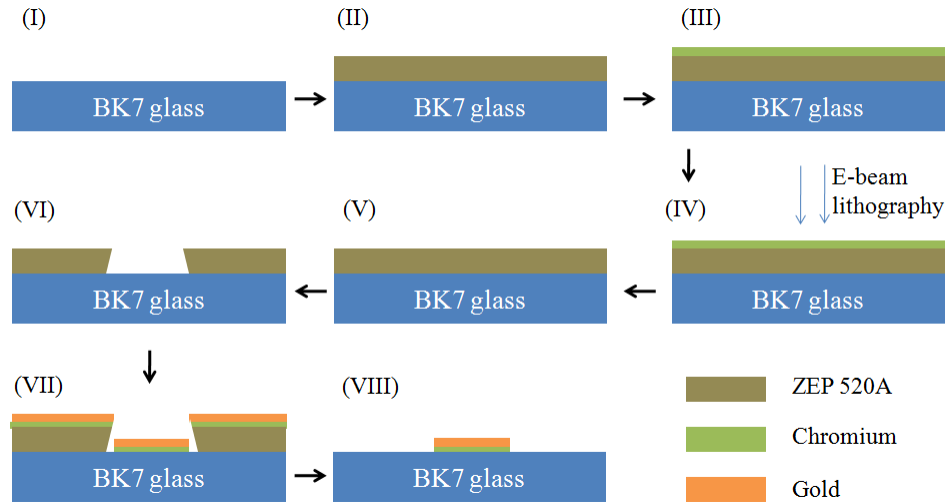


Figure 4.4: Scheme of the fabrication of the periodic array of elliptical gold nanodisks.

and 50 nm gold were sequentially deposited on the patterned photoresist by electron beam evaporation deposition. Finally a lift-off process of the sample immersed into N-methyl-2-pyrrolidone solvent removed the photoresist together with the metal on its top, leaving the periodic array of gold nanodisks on the BK7 substrate. It should be noted, that, during the evaporation deposition of the sacrificial chromium layer, the photoresist was exposed to the high-temperature vapors. The EBL exposure dose thus has to be calibrated to compensate this background exposure.

The atomic force microscope (AFM) images of fabricated nanodisk arrays are presented in Figure 4.5. The lattice constants of the fabricated arrays are 500 nm, 550 nm and 600 nm, respectively and the fabricated nanodisks are about 50 nm in height and in slightly elliptical shape with average diameters equal to 190 nm and 215 nm, respectively. A microscope image of the fabricated device is presented in Figure 4.6. The fabricated gold nanodisk array overlapped with the fabricated waveguide very well.

4.3 Waveguide transmission measurement

The extinction spectra of the fabricated devices were measured by a waveguide transmission setup [22]. The scheme of the setup is shown in Figure 4.7(a). Broad-band light (360 nm - 2000 nm) from the light source (HL-2000, Ocean Optics, USA) is first

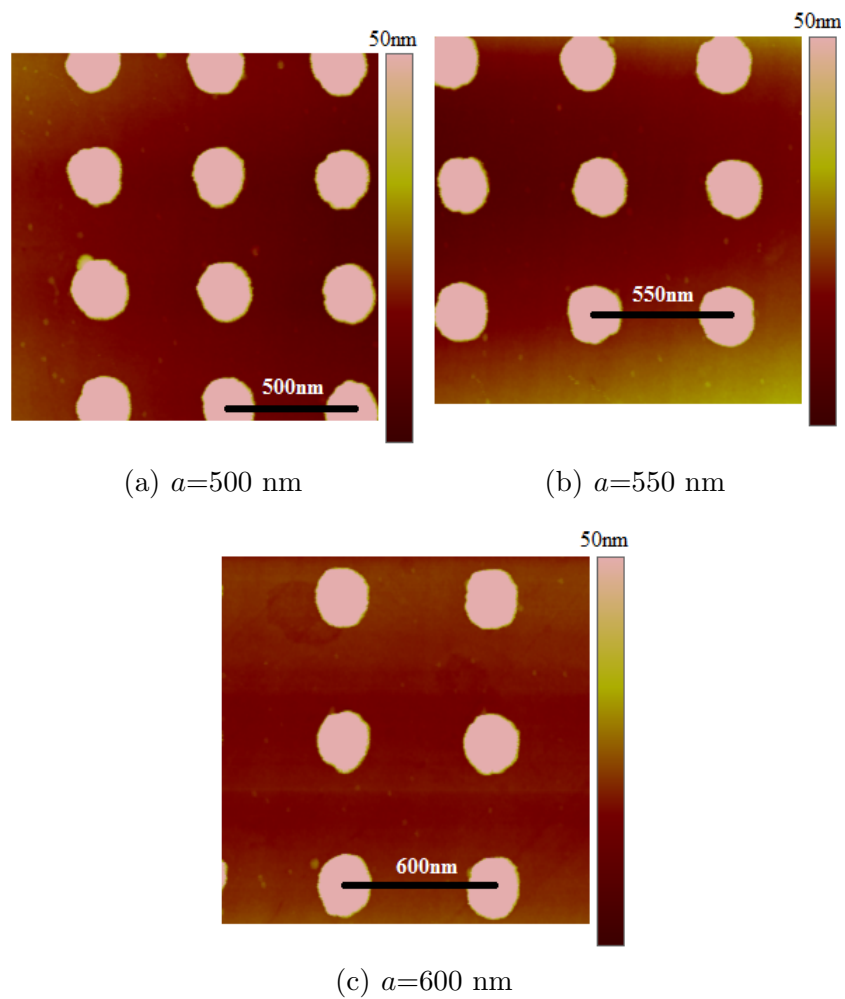


Figure 4.5: AFM images of fabricated nanodisk arrays for different lattice constants. The images are the height profile acquired using the tapping mode.

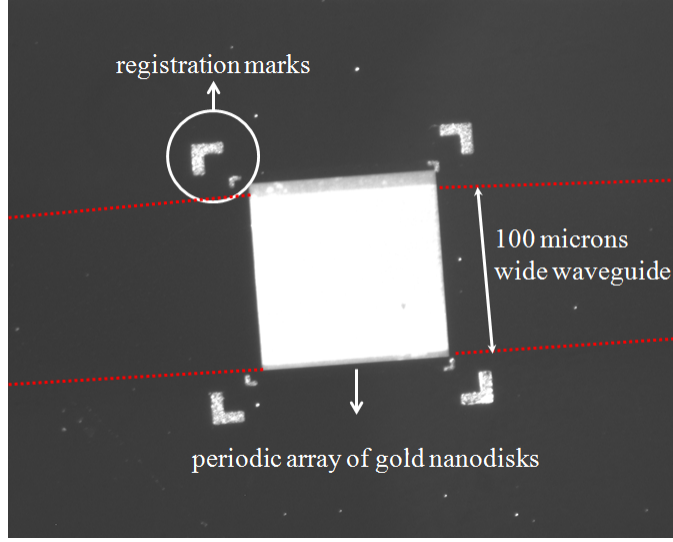


Figure 4.6: Microscope image of the fabricated gold nanoparticles array, waveguide and the registration marks. The red dotted lines serve as guide for eyes to find the boundaries of the tapered waveguide.

coupled into a fiber (Ocean Optics, USA) and collimated into a parallel beam. The beam is then focused by an objective lens into a $40 \mu\text{m}$ spot onto the entrance of the waveguide end-surface. The transmitted light is collected by another objective lens and coupled into a spectrometer (HR2000, Ocean Optics, USA) measuring an intensity spectrum. Alignment stages are used for finely adjusting the positions of the focused beam spot to optimize the coupling efficiency of light into the waveguide. A polarizer is used to selectively excite the TE or TM waveguide modes. To measure the extinction spectrum of a sensor channel, a reference intensity spectrum $I_{ref}(\lambda)$ is first measured from an empty waveguide channel and then the intensity spectrum from a waveguide channel with gold nanoparticles on top $I_{dev}(\lambda)$ is measured under the same condition. The extinction spectrum for the corresponding device is given by

$$Ext(\lambda) = -\log_{10} \frac{I_{dev}(\lambda)}{I_{ref}(\lambda)} \quad (4.1)$$

4.4 Experimental results

A simple fluidic chamber was built on top of the waveguides using a silicone isolator and a piece of microscope slide (Sigma-Aldrich). Water was introduced into the cham-

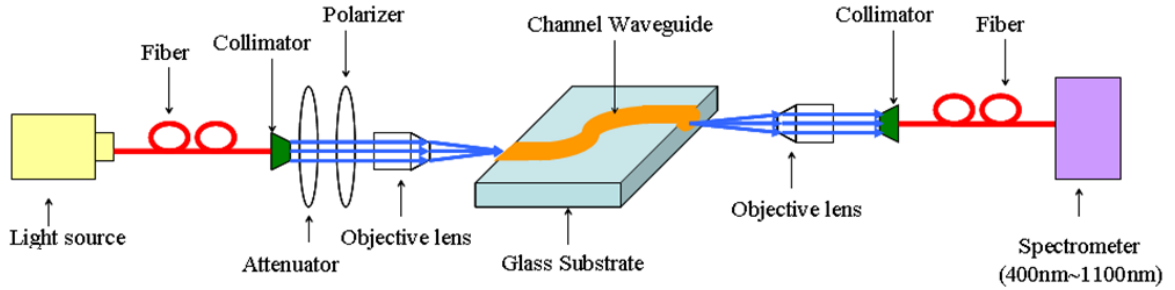
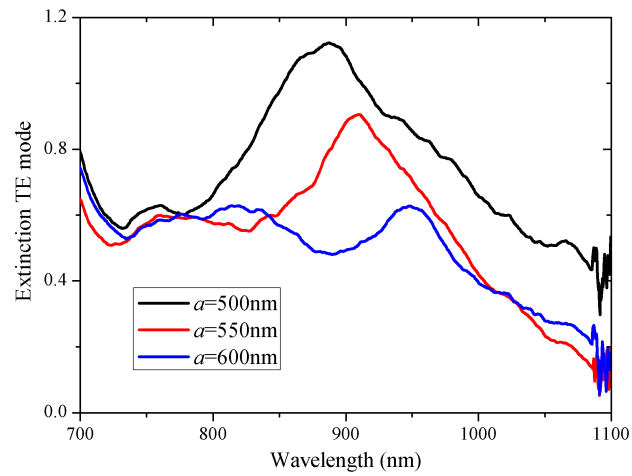


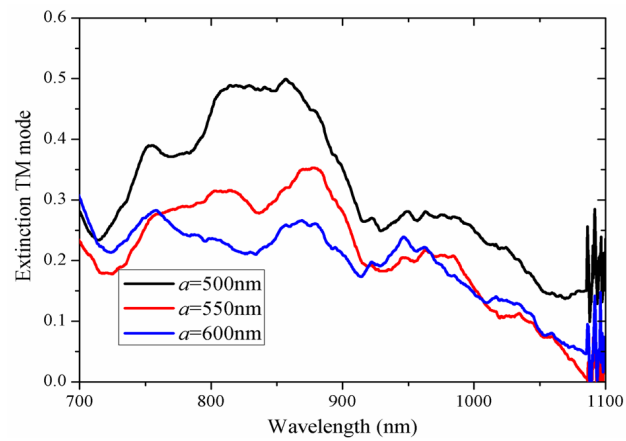
Figure 4.7: Scheme of the waveguide transmission setup.

ber so that each nanoplasmonic structure was measured under water background. The TE and TM mode correspond to different polarization directions relative to the geometry of the gold nanodisks, as shown in Figure 4.1. For the TE mode polarization, the electric field is oscillating along the longer axis of the ellipse while for the TM mode polarization, the electric field is oscillating along the shorter axis and the vertical axis of the ellipse. It should be noted, that, the double-S bends were implemented into the waveguide pattern design so that higher order waveguide modes were expected to be effectively filtered out. Therefore, the waveguide modes interacting with the gold nanodisks were predominantly fundamental TE_0 and TM_0 modes.

The measured extinction spectra for the TE and TM modes are presented in Figure 4.8(a) and Figure 4.8(b), respectively. It could be observed that, the TE and TM mode excite distinctively different LSPR peaks. A single peak appears for the TE mode and as the lattice constant increases, this peak red-shifts. For the TM mode, there exist multiple peaks, corresponding to the two polarization directions present in the TM mode indicated in Figure 4.1. Due to the silver colloids produced during the ion-exchange process, the optical loss of the waveguide is very high, leading to a very low signal-to-noise ratio. The measured extinction spectra were thus quite noisy. We attempted to change the refractive index of the dielectric environment surrounding the gold nanoparticles and measured the extinction spectra, but the peak-shifts were found to be very difficult to quantify accurately due to the noise. Sensing applications using this structure require further improvements in the quality of the waveguides.



(a) TE mode



(b) TM mode

Figure 4.8: Measured extinction spectra for the structures of different lattice constants coupled with (a) TE_0 mode and (b) TM_0 mode of the waveguide.

4.5 FDTD simulation

We carried out 3-D finite difference time domain (FDTD) simulations to further study the periodic arrays of gold nanodisks coupled with the evanescent field of an optical waveguide. The configuration of the simulation is given in Figure 4.9, which is a similar configuration used in our previous work [26]. The structures of interest are 2-D periodic arrays of gold nanodisks located on top of the waveguide with the periodic lattice in the X-Y plane. The gold nanodisks have an elliptical shape with the same geometries as the fabricated structures. Periodic boundaries are applied in the Y directions, and the length of simulation region in the Y direction is equal to a_y of the periodic array. This configuration is equivalent to simulating a periodic array infinitely extended in the Y direction. Since the waveguide mode propagates from left into right, periodic boundaries could not be applied in the X directions, due to the phase difference along the propagation path of the wave. In stead, perfectly matched layers (PMLs) are used as boundaries and 8 columns of gold nanoparticles are used in the X direction to simulate the effects of periodicity in this direction.

Initially, we attempted to simulate the waveguide configuration exactly following the refractive index profile shown in Figure 4.2(b). However, since the diffusion depth is a few microns, the simulation with such a thick layer was found to be too computationally intensive. Alternatively, we can make reasonable approximations towards the glass waveguides. The gold nanodisks are excited by the evanescent field which is basically determined by the effective refractive index of the waveguide mode n_{eff} and the cover refractive index n_c . In the simulation presented in this paper, we approximated the glass waveguide using a step-index waveguide with substrate refractive index $n_{sub} = 1.55$, the slab refractive index $n_s = 1.65$ and the slab thickness is equal to 300 nm. The cover refractive index was chosen to be $n_c = 1.33$, i.e. water, identical to the experiments. This slab waveguide configuration leads to a n_{eff} of the fundamental TE_0 mode between 1.55 and 1.56 in the wavelength range from 930 nm to 700 nm, which is very close to the n_{eff} characterized from the fundamental TE_0 mode of the fabricated slab waveguide. Using such an approximation, the waveguide layer in the simulation is sufficiently thin enough, making it possible to be computed.

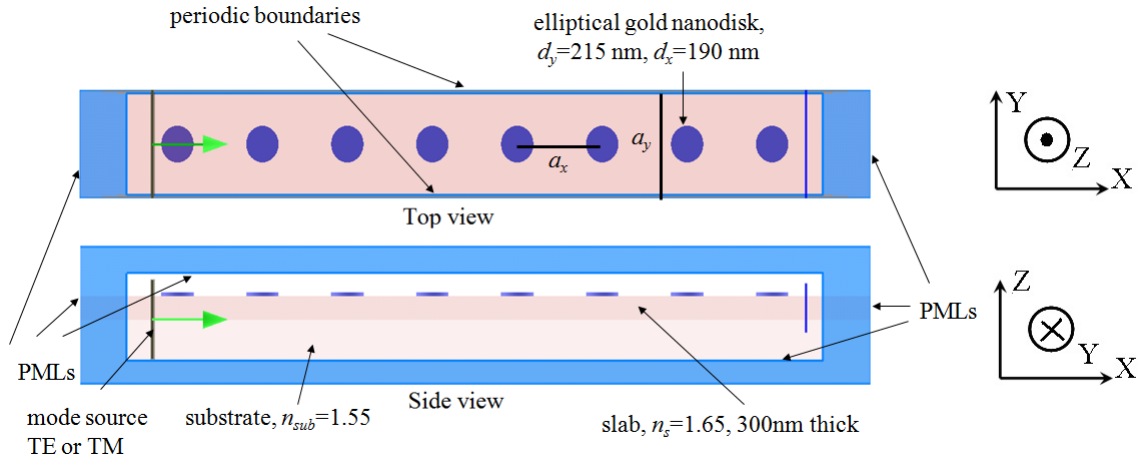


Figure 4.9: 3-D FDTD simulation configuration. Both top view and side view of the simulation configuration are presented. Periodic boundaries are applied in Y directions. PMLs boundaries applied in X and Z directions. 8 columns of gold nanodisks are created along X direction to simulate the effects of periodicity in the X direction.

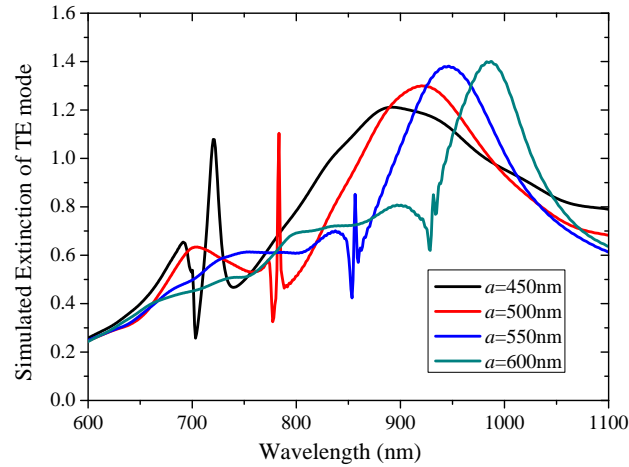
4.6 Simulation results

The TE and TM mode correspond to different polarization directions. The TE mode has only one direction of polarization. For the sake of brevity, only TE_0 mode is simulated for the nanodisk arrays of different lattice constants. The simulation results are presented in Figure 4.10. The simulated spectra of the changing lattice constant a are shown in Figure 4.10(a). To understand these spectra in more detail, the spectrum for the structure of $a = 500$ nm is additionally plotted as black line in Figure 4.10(b). Also plotted is the simulated spectrum (red line) for a coating of a 4 nm dielectric shell with a refractive index of 1.44 encapsulating the gold nanodisks, mimicking the biomolecules binding to the surface of the gold in LSPR sensing applications. For convenience of discussion, the spectral features were attributed into quadrupolar peak, dipolar peak, sharp extinction peak, extinction dip #1 and extinction dip #2, which are all marked separately in Figure 4.10(b). The behavior of quadrupolar peaks is consistent with our previous finding [26]. Upon coating, the peak red-shifts by more than 6 nm for the structure $a = 500$ nm. As the lattice constant increases, the dipolar peak red-shifts and the peak linewidth narrows, which is consistent with the experimental findings. However, the spectral positions of simulated peaks do not match well with the measured ones owing to the essentially different waveguide

configurations. Upon coating, the dipolar peak of the structure $a = 500$ nm red-shifts by around 5 nm. These indicated that the quadrupolar peak and the dipolar peak demonstrate similar sensing characteristics.

The most interesting features in the simulated spectra are the sharp extinction peaks and dips, located very close to each other in the spectrum. In order to understand the origins of these features, the sharp extinction peaks and the dips are plotted vs. lattice constant in Figure 4.11. The solid line is defined as $\lambda = a \times n_{eff}$, which indicates the relation of these features with the waveguide mode. In order to examine these features closely, the mode profiles of the extinction peak and the extinction dip#1 for the structure $a = 500$ nm were simulated and are plotted in Figure 4.13 and Figure 4.14 respectively. It should be noted that the color bars used in these two figures are in different scales. It was found, that, at the extinction peaks, the mode profile indicates very strong enhancement of electromagnetic fields of the quadrupolar mode in the periodic array. However, at the extinction dip, the plasmon resonance of the gold nanodisks is suppressed, without obvious quadrupolar mode features. The primary difference is that for the extinction peak, the nodes of the electromagnetic field are under the gold nanodisks while for the extinction dip, the nodes are between the nanodisks.

According to the relationship depicted in Figure 4.11, the extinction peak wavelength and dip wavelength follow the solid line closely. This indicates the effects related to the photonic band gap. This can be explained by considering the 2-D periodic array as a superposition of a 1-D photonic crystal in the X direction and a 1-D photonic crystal in Y direction. The Bragg reflection wavelength of a 1-D photonic crystal structure is given by $\lambda_b = 2a \times n_{eff}/m$, where m is the grating order. In this case, since the lattice configuration is square, $a_x = a_y = a$, the second order Bragg reflection wavelength is given as $\lambda_b = a \times n_{eff}$. This wavelength actually corresponds to the second photonic band gap in the 1-D photonic crystal [13]. For waves with wavelengths close to λ_b , the waves propagating in opposite directions interfere with each other and the result is the formation of standing waves of two types of arrangement: one with the nodes under gold nanodisks which manifests itself in a sharp extinction peak and the other with the nodes between the gold nanodisks which leads to a strong extinction dip. This extinction dip is similar to the selective suppression reported from normal transmission of periodic array of gold nanoparticles on top of waveguides [16, 17] and the sharp extinction peak is similar to the grating-induced



(a) simulated spectra

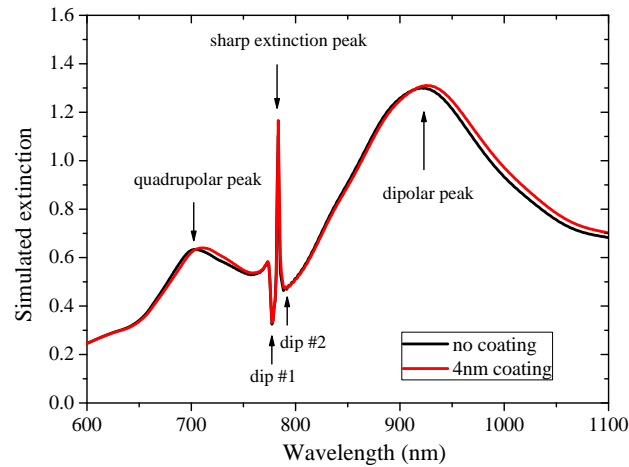
(b) spectra of $a = 500$ nm

Figure 4.10: FDTD simulation results of a periodic array (square lattice) of gold nanodisks on top of a waveguide. (a) Simulated extinction spectra with changing lattice constant of a square lattice coupled to the TE_0 mode. Lattice constant a of each curve are given in the legend. (b) The peak features associated with the structure with lattice constant $a = 500$ nm. The black line is the spectrum of the bare nanodisks while the red line is the spectrum of the nanodisks coated with a 4 nm shell. The important spectral features are marked on the spectrum. With the coating, the quadrupolar peak and dipolar peak red-shift, but the sharp extinction peak and dips do not shift significantly.

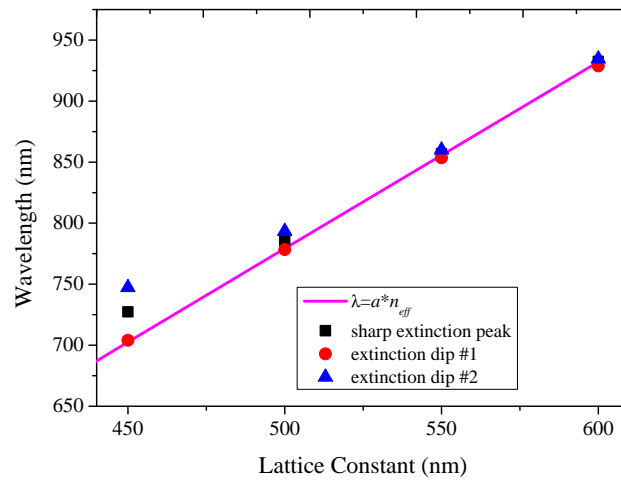


Figure 4.11: Spectral positions of the sharp extinction peak and the dips in the extinction spectra. The solid line depicts the second order Bragg reflection wavelength.

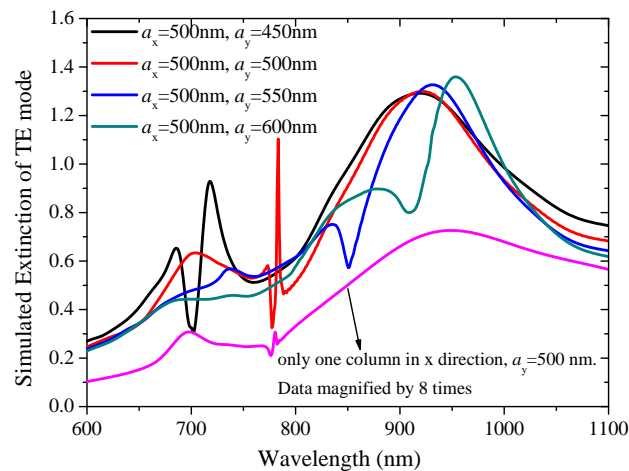


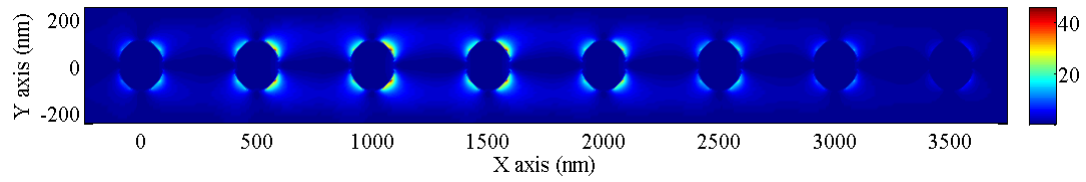
Figure 4.12: Simulated extinction spectra of unequal lattice constant configurations. a_x and a_y of each curve are given in the legend. The lowest curve is obtained from a structure with only 1 column of gold nanodisks in the X direction, i.e. without any periodicity in X direction. This curve represents the response of a 1-D array, periodic in the Y direction. To show the data effectively, the data of this curve has been multiplied by a factor of 8.

modes reported from normal transmission of gold nanoparticles [21].

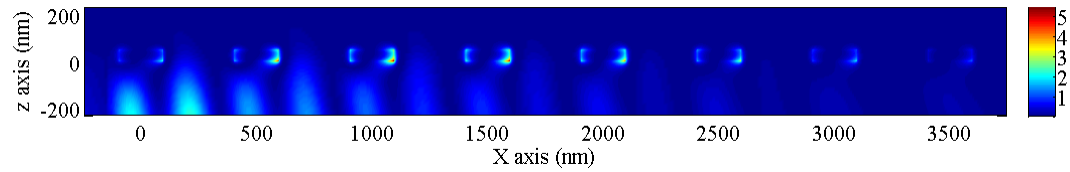
We also found from the simulations, that, the simulated extinction peaks and dips are more affected by the lattice constant in Y directions. As shown in Figure 4.12, by simulating the periodic arrays with unequal a_x and a_y , one can see that the locations of the sharp peak and dip are basically dependent on a_y only. In an additional simulation, we simulated the structure with only one column of gold nanodisks in the X direction, i.e., a one dimensional array with a periodicity only in the Y direction. The sharp extinction peak and dip still exist, but the amplitudes are much weaker. According to this comparison, the locations of the extinction peak and dip are strongly affected by the periodicity in the Y direction while the periodicity in the X direction only affects the amplitudes. We believe that a_x and a_y in reality should work equally. However, due to the simulation methods being used here, only finite number of gold nanoparticles could be simulated in X direction, which is very likely not sufficient to reveal the strong influence of a_x . In the Y direction, the equivalent simulated structure is an infinitely extended periodic array, which gives stronger couplings of the array. A similar phenomenon that the scattering line-shapes depending on the number of coupling nanoparticles can also be found from the discrete dipole approximation (DDA) calculations reported by Hicks et al. [20].

It should be pointed out, the sharp extinction peaks reported here are of quadrupolar nature, which are different from the grating-induced modes caused by dipolar interactions reported by Felidj et al. [21]. Specifically, a dipolar resonator with polarization in the Y direction, scatters light mainly along the X-Z plane, and the grating-induced modes are thus more affected by a_x . For a quadrupolar resonator, light is scattered in more directions and the interactions of the periodic array are affected by periodicities in both directions. Due to the limited number of nanodisks in the X direction in our study, the grating-induced mode in this case is basically determined by a_y . It can be expected that with larger number of periodicities in the X direction, a dependence of the grating-induced mode on both periodicities should be seen.

The sharp extinction peak and dip are located very close to each other, which might offer control of light in unique ways. However, the sharp extinction peak and the dip were found to be not sensitive to the surface bound layer as shown in Figure 4.10(b), meaning that these interesting features are, unfortunately, not appropriate for sensing applications.

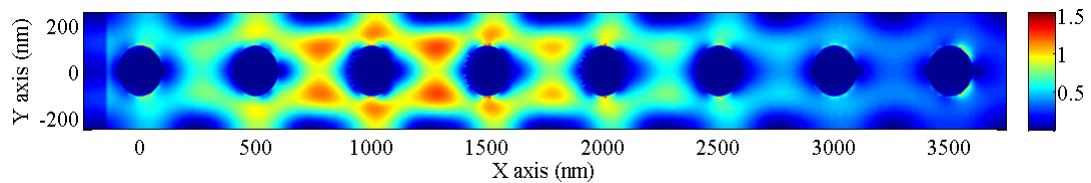


(a) X-Y cut of field profile, at sharp extinction peak of device $a = 500$ nm

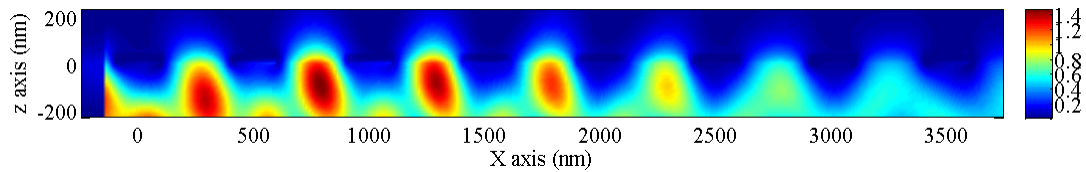


(b) X-Z cut of field profile, at sharp extinction peak of device $a = 500$ nm

Figure 4.13: The simulated mode profile at the wavelength of the sharp extinction peak for the device $a = 500$ nm. The X-Y cut is the horizontal cut crossing the center of the nanodisks and the X-Z cut is the vertical cut crossing the center of the nanodisks.



(a) X-Y cut of field profile, at the extinction dip #1 of device $a = 500$ nm



(b) X-Z cut of field profile, at the extinction dip #1 of device $a = 500$ nm

Figure 4.14: The simulated mode profile at the wavelength of the extinction dip for the device $a = 500$ nm. The X-Y cut is the horizontal cut crossing the center of the nanodisks and the X-Z cut is the vertical cut crossing the center of the nanodisks.

4.7 Conclusion

In this paper, we have first carried out experiments to study the periodic array of gold nanodisks coupled with the evanescent field of waveguide modes. The LSPRs of the structure were found to depend on lattice constants and the mode polarizations. However, due to the low quality of the waveguide, sensing applications using the fabricated sensor was not yet successful.

To understand the interactions of the periodic array in more detail and to investigate the overlap between photonic band gap and the LSPR peak, we carried out the 3-D FDTD simulations. The quadrupolar peak and the dipolar peak were both discussed in detail, and they were both appropriate for sensing applications. We found in the simulation, a strong extinction dip and a sharp extinction peak, very close to in each other in the spectrum, which were not found experimentally due to the high noise level. A closer study revealed that the strong dip is due to the suppressed plasmon resonance by the photonic band gap while the sharp extinction peak is a grating-induced quadrupolar mode. The unique properties of these modes were discussed in detail, but these features were not sensitive to changes in the surface-bound layer.

4.8 Acknowledgements

The authors acknowledge the funding from BIOPSY, a strategic network funded by Natural Sciences and Engineering Research Council of Canada (NSERC). We would also like to acknowledge the funding of TEN program from Canadian Institute for Photonic Innovations (CIPI). We would like to thank Qiuquan Guo, Jun Yang in Department of Mechanical and Materials Engineering, University of Western Ontario for the help in AFM investigations. The device fabrication was performed at the University of Western Ontario Nanofabrication Facility. The simulations were carried out using SHARCNET computing facilities. We would also like to acknowledge the technical support on the 3-D FDTD simulations from Lumerical Inc. S. Mittler likes to acknowledge the Canadian government for the CRC program.

References

- [1] S. Sun, C. B. Murray, D. Weller, L. Folks, and A. Moser, “Monodisperse fept nanoparticles and ferromagnetic fept nanocrystal superlattices,” *Science*, vol. 287, no. 5460, pp. 1989–1992, 2000.
- [2] C. J. Kiely, J. Fink, M. Brust, D. Bethell, and D. J. Schiffrin, “Spontaneous ordering of bimodal ensembles of nanoscopic gold clusters,” *Nature*, vol. 396, pp. 444–446, 1998.
- [3] D. I. Gittins, D. Bethell, D. J. Schiffrin, and R. J. Nichols, “A nanometre-scale electronic switch consisting of a metal cluster and redox-addressable groups,” *Nature*, vol. 408, pp. 67–69, 2000.
- [4] R. P. Andres, J. D. Bielefeld, J. I. Henderson, D. B. Janes, V. R. Kolagunta, C. P. Kubiak, W. J. Mahoney, and R. G. Osifchin, “Self-assembly of a two-dimensional superlattice of molecularly linked metal clusters,” *Science*, vol. 273, no. 5282, pp. 1690–1693, 1996.
- [5] C. L. Haynes, A. D. McFarland, and R. P. V. Duyne, “Surface-enhanced raman spectroscopy,” *Analytical Chemistry*, vol. 77, no. 17, pp. 338 A–346 A, 2005.
- [6] C. T. Nguyen, J. T. Nguyen, S. Rutledge, J. Zhang, C. Wang, and G. C. Walker, “Detection of chronic lymphocytic leukemia cell surface markers using surface enhanced raman scattering gold nanoparticles,” *Cancer Letters*, vol. 292, pp. 91–97, 2010.
- [7] K. A. Willets and R. P. Van Duyne, “Localized surface plasmon resonance spectroscopy and sensing,” *Annu. Rev. Phys. Chem.*, vol. 58, pp. 267–297, 2007.
- [8] J. N. Anker, W. P. Hall, O. Lyandres, N. C. Shah, J. Zhao, and R. P. Van Duyne, “Biosensing with plasmonic nanosensors,” *Nature Materials*, vol. 7, pp. 442–453, 2008.

- [9] P. Englebienne, “Use of colloidal gold surface plasmon resonance peak shift to infer affinity constants from the interactions between protein antigens and antibodies specific for single or multiple epitopes,” *the Analyst*, vol. 123, pp. 1599–1603, 1998.
- [10] A. D. McFarland and R. P. Van Duyne, “Single silver nanoparticles as real-time optical sensors with zeptomole sensitivity,” *Nano Letters*, vol. 3, no. 8, pp. 1057–1062, 2003.
- [11] A. J. Haes and R. P. Van Duyne, “A nanoscale optical biosensor: Sensitivity and selectivity of an approach based on the localized surface plasmon resonance spectroscopy of triangular silver nanoparticles,” *Journal of the American Chemical Society*, vol. 124, no. 35, pp. 10 596–10 604, 2002.
- [12] G. Raschke, S. Kowarik, T. Franzl, C. Sonnichsen, T. A. Klar, J. Feldmann, A. Nichtl, and K. Kurzinger, “Biomolecular recognition based on single gold nanoparticle light scattering,” *Nano Letters*, vol. 3, no. 7, pp. 935–938, 2003.
- [13] J. D. Joannopoulos, R. D. Meade, and J. N. Winn, *Photonic Crystals: Molding the Flow of Light*. Princeton University Press, 1995.
- [14] M. Meier, A. Wokaun, and P. F. Liao, “Enhanced fields on rough surfaces: dipolar interactions among particles of sizes exceeding the Rayleigh limit,” *J. Opt. Soc. Am. B*, vol. 2, no. 6, pp. 931–949, 1985.
- [15] B. Lamprecht, G. Schider, R. T. Lechner, H. Ditlbacher, J. R. Krenn, A. Leitner, and F. R. Aussenegg, “Metal nanoparticle gratings: influence of dipolar particle interaction on the plasmon resonance,” *Phys. Rev. Lett.*, vol. 84, no. 20, pp. 4721–4724, 2000.
- [16] S. Linden, A. Christ, J. Kuhl, and H. Giessen, “Selective suppression of extinction within the plasmon resonance of gold nanoparticles,” *Appl. Phys. B*, vol. 73, pp. 311–316, 2001.
- [17] S. Linden, J. Kuhl, and H. Giessen, “Controlling the interaction between light and gold nanoparticles: selective suppression of extinction,” *Phys. Rev. Lett.*, vol. 86, no. 20, pp. 4688–4691, 2001.

- [18] S. Zou, N. Janel, and G. C. Schatz, "Silver nanoparticle array structures that produce remarkably narrow plasmon lineshapes," *J. Chem. Phys.*, vol. 120, no. 23, pp. 10 871–10 875, 2004.
- [19] S. Zou and G. C. Schatz, "Narrow plasmonic/photonic extinction and scattering line shapes for one and two dimensional silver nanoparticle arrays," *J. Chem. Phys.*, vol. 121, no. 24, pp. 12 606–12 612, 2004.
- [20] E. M. Hicks, S. Zou, G. C. Schatz, K. G. Spears, R. P. Van Duyne, L. Gunnarsson, T. Rindzevicius, B. Kasemo, and M. Kall, "Controlling plasmon line shapes through diffractive coupling in linear arrays of cylindrical nanoparticles fabricated by electron beam lithography," *Nano Letters*, vol. 5, no. 6, pp. 1065–1070, 2005.
- [21] N. Felidj, G. Laurent, J. Aubard, G. Levi, A. Hohenau, J. R. Krenn, and F. R. Aussenegg, "Grating-induced plasmon mode in gold nanoparticle arrays," *J. Chem. Phys.*, vol. 123, p. 221103, 2005.
- [22] A. K. A. Aliganga, I. Lieberwirth, G. Glasser, A.-S. Duwez, Y. Sun, and S. Mittler, "Fabrication of equally oriented pancake shaped gold nanoparticles by SAM-templated OMCVD and their optical response," *Organic Electronics*, vol. 8, no. 2-3, pp. 161 – 174, 2007.
- [23] P. Rooney, A. Rezaee, S. Xu, T. Manifar, A. Hassanzadeh, G. Podoprygorina, V. Böhmer, C. Rangan, and S. Mittler, "Control of surface plasmon resonances in dielectrically coated proximate gold nanoparticles immobilized on a substrate," *Phys. Rev. B*, vol. 77, p. 235446, 2008.
- [24] S. Xu, G. Podoprygorina, V. Bohmer, Z. Ding, P. Rooney, C. Rangan, and S. Mittler, "Tetraurea calix[4]arenes with sulfur functions: synthesis, dimerization to capsules, and self-assembly on gold," *Org. Biomol. Chem.*, vol. 5, pp. 558–568, 2007.
- [25] S. Hashemi Rafsanjani, T. Cheng, S. Mittler, and C. Rangan, "A novel biosensing approach based on linear arrays of immobilized gold nanoparticles," *Journal of Applied Physics*, vol. 107, no. 7, p. 094303, 2010.

- [26] H. Jiang, J. Sabarinathan, T. Manifar, and S. Mittler, “3-D FDTD analysis of gold-nanoparticle-based photoniccrystal on slab waveguide,” *J. Lightwave Technol.*, vol. 27, no. 13, pp. 2264–2270, 2009.
- [27] M. Weisser, F. Thoma, B. Menges, U. Langbein, and S. Mittler-Neher, “Fluorescence in ion exchanged BK7 glass slab waveguides and its use for scattering free loss measurements,” *Optics Communications*, vol. 153, no. 1-3, pp. 27 – 31, 1998.
- [28] A. Hassanzadeh, M. Nitsche, S. Armstrong, N. Nabavi, R. Harrison, S. J. Dixon, U. Langbein, and S. Mittler, “Optical waveguides formed by silver ion exchange in schott SG11 glass for waveguide evanescent field fluorescence microscopy: evanescent images of hek293 cells,” *J. Biomed. Opt.*, vol. 15, p. 036018, 2010.
- [29] T.-M. Lee, S. Mittler-Neher, D. Neher, G. Stegeman, C. Roux, M. Leclerc, J. Martin, and S. Najafi, “Side-chain dilution effects on the optical properties of poly[3-alkylthiophene]s,” *Optical Materials*, vol. 1, no. 2, pp. 65 – 70, 1992.
- [30] H. Jiang and J. Sabarinathan, “Effects of coherent interactions on the sensing characteristics of near-infrared gold nanorings,” *The Journal of Physical Chemistry C*, vol. 114, no. 36, pp. 15 243–15 250, 2010.

Chapter 5

A Biosensor based on Periodic Arrays of Gold Nanodisks under Normal Transmission ¹

5.1 Introduction

Noble metal nanoparticles have been widely investigated in label-free biological sensor applications due to the localized surface plasmon resonance (LSPR), which is a coherent oscillation of the free electron gas in metal nanoparticles excited by electromagnetic radiation. When molecules bind to the surface of nanoparticles, a shift in the resonance peak position can be detected in absorption spectroscopy [1–8]. Sensors based on LSPR are highly sensitive and label-free, i.e. functioning without tags. LSPR sensors are therefore very useful in studying biomolecular interactions and provide real-time information on binding kinetics and concentrations of the target biomolecules. This information is valuable for applications in medical diagnostics, such as the detection of virus [9] and in cancer diagnostics [10]. The optical detection system used for LSPR sensors can be achieved using common laboratory optical and mechanical components, making the equipment more cost-effective than the conventional surface plasmon resonance sensor.

Improving the limit of detection of the LSPR sensor is the main focus of this field and the essential target is to increase the sensitivity and to reduce the uncertainty in determining the resonance position [11, 12]. The sensitivity of metal nanoparticles is highly dependent on the resonance wavelength [13, 14], especially when the

1. A version of this chapter is in preparation for publication: H. Jiang, E. Ertorer, J. Sabarinathan and S. Mittler, 'A biosensor based on periodic array of gold nanodisks under normal transmission'.

nanoparticles are embedded in a homogeneous medium [13]. For the metal nanoparticles immobilized on a substrate, the sensitivity is found to be significantly affected by the spatial overlap between the resonance mode and the substrate [15–19]. Other plasmon characteristics, such as the field decay length and field confinement, also strongly affect the sensitivity [11]. The detection uncertainty is determined by the measurement system, signal-to-noise (S/N) ratio of the spectrum and the spectral linewidth [11, 12]. Among these factors, the spectral linewidth is a directly inherent property of the metal nanoparticles being used. To reduce the detection uncertainty, a sharp spectral line shape (defined by full width at half maximum (fwhm)) is favored.

Considering the spectral linewidth, single nanoparticles [4, 6, 18, 20] are more advantageous than a randomly-interacting ensemble with inhomogeneous broadening effects. For coherently-interacting nanoparticle arrays, however, the linewidth can be significantly reduced owing to the coherent interactions of the nanoparticles in a periodic array, suggesting that a periodic array can perform better than single nanoparticles in LSPR sensing [21]. Another significant advantage of using periodic arrays is that, metal nanoparticles can be closely-packed into a very high density without broadening the extinction peak lineshape, which can increase the strength of the extinction or scattering signal and thus improve the sensor’s S/N ratio. In addition, the periodic array can tune the resonance over a wide range of wavelengths, very convenient for optimizing the sensor performance. Different periodic arrays with well separated LSPR spectrum ranges may open new routes towards multiplexed detections.

In this work, we demonstrate a biosensor based on periodic arrays of gold nanodisks. The sensor is schematically depicted in Figure 5.1. The array of gold nanodisks is patterned into a 2-D square lattice periodic array on top of a BK7 glass substrate. The diameter of the nanodisk d is around 230 nm, the height h is around 50 nm and the lattice constant a (also called periodicities, center-to-center particle spacings) varies from 400 nm to 650 nm with incremental steps of 50 nm. The extinction peak of the sensor is measured by a transmission setup ². In this paper, first the sensing characteristics will be presented and discussed. Then an application in detecting an antibody-antigen recognition will be demonstrated.

2. The setup is described in section 2.3.1.

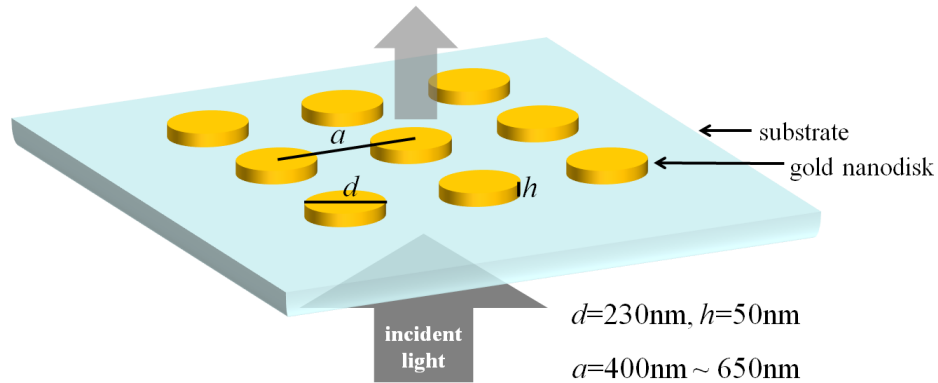


Figure 5.1: Scheme of the sensor configuration. The geometrical parameters are defined and summarized in the plot.

5.2 Experiment

5.2.1 Sample fabrication and measurement

The gold nanodisk arrays in square lattice were fabricated on BK7 glass substrates (Fisher Scientific Inc.) by electron beam lithography (EBL) technique [21]. The fabrication process is schematically depicted in Figure 5.2. After the BK7 substrate was thoroughly cleaned using nanostrip (Cyantek Inc.), 300 nm thick photoresist (ZEP520A, ZEON Corporation) was first spin-coated on top. A 2 nm thick sacrificial chromium layer was then evaporated on top of the photoresist to make the substrate sufficiently conductive. Pattern of nanodisk arrays, accurately controlled by the EBL system, were then exposed into the photoresist. After EBL, the chromium layer was first removed by a chromium etchant (Cr etchant 1020, Transene Company Inc.) followed by developing the photoresist in amyl acetate (Sigma-Aldrich) for 180 seconds. After developing the photoresist, 2 nm chromium and 50 nm gold were sequentially deposited on the patterned photoresist by electron beam evaporation deposition. Finally a lift-off process of the sample immersed into N-methyl-2-pyrrolidone solvent removed the photoresist together with metal on its top, leaving the periodic array of gold nanodisks on the BK7 substrate. The fabricated gold nanodisks are in circular shape with diameters equal to 230 nm and a height of 50 nm.

The fabricated sensor device was integrated with a transparent flow cell for conveniently introducing chemical solutions into the device. The flow cell was constructed by sealing the sensor device with a cover glass (soda-lime microscope slide)

on top, in a similar configuration described by Weisser et al. [22]. As demonstrated in Figure 5.3, glasses were used on both sides for their excellent optical quality in terms of transmission in the near-infrared spectral regime. In comparison, the widely used PDMS fluidic channels are not flat enough which produces a severe interference pattern in the measured extinction spectra. The sensor device and the cover glass were sealed by a 500 μm thick silicone isolator film between them. The soft silicone film, with predefined fluidic channel pattern, seals the two glasses by applying a mild mechanical pressure. Ports were mechanically drilled through the cover glass as inlets and outlets for the fluids. In order to seal each port, one piece of PDMS film was permanently bonded to the cover glass at an elevated temperature following an UV ozone treatment. The steel injection tubes were then inserted through the PDMS, through the ports and into the fluidic channel. This method provides a tightly sealed fluidic channel for the sensor device, with great optical transparency in the near-infrared. In addition, since no glue was involved in the construction of the flow cell, the possibility of the diffused glue compounds contaminating the sensor surface was completely avoided.

The extinction spectra of the sensor were measured by the transmission of linearly polarized (in the direction along an axis of periodicity) broadband light focused by a 10X objective (NA = 0.25) onto the device surface positioned perpendicular to the beam. The beam size to interrogate the device is around $40 \mu\text{m} \times 40 \mu\text{m}$, which is sufficiently smaller than the size of the fabricated array in order to eliminate edge effects. The transmitted light was collected by a 20X objective (NA = 0.2, working distance = 20 mm), coupled into a spectrometer (HR2000, Ocean Optics, 2048 pixels). The extinction spectrum was calculated as $Ext(\lambda) = 1 - I_{dev}(\lambda)/I_{ref}(\lambda)$, with $I_{dev}(\lambda)$ being light transmitted through nanoparticles and $I_{ref}(\lambda)$ being the reference spectrum.

5.3 Sensing characteristics

The measured spectra of the devices immersed in water are plotted in Figure 5.4. The measured spectra show the dipolar resonance of the gold nanodisks is strongly dependent on the lattice constant. The LSPR peak wavelength λ_{LSPR} and linewidth fwhm are plotted against the lattice constant in Figure 5.5(a) and (b). Also plotted

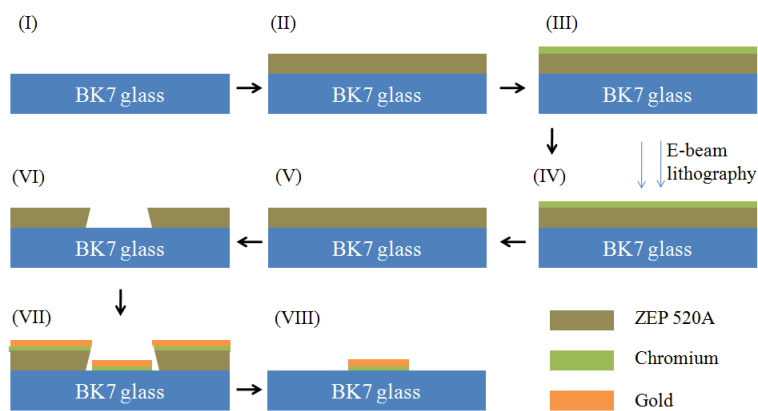


Figure 5.2: Fabrication scheme for periodic arrays of gold nanodisks.

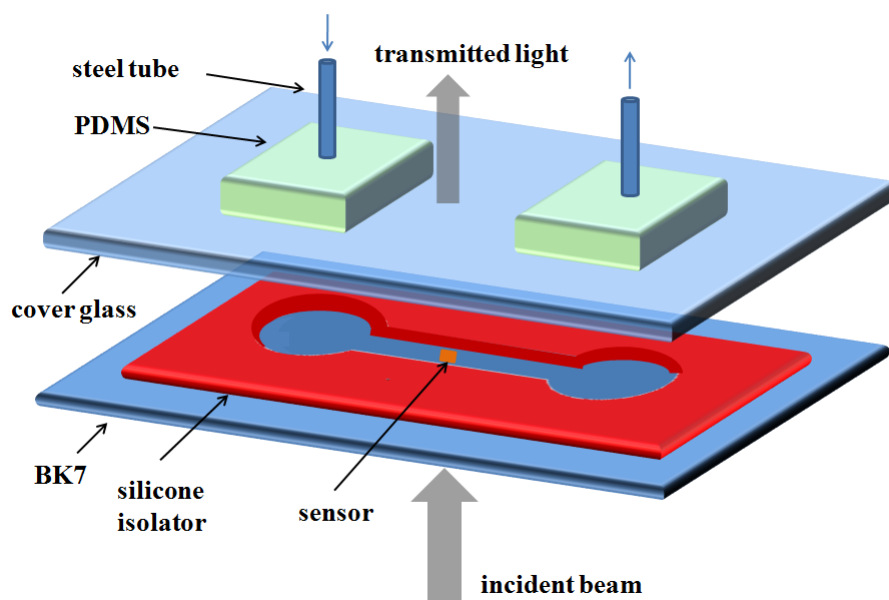


Figure 5.3: Construction of transparent flow cell for transmission measurements. The construction follows the idea reported by Weisser et al. [22].

are the results from 3-D finite difference time domain (FDTD) simulations using the configuration described elsewhere [21, 23] ³.

The dependence of the plasmon peak of the periodic array on the lattice constants has been investigated by many researchers. Meier et al. have theoretically studied the dipolar interactions of periodic arrays of nanoparticles and predicted array effects on the plasmon peak and the radiative damping [24], which have been observed in many experiments on 2-D periodic array of metal nanoparticles [25–28]. The trend of the peak wavelength and linewidth changes is determined by the coupling of the periodic gold nanoparticles array through the grating order at a grazing angle [24, 25]. At a given wavelength λ , the condition for the emergence of the radiative grating order is described by the critical grating constant a_c , meaning that for $a \leq a_c$ the grating order is evanescent and for $a \geq a_c$ the grating order is radiative [24, 25]. For the 1st grating order propagating in the substrate at a grazing angle, $\lambda = n_{sub} \times a_c$, where $n_{sub} = 1.515$, the refractive index of the glass substrate. This relation is plotted as the solid line in Figure 5.5(a) to help determining whether the substrate grating order is evanescent or radiative. For the range of lattice constants studied in this work, a is always smaller than a_c meaning that the grating order is always of evanescent nature.

As the lattice constant increases, the LSPR peak red-shifts and the linewidth narrows significantly. In the experiments, as the a increases from 400 nm into 650 nm, the LSPR peak shifts from 801 nm into 1011 nm while the fwhm decreases from 270 nm to 72 nm. The bulk refractive index sensitivity m_B is defined as $m_B = \delta\lambda_{LSPR}/\delta n_B$ where n_B is the background refractive index of the solvent. In order to measure m_B , water and isopropanol (IPA) mixtures in different ratios were injected onto the sensor to induce a change of n_B . The extinction peak of each solvent refractive index was measured and the sensitivity was determined from the slope of the linear fit of λ_{LSPR} vs. n_B . The bulk refractive index sensing figure of merit is defined as $FOM_B = m_B/\text{fwhm}$ and calculated from the measured m_B and fwhm. In this work, we use the wavelength unit to calculate the figure of merit. The figure of merit calculated in energy units or wavelength units are approximately equivalent [29]. The measured FOM_B are plotted against the lattice constant in Figure 5.5(c). The bulk refractive index figure of merit can increase from 0.9 into 3.8: an enhancement

3. The similar FDTD configuration as described in section 2.1.4

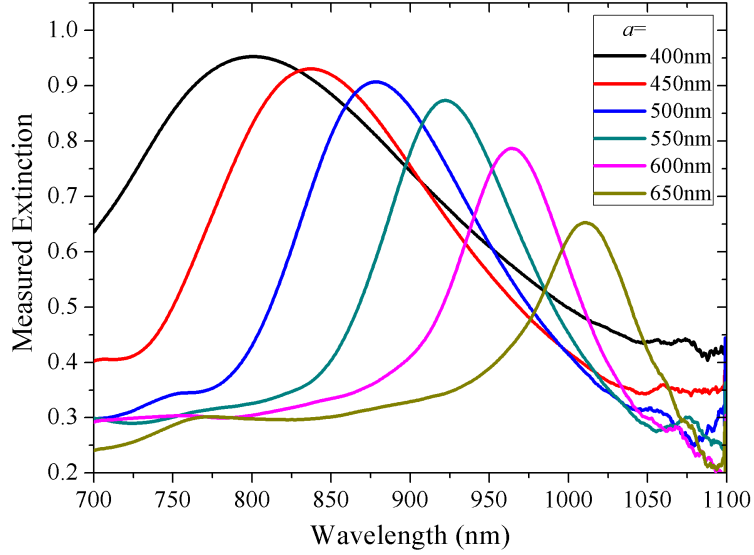


Figure 5.4: Measured extinction spectra of devices with different lattice constants immersed in water. The lattice constant changes from 400 nm to 650 nm, incremental steps of 50 nm.

of nearly half an order of magnitude. This improvement is mainly obtained from the sharpened extinction peak due to the coherent interactions in the periodic array [21].

In order to track the the peak-shift with high resolution, we followed the method described by Dahlin et al. [30] to calculate the centroid peak, λ_c , of each spectrum⁴. The detection uncertainty $\Delta\lambda_{un}$ in quantifying the peak location for each array was estimated from the statistical standard deviation of λ_c recorded over 10 minutes and plotted as the blue triangles in the bottom panel of Figure 5.6. The refractive index (RI) resolution is defined as $\Delta n_B = 3\Delta\lambda_{un}/m_B$ and plotted together with the detection uncertainty. This definition is related to the desired confidence level in determining the peak shift [31]. It can be seen that, as the lattice constant increases, the RI resolution first decreases and then increases. The best RI resolution is $< 1.5 \times 10^{-4}$ refractive index unit (RIU), which is obtained from the lattice configuration of $a = 550$ nm. The corresponding detection uncertainty is 0.011 nm.

The RI resolution in this case is mainly governed by the detection uncertainty, because the change in the sensitivity is much less significant. It should be noted that the detection resolution is actually determined by the nanoplasmonic structure and the detection system together. The aforementioned figure of merit is a value to

4. This method is explained in detail in section 2.3.2

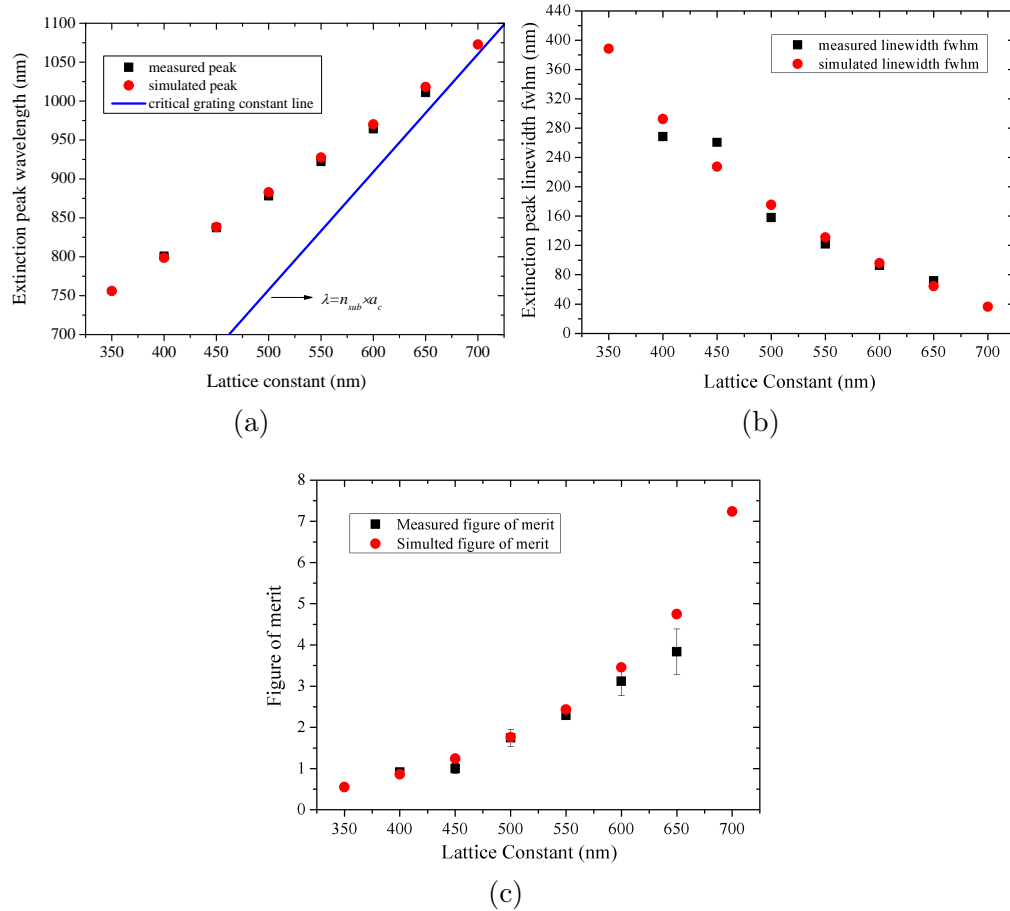


Figure 5.5: Sensing characteristics of the extinction peaks for different lattice constants a . (a) The LSPR peak λ_{LSPR} vs. a . (b) The linewidth fwhm vs. a . (c) Figure of merit FOM_B vs. a . The black squares are the measured data while the red circles represent the simulation results.

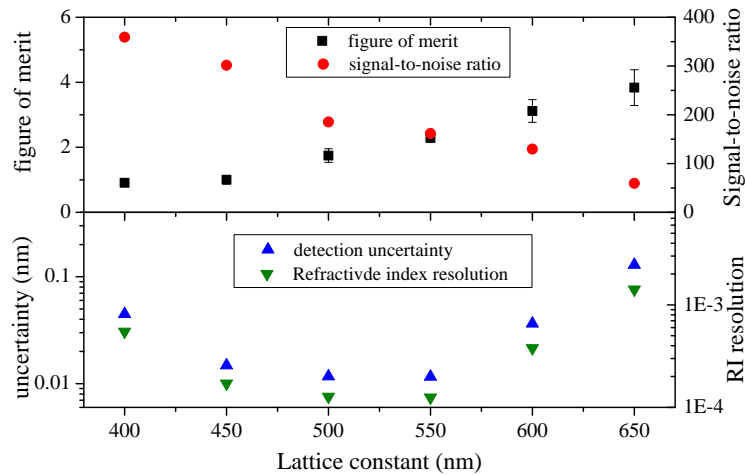


Figure 5.6: Experimental detection uncertainty, refractive index resolution, figure of merit and signal-to-noise ratio, for varying lattice constants. In the top figure, fwhm and the signal-to-noise ratio are plotted, while in the bottom panel, the detection uncertainty and the refractive index resolution are shown in logarithmic scale.

describe the inherent sensing ability of a nanoplasmonic structure but the sensor's resolution in reality is additionally affected by the signal-to-noise (S/N) ratio. For the convenience of discussion, the figure of merit and the S/N ratio are both plotted in the top panel of Figure 5.6. Due to the configuration of the light source, the optics in the detection system and the responsive range of the spectrometer, the S/N ratio is a wavelength-dependent value. In this experiment, the S/N ratio is given by the $S(\lambda)/\sigma(\lambda)$, where $S(\lambda)$ is the intensity spectrum and $\sigma(\lambda)$ is the statistical standard deviation in the intensity spectrum recorded over 30 minutes. The measured S/N ratio is plotted in Figure 5.7. The S/N ratio for each lattice constant is given by the S/N ratio of the corresponding extinction peak wavelength. With increasing lattice constant, although the figure of merit of the nanoplasmonic structure increases, the S/N ratio of the detection system decreases. These two independent factors are taking opposite effects and the overall effect is the optimized RI resolution for the lattice constant in the medium range. This implies that to improve the RI resolution of an LSPR sensor equipment, the nanoplasmonic structure with high figure of merit should be equipped with a matched detection system providing high S/N ratio in the corresponding spectral range. The spectrum tunability of the periodic arrays offers the flexibility to achieve this match.

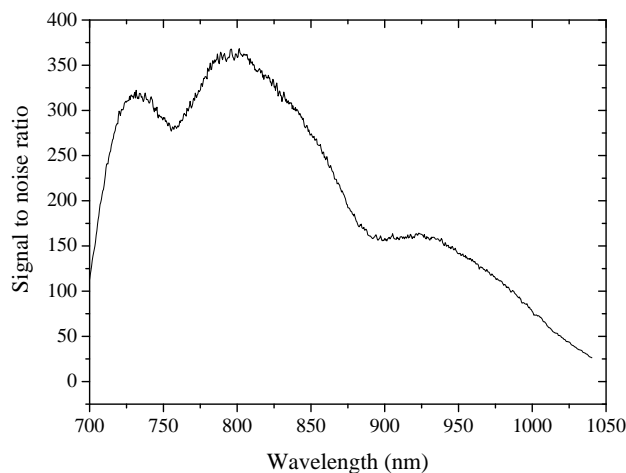


Figure 5.7: Signal-to-noise ratio determined from the statistics of the measured intensity spectra recorded over 30 minutes.

5.4 Antibody-antigen recognition

For sensing applications, we chose the lattice configuration with the best RI resolution, i.e. $a = 550$ nm. We implemented this sensor to detect the binding of an antigen onto the antibody immobilized on the sensor surface. The chosen antibody is anti-human IgG (Sigma Aldrich) and the antigen is human IgG (Sigma Aldrich). Such a study provides a proof of concept for applying this sensor in medical diagnostics, such as early detection of leukemia and lung cancer.

We first implemented the biotin-streptavidin interaction to immobilize the antibody on the surface of gold. The basic strategy is to first immobilize streptavidin on the surface of gold and then introduce the biotinylated antibody which bind to streptavidin. To immobilize streptavidin, we follow the procedures described by Choi et al. [32]. The procedures are schematically shown in Figure 5.8(a) and the corresponding sensor response for the entire surface functionalization procedures is given in Figure 5.8(b). The extinction spectrum was acquired every 15 seconds. After the sample ($a = 550$ nm) was thoroughly cleaned using nanostrip (Cyantek Inc.) and mounted with the flow cell, a mixture of 3-mercaptopropanol (3-MPOH) and 11-mercaptopundecanoic acid (11-MUA) in absolute ethanol was continuously flown on the sensor surface at $1 \mu\text{L}/\text{min}$ for 18 hours to form a well organized self-assembled monolayer (SAM) with carboxylic and hydroxyl terminal groups on the surface of gold nanodisks. The flow rate was controlled by a syringe pump (Braintree Scientific, Inc.). The molar ratio of

3-MPOH and 11-MUA is 10:1, and the total concentration is 10 mM. Then ethanol followed by deionized water was flown at 1 mL/min for 30 minutes to thoroughly rinse the surface. A 1:1 mixture of 0.2 M 1-ethyl-3-(3-dimethylaminopropyl) carbodiimide (EDC) and 0.4 M N-hydroxysuccinimide (NHS) solutions was then flown onto the sensor at 10 $\mu\text{L}/\text{min}$ for 3 hours to activate the terminal carboxylic groups into amine-reactive succinimide esters. Then streptavidin (200 $\mu\text{g}/\text{mL}$) (Sigma-Aldrich) in PBS buffer (pH = 7.4) (Sigma-Aldrich) was injected at a rate of 10 $\mu\text{L}/\text{min}$ for 25 minutes and bonded to the activated carboxylic terminal groups of the mixed SAM. This procedure was repeated to enhance the immobilization. After rinsing the sensor with PBS buffer, 10 $\mu\text{g}/\text{mL}$ bovine serum albumin (BSA) (Sigma-Aldrich) in PBS buffer was flown at 10 $\mu\text{L}/\text{min}$ for 30 minutes, in order to block the non-reacted sites. As observed in Figure 5.8(b), the peak red-shifts due to the binding of the streptavidin and BSA to the surface of gold nanodisks. In the following, biotinylated anti-human IgG (10 $\mu\text{g}/\text{mL}$) in PBS buffer is flown onto the sensor at 10 $\mu\text{L}/\text{min}$ for more than one hour. The biotinylated antibody binds to streptavidin and a saturated red-shift of around 0.7 nm was acquired in the end. This procedure was repeated to enhance the immobilization. Then the sensor was thoroughly rinsed with PBS solution and a stable baseline signal was acquired.

To sense biomolecular recognition, human IgG of different concentrations (1 ng/mL \sim 100 $\mu\text{g}/\text{mL}$) were sequentially tested in an order of increasing concentration. Each concentration of human IgG was continuously flown onto the sensor at 10 $\mu\text{L}/\text{min}$ for 15 minutes. The human IgG biomolecules bind to the anti-human IgG and gradually reached equilibrium. Then PBS was injected to rinse off the non-specific bound molecules and the sensor signal corresponding to each concentration was reported from the spectra acquired 1 minute after rinsing. After the sensor was rinsed for 15 minutes, a higher concentration of human IgG was injected and the same detection scheme was carried out repeatedly. The sensor response vs. concentration was plotted in Figure 5.9. The peak shift above the red line can be trusted to be real detectable shift. It can be determined from this graph that the limit of detection is better than 1 ng/mL.

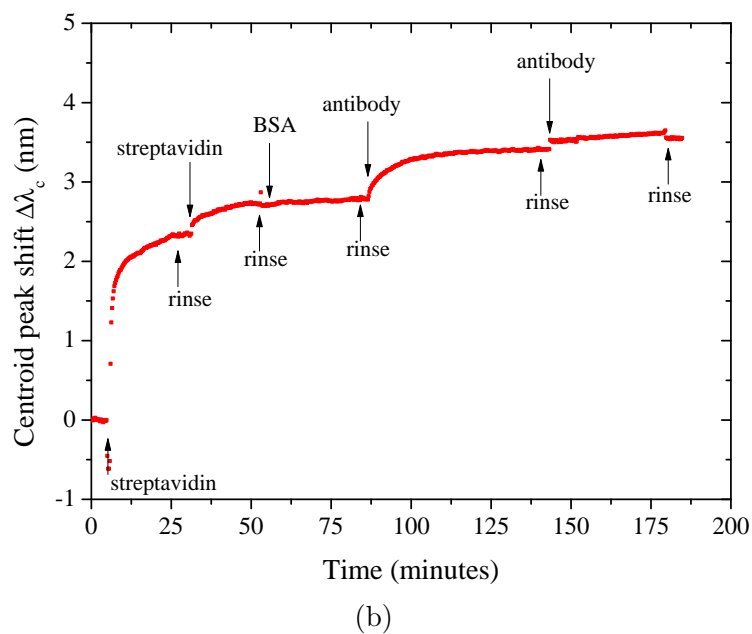
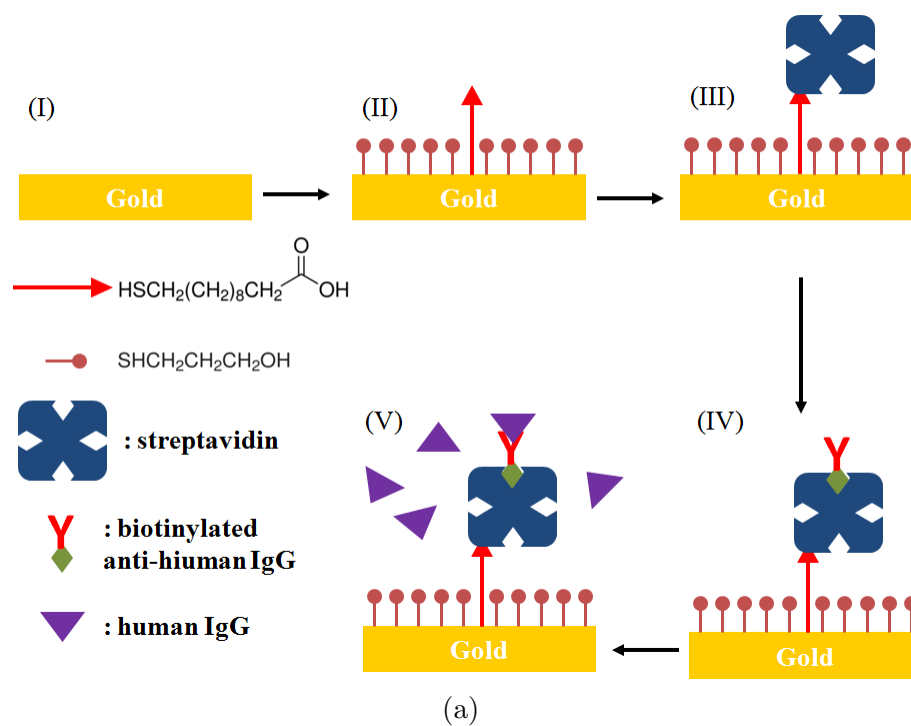


Figure 5.8: The surface chemistry procedures for detecting antibody-antigen recognition. a) Schematic of the chemistry procedures. b) Real-time sensor response recorded during the immobilization of antibody.

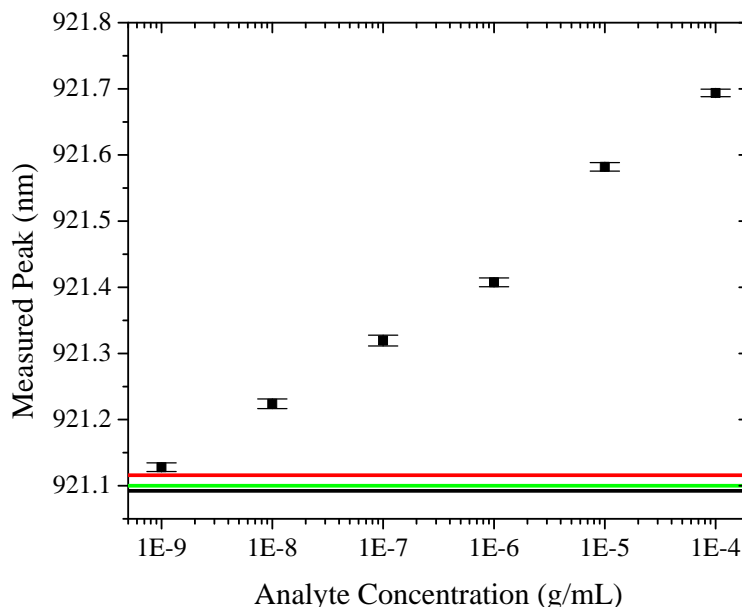


Figure 5.9: Dose response of human IgG binding to anti-human IgG immobilized on the gold surface. The black horizontal line is the base line signal while the green line marks the detection uncertainty. The red line is the decision making threshold which marks the baseline plus three times the detection uncertainty.

5.5 Discussion

Although the sensor can basically function, the peak shift is not as large as expected. A simple simulation showed that, upon full coverage of the biomolecules, at least 3 nm peak shift should be obtained. In our experiment, the maximum peak shift is less than 1 nm. The reasons for this were the low quality of the implemented surface chemistry, which could not reveal the sensor's full potential. In addition, the SAM layer on the surface of gold nanodisks is not robust enough, which can be easily destroyed when a strong basic condition was introduced for the purpose of dissociating the antibody-antigen binding. Improvement on the surface chemistry is necessary, and a possible approach might be an implementation of a polyethylene glycol (PEG) based SAM layer [33].

The sensor based on a random ensemble of nanodisks reported by Chen et al. [10] can reach a detection uncertainty of 9.9×10^{-5} nm and a limit of detection of 8.1 pg/mL in detecting bBSA, which are much better than the values obtained in this work. It should be pointed out, that, the differences are due to the detection system and surface chemistry rather than the inherent properties of the nanoplasmonic

structure. The achieved figure of merit of the periodic array is around 3.8, which is an excellent number compared to other gold nanoparticle devices summarized by Mayer et al. [34]. The periodic array has narrow extinction peak linewidths while providing large extinction cross-sections due to the densely packed periodic array. It can be reasonably expected that our sensor based on periodic arrays of gold nanodisks, if equipped with high quality surface chemistry and high S/N ratio detection system, could potentially reach comparable limit of detection.

5.6 Conclusion

In this paper, we described a biosensor based on the periodic array of gold nanodisks. The sensor structures with varying lattice constant were fabricated and studied experimentally and in simulations. The important sensing characteristics, including LSPR peak wavelength, peak linewidth fwhm, figure of merit, detection uncertainty and refractive index resolution, were investigated in detail. The effects of signal-to-noise on the sensor's performance were also studied. The highest obtained figure of merit is around 3.8 from the structure with $a = 650$ nm. The best refractive index resolution $< 1.5 \times 10^{-4}$ RIU was obtained from the structure with $a = 550$ nm. The structure with $a = 550$ nm was used in the biosensing application to detect the binding of human IgG to the anti-human IgG antibody. The sensor was able to reach a limit of detection better than 1 ng/mL.

5.7 Acknowledgements

The authors acknowledge the funding from BIOPSY, a strategic network funded by Natural Sciences and Engineering Research Council of Canada (NSERC). We would also like to acknowledge the funding of TEN program from Canadian Institute for Photonic Innovations (CIPI). We would like to thank Tingjie Li, Jun Yang in Department of Mechanical and Materials Engineering, University of Western Ontario for constructing the flow cell. The device fabrication was performed at the University of Western Ontario Nanofabrication Facility. The simulations were carried out using SHARCNET computing facilities. We would also like to acknowledge the technical support on the 3-D FDTD simulations from Lumerical Inc. S. Mittler likes to acknowledge the Canadian government for the CRC program.

References

- [1] K. A. Willets and R. P. Van Duyne, “Localized surface plasmon resonance spectroscopy and sensing,” *Annu. Rev. Phys. Chem.*, vol. 58, pp. 267–297, 2007.
- [2] J. N. Anker, W. P. Hall, O. Lyandres, N. C. Shah, J. Zhao, and R. P. Van Duyne, “Biosensing with plasmonic nanosensors,” *Nature Materials*, vol. 7, pp. 442–453, 2008.
- [3] P. Englebienne, “Use of colloidal gold surface plasmon resonance peak shift to infer affinity constants from the interactions between protein antigens and antibodies specific for single or multiple epitopes,” *the Analyst*, vol. 123, pp. 1599–1603, 1998.
- [4] A. D. McFarland and R. P. Van Duyne, “Single silver nanoparticles as real-time optical sensors with zeptomole sensitivity,” *Nano Letters*, vol. 3, no. 8, pp. 1057–1062, 2003.
- [5] A. J. Haes and R. P. Van Duyne, “A nanoscale optical biosensor: Sensitivity and selectivity of an approach based on the localized surface plasmon resonance spectroscopy of triangular silver nanoparticles,” *Journal of the American Chemical Society*, vol. 124, no. 35, pp. 10 596–10 604, 2002.
- [6] G. Raschke, S. Kowarik, T. Franzl, C. Sonnichsen, T. A. Klar, J. Feldmann, A. Nichtl, and K. Kurzinger, “Biomolecular recognition based on single gold nanoparticle light scattering,” *Nano Letters*, vol. 3, no. 7, pp. 935–938, 2003.
- [7] P. Rooney, A. Rezaee, S. Xu, T. Manifar, A. Hassanzadeh, G. Podoprygorina, V. Böhmer, C. Rangan, and S. Mittler, “Control of surface plasmon resonances in dielectrically coated proximate gold nanoparticles immobilized on a substrate,” *Phys. Rev. B*, vol. 77, p. 235446, 2008.

- [8] A. K. A. Aliganga, I. Lieberwirth, G. Glasser, A.-S. Duwez, Y. Sun, and S. Mittler, "Fabrication of equally oriented pancake shaped gold nanoparticles by SAM-templated OMCVD and their optical response," *Organic Electronics*, vol. 8, no. 2-3, pp. 161 – 174, 2007.
- [9] A. A. Yanik, M. Huang, O. Kamohara, A. Artar, T. W. Geisbert, J. H. Connor, and H. Altug, "An optofluidic nanoplasmonic biosensor for direct detection of live viruses from biological media," *Nano Letters*, vol. 10, no. 12, pp. 4962–4969, 2010.
- [10] S. Chen, M. Svedendahl, M. Kall, L. Gunnarsson, and A. Dmitriev, "Ultra-high sensitivity made simple: nanoplasmonic label-free biosensing with an extremely low limit-of-detection for bacterial and cancer diagnostics," *Nanotechnology*, vol. 20, no. 43, p. 434015, 2009.
- [11] A. Unger and M. Kreiter, "Analyzing the performance of plasmonic resonators for dielectric sensing," *J. Phys. Chem. C*, vol. 113, pp. 12 243–12 251, 2009.
- [12] G. J. Nusz, A. C. Curry, S. M. Marinakos, A. Wax, and A. Chilkoti, "Rational selection of gold nanorod geometry for label-free plasmonic biosensors," *ACS Nano*, vol. 3, no. 4, pp. 795–806, 2009.
- [13] M. M. Miller and A. A. Lazarides, "Sensitivity of metal nanoparticle surface plasmon resonance to the dielectric environment," *J. Phys. Chem. B*, vol. 109, pp. 21 556–21 565, 2005.
- [14] R. Bukasov and J. S. Shumaker-Parry, "Highly tunable infrared extinction properties of gold nanocrescents," *Nano Letters*, vol. 7, no. 5, pp. 1113–1118, 2007.
- [15] A. Dmitriev, C. Hagglund, S. Chen, H. Fredriksson, T. Pakizeh, M. Kall, and D. S. Sutherland, "Enhanced nanoplasmonic optical sensors with reduced substrate effect," *Nano Letters*, vol. 8, no. 11, pp. 3893–3898, 2008.
- [16] E. M. Larsson, J. Alegret, M. Kall, and D. S. Sutherland, "Sensing characteristics of NIR localized surface plasmon resonances in gold nanorings for application as ultrasensitive biosensors," *Nano Letters*, vol. 7, no. 5, pp. 1256–1263, 2007.
- [17] C. Novo, A. M. Funston, I. Pastoriza-Santos, L. M. Liz-Marzan, and P. Mulvaney, "Influence of medium refractive index on the optical properties of single gold

- triangular prisms on a substrate,” *J. Phys. Chem. C.*, vol. 112, no. 1, pp. 3–7, 2008.
- [18] L. J. Sherry, S.-H. Chang, G. C. Schatz, R. P. Van Duyne, B. J. Wiley, and Y. Xia, “Localized surface plasmon resonance spectroscopy of single silver nanocubes,” *Nano Letters*, vol. 5, no. 10, pp. 2034–2038, 2005.
- [19] W. A. Murray, B. Auguie, and W. L. Barnes, “Sensitivity of localized surface plasmon resonances to bulk and local changes in the optical environment,” *J. Phys. Chem. C*, vol. 113, pp. 5120–5125, 2009.
- [20] L. J. Sherry, R. Jin, C. A. Mirkin, G. C. Schatz, and R. P. Van Duyne, “Localized surface plasmon resonance spectroscopy of single silver triangular nanoprisms,” *Nano Letters*, vol. 6, no. 9, pp. 2060–2065, 2006.
- [21] H. Jiang and J. Sabarinathan, “Effects of coherent interactions on the sensing characteristics of near-infrared gold nanorings,” *The Journal of Physical Chemistry C*, vol. 114, no. 36, pp. 15 243–15 250, 2010.
- [22] M. Weisser, G. Tovar, S. Mittler-Neher, W. Knoll, F. Brosinger, H. Freimuth, M. Lacher, and W. Ehrfeld, “Specific bio-recognition reactions observed with an integrated Mach-Zehnder interferometer,” *Biosensors and Bioelectronics*, vol. 14, no. 4, pp. 405 – 411, 1999.
- [23] H. Jiang, J. Sabarinathan, T. Manifar, and S. Mittler, “3-D FDTD analysis of gold-nanoparticle-based photoniccrystal on slab waveguide,” *J. Lightwave Technol.*, vol. 27, no. 13, pp. 2264–2270, 2009.
- [24] M. Meier, A. Wokaun, and P. F. Liao, “Enhanced fields on rough surfaces: dipolar interactions among particles of sizes exceeding the rayleigh limit,” *J. Opt. Soc. Am. B*, vol. 2, no. 6, pp. 931–949, 1985.
- [25] B. Lamprecht, G. Schider, R. T. Lechner, H. Ditlbacher, J. R. Krenn, A. Leitner, and F. R. Aussenegg, “Metal nanoparticle gratings: influence of dipolar particle interaction on the plasmon resonance,” *Phys. Rev. Lett.*, vol. 84, no. 20, pp. 4721–4724, 2000.

- [26] J. Sung, E. M. Hicks, R. P. Van Duyne, and K. G. Spears, "Nanosphere spectroscopy: dipole coupling in two-dimensional arrays of L-shaped silver nanoparticles," *J. Phys. Chem. C*, vol. 111, pp. 10 368–10 376, 2007.
- [27] J. Sung, E. M. Hicks, R. P. Van Duyne, and K. G. Spears, "Nanoparticle spectroscopy: plasmon coupling in finite-sized two-dimensional arrays of cylindrical silver nanoparticles," *The Journal of Physical Chemistry C*, vol. 112, no. 11, pp. 4091–4096, 2008.
- [28] C. L. Haynes, A. D. McFarland, L. Zhao, R. P. Van Duyne, G. C. Schatz, L. Gunnarsson, J. Prikulis, B. Kasemo, and M. Kall, "Nanoparticle optics: The importance of radiative dipole coupling in two-dimensional nanoparticle arrays," *J. Phys. Chem. B*, vol. 107, pp. 7337–7342, 2003.
- [29] M. A. Otte, B. Sepulveda, W. Ni, J. P. Juste, L. M. Liz-Marzan, and L. M. Lechuga, "Identification of the optimal spectral region for plasmonic and nanoplasmonic sensing," *ACS Nano*, vol. 4, no. 1, pp. 349–357, 2010.
- [30] A. B. Dahlin, J. O. Tegenfeldt, and F. Hook, "Improving the instrumental resolution of sensors based on localized surface plasmon resonance," *Analytical Chemistry*, vol. 78, no. 13, pp. 4416–4423, 2006.
- [31] J. Homola and M. Piliarik, "Surface plasmon resonance (SPR) sensors," in *Surface Plasmon Resonance Based Sensors*, ser. Springer Series on Chemical Sensors and Biosensors, J. Homola and O. S. Wolfbeis, Eds. Springer Berlin Heidelberg, 2006, vol. 4, pp. 45–67.
- [32] S. H. Choi, J. W. Lee, and S. J. Sim, "Enhanced performance of a surface plasmon resonance immunosensor for detecting Ab-GAD antibody based on the modified self-assembled monolayers," *Biosensors and Bioelectronics*, vol. 21, no. 2, pp. 378 – 383, 2005.
- [33] J. M. Harris, *Poly(ethylene glycol) Chemistry: biotechnical and biomedical applications*. Plenum Press, New York, 1992.
- [34] K. M. Mayer and J. H. Hafner, "Localized surface plasmon resonance sensors," *Chemical Reviews*, vol. 111, no. 6, pp. 3828–3857, 2011.

Chapter 6

Near-infrared optical response of thin film pH-sensitive hydrogel coated on a gold nanocrescent array¹

6.1 Introduction

Localized Surface Plasmon Resonance (LSPR) of noble metal nanoparticles has been proven to be very important in chemical and biological sensor applications [1, 2]. Due to the strong field confinement effects and large extinction cross-section, metal nanoparticles are very sensitive to the dielectric environment close to the surface, with the field decay length in the nanometer scale. They have already been widely investigated in detecting the shift of the LSPR peak owing to the change in the refractive index of a surface bound layer, such as binding of target biomolecules to receptors immobilized on the surface [3]. The LSPR of metal nanoparticles depends on the geometry, composition, dielectric environment and the interactions among particles. Among metal nanoparticles of different materials, gold nanoparticles were chosen due to their resistance to surface oxidation to guarantee stable sensor performance over a long period. Gold nanoparticles of specially engineered geometries have shown near-infrared LSPR which is more sensitive than their visible counterparts [4]. Gold nanoparticles with symmetric shapes, such as gold nanoshells [5] and nanorings [6], have been previously demonstrated with tunable LSPR. A type of asymmetric shaped gold nanoparticles, named gold nanocrescent, has been demonstrated with highly tunable near-infrared resonances and strong field confinement at the tips [7–9].

Hydrogels are polymeric networks produced by the reaction of one or more monomers which are able to retain water within their structure without dissolution.

1. A version of this chapter has been published. H. Jiang, J. Markowski and J. Sabarinathan, published in *Optics Express*, 17 (24), pp. 21802-21807, 2009. (see Appendix B for copyright permission)

Hydrogels are used in a wide range of applications including drug delivery systems, absorbents, soil water retainers, contact lenses, and membrane materials [10]. Over the past decade, hydrogels have also been demonstrated to show promise in the realm of sensing [11–14]. They swell or contract upon hydration due to the hydrophilic nature of the polymer chains, and their swelling is limited by the degree of cross-linking of the polymer network. Due to its aqueous environment, hydrogels are biocompatible by nature. This biocompatible property is highly attractive for biosensing applications, which may involve the immobilization of biological recognition elements such as enzymes [11], antibodies, nucleic acids, etc.

Combining LSPR spectroscopy with hydrogel thin films open new possibilities for LSPR sensor applications, because the hydrogel can be engineered to change their swelling properties in response to a wide variety of chemical and physical stimuli such as pH, ionic strength, solvent composition, buffer composition, temperature, pressure, electromagnetic radiation, and photoelectric stimulus [15]. Towards this goal, the optical response of the hydrogel thin film on LSPR transducers must be well studied. Mack et al. have demonstrated a pH sensor based on a hydrogel-coated gold plasmonic structure [16]. The swelling or shrinking of the hydrogel, when exposed to different pH solutions, is transduced into a change of the integrated transmitted intensity. Here we report the fabrication (by electron beam lithography) of a close-packed periodic array of gold nanocrescent structures (Figure 6.1(a)) and its demonstration as a transducer for very sensitive detection of the swelling of a pH-sensitive hydrogel thin film. Both the wavelength-shift sensing and integrated transmission sensing in the near-infrared regime due to the refractive index change of hydrogel thin film have been demonstrated.

6.2 Fabrication of the sensor device

Electron beam lithography is used to fabricate gold nanocrescents with sharp tips and the fabrication process is schematically demonstrated in Figure 6.1(c). A glass slide is used as the substrate, which has its surface pretreated with a 25 nm coating of indium tin oxide in order to make the surface conductive. Electron beam lithography is used to expose periodic circular lines on a 200 nm thick layer of photoresist (ZEP 520A, ZEON corporation) coated on the substrate. The lattice constant is 330 nm and the diameter of the circle is 220 nm. When developing the photoresist, the thin

film turns into a pattern of circular posts centered inside the periodic array of circular holes. Due to the proximity effects in electron beam exposure and the undercutting sidewall profile of ZEP, each post has a very narrow base in contact with the substrate. From the surface tension during the drying of the sample, each post collapses as a consequence onto one edge of the hole which yields a crescent-shape opening, as can be clearly observed in Figure 6.1(b). A 2 nm layer of titanium and a 50 nm layer of gold are sequentially deposited by physical vapor deposition followed by metal lift-off in solution. The geometries of the fabricated nanocrescents are easily controlled by electron beam exposure dose on the photoresist. The fabricated gold nanocrescents shown in Figure 6.1(a) have an average outer diameter of 260 nm, tip-to-tip distance of 150 nm and wall thickness of approximately 80 nm. The fabricated tips have sub-15nm sharp features, which is very difficult to achieve by directly exposing the crescent shape pattern onto the photoresist. Our method can precisely control both the shapes and the locations of each gold nanocrescent which makes it possible to study the array effects, either in square or hexagonal lattice. The major drawback of our method is that the surface-tension-induced orientation of the fabricated nanocrescent cannot yet be controlled. In comparison, the gold nanocrescents fabricated via nanosphere lithography (NSL) are controlled by sizes and locations of the nanospheres and the tilted deposition angle [7–9]. Recently, Retsh et al. have demonstrated a low cost process for fabricating the large area ordered gold nanocrescent array using a shadow mask prepared by reducing sizes of hexagonally close-packed colloidal nanospheres [17].

A pH-sensitive hydrogel based on poly(hydroxyethyl methacrylate-co-methacrylic acid) was developed as the sensing layer for the gold nanocrescent structure. Prior to coating the poly(HEMA-co-MAA) onto the surface, the devices were treated with 3-(trimethoxysilyl)propyl methacrylate to promote bonding to the surface using a previously described silanization method [18]. Hydroxyethyl methacrylate (HEMA) was mixed with 8 mol% ethylene glycol dimethacrylate (EDMA) and 6 mol% methacrylic acid (MAA) and prepared in an equal volume of isopropanol as the solvent. The MAA monomers allow the hydrogel to change its volume reversibly by swelling or shrinking as a function of the pH of the buffering medium that is used to bathe the gel. 2% w/v of 2,2-Dimethoxy-2-phenylacetophenone (DMPA) photoinitiator was added and slowly mixed into the solution. In order to grow the polymer, the solution was mixed, degassed in a stream of nitrogen, and exposed to UV for 30 seconds to initiate

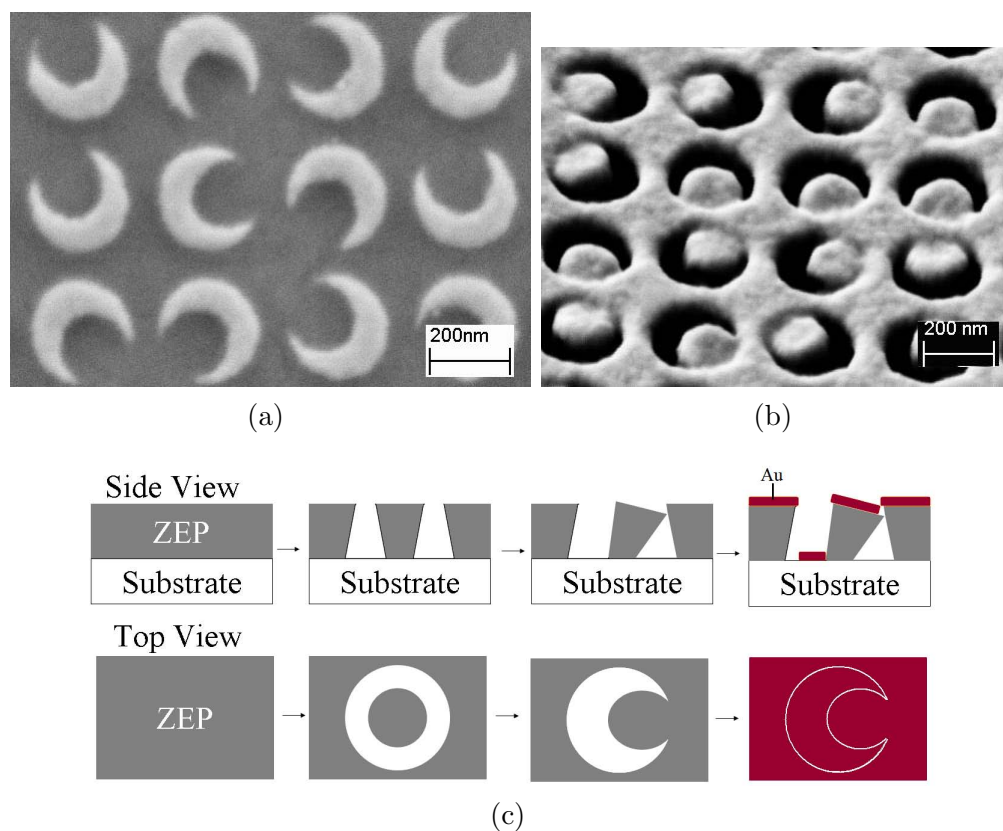


Figure 6.1: Fabrication of the gold nanocrescent array. (a) SEM micrograph of the fabricated gold nanocrescent array structure. (b) SEM micrograph at a tilted angle of the developed photoresist thin film coated with gold. (c) Schematic of the fabrication process of the gold nanocrescents.

the free radical reaction at room temperature. This pre-polymerization process was repeated once more. The grown polymeric solution was then spin-coated on the gold nanocrescent structure at 4000 rpm for 30 seconds to produce a gel of thickness ca. 150 nm. The device was subsequently placed into a chamber, purged with nitrogen to produce an oxygen-free environment, and was finally cured by UV light for 10 minutes at room temperature. The fabricated hydrogel thin film has been demonstrated to be very robust, as it was effectively studied to show good results even after 30 days of storage.

6.3 Measurement and simulation of the LSPR

The LSPR of the gold nanocrescent array was measured by normal transmission of focused, unpolarized, near-infrared broadband light (1200 nm \sim 2000 nm), analyzed by a 0.8 m high-resolution spectrograph and InGaAs detector. Unpolarized light was used because of the random orientations of the fabricated nanocrescents. The extinction spectrum $Ext(\lambda)$ and the transmission spectrum $T(\lambda)$ are given by:

$$Ext(\lambda) = -\ln(T(\lambda)) = -\ln(I(\lambda)/I_{ref}(\lambda)) \quad (6.1)$$

where $I(\lambda)$ is the transmitted light intensity spectrum through the gold nanocrescent and $I_{ref}(\lambda)$ is the reference spectrum.

Before coating the hydrogel, two extinction peaks were acquired from the bare device in the near-infrared spectral range, one located at 1310 nm (peak 'W₀'), the other at 1672 nm (peak 'C₁'), as shown in Figure 6.2. After coating the xerogel (dehydrated hydrogel) on the surface of the device, a change of refractive index around 0.47 is induced. As shown in the dotted line in Figure 6.2, the peak C₁ red-shifts to 1828 nm, which roughly corresponds to a bulk refractive index sensitivity of 332 nm/RIU. This is lower than other gold nanocrescents with similar size [7]. We attribute this reduction in sensitivity to the smooth rounded profile of the top edges of the fabricated nanocrescents in our method and the substrate with relatively high index due to ITO. It should be noted that after coating, the peak W₀ also red-shifts by a smaller amount but becomes significantly lower in magnitude and another weak peak 'W₁' appears around 1600 nm. In addition, the slope of another strong peak 'U₁' at shorter wavelength begins to enter the detection range.

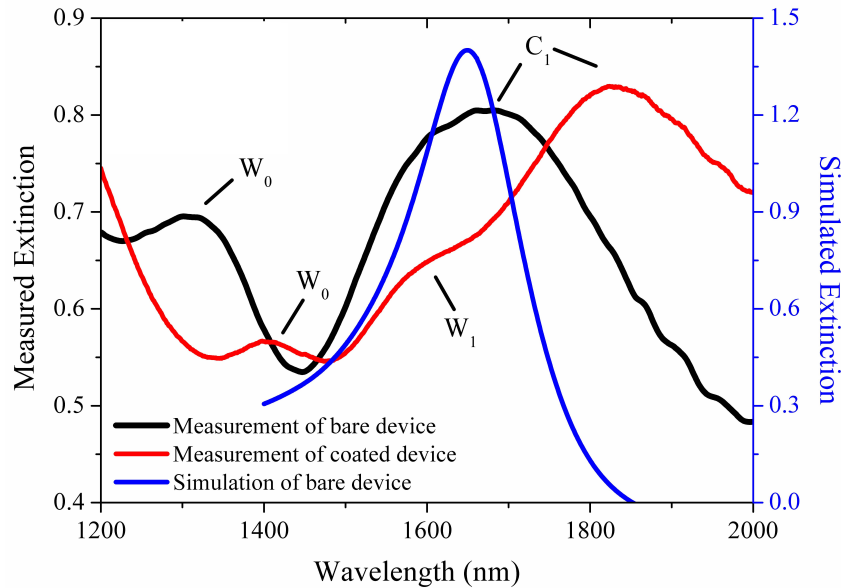


Figure 6.2: Measured and simulated extinction spectra of the fabricated device. The black line represents measurement on the bare device without coating and the red line represents measurement on the device coated with xerogel. The blue line represents simulation of the bare device.

To understand these peaks, the LSPR of a single gold nanocrescent is simulated by three-dimensional FDTD simulations incorporating a non-uniform mesh [19]. The simulated spectra are plotted together with the measured spectra in Figure 6.2. According to the simulations, peak C_1 is excited by the light polarized parallel to the long axis of the nanocrescent (longitudinal resonance). When the light is polarized parallel to the short axis of the nanocrescent (transverse resonance), one strong peak is obtained at 947 nm, which should correspond to peak U_1 . However, the existence of the W_0 and W_1 cannot be resolved in FDTD simulations. The origin of these peaks is probably the interactions between the gold nanocrescents. Due to the random orientation of gold nanocrescents, the tips of some neighboring gold nanocrescents can be very close with a distance comparable to the field decay length, leading to strong near-field couplings. Such an effect could explain the broad feature of the LSPR peak and the existence of W_0 and W_1 peaks.

6.4 Sensor response vs. pH

We used the C_1 peak to detect the response of the coated hydrogel thin film. Buffer solutions titrated to various pH levels were introduced onto the device through a fluidic channel built on top of the device. For measurements of each specific pH solution, we waited 15 minutes for the device to reach equilibrium state. We began with $\text{pH} = 3.08$, and progressively increased the pH, which causes the hydrogel to swell.

When the solution is first introduced, the xerogel swells as it absorbs the water, effectively reducing the refractive index of the sensing layer because water has a lower refractive index ($n = 1.33$) than our hydrogel ($n \approx 1.47$). As the pH is gradually increased from 3.08 to 9.08, the hydrogel swells under electrostatic repulsion due to the ionization of carboxylic groups. Swelling occurs when the pH of the swelling medium rises above the pK_a of the moiety, which has been studied to be 4.50 [14], causing the hydrogel to become more hydrophilic and absorb more water, which decreases the refractive index.

This decrease in refractive index is transduced into a change in the measured extinction spectrum, as shown in Figure 6.3(a). As the pH increases, the longitudinal extinction peak wavelength λ_{max} decreases, and the extinction amplitude decreases as well. The latter is equivalent to increasing transmission $T(\lambda)$. Therefore, the swelling behavior of the hydrogel under increasing pH can be transduced into two characteristic responses, one is λ_{max} , the other is the transmission $T(\lambda)$ integrated from 1700 nm to 1840 nm. This spectral range is selected for optimum signal noise ratio which is strongly affected by near-infrared water absorption. Both responses are plotted in Figure 6.3(b) and the details of the trends show that they are very consistent with each other.

The two responses were fitted into titration curves using the Henderson-Hasselbalch equation (Equation 6.2) for the cross-linked polymers [20, 21]:

$$\text{pH} = pK_a - n_p \log \frac{1 - \alpha}{\alpha} \quad (6.2)$$

pK_a is the apparent dissociation constant of the cross-linked polymer, n_p is the correction for the distribution of the MAA groups in the polymer and α is the degree of polymer dissociation which is assumed to be linearly related to the sensor responses. The best fit of the titration curves for both responses are plotted as the solid lines in

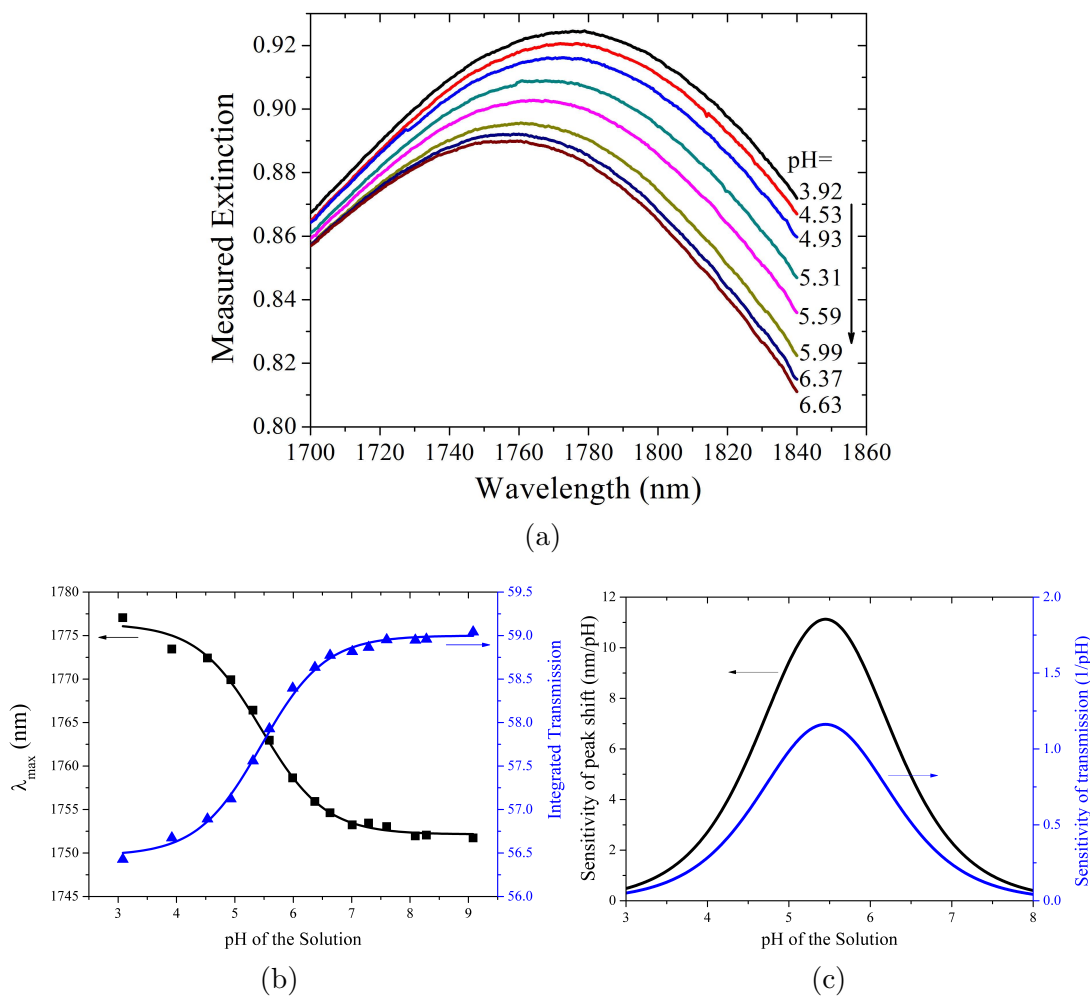


Figure 6.3: Sensor response of the gold nanocrescent array structure coated with hydrogel thin film. (a) Measured extinction spectra of the device for detecting buffered solutions of increasing pH. (b) Response of λ_{max} (black squares) and the integrated transmission (blue triangles) obtained from the measured extinction spectra. The solid lines are the titration curves fitted into the experimental data. (c) Sensitivity for shift of λ_{max} (black curve) and sensitivity for transmission (blue curve) vs. pH calculated from the fitted response curves.

Figure 6.3(b), which yields the fit parameters of $pK_a = 5.45$, $n_p = 1.25$. These values are consistent with previous studies of poly(HEMA-co-MAA) polymers [14, 21].

The sensitivities calculated from the fitted response curves are plotted in Figure 6.3(c). The most sensitive detection range of our hydrogel lies in the pH range centered at the point of $\text{pH} = pK_a$, which is the inflection point of the titration response curves. At $\text{pH} = pK_a$, the sensitivity of the extinction peak shift is 11.1 nm/pH unit while the sensitivity of the transmission is 1.16 /pH unit. The sensitive range is thus determined to be 4.5~6.4 with the boundaries where the sensitivity decreases by half. As the hydrogel swells in this range, λ_{max} blue-shifts from 1772 nm into 1755 nm, and the integrated transmission response increases from 56.8 into 58.6. It should be noted that when pH is increased beyond 8.0, no further significant shift is acquired because all ionizable groups have been ionized.

6.5 Discussions

Due to the random orientations of gold nanocrescents, the LSPR peak is significantly broadened by near-field effects. The Figure of Merit (FOM, peak-shift per refractive index unit divided by peak width calculated in eV) is around 0.4. Future implementations are expected to provide control for the orientations of gold nanocrescent and the optimum design of the lattice constants leading to an improved FOM. The uncertainty in determining the peak-shift is estimated from the experiment to be better than 0.5 nm, which yields detection accuracy around 0.045 pH unit. It should be emphasized that, the LSPR spectroscopy can reach a detection resolution $\sim 10^{-4}$ nm range. Combining the hydrogel thin film and LSPR spectroscopy can potentially achieve higher resolution than existing hydrogel sensors. The performance can also be further optimized in terms of sensitivity by modifying the ratios of the constituent monomers [14]. It should be mentioned that the sensor shows repeatable results even after 30 days of storage. The chemiresponsive nature of pH-sensitive hydrogels may be exploited for biosensing purposes, such as to monitor the concentration of H^+ produced in the biocatalytic reaction of organophosphorus compound [12].

6.6 Acknowledgements

The authors would like to acknowledge Natural Sciences and Engineering Research Council of Canada (NSERC), CMC Microsystems and Canada Foundation for Innovation (CFI) for funding this research work. The device fabrication was done at the University of Western Ontario Nanofabrication facility.

References

- [1] K. A. Willets and R. P. Van Duyne, “Localized surface plasmon resonance spectroscopy and sensing,” *Annu. Rev. Phys. Chem.*, vol. 58, pp. 267–297, 2007.
- [2] J. N. Anker, W. P. Hall, O. Lyandres, N. C. Shah, J. Zhao, and R. P. Van Duyne, “Biosensing with plasmonic nanosensors,” *Nature Materials*, vol. 7, pp. 442–453, 2008.
- [3] P. Englebienne, “Use of colloidal gold surface plasmon resonance peak shift to infer affinity constants from the interactions between protein antigens and antibodies specific for single or multiple epitopes,” *the Analyst*, vol. 123, pp. 1599–1603, 1998.
- [4] M. M. Miller and A. A. Lazarides, “Sensitivity of metal nanoparticle surface plasmon resonance to the dielectric environment,” *J. Phys. Chem. B*, vol. 109, pp. 21 556–21 565, 2005.
- [5] C. L. Nehl, N. K. Grady, G. P. Goodrich, F. Tam, N. J. Halas, and J. H. Hafner, “Scattering spectra of single gold nanoshells,” *Nano Letters*, vol. 4, no. 12, pp. 2355–2359, 2004.
- [6] J. Aizpurua, P. Hanarp, D. S. Sutherland, M. Kall, G. W. Bryant, and F. J. Garcia de Abajo, “Optical properties of gold nanorings,” *Phys. Rev. Lett.*, vol. 90, no. 5, p. 057401, 2003.
- [7] R. Bukasov and J. S. Shumaker-Parry, “Highly tunable infrared extinction properties of gold nanocrescents,” *Nano Letters*, vol. 7, no. 5, pp. 1113–1118, 2007.
- [8] H. Rochholz, N. Bocchio, and M. Kreiter, “Tuning resonances on crescent-shaped noble-metal nanoparticles,” *New Journal of Physics*, vol. 9, no. 3, p. 53, 2007.
- [9] N. L. Bocchio, A. Unger, M. Alvarez, and M. Kreiter, “Thin layer sensing with multipolar plasmonic resonances,” *J. Phys. Chem. C*, vol. 112, pp. 14 355–14 359, 2008.

- [10] T. Toyochi, *Phase Transitions of Gels*. American Chemical Society symposium, 1992, ch. 2, pp. 1–21.
- [11] M. Zourob, A. Simonian, J. Wild, S. Mohr, X. Fan, I. Abdulhalim, and N. J. Goddard, “Optical leaky waveguide biosensors for the detection of organophosphorus pesticides,” *Analyst*, vol. 132, pp. 114–120, 2007.
- [12] J. Walker, K. Kimble, and S. Asher, “Photonic crystal sensor for organophosphate nerve agents utilizing the organophosphorus hydrolase enzyme,” *Analytical and Bioanalytical Chemistry*, vol. 389, pp. 2115–2124, 2007.
- [13] L. A. DeLouise, P. M. Fauchet, B. L. Miller, and A. A. Pentland, “Hydrogel-supported optical-microcavity sensors,” *Advanced Materials*, vol. 17, no. 18, pp. 2199–2203, 2005.
- [14] A. J. Marshall, J. Blyth, C. A. B. Davidson, and C. R. Lowe, “pH-sensitive holographic sensors,” *Analytical Chemistry*, vol. 75, no. 17, pp. 4423–4431, 2003.
- [15] A. R. Khare and N. A. Peppas, “Swelling/deswelling of anionic copolymer gels.” *Biomaterials*, vol. 16, no. 7, pp. 559–567, 1995.
- [16] N. H. Mack, J. W. Wackerly, V. Malyarchuk, J. A. Rogers, J. S. Moore, and R. G. Nuzzo, “Optical transduction of chemical forces,” *Nano Letters*, vol. 7, no. 3, pp. 733–737, 2007.
- [17] M. Retsch, M. Tamm, N. Bocchio, N. Horn, R. Forch, U. Jonas, and M. Kreiter, “Parallel preparation of densely packed arrays of 150-nm gold-nanocrescent resonators in three dimensions,” *Small*, vol. 5, no. 18, pp. 2105–2110, 2009.
- [18] M. Dawgul, D. G. Pijanowska, A. Krzyskow, J. Kruk, and W. Torbicz, “An influence of polyhema gate layer on properties of chemfets,” *Sensors*, vol. 3, no. 6, pp. 146–159, 2003.
- [19] H. Jiang, J. Sabarinathan, T. Manifar, and S. Mittler, “3-D FDTD analysis of gold-nanoparticle-based photonic crystal on slab waveguide,” *J. Lightwave Technol.*, vol. 27, no. 13, pp. 2264–2270, 2009.
- [20] A. Katchalsky and P. Spitnik, “Potentiometric titrations of polymethacrylic acid,” *Journal of Polymer Science*, vol. 2, no. 4, pp. 432–446, 1947.

- [21] S. Fisher and R. Kunin, "Effect of cross-linking on the properties of carboxylic polymers. i. apparent dissociation constants of acrylic and methacrylic acid polymers," *The Journal of Physical Chemistry*, vol. 60, no. 8, pp. 1030–1032, 1956.

Chapter 7

Effects of Coherent Interactions on the Sensing Characteristics of Near-Infrared Gold Nanorings ¹

7.1 Introduction

Noble metal nanoparticles have been widely investigated in label-free biological/chemical sensor applications due to the localized surface plasmon resonance (LSPR), which is a coherent oscillation of conduction electrons in metal nanoparticles excited by electromagnetic radiation. When biomolecules bind to the surface of particles or when a change in the refractive index of a surface bound layer is induced by chemical stimuli, a shift in the resonance peak can be detected in the LSPR spectroscopy [1–7]. Pushing the performance of LSPR sensors towards single molecule detection range is currently the focus of intensive research. Recently, the factors to evaluate the LSPR sensor performance have been summarized and discussed by Unger et al. [8] and by Nusz et al. [9]. In order to improve the performance, the essential target is to increase the sensitivity and to reduce the uncertainty in determining the resonance position [8, 9].

The sensitivity of metal nanoparticles is highly dependent on the resonance wavelength [10, 11], especially when the nanoparticles are embedded in a homogeneous medium [10]. For the metal nanoparticles immobilized on a substrate, the sensitivity is found to be significantly affected by the spatial overlap between the resonance mode

1. A version of this chapter has been published. H. Jiang, J. Sabarinathan and S. Mittler, published in *Journal of Physical Chemistry C*, 114 (36), pp 15243-15250, 2010. Reprinted (adapted) with permission from (H. Jiang, J. Sabarinathan and S. Mittler 'Effects of Coherent Interactions on the Sensing Characteristics of Near-Infrared Gold Nanorings', *Journal of Physical Chemistry C*, 114 (36), pp 15243-15250, 2010). ©2010 American Chemical Society. (see Appendix C for copyright permission)

and the substrate [12–16]. Other plasmon characteristics, such as the field decay length and field confinement, also strongly affect the sensitivity [8]. The detection uncertainty is determined by the measurement system, signal noise ratio (SNR) of the spectrum and the spectral linewidth [8, 9]. Among these factors, the spectral linewidth is a directly inherent property of the metal nanoparticles being used. To reduce the detection uncertainty, a sharp spectral line shape (defined by full width at half maximum (fwhm)) is favored.

Considering the spectral linewidth, single nanoparticles [4, 6, 15, 17] are more advantageous than a randomly-interacting ensemble with inhomogeneous broadening effects. For coherently-interacting nanoparticle array, however, the linewidth can be significantly reduced owing to the coherent interactions of nanoparticles in a periodic array. This implies that a higher sensing figure of merit (FOM) can be potentially achieved from the periodic array of nanoparticles than the single nanoparticle or random ensembles. In addition, the periodic array also provides advantages such as spectral tunability, array-type integration and densely-packed nanoparticles for large extinction cross section. The advancement in nanofabrication technologies has allowed for large-scale and low-cost fabrication of such nanostructures, such as those fabricated by nanosphere lithography (NSL) [5, 18] and by nanoimprint lithography (NIL) [19].

The dependence of the plasmon peak of the periodic array on the lattice constants (particle spacings) has been investigated by many researchers. Meier et al. have theoretically studied the dipolar interactions of periodic array of nanoparticles and predicted the array effects on the plasmon peak and radiative damping [20], which have been observed in many experiments on 2D periodic array of gold and silver nanoparticles [21–24]. Narrow extinction peaks have been reported from the periodic array of gold nanoparticles on optical waveguide [25, 26]. The sharp plasmon peak due to coherent interactions of disordered silver nanoparticles array has been demonstrated [27]. The sharp grating-induced plasmon mode of periodic array of metal nanoparticles has been studied theoretically and experimentally [28–31].

To our best knowledge, the effects of coherent interactions on the sensing characteristics of the periodic array have yet to be fully investigated. In this paper, we present sensing characteristics of 2D periodic array of gold nanorings in square lattice. Specifically, we tuned the lattice constant and studied the sensitivity and figure of merit. The gold nanorings were chosen due to their near-infrared resonance

wavelength demonstrated with high sensitivity [10, 13, 19, 32, 33]. In addition, the sensing device with near-infrared wavelength can be easily integrated into the silicon photonic platform. We believe the results and insights obtained through this systematic study are important in designing LSPR sensors based on a periodic array of metal nanoparticles.

7.2 Experiment

7.2.1 Sample fabrication and measurement

The periodic arrays of gold nanorings with 2D square lattices were fabricated on glass substrate coated with 25 nm conductive Indium Tin Oxide (ITO) layer. Electron beam lithography (EBL) technique was implemented for its ability to precisely control the geometry and position of each nanoparticle at the same time. Patterns of periodic nanorings were exposed onto a 150 nm layer of photoresist (ZEP 520A, ZEON corporation) spin-coated on the substrate. Each device has a different lattice constant a which was varied from 350 nm to 1000 nm with a step of 50 nm. To calibrate the proximity effects, the exposure dose was varied from 0.35 nC/cm to 0.45 nC/cm for different lattice configurations. The area of each device is $60 \mu\text{m} \times 60 \mu\text{m}$. After developing the photoresist, a 2 nm layer of titanium and a 50 nm layer of gold were sequentially deposited by physical vapor deposition, followed by UV exposure to decompose the photoresist. Then a lift-off process of the sample immersed into N-methyl-2-pyrrolidone solvent yielded the periodic array of gold nanorings on the substrate.

The extinction spectrum of each device was measured by the transmission of linearly polarized near-infrared broadband light (900 nm - 1600 nm) focused by a 10X objective (NA=0.25) onto the device surface positioned perpendicular to the beam. The beam size to interrogate the device is around $80 \mu\text{m} \times 80 \mu\text{m}$. The transmitted light was collected by a 50X objective (NA=0.8), coupled into a 0.8 m spectrograph and analyzed by an InGaAs detector. The extinction spectrum was calculated by $Ext(\lambda) = 1 - I_{dev}(\lambda)/I_{ref}(\lambda)$, with $I_{dev}(\lambda)$ being light transmitted through nanoparticles and $I_{ref}(\lambda)$ being the reference spectrum.

7.2.2 Experimental results

The fabricated periodic nanostructures were characterized by scanning electron microscope (SEM). Examples of the fabricated nanorings with $a=400$ nm, 600 nm, 800 nm and 1000 nm are given in Figure 7.1. The fabricated nanoring has an average center diameter around 220 nm and average wall thickness of 33 nm. The variation in the wall thickness is estimated to be 5 nm. The extinction spectra measured on the bare devices with different lattice constants are plotted in Figure 7.1(e). The polarization direction of incident light is given by the arrow drawn relative to the inset image. The gold nanoring arrays demonstrate near-infrared LSPR peaks of dipolar modes in the spectral range from 1150 nm to 1300 nm.

As observed in the measured spectra, the dipolar resonance of gold nanorings is strongly dependent on the lattice constant. The LSPR peak wavelength λ_{LSPR} and linewidth fwhm are plotted against the lattice constant in Figure 7.2(a). The LSPR peaks for the bare devices in air (black solid squares) and the devices coated with a 300 nm layer of PMMA polymer (red solid circles) are both given. By coating the PMMA polymer on the devices, a change in the bulk refractive index n_B of the sensing region was introduced ($n_B = 1$ for bare devices in air and $n_B \approx 1.478$ for coated devices in PMMA). The trend of the peak wavelength and linewidth is determined by the coupling of the periodic gold nanoparticles through the grating order at a grazing angle [20, 21]. At a given wavelength λ , the condition for the emergence of the radiative grating order is described by the critical grating constant a_c , meaning that for $a \leq a_c$ the grating order is evanescent and for $a \geq a_c$ the grating order is radiative [20, 21]. For the 1st grating order propagating in the substrate at a grazing angle, $\lambda = n_{sub} \times a_c$, where $n_{sub}=1.56$ is the refractive index of the glass substrate. This relation is plotted as the solid line in Figure 7.2(a) to assist in determining that for a given LSPR peak at the corresponding lattice constant, whether the substrate grating order is evanescent or radiative. For either the bare devices in air or devices coated by PMMA, the LSPR peak red-shifts with increasing lattice constant and begins to blue-shift when the λ_{LSPR} curve crosses the critical grating constant line. The crossing point is defined as resonant lattice constant a_{res} (sometimes denoted as $d_{c,res}$ [21] or D_{crit} [22]), which approximately gives the lattice constant for the maxima red-shift. For $a < a_{res}$, the LSPR peaks are above the critical grating constant line and the substrate grating order is evanescent because $a < \lambda_{LSPR}/n_{sub}$. For $a > a_{res}$, the LSPR peaks are below the critical grating constant line and the substrate grating

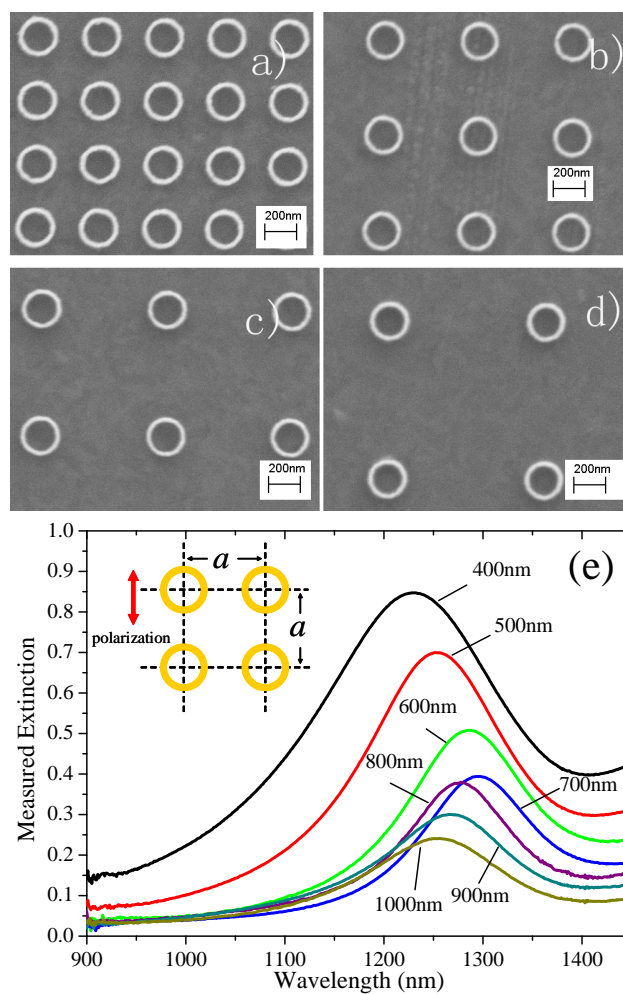


Figure 7.1: The fabricated nanorings and measured extinction spectra. SEM micrographs of fabricated periodic array of gold nanorings with lattice constant equal to (a) 400 nm (b) 600 nm (c) 800 nm and (d) 1000 nm. (e) The selected measured extinction spectra for bare devices of gold nanorings, with a from 400 nm to 1000 nm, in a step of 100 nm.

order is radiative because $a > \lambda_{LSPR}/n_{sub}$. It should be stressed that the resonant lattice constant a_{res} is dependent on the dielectric environment around the nanorings. For bare nanorings in air, $a_{res}^{air} \approx 822$ nm; for devices coated by PMMA, $a_{res}^{PMMA} \approx 1000$ nm (the superscript indicates the dielectric environment). The resonant lattice constant of the coated device is larger than the bare device because the coated device has longer LSPR wavelength so that the LSPR curve crosses the critical grating constant line at a larger lattice constant.

For the different lattice constants investigated, the LSPR peaks of the bare nanorings can be tuned in the range 1180 nm \sim 1295 nm. Certain discontinuities in the λ_{LSPR} curves are due to fabrication uncertainties. In the fabrication process, the exposure dose is increased for larger lattice constants to calibrate for the proximity effects. These discontinuity points in the λ_{LSPR} curves correspond to the lattice constants for which the dose begins to increase. As the lattice constant increases, the LSPR peak wavelength and linewidth are both significantly affected when the substrate grating order is changed from an evanescent nature into a radiative nature. The linewidth fwhm of the bare device in air is plotted as open triangles in Figure 7.2(a). With increasing lattice constant, the linewidth significantly narrows in the range $a \leq a_{res}^{air}$, where the grating order is evanescent; in the range $a \geq a_{res}^{air}$, the grating order is radiative and the linewidth significantly broadens due to radiative damping. The minimum linewidth appears for lattice constant about 70 nm smaller than a_{res}^{air} . By changing the lattice constant, the linewidth of the gold nanorings can be reduced from 0.33 eV to 0.11 eV. These trends of LSPR peak and linewidth are consistent with what have been demonstrated for dipolar interactions of periodic array of metal nanoparticles [20, 21, 31].

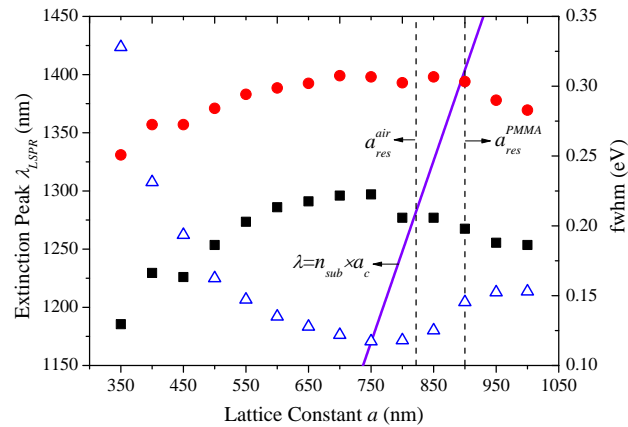
The LSPR peak wavelength shift $\Delta\lambda_{LSPR}$ of the gold nanorings from bare device to PMMA-coated device is plotted against lattice constant a as solid squares in Figure 7.2(b). In the range $a \leq a_{res}^{air}$, $\Delta\lambda_{LSPR}$ decreases with increasing a . The decrease relative to the maximum wavelength shift is about 30%. The reason of the decrease in sensitivity is due to decreased field confinement which will be investigated in detail with the assistance of the numerical calculations later in this article in the discussions section. In the range $a \geq a_{res}^{air}$, $\Delta\lambda_{LSPR}$ significantly increases with increasing a and begins to decrease when a further increases beyond a_{res}^{PMMA} . The increase in the wavelength shift can be understood from the curve of λ_{LSPR} . The maximum red-shift for PMMA-coated device occurs at a_{res}^{PMMA} which is larger than

a_{res}^{air} . As a increases in the range $a_{res}^{air} \leq a \leq a_{res}^{PMMA}$, the LSPR peak of bare device blue-shifts (radiative grating order range) but the LSPR peak of the coated device still red-shifts (evanescent grating order range). As a result, $\Delta\lambda_{LSPR}$ is significantly increased in this range. In the range $a > a_{res}^{PMMA}$, the blue-shift of the coated device is more significant than the bare device and leads to the decreased wavelength shift. This indicates that the sensitivity of the periodic array is significantly affected by the coherent interactions. The shift of LSPR peak in response to the change of dielectric environment is strongly enhanced in the radiative grating order range. The same effects can also be observed from the published experimental studies by Sung et al. on two dimensional periodic array of V-shaped silver nanoparticles, if we consider the peak shift from the device in nitrogen to the device immersed in benzene [22].

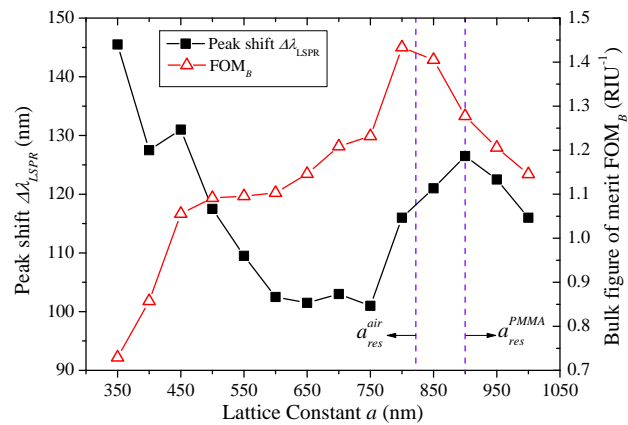
The bulk index sensitivity is defined as $m_B = \delta P_{LSPR} / \delta n_B$, with P_{LSPR} being the LSPR resonance peak either in wavelength unit as λ_{LSPR} or in energy unit as ω_{LSPR} . The bulk index sensing figure of merit is defined as $FOM_B = m_B / \text{fwhm}$, with both m_B and fwhm in energy units [15]. It should be noted that the figure of merit calculated in energy units or wavelength units are approximately equivalent [34]. In our case, we use the LSPR peak shift from bare device to PMMA-coated device to estimate the bulk index sensitivity for the bare device. The FOM_B is shown as open triangles in Figure 7.2(b). Despite the change in sensitivity with lattice constant, the bulk sensing figure of merit is more heavily dependent on the linewidth. When $a \leq a_{res}^{air}$, the FOM_B increases with increasing a due to the peak sharpening effects, even though the peak shift decreases in this range. When $a \geq a_{res}^{air}$, FOM_B decreases with increasing a , due to the broadened line shape regardless of the enhanced wavelength shift in this range. The maximum FOM_B occurs at the lattice constant close to the resonant lattice constant. By changing the lattice constant, the FOM_B can be tuned from 0.73 to 1.43 for gold nanorings. This indicates that for a specific type of metal nanoparticles, the bulk sensing figure of merit of the periodic array is significantly affected by the lattice constant due to coherent interactions.

7.3 Numerical calculations

In order to better investigate the sensing characteristics and to compare the periodic array to a single isolated nanoparticle, we carried out 3D Finite Difference Time Domain (FDTD) simulations incorporating a rectangular non-uniform mesh [35], using



(a)



(b)

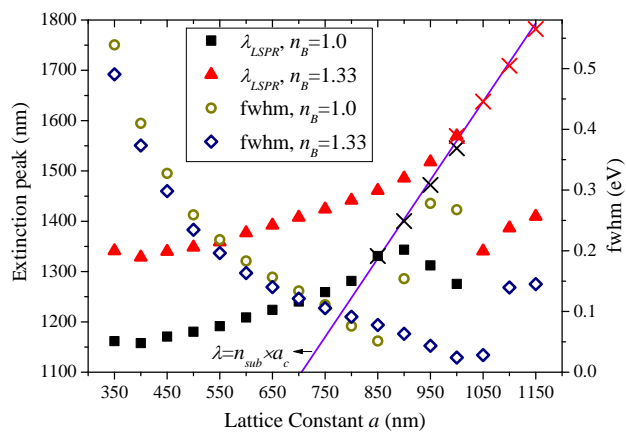
Figure 7.2: The measured spectral and sensing characteristics of periodic array of gold nanorings vs. lattice constant a . (a) The LSPR peaks of bare device (black solid squares), PMMA-coated device (red solid circles) and linewidths of bare device (blue open triangles). The solid line gives the condition for the emergence of the radiative substrate grating order. The vertical dashed lines mark the resonant lattice constant for bare device and coated device respectively. (b) The LSPR peak wavelength shift from bare device to coated device and bulk figure of merit.

a grid size of 4 nm to mesh the gold nanorings region. To simulate a periodic array of nanorings, periodic boundaries were applied in the directions of periodicities, with the lateral size of simulation region equal to the corresponding lattice constant, and Perfectly Matched Layers (PML) were applied to other directions. To simulate a single nanoparticle, PML boundaries were applied to all simulation boundaries.

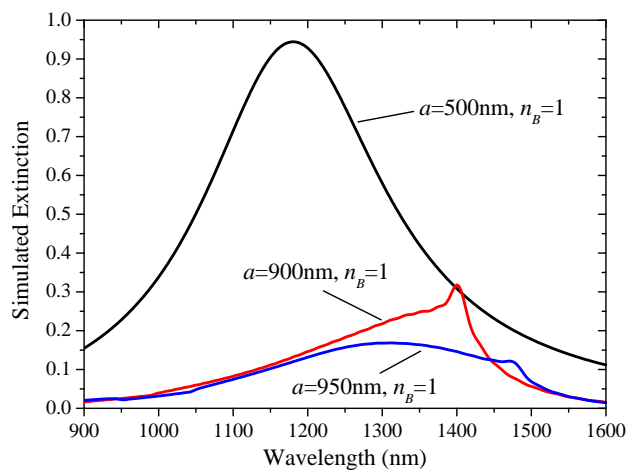
To find the bulk index sensitivity of gold nanorings array, two bulk refractive indices $n_B = 1$ and $n_B = 1.33$ were first simulated, which correspond to the situation of the bare device in air and the device immersed in water respectively. Figure 7.3(a) demonstrates the LSPR peaks (black solid squares for $n_B = 1$ and red solid triangles for $n_B = 1.33$) and linewidth fwhm (yellow open circles for $n_B = 1$ and blue open diamonds for $n_B = 1.33$). The effects of the coherent interactions on the LSPR peaks and the linewidth are consistent with the experimental results. The resonant lattice constant for maxima red-shift is $a_{res}^{air} = 850$ nm for bare device in air and $a_{res}^{water} = 1000$ nm for device in water, respectively. Compared to experimental results, nanorings in the simulations are different in two aspects. Firstly, in simulations, when a is close to or larger than a_{res} , grating-induced modes are observed in the extinction spectra, appearing as a relatively narrow shoulder on the LSPR peak (Figure 7.3(b)). The peaks of grating induced-modes are plotted as crosses in Figure 7.3(a) and they closely follow the line $\lambda = n_{sub} \times a$. Such grating-induced modes have been experimentally demonstrated for visible nanoparticle arrays [30, 31]. However, the grating-induced modes were not observed in our experiments. Unlike the simulated nanorings in perfect infinite arrays, the nanorings in experiments are in semi-infinite arrays with lattice imperfections and size distributions of nanoparticles. Due to the electromagnetic coupling between the inner and outer nanoring walls, the plasmon resonance of individual nanoring is very sensitive to the size of the nanorings [32]. The ITO coating on the surface of the glass used in experiments is frequency dependent and absorptive for infrared spectrum and may reduce the strength of the coherent interactions as well. It should also be noted that in the published experimental studies related to the grating-induced peak [30, 31, 36], the peak is strong and sharp mostly under the index matching condition, which is not the same configuration in our experiments. These effects can possibly prevent the grating-induced modes from being clearly observed in our experiments. It should be noted that the strength of the grating-induced mode is strongly affected by the spectral spacing between LSPR peak and the grating-induced peak [31]. When a is very close to a_{res} , such as for a

= 900 nm and $n_B = 1$ (Figure 7.3(b)), the grating-induced mode dominates in the simulated extinction spectrum. When a is comparatively larger than a_{res} , such as for $a = 950$ nm and $n_B = 1$ (Figure 7.3(b)), the grating-induced mode is much weaker. The LSPR peak in this case dominates in the extinction spectrum. Secondly, the nanorings in simulations are more sensitive to the change of the bulk refractive index. This is mainly due to the structural differences between fabricated and simulated nanorings. The nanorings in simulations have sharp corners both on the top and bottom edges while in the fabricated nanorings, the edges not in contact with substrate are rounded. In addition, the 25 nm thick conductive ITO coating on the substrate used in experiments is absorptive for near-infrared spectrum and has high refractive index, which may possibly reduce the sensitivity [37]. In order to avoid the possible waveguide effects owing to the layered substrate and to guarantee the generality of the conclusions from numerical simulations, the ITO layer in simulations is treated as a 25nm layer of slightly absorbing material with the real part of refractive index equal to the rest of the glass substrate.

To find the bulk index sensitivity around $n_B = 1.0$, simulations were carried out for n_B from 1.00 to 1.04. The bulk sensitivity m_B was then obtained from the slope of the linear regression fits. Similarly, to find the sensitivity around $n_B = 1.33$, simulations were carried out for n_B from 1.33 to 1.37. In addition, to provide more physical insights into the sensitivity dependence, $n_B = 1.1, 1.2$ and 1.3 were also simulated. The simulated response of extinction peaks vs. n_B for each periodic array as well as a single gold nanoring are plotted together in Figure 7.4. In Figure 7.4(a), for $a \leq 800$ nm, no grating-induced mode exists. The response of the array is very linear and similar to that of the single nanoring (the bulk sensing characteristics of a single nanoring is summarized in Table 7.1), except for the slightly decreasing slope with increasing lattice constant. In Figure 7.4(b), for $a = 850, 900$ nm and n_B around 1.0, the grating-induced modes are dominating in the extinction spectra. The bulk sensitivity is very low in this situation because the grating-induced mode is mainly determined by the refractive index of the substrate, approximately given by $n_{sub} \times a$ [31]. This situation suggests that when a dominating grating-induced mode corresponding to the substrate grating order is excited, the sensitivity of the extinction peak will be substantially suppressed. Given sufficiently large n_B , the LSPR peak dominates again and behaves similarly to those shown in Figure 7.4(a). In Figure 7.4(c), for $a = 950, 1000$ nm and n_B around 1.0, the grating-induced mode



(a)



(b)

Figure 7.3: Simulation results for $n_B = 1.0$ and $n_B = 1.33$. (a) The extinction peaks and the fwhm for $n_B = 1.0$ and $n_B = 1.33$. The solid symbols are LSPR peaks, the crosses are grating-induced mode peaks and the open symbols are linewidth fwhm. (b) Examples of simulated extinction spectra.

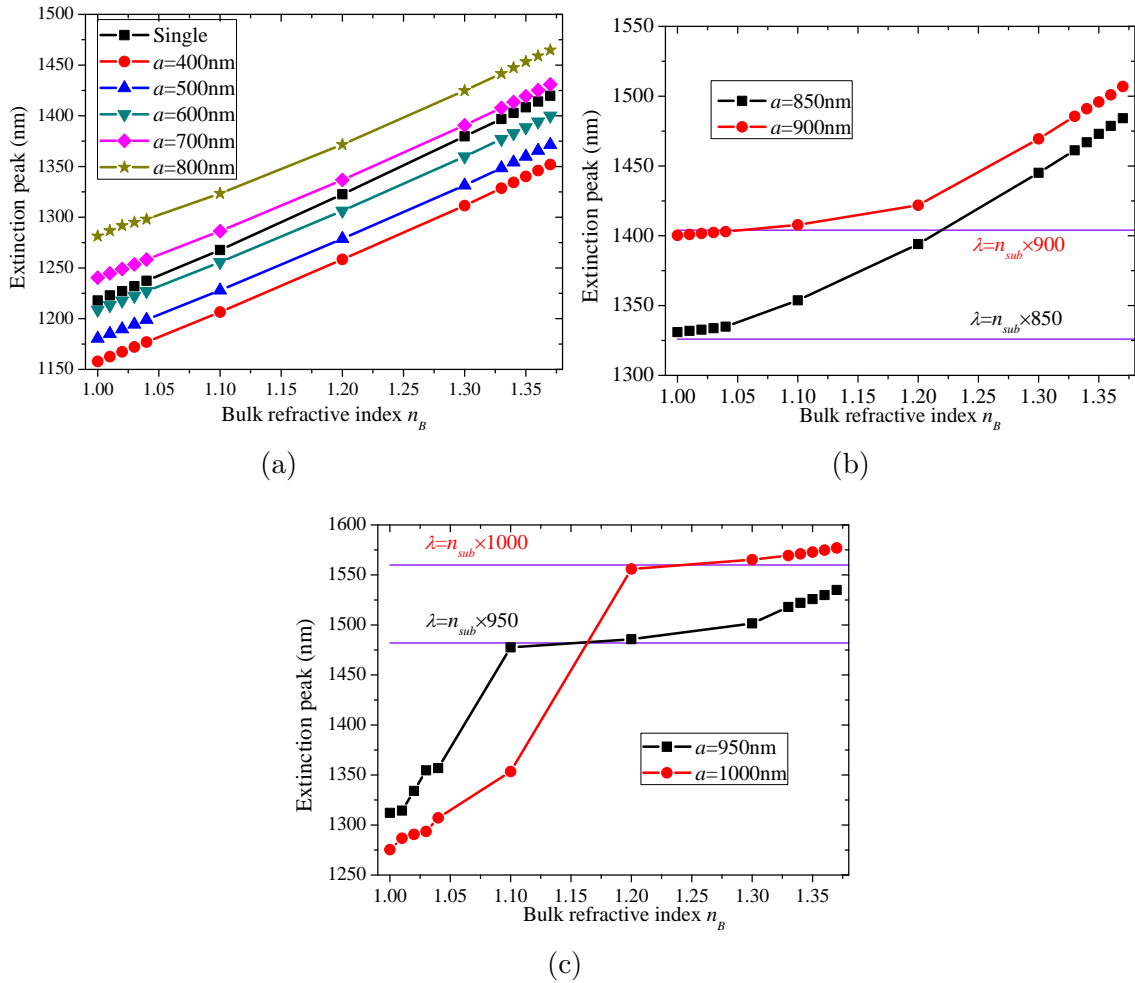


Figure 7.4: The extinction peaks vs. bulk refractive index of (a) the single nanoring and arrays with $a = 400, 500, 600, 700, 800$ nm, (b) arrays with $a = 850, 900$ nm and (c) arrays with $a = 950, 1000$ nm.

is weak and the extinction peak exhibits very high sensitivity within a small range of n_B , which is consistent with the experimental finding of enhanced peak shift in the radiative grating order range.

The calculated bulk sensitivity and bulk figure of merit are shown as solid symbols in Figure 7.5(a) and (b) (open symbols are the cases where grating-induced modes dominate in the extinction spectra). Both the trends are consistent with experimental findings except the strong dip due to the substrate grating-induced mode. Excluding the effects of grating-induced modes, we consider only the sensing characteristics for the points plotted as solid symbols in Figure 7.5(a) and (b). As a

Table 7.1: Simulated spectral and sensing characteristics of a single gold nanoring on substrate

n_B	P_{LSPR}		fwhm		m_B		FOM _B (1/RIU)	m_S (nm/nm)	FOM _S (1/nm)
	nm	eV	nm	eV	nm/RIU	eV/RIU			
1	1218.0	1.0181	326.6	0.3060	480.1	0.3950	1.29	4.531	0.0139
1.33	1396.8	0.8877	387.9	0.2823	637.3	0.3571	1.27	1.471	0.0038

increases in the evanescent grating order range ($a < a_{res}^{air}$ for bare device, $a < a_{res}^{water}$ for device in water), the bulk sensitivity for $n_B = 1.0$ decreases from 503 nm/RIU into 415 nm/RIU and the sensitivity for $n_B = 1.33$ decreases from 603 nm/RIU into 417 nm/RIU. On the contrary, the bulk sensing figure of merit increases due to the narrowing line shape. These are the same trends observed in the experiments for the evanescent grating order range. As a enters the radiative grating order range ($a > a_{res}^{air}$ for bare device, $a > a_{res}^{water}$ for device in water), the bulk sensitivity is higher than the evanescent grating order range. However, the figure of merit in the radiative grating order range is only comparable to that in the evanescent grating order range, due to the significantly broadened line shape in radiative grating order range. It should be emphasized that, the maximum FOM_B achieved for the array is more than three times higher than the single nanoring.

In addition to the sensing characteristics for the bulk index sensing, we also studied the ability of the periodic array to detect the binding of molecules to the surface of gold nanorings. We calculated the surface sensitivity by simulating a very thin dielectric layer with refractive index $n_S = 1.45$ uniformly coated on the surface of gold nanorings. The surface sensitivity is given by $m_S = \delta\lambda_{LSPR}/\delta d_S$, where d_S is the thickness of the coated film on the surface of gold nanoparticles. We simulated $d_S = 0$ nm, 5 nm, 10 nm and 20 nm and m_S was obtained from the slope of linear regression fits. Two different background refractive indices $n_B = 1.0$ and $n_B = 1.33$ were simulated to compare the two most common situations of measuring the dried device in air or measuring the device immersed in solution. The surface sensing figure of merit is expressed as $FOM_S = m_S/\text{fwhm}$, with both m_S and fwhm in wavelength units for convenience [34]. It can be observed that the surface sensing sensitivity and figure of merit follow the same trends as that of the bulk sensing. This finding is further corroborated by the fact that the field decay length calculated from the simulated mode profile shows only small variations with lattice constant. The surface sensitivity and figure of merit for the device in air are more than 3 times higher than in water because the former case provides much larger refractive index contrast between the adsorbate material and the background dielectric environment. The highest surface figure of merit of the periodic array is around 2.5 times higher than the single nanoring given in Table 7.1.

It can be observed that the highest figure of merit of the lattice constant in the evanescent or radiative grating order range are comparable to each other. However,

the lattice constant in the radiative grating order range has several other disadvantages for LSPR sensing applications. Firstly, the extinction spectrum in the radiative grating order range strongly deviates from the Lorentzian curve which will bring additional uncertainties into fitting the data. Secondly, the extinction signal is low due to low density of particles with large particle spacings and will reduce the signal noise ratio. Thirdly, the high sensitivity in radiative grating order range is only available in a small dynamic range when the LSPR peaks are well below the critical grating constant line. Therefore, for the periodic array of metal nanoparticles under coherent interactions through the substrate grating order, the optimum lattice constant for LSPR sensing should be chosen from the highest figure of merit point in the evanescent grating order range. It should be stressed that the optimum lattice constant also depends on the bulk dielectric environment, for example, 750 nm - 800 nm for the bare device in air and 900 nm - 950 nm for the device immersed in water.

7.4 Discussions

Both the simulations and experiments showed that the sensitivity decreases with increasing a in the evanescent grating order range ($a < a_{res}$). However, such a phenomenon is quite different than expected, considering that a larger a in this range gives stronger coherent interactions and a longer resonance wavelength. It can be argued that under the stronger coherent interactions, the almost in-phase additions of scattered light enhances the optical field [21] and should increase the sensitivity. In addition, if we consider the array as a resonant structure on the same substrate, the sensitivity should increase with a longer resonance wavelength [10, 11]. Our hypothesis is that, although the devices are arrays of same nanoparticles located on the same substrate, the optical field confinement and substrate effects for each array are modified by the coherent interactions controlled by the lattice constant. In our case, the substrate effects cannot be evaluated from the contact areas or geometrical relations between nanoparticles and substrates, since this is the same for all configurations. Unger et al. have suggested a confinement factor C to evaluate how strong the electrical field is localized to the sensing region[8]. In our case, the

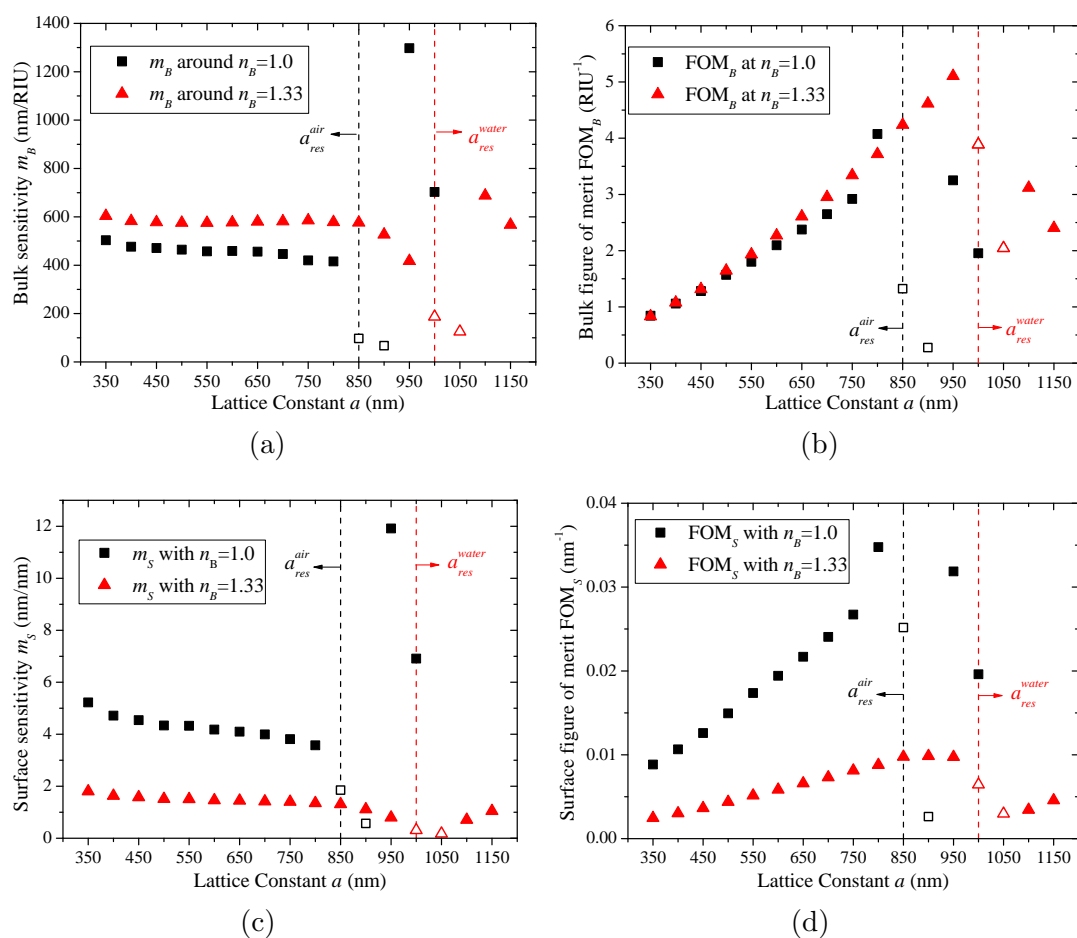


Figure 7.5: The simulated sensing characteristics as a function of lattice constant: (a) bulk sensitivity, (b) bulk sensing figure of merit, (c) surface sensitivity and (d) surface sensing figure of merit. The solid symbols are for the situation where LSPR resonances dominate in the extinction spectra and open symbols for the situation where grating-induced modes dominate. The vertical dashed lines mark the resonant lattice constant for bare device in air and device in water respectively.

confinement factor C can be given by

$$C = \frac{\int_{V_1} n^2 |\vec{E}|^2 dV}{\int_{V_g} \epsilon_{\text{eff}} |\vec{E}|^2 dV + \int_{V_{\text{sub}}} n_{\text{sub}}^2 |\vec{E}|^2 dV + \int_{V_1} n^2 |\vec{E}|^2 dV} \quad (7.1)$$

where V_1 is the sensing region (the region above the substrate where the analyte occupies), V_g is the volume of gold and V_{sub} is the substrate region. The integration is performed on the electric field mode profile of a unit cell of the simulation. In order to calculate the near-field effects, only electric field with enhancement larger than 2 is taken into the integral and the radiating field is neglected [8].

The confinement factor given in Equation 7.1 can also be interpreted as electromagnetic field energy in the sensing region divided by the energy in all space. Referring to the electromagnetic energy density in a dispersive and absorptive material with complex refractive index $n'(\omega) + i\kappa(\omega)$ [38], the effective dielectric constant ϵ_{eff} in our calculation is given as

$$\epsilon_{\text{eff}} = n'^2 + \frac{2\omega n' \kappa}{\Gamma_e} \quad (7.2)$$

where Γ_e is the damping coefficient in the Drude model ($\Gamma_e = 0.0257$ eV, as determined by fitting material optical constants into the Drude model).

The calculated confinement factor C for $n_B = 1.0$ and $n_B = 1.33$ are shown in Figure 7.6. Compared to the sensitivity curve in Figure 7.5(a) and (c), in the evanescent grating order range ($a < a_{\text{res}}^{\text{air}}$ for bare device, $a < a_{\text{res}}^{\text{water}}$ for device in water), confinement factor follows the smoothly decreasing trend of sensitivity except the strongly suppressed sensitivity owing to the substrate grating-induced modes. As a increases, the confinement factor indicates the proportion of electromagnetic energy confined in the sensing region decreases, caused by the coherent interactions of the periodic array. As a increases in this range, the optical field within the substrate is greatly enhanced due to the almost in-phase additions of scattered light carried by the substrate grating order. In comparison, the optical field in the sensing region is not as much affected. The overall effect is significantly reduced field confinement factor which indicates enhanced substrate effects. Therefore, as the lattice constant increases in the evanescent grating order range, the growing coherent interactions lead to decreased sensitivity. It should be stressed that the confinement factor is

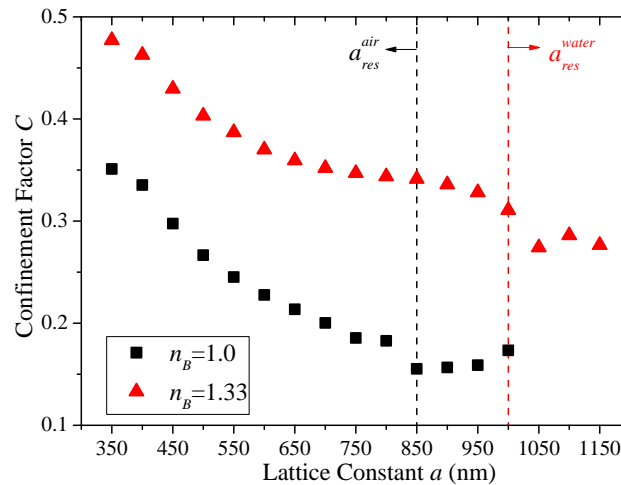


Figure 7.6: The calculated confinement factor vs. lattice constant a . The vertical dashed lines mark the resonant lattice constant for bare device in air and device in water respectively.

only strictly defined for a small perturbation of the sensing region [8]. Therefore, it can only provide qualitative analysis of the sensitivity in our study. The enhanced sensitivity in the radiative grating order range ($a > a_{res}^{air}$ for bare device, $a > a_{res}^{water}$ for device in water) cannot be observed from the curves of C because the calculation considered only near-field and neglected the radiating field. The physical origins for this enhanced sensitivity are probably related to the radiative nature of the grating order and require further investigations.

Compared to other experimental studies, Larsson et al. [13] have studied the LSPR sensor based on randomly distributed ensemble of gold nanorings with bulk figure of merit ~ 2 and bulk sensitivity up to 880 nm/RIU. In our experiments on gold nanorings, the highest bulk figure of merit is 1.43, which is lower than the reported value. It should be noted that the estimated bulk sensitivity of our nanoring is less than 300 nm/RIU which is much lower than the reported sensitivity. This low sensitivity is not due to the array effects but rather due to the structural features (smooth rounded profile on the top edges) of our fabricated nanorings and the high refractive index ITO conductive coating on the glass substrate. The importance of our experimental results is that a good figure of merit can be achieved from an optimized periodic array consisted of nanoparticles of medium sensitivity. The simulation has predicted a bulk sensing figure of merit at least 3 times higher than the single nanoring and surface sensing figure of merit around 2.5 times higher than the single nanoring.

It should be pointed out that, besides the dipolar mode of the gold nanorings, we have also studied the multipolar mode of split gold nanorings. According to our study in experiments and simulations, we found that the multipolar resonance of split nanorings follows the same trend as the dipolar resonance of gold nanorings. In comparison, the split nanorings demonstrate better sensing characteristics than closed nanorings. This implies that the theories of the periodic effects on the dipolar interactions of metal nanoparticles can be extended to higher order plasmon resonances as long as the interactions are coherent in nature.

7.5 Conclusions

According to our study, patterning the gold nanoparticles into a periodic array is an effective strategy to improve the sensing figure of merit. The improvement is mainly obtained from the controllable narrow spectral linewidth due to coherent interactions of the periodic array. The optimum lattice configuration as discussed, is the lattice constant with the highest figure of merit in the evanescent grating order range. The simulation shows the bulk sensing figure of merit of the array can be three times higher than the single nanoring and the surface sensing figure of merit can be 2.5 times higher than the single nanoring.

In the evanescent grating order range, as the lattice constant increases, the figure of merit increases due to significantly reduced linewidth. The sensitivity decreases with increasing lattice constant because the coherent interactions cause the optical field confinement in the sensing region to decrease. In the radiative grating order range, as lattice constant increases, the figure of merit decreases due to the radiative damping. In this range, the device has very high sensitivity but it has been discussed to be disadvantageous for LSPR sensor applications.

The grating-induced modes, corresponding to the substrate grating order, were observed in simulations but not in experiments. Since the grating-induced peaks are mainly determined by the refractive index of the substrate, its sensitivity is very low. The consequence is strongly suppressed sensitivity and very low figure of merit when this grating-induced mode dominates in the extinction spectra.

7.6 Acknowledgements

The authors acknowledge Natural Sciences and Engineering Research Council of Canada (NSERC), CMC Microsystems and Canada Foundation for Innovation (CFI) for funding this research work. The device fabrication was done at the University of Western Ontario Nanofabrication facility. The simulations were carried out using SHARCNET computing facilities. The authors acknowledge student funding for Hao Jiang from BiopSys (NSERC Network Centers for Excellence) grant.

References

- [1] K. A. Willets and R. P. Van Duyne, “Localized surface plasmon resonance spectroscopy and sensing,” *Annu. Rev. Phys. Chem.*, vol. 58, pp. 267–297, 2007.
- [2] J. N. Anker, W. P. Hall, O. Lyandres, N. C. Shah, J. Zhao, and R. P. Van Duyne, “Biosensing with plasmonic nanosensors,” *Nature Materials*, vol. 7, pp. 442–453, 2008.
- [3] P. Englebienne, “Use of colloidal gold surface plasmon resonance peak shift to infer affinity constants from the interactions between protein antigens and antibodies specific for single or multiple epitopes,” *the Analyst*, vol. 123, pp. 1599–1603, 1998.
- [4] A. D. McFarland and R. P. Van Duyne, “Single silver nanoparticles as real-time optical sensors with zeptomole sensitivity,” *Nano Letters*, vol. 3, no. 8, pp. 1057–1062, 2003.
- [5] A. J. Haes and R. P. Van Duyne, “A nanoscale optical biosensor: Sensitivity and selectivity of an approach based on the localized surface plasmon resonance spectroscopy of triangular silver nanoparticles,” *Journal of the American Chemical Society*, vol. 124, no. 35, pp. 10 596–10 604, 2002.
- [6] G. Raschke, S. Kowarik, T. Franzl, C. Sonnichsen, T. A. Klar, J. Feldmann, A. Nichtl, and K. Kurzinger, “Biomolecular recognition based on single gold nanoparticle light scattering,” *Nano Letters*, vol. 3, no. 7, pp. 935–938, 2003.
- [7] H. Jiang, J. Markowski, and J. Sabarinathan, “Near-infrared optical response of thin film pH-sensitive hydrogel coated on a gold nanocrescent array,” *Optics Express*, vol. 17, no. 24, pp. 21 802–21 807, 2009.
- [8] A. Unger and M. Kreiter, “Analyzing the performance of plasmonic resonators for dielectric sensing,” *J. Phys. Chem. C*, vol. 113, pp. 12 243–12 251, 2009.

- [9] G. J. Nusz, A. C. Curry, S. M. Marinakos, A. Wax, and A. Chilkoti, “Rational selection of gold nanorod geometry for label-free plasmonic biosensors,” *ACS Nano*, vol. 3, no. 4, pp. 795–806, 2009.
- [10] M. M. Miller and A. A. Lazarides, “Sensitivity of metal nanoparticle surface plasmon resonance to the dielectric environment,” *J. Phys. Chem. B*, vol. 109, pp. 21 556–21 565, 2005.
- [11] R. Bukasov and J. S. Shumaker-Parry, “Highly tunable infrared extinction properties of gold nanocrescents,” *Nano Letters*, vol. 7, no. 5, pp. 1113–1118, 2007.
- [12] A. Dmitriev, C. Hagglund, S. Chen, H. Fredriksson, T. Pakizeh, M. Kall, and D. S. Sutherland, “Enhanced nanoplasmonic optical sensors with reduced substrate effect,” *Nano Letters*, vol. 8, no. 11, pp. 3893–3898, 2008.
- [13] E. M. Larsson, J. Alegret, M. Kall, and D. S. Sutherland, “Sensing characteristics of NIR localized surface plasmon resonances in gold nanorings for application as ultrasensitive biosensors,” *Nano Letters*, vol. 7, no. 5, pp. 1256–1263, 2007.
- [14] C. Novo, A. M. Funston, I. Pastoriza-Santos, L. M. Liz-Marzan, and P. Mulvaney, “Influence of medium refractive index on the optical properties of single gold triangular prisms on a substrate,” *J. Phys. Chem. C*, vol. 112, no. 1, pp. 3–7, 2008.
- [15] L. J. Sherry, S.-H. Chang, G. C. Schatz, R. P. Van Duyne, B. J. Wiley, and Y. Xia, “Localized surface plasmon resonance spectroscopy of single silver nanocubes,” *Nano Letters*, vol. 5, no. 10, pp. 2034–2038, 2005.
- [16] W. A. Murray, B. Auguie, and W. L. Barnes, “Sensitivity of localized surface plasmon resonances to bulk and local changes in the optical environment,” *J. Phys. Chem. C*, vol. 113, pp. 5120–5125, 2009.
- [17] L. J. Sherry, R. Jin, C. A. Mirkin, G. C. Schatz, and R. P. Van Duyne, “Localized surface plasmon resonance spectroscopy of single silver triangular nanoprisms,” *Nano Letters*, vol. 6, no. 9, pp. 2060–2065, 2006.
- [18] M. Retsch, M. Tamm, N. Bocchio, N. Horn, R. Forch, U. Jonas, and M. Kreiter, “Parallel preparation of densely packed arrays of 150-nm gold-nanocrescent resonators in three dimensions,” *Small*, vol. 5, no. 18, pp. 2105–2110, 2009.

- [19] S. Kim, J.-M. Jung, D.-G. Choi, H.-T. Jung, and S.-M. Yang, "Patterned arrays of Au rings for localized surface plasmon resonance," *Langmuir*, vol. 22, pp. 7109–7112, 2006.
- [20] M. Meier, A. Wokaun, and P. F. Liao, "Enhanced fields on rough surfaces: dipolar interactions among particles of sizes exceeding the Rayleigh limit," *J. Opt. Soc. Am. B*, vol. 2, no. 6, pp. 931–949, 1985.
- [21] B. Lamprecht, G. Schider, R. T. Lechner, H. Ditlbacher, J. R. Krenn, A. Leitner, and F. R. Aussenegg, "Metal nanoparticle gratings: influence of dipolar particle interaction on the plasmon resonance," *Phys. Rev. Lett.*, vol. 84, no. 20, pp. 4721–4724, 2000.
- [22] J. Sung, E. M. Hicks, R. P. Van Duyne, and K. G. Spears, "Nanosphere spectroscopy: dipole coupling in two-dimensional arrays of L-shaped silver nanoparticles," *J. Phys. Chem. C*, vol. 111, pp. 10 368–10 376, 2007.
- [23] J. Sung, E. M. Hicks, R. P. Van Duyne, and K. G. Spears, "Nanoparticle spectroscopy: plasmon coupling in finite-sized two-dimensional arrays of cylindrical silver nanoparticles," *The Journal of Physical Chemistry C*, vol. 112, no. 11, pp. 4091–4096, 2008.
- [24] C. L. Haynes, A. D. McFarland, L. Zhao, R. P. Van Duyne, G. C. Schatz, L. Gunnarsson, J. Prikulis, B. Kasemo, and M. Kall, "Nanoparticle optics: The importance of radiative dipole coupling in two-dimensional nanoparticle arrays," *J. Phys. Chem. B*, vol. 107, pp. 7337–7342, 2003.
- [25] S. Linden, A. Christ, J. Kuhl, and H. Giessen, "Selective suppression of extinction within the plasmon resonance of gold nanoparticles," *Appl. Phys. B*, vol. 73, pp. 311–316, 2001.
- [26] S. Linden, J. Kuhl, and H. Giessen, "Controlling the interaction between light and gold nanoparticles: selective suppression of extinction," *Phys. Rev. Lett.*, vol. 86, no. 20, pp. 4688–4691, 2001.
- [27] S. Malynych and G. Chumanov, "Light-induced coherent interactions between silver nanoparticles in two-dimensional arrays," *J. Am. Chem. Soc.*, vol. 125, pp. 2896–2898, 2003.

- [28] S. Zou, N. Janel, and G. C. Schatz, "Silver nanoparticle array structures that produce remarkably narrow plasmon lineshapes," *J. Chem. Phys.*, vol. 120, no. 23, pp. 10 871–10 875, 2004.
- [29] S. Zou and G. C. Schatz, "Narrow plasmonic/photonic extinction and scattering line shapes for one and two dimensional silver nanoparticle arrays," *J. Chem. Phys.*, vol. 121, no. 24, pp. 12 606–12 612, 2004.
- [30] E. M. Hicks, S. Zou, G. C. Schatz, K. G. Spears, R. P. Van Duyne, L. Gunnarsson, T. Rindzevicius, B. Kasemo, and M. Kall, "Controlling plasmon line shapes through diffractive coupling in linear arrays of cylindrical nanoparticles fabricated by electron beam lithography," *Nano Letters*, vol. 5, no. 6, pp. 1065–1070, 2005.
- [31] N. Felidj, G. Laurent, J. Aubard, G. Levi, A. Hohenau, J. R. Krenn, and F. R. Aussenegg, "Grating-induced plasmon mode in gold nanoparticle arrays," *J. Chem. Phys.*, vol. 123, p. 221103, 2005.
- [32] J. Aizpurua, P. Hanarp, D. S. Sutherland, M. Kall, G. W. Bryant, and F. J. Garcia de Abajo, "Optical properties of gold nanorings," *Phys. Rev. Lett.*, vol. 90, no. 5, p. 057401, 2003.
- [33] S. D. Liu, Z. S. Zhang, and Q. Q. Wang, "High sensitivity and large field enhancement of symmetry broken Au nanorings: effect of multipolar plasmon resonance and propagation," *Optics Express*, vol. 17, no. 4, pp. 2906–2917, 2009.
- [34] M. A. Otte, B. Sepulveda, W. Ni, J. P. Juste, L. M. Liz-Marzan, and L. M. Lechuga, "Identification of the optimal spectral region for plasmonic and nanoplasmonic sensing," *ACS Nano*, vol. 4, no. 1, pp. 349–357, 2010.
- [35] H. Jiang, J. Sabarinathan, T. Manifar, and S. Mittler, "3-D FDTD analysis of gold-nanoparticle-based photoniccrystal on slab waveguide," *J. Lightwave Technol.*, vol. 27, no. 13, pp. 2264–2270, 2009.
- [36] B. Auguie and W. L. Barnes, "Diffractive coupling in gold nanoparticle arrays and the effect of disorder," *Optics Letters*, vol. 34, no. 4, pp. 401–403, 2009.

- [37] M. D. Malinsky, K. L. Kelly, G. C. Schatz, and R. P. Van Duyne, “Nanosphere lithography: effect of substrate on the localized surface plasmon resonance spectrum of silver nanoparticles,” *J. Phys. Chem. B*, vol. 105, pp. 2343–2350, 2001.
- [38] R. Ruppin, “Electromagnetic energy density in a dispersive and absorptive material,” *Physics Letters A*, vol. 299, pp. 309–312, 2002.

Chapter 8

A Nanoplasmonic Sensor based on Gold Nanoring Arrays Operating in the Optical Communication Window ¹

8.1 Introduction

Gold nanorings have been demonstrated with unique nano-optical properties [1]. Due to the strong electromagnetic coupling between inner and outer ring walls, the localized surface plasmon resonance (LSPR) of gold nanorings can be tuned into the infrared spectral range by changing the ratio of ring thickness to its radius, providing an effective platform for studying the strong electromagnetic field confinement and enhancement in the near-infrared range. Compared to other near-infrared candidates such as gold nanoshells [2], gold nanorings are advantageous as being vacant in the 'hot spot' surrounded by the inner walls, thus accessible by the analytes of interest. These features make gold nanorings promising candidates in several fast developing research areas, including highly sensitive nanoplasmonic sensing [3–6] and surface enhanced near-infrared Raman spectroscopy [7].

Towards plasmonic sensing applications, in order to reach a better limit of detection, the essential target is to increase the sensitivity and to reduce the uncertainty in determining the resonance position [8, 9]. The sensitivity is affected by nanoparticle compositions, sizes, geometries, and substrate effects [3, 10–13]. The uncertainty is related to the signal noise ratio of the instruments and the extinction peak linewidth, the latter of which could be effectively reduced by coherent interactions in a periodic array [14–18].

1. A version of this chapter has been submitted for publication. H. Jiang, J. Sabarinathan, T. Li, J. Yang and S. Mittler submitted to *Journal of Physical Chemistry C*, 10/05/2011

In our previous theoretical studies of periodic array of gold nanorings [6], we found that as the lattice constant increases in the evanescent grating order range, the LSPR peak significantly sharpens and the sensing figure of merit of the array is greatly improved. The highest figure of merit of the periodic array could be three times higher than the single nanoring. In addition, the LSPR peak wavelength was found to be tunable over a large spectral range and the sensitivity was found to decrease abnormally when the grating-induced modes begin to take effect. All these tendencies make it possible to produce a nanoplasmonic sensor based on periodic array functioning in desired spectral range with high figure of merit.

From engineering point of view, in order to reduce the signal to noise ratio in the detection setup, a functioning spectral window has to be first determined with appropriate light source, passive optical components, photodetectors. Due to the mature technologies developed for the fiber-optic communication, the spectral range falling in the optical communication window is advantageous. In addition, the water shows several strong absorption peaks in the near-infrared range at 1200 nm, 1450 nm and 1950 nm. These wavelength should be avoided to minimize the effect of water absorption in detection. We proposed a detection scheme based on tunable laser functioning in the range 1460 nm - 1610 nm and InGaAs photodetectors. Compared to the broadband light source, the laser has stable output with coherent and high intensity light which could be directly coupled into the single mode fiber designed for optical communication. The tunable laser also makes it possible to acquire a very high resolution spectrum in seconds which is required for studying the binding kinetics of biomolecules. In addition, various high performance passive and active optical components are also commercially available in this range.

In the following, we carried out experiments and simulations to study the periodic array of gold nanorings lithographically patterned on pyrex substrate. The dependence of the extinction peak, peak linewidth, sensitivity and figure of merit on the lattice constant denoted as ' a ' will be investigated in detail to optimize the sensor performance for the proposed spectral range 1460 nm - 1610 nm. A biosensing application with the optimized sensor configuration has also been demonstrated.

8.2 Research methods

8.2.1 Sample fabrication and measurement

The gold nanorings arrays in square lattice were fabricated on pyrex substrates by electron beam lithography (EBL) technique for its ability to precisely control the geometry and position of each nanoring at the same time. The challenge is that the non-conductive glass substrate has to be made conductive for EBL purpose. In our previous study [6], we introduced a 25 nm thick indium tin oxide (ITO) conductive layer on top of the glass, however, this layer was found to decrease the sensor sensitivity by more than 30%, probably due to its lossy nature in the near-infrared spectral range. In this study, the problem was overcome by depositing a chromium sacrificial layer on top of the photoresist prior to the EBL. The detailed fabrication procedures were schematically described in Figure 8.1(a). After the pyrex substrate was thoroughly cleaned, 300 nm thick photoresist (ZEP520A, ZEON Corporation) was first spin-coated on top. A 20 nm thick chromium was then deposited on top of the photoresist by sputtering deposition technique to make the substrate conductive. Patterns of nanorings arrays, accurately controlled by the EBL system, were then exposed onto the photoresist. After EBL, the chromium layer was first removed by chromium etchant (Cr etchant 1020, Transene Company Inc) followed by developing the photoresist in amyl acetate for 180 seconds. After developing the photoresist, 2 nm chromium and 50 nm gold were sequentially deposited on the patterned photoresist by electron beam evaporation deposition. Finally a lift-off process of the sample immersed into N-methyl-2-pyrrolidone solvent yielded the periodic array of gold nanorings on the pyrex substrate. It should be noted that, the photoresist is very sensitive to the high-temperature plasmons generated in the sputtering deposition, even for a short deposition time. As a result, the EBL exposure dose has to be well calibrated by considering both the proximity effects which are different for each unique lattice configuration and the background exposure from sputtering deposition. Through dose tests, the exposure line dose was determined to be exponentially increasing from 0.11 nC/cm into 0.12 nC/cm for the lattice constant varying from 600 nm to 1100 nm.

The scanning electron microscope (SEM) images of the fabricated structures are presented in Figure 8.1(b). The geometries of the fabricated nanorings were acquired from each images by using an image processing program. The center diameters of fab-

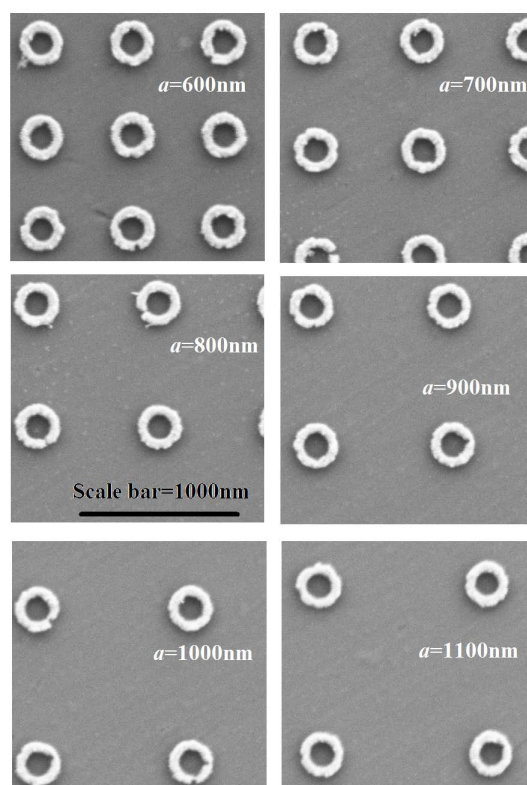
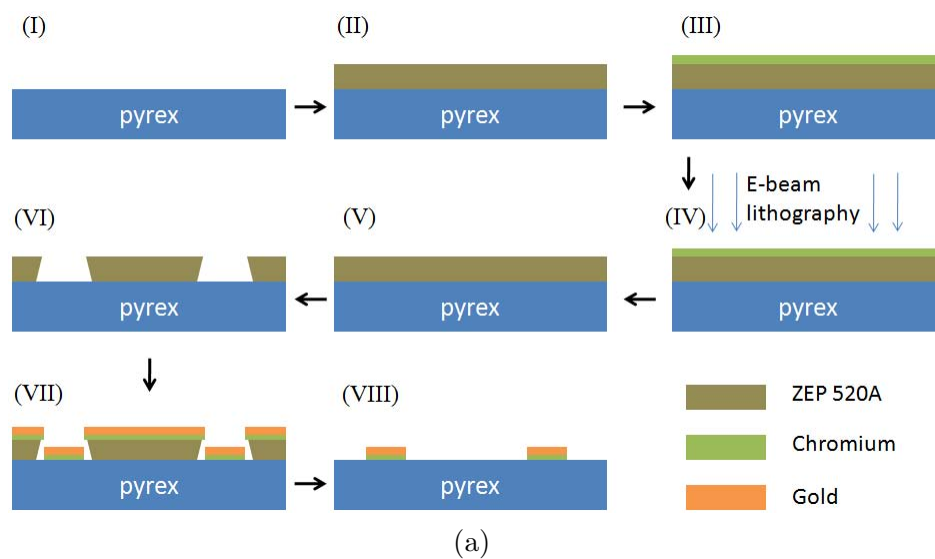
ricated nanorings were measured to be approximately 235 nm and the wall thickness were found to be around 59 nm with a standard deviation around 2.5 nm.

The fabricated device was integrated with a transparent flow cell for conveniently introducing chemical solutions into the device. The flow cell was constructed by sealing the sensor device (on pyrex substrate) with a cover glass (soda-lime microscope slide) on top (Figure Figure 8.2). Glasses were used on both sides for their great optical quality in terms of transmission in the near-infrared spectral range. In comparison, the widely used PDMS fluidic channels suffer from strong optical absorption in this range and were therefore not feasible for this work. The sensor device and the cover glass were sealed by a 500 μm thick silicone isolator film between them. The soft silicone film, with predefined fluidic channel patterns, seals the two glasses by applying a mild mechanical pressure. Ports were mechanically drilled through the cover glass as inlets and outlets for the fluids. In order to seal each port, one small piece of transparent PDMS film was permanently bonded to the cover glass at an elevated temperature following an UV ozone treatment. The steel injection tubes were then inserted through the PDMS, through the ports and into the fluidic channel. This method provides a tightly sealed fluidic channel for the sensor device, with great optical transparency in the near-infrared spectral range. In addition, since no glue was involved in the construction of the flow cell, the possibility of the diffused glue contaminating the sensor surface was completely avoided.

The extinction spectra of each device were measured by the transmission of linearly polarized near-infrared broadband light (1100 nm - 1700 nm) focused by a 10X objective (NA=0.25) onto the device surface positioned perpendicular to the beam. The beam size to interrogate the device is around 40 μm \times 40 μm , which is much smaller than the device in order to eliminate edge effects. The transmitted light was collected by a 20X objective (NA=0.2, working distance=20 mm), coupled into a 0.8 m spectrograph and analyzed by an InGaAs detector. The extinction spectrum was calculated by $Ext(\lambda) = 1 - I_{dev}(\lambda)/I_{ref}(\lambda)$, with $I_{dev}(\lambda)$ being light transmitted through nanoparticles and $I_{ref}(\lambda)$ being the reference spectrum.

8.2.2 Numerical simulations

3-D Finite Difference Time Domain (FDTD) simulations were carried out to simulate the nanorings arrays. Periodic boundaries were applied in the directions of period-



(b)

Figure 8.1: Fabrication of the gold nanorings on pyrex substrate. (a) schematic of the fabrication process, (b) SEM images of the fabricated nanorings with lattice constant from 600 nm to 1100 nm, after the sample being coated by a 3 nm Osmium for imaging purpose.

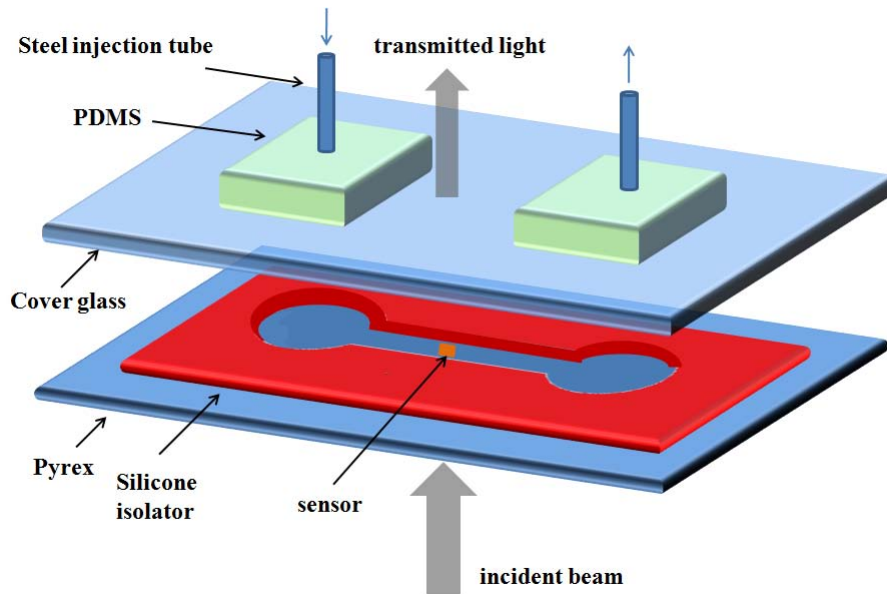


Figure 8.2: Construction of transparent flow cell for near-infrared transmission measurement.

iciencies, with the lateral size of simulation region equal to the corresponding lattice constant, and Perfectly Matched Layers (PML) were applied onto other directions. A non-uniform mesh configuration was implemented with a grid size of 4nm to mesh the gold nanorings [19]. A plane wave source was excited and propagated perpendicular to the plane of periodicity. The transmitted power through the nanorings was recorded by the power monitor. It should be emphasized that the FDTD model with periodic boundaries actually simulates a perfectly infinite-sized periodic array of exactly identical nanorings. In comparison, the fabricated structures were finite-sized periodic array, with inevitable minor lattice dislocations and variations of individual nanoring. To simulate the real fabricated structures in FDTD would become impractical as the computational intensity will abruptly increase with the number of nanorings in the simulation region.

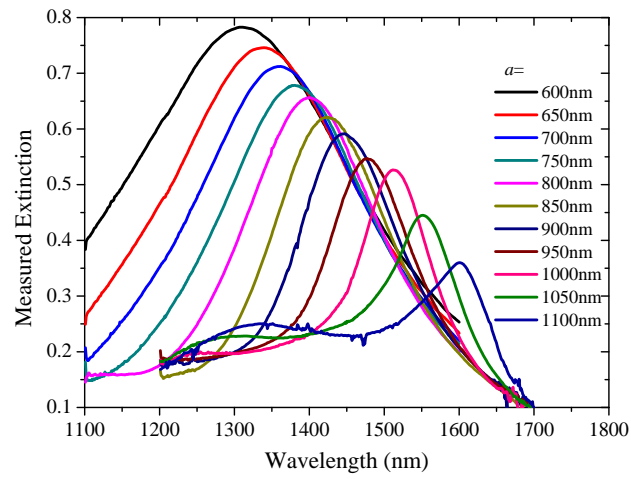
8.3 Results and discussions

The measured and simulated extinction spectra of the periodic array in water were plotted in Figure 8.3 for lattice constant from 600 nm to 1100 nm. The measured spectra matched well with the simulated ones. The characteristics of the extinction

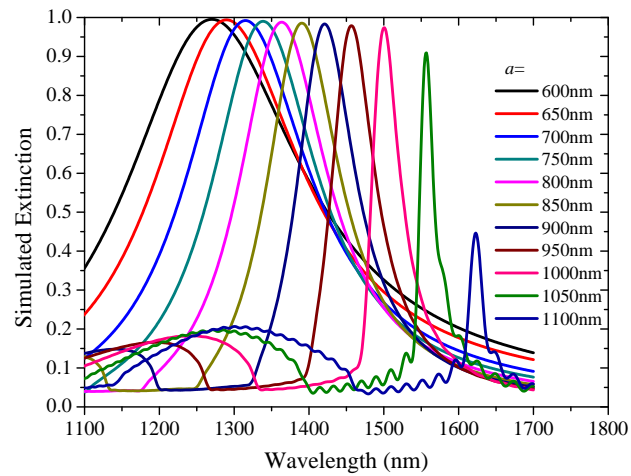
peaks, including peak wavelength λ_{LSPR} and peak linewidth fwhm (full width half maximum), were acquired from the extinction spectra and plotted in Figure 8.4. As the lattice constant increases, the peak significantly red-shifts and narrows, due to the coherent interactions of the periodic array through substrate grating order. This trend is consistent with previous studies [6, 14, 15] for the lattice constant in the evanescent grating order range, i.e. $a < a_{res}$, where a_{res} is the lattice constant for the maximal red-shift, approximately determined from the crossing point of the curve $\lambda_{LSPR}(a)$ and the critical grating constant line defined by $\lambda(a) = n_{sub} \times a$, where n_{sub} is the refractive index of the substrate.

According to our previous study [6], the radiative grating order range, $a > a_{res}$, is not appropriate for the sensor applications due to the complicated extinction spectral shape and nonlinear response vs. refractive index. In addition, the optimized lattice constant should lie in the range smaller than and close to a_{res} [6]. Therefore, in the experiment, only the lattice constant from 600 nm to 1100 nm was investigated for optimizing the sensor in the desired spectral range. By comparing the simulation and experiment results, it can be clearly seen that the measured extinction peak is broader and the measured extinction amplitude is smaller, than the simulated one. This is due to the uncertainty in the fabrication, which leads to the imperfect geometry of the fabricated nanorings and reduces the strength of the coherent interactions. This phenomenon has also been reported by Hicks et al. [20] for the one dimensional periodic array of silver nanoparticles.

In the experimental results, the peak red-shifts from 1310 nm into 1600 nm and the peak linewidth fwhm decreases from 384 nm into 78 nm. This wide range tuning capability made the nanorings array it possible for the nanoring to operate within the proposed spectral range, given an appropriate lattice constant. For the wavelength-shift interrogation, at least the portion of the extinction spectra above half-maximum should be interrogated, in order to determine the extinction peak wavelength by fitting the spectrum into a Lorentz curve. This interrogation spectral range can be defined as $\lambda_{LSPR} - fwhm/2 < \lambda < \lambda_{LSPR} + fwhm/2$, for a given lattice constant. The curve of measured extinction peak λ_{LSPR} , $\lambda_{LSPR} - fwhm/2$ and $\lambda_{LSPR} + fwhm/2$ as a function of lattice constant are plotted in Figure 8.5 as solid black, blue and red lines, respectively. For wavelength-shift interrogation, the detection system should cover at least the spectral range given between the blue and red lines, for each given lattice constant. The proposed spectral range 1460 nm - 1610



(a)



(b)

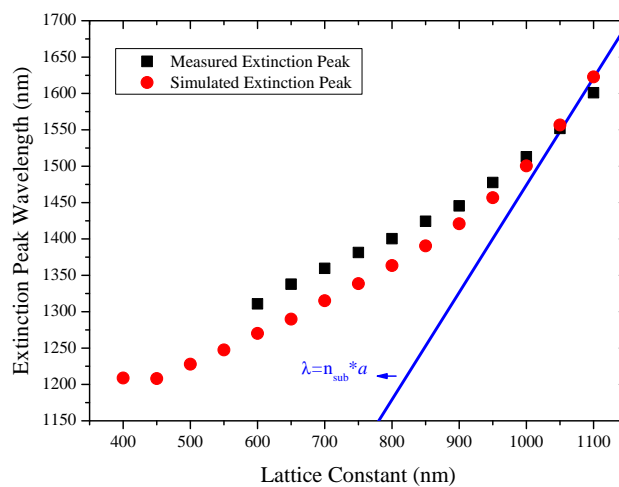
Figure 8.3: The extinction spectra of the structures of different lattice constants in water: (a) experimental results, (b) simulation results.

nm was marked as a gray shadow region in Figure 8.5. It can be determined that the lattice constants $1000 \text{ nm} < a < 1060 \text{ nm}$, marked as the green shadow region, can satisfy the aforementioned requirements to interrogate the wavelength-shift of the sensor in the proposed spectral range.

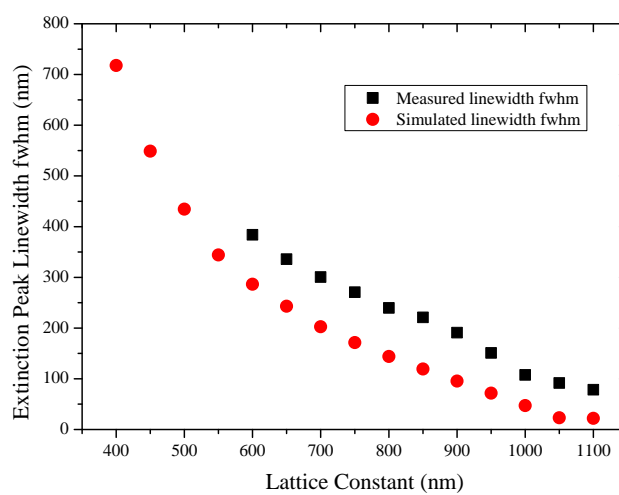
Since the function of the label-free nanoplasmonic sensor is based on detecting the change of the refractive index very close to the surface of the nanoparticles, it is important to find the bulk index sensitivity, defined as $m_B = \delta\lambda_{LSPR}/\delta n_B$, with n_B being the bulk refractive index. The relevant bulk index sensing figure of merit is defined as $FOM_B = m_B/\text{fwhm}$. It should be noted that the figure of merit calculated in energy units or wavelength units are approximately equivalent [21]. For the sake of brevity, wavelength units are used in this work. In order to measure the bulk index sensitivity, water and IPA mixtures in different ratios were injected into the sensor to induce a change of n_B . The extinction peak of each refractive index was measured and the sensitivity was determined from the slope of linear fit of λ_{LSPR} vs. n_B . Similarly, in FDTD simulations, $n_B = 1.33, 1.35, 1.37$ were simulated for each structure to find the sensitivity of nanorings array in a water background.

The measured and simulated bulk index sensitivity and figure of merit were presented in Figure 8.6. There are errors in the measured sensitivity because the refractive index of the water/IPA mixtures were only able to be calibrated at 589 nm wavelength, which is not very accurate for the near-infrared spectral range of interest. The measured sensitivity curve matched well with simulated one in the range $a \leq 900$ nm. However, for $a > 900$ nm, as a increases, the measured sensitivity decreases by a much smaller amount than the simulated ones. According to our previous theoretical studies [6], the abnormal decrease of the sensitivity is due to the strong coherent interaction of the periodic array. For a close to a_{res} , this coherent interaction greatly enhanced the electromagnetic field within the substrate, leading to a decreased field confinement within the sensing region. Therefore, it could be reasoned that this decrease of sensitivity in experiment would not be as obvious because the fabricated nanorings were not exactly identical, which reduces the coherency of the interaction of the array.

Despite the change in sensitivity with lattice constant, the bulk sensing figure of merit is more heavily dependent on the linewidth. As a increases, the FOM_B increases, primarily due to the peak sharpening effects. By changing the lattice constant, the measured FOM_B can be tuned from 1.4 into 5.1. The differences between



(a)



(b)

Figure 8.4: The characteristics of the extinction peaks of measured and simulated spectra under water background: (a) extinction peak wavelength λ_{LSPR} , (b) extinction peak linewidth fwhm.

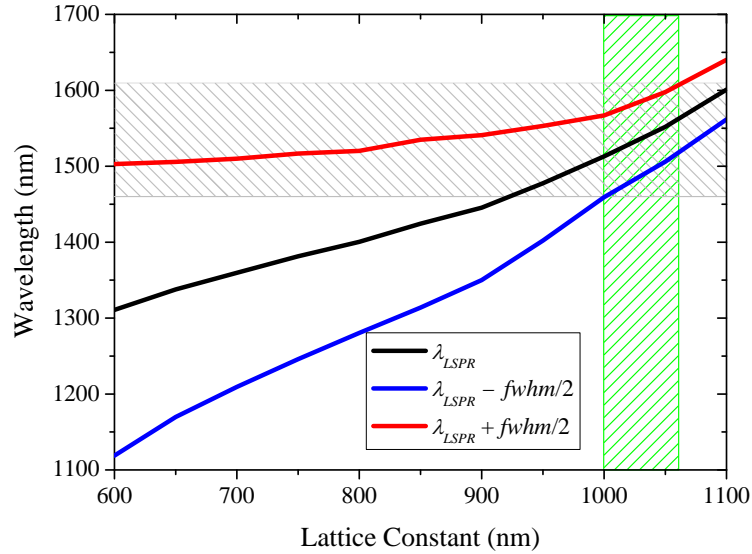
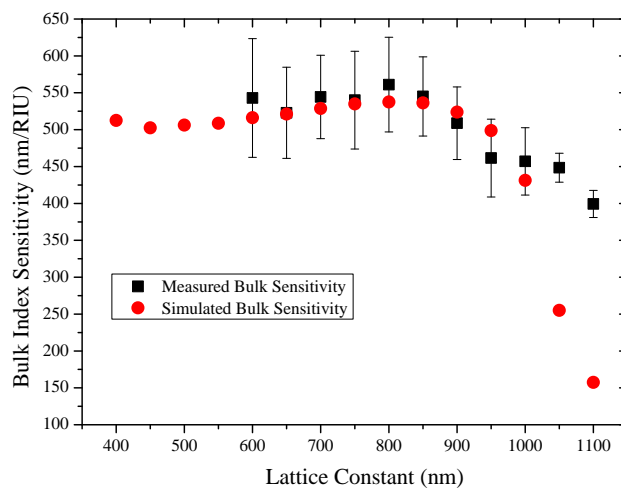


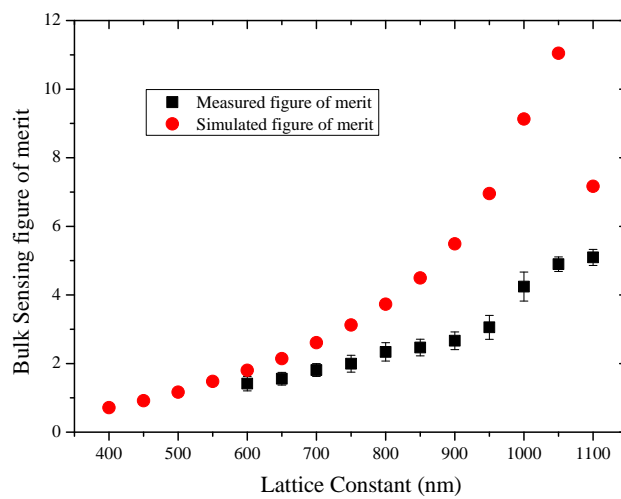
Figure 8.5: The interrogation spectral range for each lattice constant determined by the extinction peak wavelength and linewidth. The gray shadow region covers the proposed spectral range; the green shadow region covers the lattice constants satisfying the requirements.

simulated and measured figure of merit result from the aforementioned discrepancies in peak linewidth and bulk sensitivity together.

It should be emphasized that, for the lattice constants $1000 \text{ nm} < a < 1060 \text{ nm}$, functioning within the proposed spectral range, the figure of merit is high. Therefore, $1000 \text{ nm} < a < 1060 \text{ nm}$ is the optimized lattice constant range for wavelength-shift interrogation by considering the peak wavelength, peak linewidth and bulk sensing figure of merit together. Out of this range, we chose the device $a = 1000 \text{ nm}$ as the best lattice configuration by additionally considering the possibility of using 1550 nm laser intensity interrogation in the future because the 1550 nm interrogation wavelength is longer than the extinction peak wavelength and locates on the fast decaying slope of the extinction spectrum which gives large sensitivity in intensity change. For $a = 1000 \text{ nm}$, the obtained bulk index sensitivity is around 457 nm/RIU and the bulk index figure of merit is around 4.2 . Compared to other experimental studies, Larsson et al. [3] have studied the LSPR sensor based on randomly distributed ensemble of gold nanorings on pyrex substrate with bulk sensitivity up to 880 nm/RIU and bulk index figure of merit ~ 2 . This indicates that the periodic array effects can greatly improve the figure of merit of the sensor compared to randomly distributed nanorings.



(a)



(b)

Figure 8.6: The experimental and simulation results of the gold nanorings array: (a) bulk index sensitivity, (b) figure of merit.

8.4 Biosensor applications

To explore the biosensor applications of the nanoring arrays, we carried out experiments to detect binding of biotins to the streptavidins immobilized onto the surface of the gold nanorings. The molecular pair of streptavidins and biotins have extraordinary high affinity, with a dissociation constant on the order of 10^{-14} M. It should be noted that biotin molecules are very small molecules with molecular weight of 244 Dalton. The capability of the sensor to detect such small molecules provide important information on the sensor performance.

To immobilize the streptavidins, we followed the procedures described by Choi et al. [22]. The procedures are shown in Figure 8.7(a). After the sample ($a = 1000$ nm) was thoroughly cleaned and mounted onto the flow cell, a mixture of 3-mercaptopropanol (3-MPOH) and 11-mercaptoundecanoic acid (11-MUA) in absolute ethanol was continuously flowed on the sensor surface at $1 \mu\text{L}/\text{min}$ for 18 hours to form a well organized self-assembled monolayer (SAM) with carboxylic and hydroxyl terminal groups on the surface of gold nanorings. The molar ratio of 3-MPOH and 11-MUA is 10:1, and the total concentration is 10 mM. Then ethanol followed by deionized water was flowed at $1\text{mL}/\text{min}$ for 30 minutes to thoroughly rinse the surface. A 1:1 mixture of 0.2 M 1-ethyl-3-(3-dimethylaminopropyl) carbodiimide (EDC) and 0.4 M N-hydroxysuccinimide (NHS) solutions was flowed into the sensor at $10 \mu\text{L}/\text{min}$ for 3 hours to activate the terminal carboxylic groups into amine-reactive succinimide esters. Then streptavidins ($360 \mu\text{g}/\text{mL}$) in PBS buffer ($\text{pH} = 7.4$) was injected at a rate of $10 \mu\text{L}/\text{min}$. The sensor was incubated for 1 hour and the streptavidin biomolecules were covalently linked to the carboxylic terminal groups of the mixed SAM. After rinsing the sensor with PBS buffer, $10 \mu\text{g}/\text{mL}$ bovine serum albumin (BSA) in PBS buffer was flowed at $10 \mu\text{L}/\text{min}$ for 30 minutes, in order to block the non-reacted sites. As observed in Figure 8.7(b), the peak red-shift due to the binding of streptavidins and BSA to the surface of gold. Biotins in PBS buffer with increasing concentrations from $1 \mu\text{g}/\text{mL}$ to $1\text{mg}/\text{mL}$ were sequentially injected into the sensor. For each concentration, the solution was continuously flowed at $10 \mu\text{L}/\text{min}$ for 10 minutes to reach equilibrium. Then PBS buffer was injected to rinse the sensor for 5 minutes to rinse out weakly adsorbed biotins, and the extinction spectrum is then recorded.

The amount of peak shift due to the binding of biotins to the streptavidins

was plotted against the concentration of biotins in Figure 8.7(c). The peak shift is linearly dependent on the logarithmic of the analyte concentration. The uncertainty in determining the peak is around 0.03 nm, and the limit of detection (LOD) is estimated to be better than 50 ng/mL or equally 200 nM. Our sensor is comparable to the plasmonic nanorod metamaterials with a LOD of 300nM [23]. Compared to the conventional SPR thin film sensor with a LOD of $> 100 \mu\text{M}$ (reported in [23]), our sensor is more than two orders of magnitude better.

8.5 Conclusions

We have successfully produced a near-infrared nanoplasmonic sensor based on periodic array of gold nanorings fabricated on pyrex. The dependence of the sensing characteristics on the lattice constant was studied in experiments and matched qualitatively with FDTD simulations. The differences in quantities were mainly due to the different magnitudes of coherent interactions between experiments and simulations. We have proposed a near-infrared sensing scheme to interrogate the wavelength-shift within the spectral window 1460 nm - 1610 nm, to benefit from the technologies developed for fiber-optic communication. It should be noted that this proposed range is rather narrow for wavelength-shift interrogation of random or single near-infrared nanoparticles, which generally have much larger linewidth. The periodic array, with significantly reduced linewidth, makes it practical to function within this narrow spectral range. To function in the proposed range, the optimized sensor satisfied all the required conditions in terms of the peak wavelength and peak linewidth, and, at the same time, achieved a figure of merit larger than 4. In detecting the small molecules such as biotins, the sensor can reach a limit of detection around 200 nM, better than the conventional SPR sensor.

8.6 Acknowledgements

The authors acknowledge Natural Sciences and Engineering Research Council of Canada (NSERC), CMC Microsystems and Canada Foundation for Innovation (CFI) for funding this research work. The authors acknowledge student funding for Hao

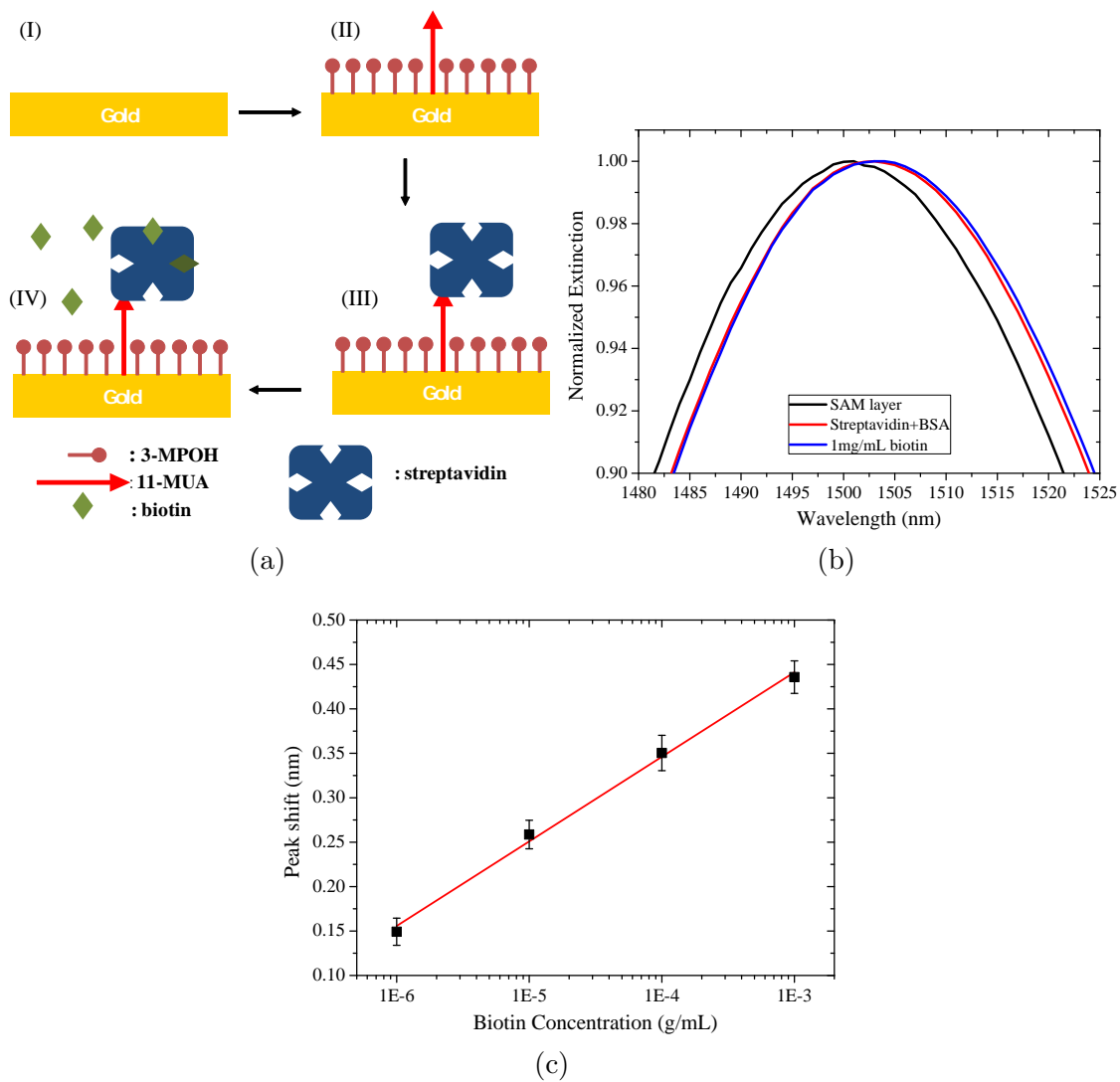


Figure 8.7: Sensor response of device $a=1000$ nm for detection of the biotin molecules. (a) schematic for the surface chemistry procedures, (b) extinction peaks in each step of surface functionalization, (c) peak shift due to different concentration of biotins. The straight line serves as guide for eyes.

Jiang from BiopSys (NSERC Network Centers for Excellence) grant. The device fabrication was done at the University of Western Ontario Nanofabrication facility. The simulations were carried out using SHARCNET computing facilities.

References

- [1] J. Aizpurua, P. Hanarp, D. S. Sutherland, M. Kall, G. W. Bryant, and F. J. Garcia de Abajo, "Optical properties of gold nanorings," *Phys. Rev. Lett.*, vol. 90, no. 5, p. 057401, 2003.
- [2] C. L. Nehl, N. K. Grady, G. P. Goodrich, F. Tam, N. J. Halas, and J. H. Hafner, "Scattering spectra of single gold nanoshells," *Nano Letters*, vol. 4, no. 12, pp. 2355–2359, 2004.
- [3] E. M. Larsson, J. Alegret, M. Kall, and D. S. Sutherland, "Sensing characteristics of NIR localized surface plasmon resonances in gold nanorings for application as ultrasensitive biosensors," *Nano Letters*, vol. 7, no. 5, pp. 1256–1263, 2007.
- [4] C.-Y. Tsai, S.-P. Lu, J.-W. Lin, and P.-T. Lee, "High sensitivity plasmonic index sensor using slablike gold nanoring arrays," *Applied Physics Letters*, vol. 98, no. 15, p. 153108, 2011.
- [5] S. D. Liu, Z. S. Zhang, and Q. Q. Wang, "High sensitivity and large field enhancement of symmetry broken Au nanorings: effect of multipolar plasmon resonance and propagation," *Opt. Express*, vol. 17, no. 4, pp. 2906–2917, 2009.
- [6] H. Jiang and J. Sabarinathan, "Effects of coherent interactions on the sensing characteristics of near-infrared gold nanorings," *The Journal of Physical Chemistry C*, vol. 114, no. 36, pp. 15 243–15 250, 2010.
- [7] S. L. Teo, V. K. Lin, R. Marty, N. Large, E. A. Llado, A. Arbouet, C. Girard, J. Aizpurua, S. Tripathy, and A. Mlayah, "Gold nanoring trimers: a versatile structure for infrared sensing," *Opt. Express*, vol. 18, no. 21, pp. 22 271–22 282, 2010.
- [8] A. Unger and M. Kreiter, "Analyzing the performance of plasmonic resonators for dielectric sensing," *J. Phys. Chem. C*, vol. 113, pp. 12 243–12 251, 2009.

- [9] G. J. Nusz, A. C. Curry, S. M. Marinakos, A. Wax, and A. Chilkoti, "Rational selection of gold nanorod geometry for label-free plasmonic biosensors," *ACS Nano*, vol. 3, no. 4, pp. 795–806, 2009.
- [10] A. Dmitriev, C. Hagglund, S. Chen, H. Fredriksson, T. Pakizeh, M. Kall, and D. S. Sutherland, "Enhanced nanoplasmonic optical sensors with reduced substrate effect," *Nano Letters*, vol. 8, no. 11, pp. 3893–3898, 2008.
- [11] C. Novo, A. M. Funston, I. Pastoriza-Santos, L. M. Liz-Marzan, and P. Mulvaney, "Influence of medium refractive index on the optical properties of single gold triangular prisms on a substrate," *J. Phys. Chem. C*, vol. 112, no. 1, pp. 3–7, 2008.
- [12] L. J. Sherry, S.-H. Chang, G. C. Schatz, R. P. Van Duyne, B. J. Wiley, and Y. Xia, "Localized surface plasmon resonance spectroscopy of single silver nanocubes," *Nano Letters*, vol. 5, no. 10, pp. 2034–2038, 2005.
- [13] W. A. Murray, B. Auguie, and W. L. Barnes, "Sensitivity of localized surface plasmon resonances to bulk and local changes in the optical environment," *J. Phys. Chem. C*, vol. 113, pp. 5120–5125, 2009.
- [14] M. Meier, A. Wokaun, and P. F. Liao, "Enhanced fields on rough surfaces: dipolar interactions among particles of sizes exceeding the Rayleigh limit," *J. Opt. Soc. Am. B*, vol. 2, no. 6, pp. 931–949, 1985.
- [15] B. Lamprecht, G. Schider, R. T. Lechner, H. Ditlbacher, J. R. Krenn, A. Leitner, and F. R. Aussenegg, "Metal nanoparticle gratings: influence of dipolar particle interaction on the plasmon resonance," *Phys. Rev. Lett.*, vol. 84, no. 20, pp. 4721–4724, 2000.
- [16] J. Sung, E. M. Hicks, R. P. Van Duyne, and K. G. Spears, "Nanosphere spectroscopy: dipole coupling in two-dimensional arrays of L-shaped silver nanoparticles," *J. Phys. Chem. C*, vol. 111, pp. 10 368–10 376, 2007.
- [17] J. Sung, E. M. Hicks, R. P. Van Duyne, and K. G. Spears, "Nanoparticle spectroscopy: plasmon coupling in finite-sized two-dimensional arrays of cylindrical silver nanoparticles," *The Journal of Physical Chemistry C*, vol. 112, no. 11, pp. 4091–4096, 2008.

- [18] C. L. Haynes, A. D. McFarland, L. Zhao, R. P. Van Duyne, G. C. Schatz, L. Gunnarsson, J. Prikulis, B. Kasemo, and M. Kall, "Nanoparticle optics: The importance of radiative dipole coupling in two-dimensional nanoparticle arrays," *J. Phys. Chem. B*, vol. 107, pp. 7337–7342, 2003.
- [19] H. Jiang, J. Sabarinathan, T. Manifar, and S. Mittler, "3-D FDTD analysis of gold-nanoparticle-based photoniccrystal on slab waveguide," *J. Lightwave Technol.*, vol. 27, no. 13, pp. 2264–2270, 2009.
- [20] E. M. Hicks, S. Zou, G. C. Schatz, K. G. Spears, R. P. Van Duyne, L. Gunnarsson, T. Rindzevicius, B. Kasemo, and M. Kall, "Controlling plasmon line shapes through diffractive coupling in linear arrays of cylindrical nanoparticles fabricated by electron beam lithography," *Nano Letters*, vol. 5, no. 6, pp. 1065–1070, 2005.
- [21] M. A. Otte, B. Sepulveda, W. Ni, J. P. Juste, L. M. Liz-Marzan, and L. M. Lechuga, "Identification of the optimal spectral region for plasmonic and nanoplasmonic sensing," *ACS Nano*, vol. 4, no. 1, pp. 349–357, 2010.
- [22] S. H. Choi, J. W. Lee, and S. J. Sim, "Enhanced performance of a surface plasmon resonance immunosensor for detecting Ab-GAD antibody based on the modified self-assembled monolayers," *Biosensors and Bioelectronics*, vol. 21, no. 2, pp. 378 – 383, 2005.
- [23] A. V. Kabashin, P. Evans, S. Pastkovsky, W. Hendren, G. A. Wurtz, R. Atkinson, R. Pollard, V. A. Podolskily, and A. V. Zayats, "Plasmonic nanorod metamaterials for biosensing," *Nature Materials*, vol. 8, pp. 867–871, 2009.

Chapter 9

Summary and Further Development

9.1 Summary

In the scope of this thesis, four types of nanoplasmonic sensor configurations based on periodic array of gold nanoparticles have been investigated. They are summarized below in the following sections.

9.1.1 Periodic arrays of gold nanodisks coupled with the evanescent field of a waveguide

Using 3-D FDTD method, the periodic array of gold nanodisks coupled with the evanescent field of a waveguide mode can be accurately simulated. In the work presented in Chapter 3, quadrupolar plasmon resonance peaks of large nanodisks were studied with different lattice constants and varying waveguide slab thicknesses. The nanodisks in the array were found to interact with each other through the light carried by second back-scattered grating order and the LSPR peak red-shifts with increasing waveguide slab thickness. The sensing applications of the structure were also proven by simulations. These theoretical investigations provide a basis for tuning the resonance of the waveguide-excited LSPR of the periodic array of gold nanoparticles.

In the work presented in Chapter 4, dipolar resonance of the periodic array of nanodisks coupled with the waveguide was investigated both in experiments and in simulations. The waveguides in experiments were fabricated in BK7 glass via thermal Ag^+ - Na^+ ion-exchange. A lithographically patterned metal mask was used to define S-bend waveguides. Periodic arrays of gold nanodisks were fabricated on top of the waveguides and the extinction spectra were measured by a waveguide transmission setup. The LSPR peak was found to red-shift with increasing lattice constant, indicating the interactions of the gold nanodisks coupled with the waveguide mode. However, due to the silver colloids produced during the ion-exchange process,

the waveguides was too lossy, leading to a very low S/N ratio. As a result, the measured spectra were very noisy and the peak shift could not be calculated with sufficiently high accuracy. Sensing applications based on these waveguides require further improvements on the quality of the waveguides. A proposed approach based on K^+ - Na^+ ion-exchange will be presented in section 9.2.1. To understand the interactions of the periodic array in more detail and to investigate the overlap between photonic band gap and the LSPR peak, 3-D FDTD simulations were carried out. The quadrupolar peak and the dipolar peak were both discussed in detail, and they were both appropriate for sensing applications. Sharp extinction dips and sharp extinction peaks were found from the simulated extinction spectra. A closer study revealed that the sharp dip are due to the suppressed plasmon resonance by the photonic band gap while the sharp extinction peaks are a quadrupolar grating-induced mode. The unique properties of these modes were discussed in detail, but these features were not sensitive to the change in a surface-bound layer, meaning that they are not appropriate for LSPR sensing applications.

The optical properties of the periodic arrays of gold nanoparticles have only been studied by other researchers from normal transmission, mainly focused on dipolar resonance modes. From this study, it was found that, the same physics of coherent interactions is still the mechanism in the waveguide transmission and for quadrupolar resonance modes. However, the difference in the waveguide transmission is that, the interaction is through the grating order carried by the waveguide mode. Such a study is an extension of the existing knowledge of the periodic array.

9.1.2 Biosensor based on periodic array of gold nanodisks under normal transmission

In Chapter 5, the biosensing application of the periodic array of gold nanodisks was successfully investigated under normal transmission, owing to sufficient S/N ratio ~ 300 of such measurement setup. The structures were fabricated on top of BK7 glass substrates and integrated with a transparent glass-based flow cell. The extinction spectra of the sensor structure were measured from the normal transmission of a broad-band light beam. The sensor's detection uncertainty was characterized in experiments and its relation to the lattice constants and S/N ratio was discussed in detail. The best refractive index resolution achieved is $< 1.5 \times 10^{-4}$ RIU, when

the lattice constant is equal to 550 nm. Through surface chemistry procedures, biotinylated antibody (anti-human IgG) was immobilized on the sensor surface and the sensor response was recorded in real-time. Human IgG with increasing concentrations were sequentially injected onto the sensor and the response for each concentration was recorded. The sensor is able to reach a limit of detection <1 ng/mL, i.e. better than a concentration of 8 pM.

An important conclusion for this study is that, the S/N ratio and figure of merit are equally important in determining the limit of detection of an LSPR sensor. A high performance LSPR sensor system should be configured with two aspects: high figure of merit of the nanostructure and high S/N ratio of the detection system.

9.1.3 Chemical sensor based on pH sensitive hydrogel thin film coated on the gold nanocrescent array

Closely-packed gold nanocrescents array with random orientations were fabricated on ITO-coated glass substrate via electron beam lithography. A pH-sensitive hydrogel thin film based on poly(hydroxyethyl methacrylate-co-methacrylic acid) was coated on top of the gold nanocrescent structure. After coating, the extinction peak around 1828 nm was attributed to the 'C₁' mode of the nanocrescent and the bulk refractive index sensitivity was estimated to be 332 nm/RIU. Chemical solutions with increasing pH values were introduced onto the sensor and the change of the pH made the hydrogel swell or shrink which lead to the shift of the extinction peak. The sensor response was interrogated both from the peak shift and from the transmitted intensity. At the point of $\text{pH} = pK_a$, which is the inflection point of the fitted titration response curves, the sensitivity of the extinction peak shift is 11.1 nm/pH while the sensitivity of the transmission is 1.16 /pH. The detection pH range was determined to be 4.5 \sim 6.4 with the boundaries where the sensitivity decreases by half. As the hydrogel swells in this range, the water content increases in the hydrogel film which decreases the refractive index. The extinction peak thus blue-shifts, from 1772 nm into 1755 nm, and the integrated transmission response increases from 56.8 into 58.6.

The detection resolution achieved from this sensor is estimated to be around 0.045 pH. It should be noted, that, there is still a lot of room to improve the detection resolution. Due to the random orientations of the gold nanocrescents, the figure of merit of this device is low, around 0.4. If such a hydrogel chemical sensor uses a

nanostructure of high figure of merit loaded in a high S/N ratio detection system, the detection resolution can be expected to be significantly improved.

9.1.4 LSPR sensor based on gold nanoring arrays

In the work presented in Chapter 7, the effects of coherent interactions on the sensing characteristics of periodic arrays of the gold nanorings were studied in detail using 3-D FDTD simulations. Patterning the gold nanoparticles into a periodic array was proved to be an effective strategy to improve the sensing figure of merit: the bulk refractive index sensing figure of merit of the array can be 3 times higher than the single nanoring and the surface sensing figure of merit can be 2.5 times higher than the single nanoring. The improvement was mainly obtained from the controllable narrow spectral linewidth due to coherent interactions of the periodic array. The optimum configuration for sensing applications using the periodic array is the lattice constant with the highest figure of merit, in the evanescent grating order range. In this range, as the lattice constant increases, the figure of merit increases due to significantly reduced linewidth, and the sensitivity decreases because the coherent interactions reduce the field confinement in the sensing region. In the radiative grating order range, as the lattice constant increases, the figure of merit decreases due to the radiative damping. Although the device in this range has very high sensitivity, it was found to be inappropriate for LSPR sensor applications due to the nonlinear response and the complicated peak shape which makes it difficult to quantify the amount of peak shift. The grating-induced modes, corresponding to the substrate grating order, were observed in simulations but not in experiments. Since the grating-induced peaks are mainly determined by the refractive index of the substrate, when the grating-induced mode dominates in the extinction spectra, the sensitivity and figure of merit are very low. These trends provide a design rule on how to engineer the particle spacing of a periodic array of metal nanoparticles to achieve the highest figure of merit for LSPR sensing.

In the work presented in Chapter 8, the trends discovered in Chapter 7 were applied in the design of a nanoplasmonic sensor based on periodic array of gold nanorings operating within the fiber-optic communication window. The dependence of the sensing characteristics on the lattice constant was studied in experiments. The experimental results matched with FDTD simulations qualitatively. The differences

in quantities were mainly due to the different magnitudes of coherent interactions between experiments and simulations. The highest achieved figure of merit from the experiment is 5.1. Compared to other gold nanoparticles listed in Table 1.1, the achieved figure of merit is among the highest. A sensing scheme was proposed to interrogate the wavelength-shift within the spectral window 1460 nm - 1610 nm, to benefit from the technologies developed for fiber-optic communication. Using the significantly reduced linewidth of the periodic array, the sensor with optimized lattice constant can function within this narrow spectral range, and, at the same time, achieve a figure of merit ~ 4.2 . The bulk refractive index sensitivity of the optimized configuration is 457 nm/RIU. As a proof of concept, the sensor was implemented in detecting biotins (small molecules with molecular weight ≈ 244 Dalton), the sensor can reach a limit of detection around 200 nM, better than the conventional SPR sensor.

9.2 Further development

9.2.1 Waveguide fabrication

The major problem in the waveguide-excited LSPR sensor is the high optical loss caused by the silver colloids produced during $\text{Ag}^+ - \text{Na}^+$ ion-exchange process. This could be overcome by an alternative technique using $\text{K}^+ - \text{Na}^+$ ion-exchange. Due to the small polarizability of potassium ions, the potassium ion-exchange can only produce an index difference an order lower than the silver ion-exchange. However, high quality single mode waveguides can be obtained. According to the study by Weiss et al. [1], ion-exchange of BK7 glass in KNO_3 at 375 °C using a 3 μm opening in aluminum mask can produce a channel waveguide of 9.2 μm wide and 3.4 μm deep, and the index contrast on the surface $\Delta n \sim 0.008$. Such a waveguide was simulated using beam propagation method (BPM), and the results are shown in Figure 9.1. The channel waveguide is single mode in the range from 600 nm to 1100 nm, very appropriate for the proposed sensor. Due to the small index contrast, the waveguide mode can match the fiber mode very closely, which is an advantage for fiber coupling. Figure 9.1(c) presents the power coupled into the waveguide mode from a 5 μm wide Gaussian beam mimicking the output of an optical fiber. The coupling efficiency is better than 80%.

Waveguide-LSPR sensor based on the K^+ - Na^+ ion-exchange waveguide can very likely exhibit high S/N ratio which can provide basis for the sensing applications using the integrated waveguides scheme shown in Figure 1.4.

9.2.2 Integration with PDMS fluidic channels for multiplexed detections

One advantage of the nanoplasmonic sensors based on the gold nanoparticles is the small scale of each sensor element. Multiple sensor elements can be integrated into the same sensor chip to achieve multiplexed detections. Specifically, each sensor element can be independently addressed by a fluidic channel and be measured without interference from other sensors. The key to achieve the multiplexed detection is a microfluidic channel device which can be integrated onto the sensor device. Polydimethylsiloxane (PDMS) microfluidic channel device has been designed and fabricated for this purpose. First an SU8 photoresist was spin-coated on the silicon wafer and patterned by photolithography to form a solid mold. A photo of the fabricated mold is presented in Figure 9.2(a). Monomers of PDMS were then casted on the mold and thermally polymerized. A degassing process by loading the coated mold in vacuum was applied before the thermal treatment to remove air bubbles inside casted PDMS film. After full polymerization, the PDMS film was peeled off from the mold and cut into individual devices. The bonding side of the PDMS device was exposed to UV for 30 min and bonded to the surface of the glass substrate. In the following, a thermal treatment created chemical bonds and made the bonding between the microfluidic device and the sensor device permanent.

A scheme on how to use the PDMS microfluidic device for multiplexed detection is shown in Figure 9.2(b). With the assistance of a microscope and alignment stage, the fluidic channels can be easily aligned with a waveguide sensor device. A microscope image of the fluidic channel aligned with the waveguide channel is shown in Figure 9.2(c). Fiducial marks on the PDMS and the fiducial marks on the sensor device are matched sufficiently close to each other. However, there are still certain challenges in using PDMS microfluidic devices. First, the PDMS has to be made very flat to avoid the effects of the optical interference at the interfaces. Such interference can add a periodic 'wave' on the measured extinction spectra, generating problems for quantification of the peak location. Second, the PDMS has strong absorption

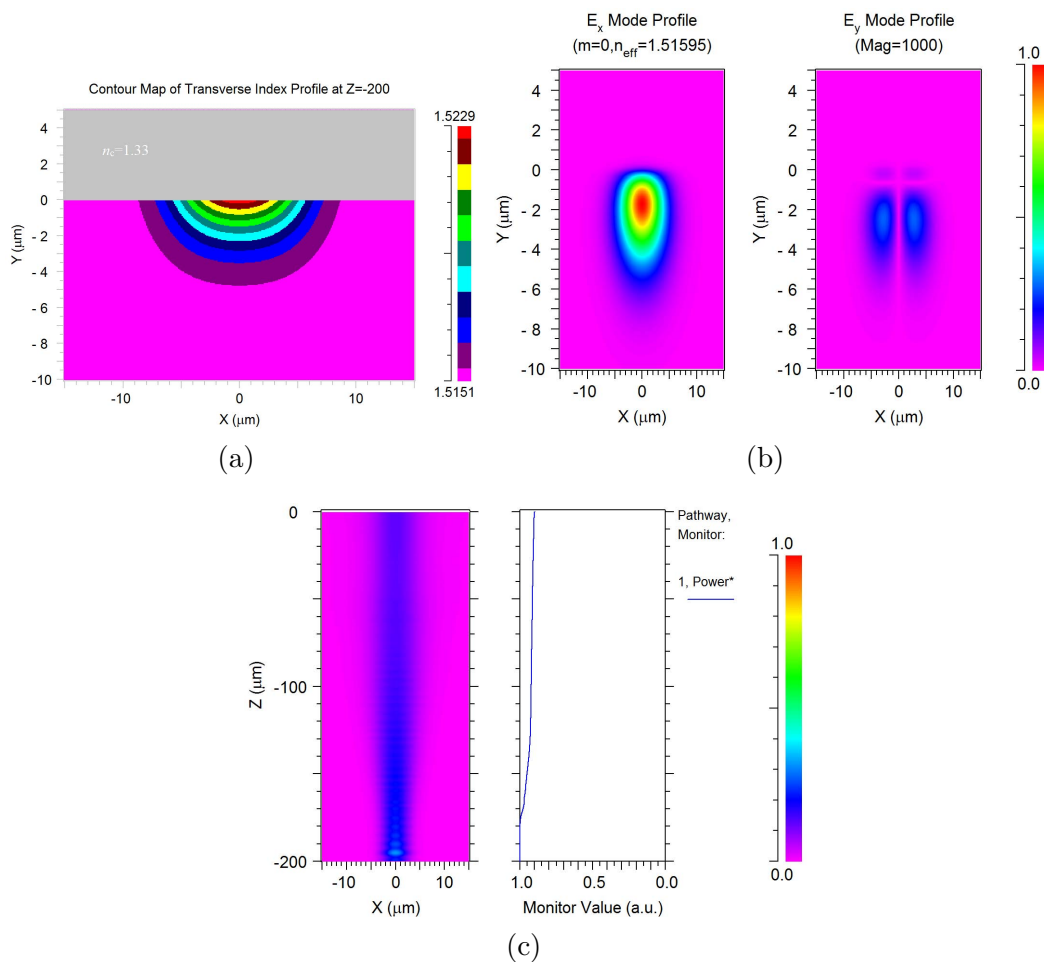


Figure 9.1: BPM simulation of the waveguide mode of K^+ - Na^+ ion-exchange waveguide. (a) Refractive index profile of the cross-section of the K^+ - Na^+ exchange on BK7 glass with 3 μm mask opening. (b) Simulated TE_0 mode at a wavelength of 800 nm. (c) Propagation of light launched into the waveguide from a 5 μm wide Gaussian beam. The entrance interface of the waveguide is located at $z = -200 \mu\text{m}$.

in the near-infrared spectrum range, which reduce the intensity of transmitted light (Figure 9.2(d)). Fortunately, there exist two windows with relatively low absorption, 1200 nm \sim 1370 nm and 1440 nm \sim 1650 nm. The optimized gold nanorings array presented in Chapter 8 can work within the second window.

9.2.3 Other development

Besides the aforementioned waveguide fabrication scheme and the integration with microfluidic devices, the nanoplasmonic sensors presented in this thesis need further development in surface chemistry, fabrication consistency and robustness. Alternative techniques to solve these issues may be poly(ethylene glycol) chemistry [2], nanosphere lithography[3], nanoimprint lithography [4, 5], etc.

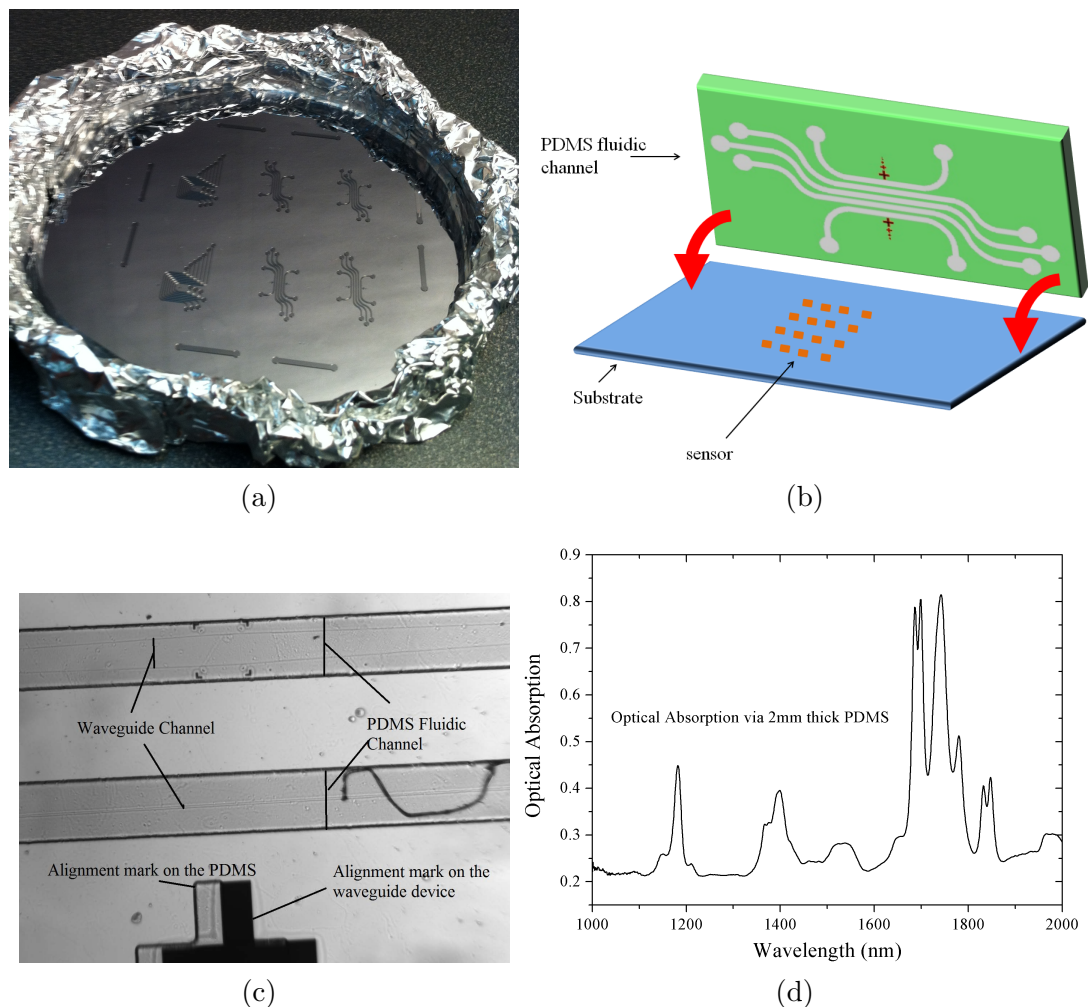



Figure 9.2: The development of the PDMS microfluidic device integrated with the nanoplasmonic sensors. (a) Photo of fabricated mold consisted of SU8 patterned on silicon wafer. Multiple microfluidic devices are integrated on the same mold. (b) Scheme of the application idea. Multiple LSPR sensor elements are patterned on the substrate. A microfluidic device consisting of multiple channels is aligned with the sensors and bonded to the glass substrate. (c) Microscope image of a microfluidic channel aligned with the channel waveguide. The fluidic channel is 200 μm wide while the waveguide is 100 μm wide. (d) Near-infrared absorption spectrum of 2 mm thick PDMS.

References

- [1] M. N. Weiss and R. Srivastava, “Determination of ion-exchanged channel waveguide profile parameters by mode-index measurements,” *Appl. Opt.*, vol. 34, no. 3, pp. 455–458, 1995.
- [2] J. M. Harris, *Poly(ethylene glycol) Chemistry: biotechnical and biomedical applications*. Plenum Press, New York, 1992.
- [3] W. Li, W. Zhao, and P. Sun, “Fabrication of highly ordered metallic arrays and silicon pillars with controllable size using nanosphere lithography,” *Physica E: Low-dimensional Systems and Nanostructures*, vol. 41, no. 8, pp. 1600 – 1603, 2009.
- [4] S. Y. Chou, P. R. Krauss, and P. J. Renstrom, “Imprint of sub-25 nm vias and trenches in polymers,” *Applied Physics Letters*, vol. 67, pp. 3114–3116, 1995.
- [5] S. Kim, J.-M. Jung, D.-G. Choi, H.-T. Jung, and S.-M. Yang, “Patterned arrays of au rings for localized surface plasmon resonance,” *Langmuir*, vol. 22, pp. 7109–7112, 2006.

Appendix A
Copyright Permission for Material
Contained in Chapter 3



Welcome | [Log in](#) | [Cart \(0\)](#) | [Manage Account](#) | [Feedback](#) | [Help](#) | [Live Help](#)

GET PERMISSION
LICENSE YOUR CONTENT
PRODUCTS AND SOLUTIONS
PARTNERS
ABOUT US

[Get Permission / Find Title](#)
 [Go](#)
[Advanced Search Options](#)

Journal of lightwave technology : a joint IEEE/OSA publication

ISSN: 0733-8724	Language: English
Publication year(s): 1983 - present	Country of publication: United States of America
Author/Editor: INSTITUTE OF ELECTRICAL AND ELECTRONICS ENGINEERS.	
Publication type: Journal	
Publisher: I E E E	
Rightsholder: IEEE - INST OF ELECTRICAL AND ELECTRONICS ENGRS	

Permission type selected: Republish or display content

Type of use selected: reuse in a thesis/dissertation

Select different permission

Article title: 3-D FDTD Analysis of Gold-Nanoparticle-Based Photonic Crystal on Slab Waveguide

Author(s): Hao Jiang

DOI: 10.1109/JLT.2008.2006577

Date: Jul 1, 2009

Volume: 27

Issue: 13

Select different article

Thesis / Dissertaion Reuse

We are happy to grant this permission. Our only requirement is that the requester provides a full credit notice to the original source (author, paper, publication), followed by the IEEE copyright notice.

[← Back](#)

Appendix B
Copyright Permission for Material
Contained in Chapter 5

Dear Dr. Jiang,

This is our official permissions statement:

OSA considers your requested use of its copyrighted materials to be permissible within the author rights granted in the Copyright Transfer Agreement submitted by the requester on acceptance for publication of his/her manuscript.

The author rights referred to above are as follows:

“OSA grants to the Author(s) (or their employers, in the case of works made for hire) the following rights. The Author(s) agree that all copies of the Work made under any of these following rights shall include notice of the OSA copyright.

- (a) The right, after publication by OSA, to use all or part of the Work without revision or modification, including the OSA-formatted version, in personal compilations or other publications consisting solely of the Author(s)' own works, including the Author(s)' personal web home page, and to make copies of all or part of the Work for the Author(s)' use for lecture or classroom purposes;
- (b) The right to post and update his or her Work on any internet site (other than the Author(s)' personal web home page) provided that all of the following conditions are met: (i) files prepared and/or formatted by OSA or its vendors are not used; (ii) access to the server does not depend on payment for access, subscription or membership fees; and (iii) any such posting made or updated after acceptance of the Work for publication includes and prominently displays the correct bibliographic data and an OSA copyright notice (e.g. "© 2001 Optical Society of America, Inc.");
- (c) All proprietary rights other than copyright, such as patent rights; and
- (d) If the Work has been prepared by an employee within the scope of his or her employment or as a work made for hire, the right to make copies of the Work for the employer's internal use.”

I hope that this will be sufficient. Please let me know if you have any questions.

Best,

Hannah

Hannah Bembia
October 17, 2011
Authorized Agent, The Optical Society

Appendix C
Copyright Permission for Material
Contained in Chapter 6



RightsLink®

Home

Create Account

Help

ACS Publications
High quality. High impact.

Title: Effects of Coherent Interactions on the Sensing Characteristics of Near-Infrared Gold Nanorings

Author: Hao Jiang et al.

Publication: The Journal of Physical Chemistry C

Publisher: American Chemical Society

Date: Sep 1, 2010

Copyright © 2010, American Chemical Society

User ID
Password
<input type="checkbox"/> Enable Auto Login
<input type="button" value="LOGIN"/>
Forgot Password/User ID?
If you're a copyright.com user, you can login to Rightslink using your copyright.com credentials. Already a Rightslink user or want to learn more?

PERMISSION/ LICENSE IS GRANTED FOR YOUR ORDER AT NO CHARGE

This type of permission/license, instead of the standard Terms & Conditions, is sent to you because no fee is being charged for your order. Please note the following:

- Permission is granted for your request in both print and electronic formats.
- If figures and/or tables were requested, they may be adapted or used in part.
- Please print this page for your records and send a copy of it to your publisher/graduate school.
- Appropriate credit for the requested material should be given as follows: "Reprinted (adapted) with permission from (COMPLETE REFERENCE CITATION). Copyright (YEAR) American Chemical Society." Insert appropriate information in place of the capitalized words.
- One-time permission is granted only for the use specified in your request. No additional uses are granted (such as derivative works or other editions). For any other uses, please submit a new request.

BACK

CLOSE WINDOW

Curriculum Vitae

Name:	Hao Jiang
Place of birth:	Heilongjiang, China
Year of birth:	1983
Post-secondary Education and Degrees:	2007-2011 Ph.D Electrical & Computer Engineering The University of Western Ontario London, Ontario, Canada
Post-secondary Education and Degrees:	2005-2007 Master Electrical & Computer Engineering The University of Western Ontario London, Ontario, Canada
Post-secondary Education and Degrees:	2001-2005 Bachelor Electronics Peking University (Beijing University) Beijing, China

Publications:

- [1] H. Jiang, J. Sabarinathan, T. Manifar and S. Mittler, '3-D FDTD analysis of gold-nanoparticle-based photonic crystal on slab waveguide', *Journal of Light-wave Technology*, 27 (13), pp. 2264-2270, 2009.
- [2] H. Jiang, J. Markowski and J. Sabarinathan, 'Near-infrared optical response of thin film pH-sensitive hydrogel coated on a gold nanocrescent array', *Optics Express*, 17 (24), pp. 21802-21807, 2009.
- [3] H. Jiang, J. Sabarinathan and S. Mittler, 'Effects of coherent interactions on the sensing characteristics of near-infrared gold nanorings', *Journal of Physical Chemistry C*, 114 (36), pp 15243-15250, 2010.